CORA Cork Open Research Archive
Cartlann Taighde Oscailte Chorcaí

Title	Broadband optical cavity absorption spectroscopy in the near-ultraviolet: applications in atmospheric chemistry
Authors	Chen, Jun
Publication date	2011
Original Citation	Chen, J., 2011. Broadband optical cavity absorption spectroscopy in the near-ultraviolet: applications in atmospheric chemistry. PhD Thesis, University College Cork.
Type of publication	Doctoral thesis
Link to publisher's version	http://library.ucc.ie/record=b2027881~S0
Rights	© 2011, Jun Chen - http://creativecommons.org/licenses/by-nc-nd/3.0/
Download date	2026-11-15 02:06:14
Item downloaded from	https://hdl.handle.net/10468/435

UCC
University College Cork, Ireland
Coláiste na hOllscoile Corcaigh

Broadband Optical Cavity Absorption Spectroscopy in the Near-Ultraviolet: Applications in Atmospheric Chemistry

A thesis submitted to

THE NATIONAL UNIVERSITY OF IRELAND



For the degree of

DOCTOR OF PHILOSOPHY

by

Jun Chen

Based on Research Performed in the
Department of Chemistry
and at
Environmental Research Institute,
University College Cork

Under the supervision of

Dr. Dean S. Venables

Head of Department

Prof. John Sodeau

April 2011

Table of Contents

INTRODUCTION..... ..1
1.1 Atmospheric photochemistry.....2
1.1.1 *Ozone*.....4
1.1.2 *The hydroxyl radical*.....6
1.1.3 *Nitrogen oxides*.....7
1.1.4 *Halogens*.....10
1.1.5 *Nitrous acid*.....13
1.1.6 *Nitrophenols*.....15
1.2 Near-ultraviolet absorption spectroscopy methods.....15
1.2.1 *Absorption measurements in the atmosphere*.....15
1.2.2 *Spectroscopic methods*.....17
1.2.3 *Incoherent broadband cavity enhanced absorption spectroscopy*.....20
1.3 Aim of the work.....21
Bibliography.....23

INCOHERENT BROADBAND CAVITY-ENHANCED SPECTROSCOPY.....35
2.1 Prior cavity absorption methods.....37
2.2 Principle of measurement.....40
2.3 Components of the spectrometer.....43
2.3.1 *The light source*.....43
2.3.2 *Spectral filtering*.....46
2.3.3 *Detector*.....48
2.4 Instrument performance.....49
2.4.1 *Allan variance study*.....49
2.4.2 *Sensitivity*.....51
2.4.3 *Effect of flow rate and pressure on the cavity signal*.....52
2.5 Calibration of the instrument.....53
2.5.1 *Spectrograph wavelength and resolution*.....53
2.5.2 Calibration of the mirror reflectivity.....55
2.6 Spectral Analysis.....61
2.6.1 *Absolute absorption*.....61
2.6.2 *Differential absorption*.....62
2.6.3 *Aerosol extinction*.....64
Bibliography.....66

FLOW CELL SPECTROMETER.....73
3.1 Introduction.....74
3.2 Experimental.....75

3.2.1 *The flow cell IBBCEAS system*.....75
3.2.2 *Mirror calibration*.....78
3.2.3 *Uncertainty of cross-sections*.....*81*
3.3 NEAR UV ABSORPTION SPECTRA.....82
3.3.1 *Sulfur dioxide*.....82
3.3.2 *Ozone*.....87
3.3.3 *Ketone spectra*.....90
3.4 THE SPECTRUM OF BROMINE MONOXIDE.....93
3.4.1 *Generation of bromine monoxide*.....93
3.4.2 *Spectral analysis and quantification of BrO, Br_2, and O_3*.....95
3.5 DISCUSSION.....100
3.6 CONCLUSIONS.....102
BIBLIOGRAPHY.....103

FIELD OBSERVATIONS.....**108**
4.1 COBRA CAMPAIGN.....110
4.1.1 *Motivation*.....110
4.1.2 *Spectrometer description*.....112
4.1.3 *Campaign results*.....115
4.2 MACE HEAD CAMPAIGN.....116
4.2.1 *Motivation*.....116
4.2.2 *The Dual Cavity Spectrometer*.....119
4.2.3 *Campaign results*.....122
BIBLIOGRAPHY.....124

SIMULATION CHAMBER MEASUREMENTS.....**128**
5.1 INTRODUCTION.....129
5.2 EXPERIMENTAL.....130
5.2.1 *IBBCEAS chamber setup*.....130
5.2.2 *Instrument Calibration*.....134
5.2.3 *Standard addition method*.....138
5.3 GAS PHASE SPECTRA.....139
5.3.1 *Benzaldehyde*.....139
5.3.2 *Alkyl nitrites*.....143
5.3.3 *Nitrophenol and methyl nitrophenol spectra*.....146
5.3.4 *Quantum yield of photolysis*.....152
5.4 OPTICAL PROPERTIES OF SECONDARY ORGANIC AEROSOL.....153
BIBLIOGRAPHY.....159

FORMAL INTERCOMPARISON OF OBSERVATIONS OF NITROUS ACID.....**166**
6.1 INTRODUCTION.....167
6.2 THE EXTRACTIVE IBBCEAS SYSTEM.....168
6.2.1 *Spectrometer design*.....168

6.2.2 *Laboratory test*.....173
6.3 FIONA CAMPAIGN.....176
6.3.1 *Introduction* 176
6.3.2 *Campaign objectives and participants*.....177
6.3.3 *Experimental details*.....180
6.4 INTERCOMPARISON RESULTS.....181
6.4.1 *Experiment 2 on 18/05/2010*.....183
6.4.2 *Experiment 3 on 25/05/2010*.....186
6.4.3 *Experiment 4 on 19/05/2010*.....188
6.4.4 *Experiment 5 on 20/05/2010*.....191
6.4.5 *Experiment 6 on 24/05/2010*.....194
6.4.6 *Experiment 7 on 26/05/2010*.....196
6.4.7 *Experiment 8 on 27/05/2010*.....199
6.5 DISCUSSION.....201
6.5.1 *Quality of results and estimated uncertainty*.....201
6.5.2 *Interferences and improvements to the spectrometer* 203
6.6 CONCLUSIONS.....204
BIBLIOGRAPHY.....205

CONCLUSIONS.....208
7.1 SUMMARY OF FINDINGS.....209
7.2 FUTURE WORK.....212
BIBLIOGRAPHY.....214

APPENDIX A.....216

Declaration

The work presented in this thesis was performed in the Department of Chemistry and the Environmental Research Institute, University College Cork during the academic years 2006-2011. This thesis is the independent work of the author and has not been submitted to any institution for the purpose of obtaining any other qualification.

_____

Jun Chen

Abstract

A novel spectroscopic method, incoherent broadband cavity enhanced absorption spectroscopy (IBBCEAS), has been modified and extended to measure absorption spectra in the near-ultraviolet with high sensitivity. The near-ultraviolet region extends from 300 to 400 nm and is particularly important in tropospheric photochemistry; absorption of near-UV light can also be exploited for sensitive trace gas measurements of several key atmospheric constituents. In this work, several IBBCEAS instruments were developed to record reference spectra and to measure trace gas concentrations in the laboratory and field. An IBBCEAS instrument was coupled to a flow cell for measuring very weak absorption spectra between 335 and 375 nm. The instrument was validated against the literature absorption spectrum of SO_2. Using the instrument, new absorption cross-sections of O_3, acetone, 2-butanone, and 2-pentanone were measured in this spectral region, where literature data diverge considerably owing to the extremely weak absorption. The instrument was also applied to quantifying low concentrations of the short-lived radical, BrO, in the presence of strong absorption by Br_2 and O_3. A different IBBCEAS system was adapted to a 4 m^3 atmosphere simulation chamber to record the absorption cross-sections of several low vapour pressure compounds, which are otherwise difficult to measure. Absorption cross-sections of benzaldehyde and the more volatile alkyl nitrites agree well with previous spectra; on this basis, the cross-sections of several nitrophenols and methyl-nitrophenols are reported for the first time. In addition, the instrument was also used to demonstrate that the optical properties of secondary organic aerosol formed following the photooxidation of isoprene can be measured.

Much of the interest in the IBBCEAS approach has been for trace gas analysis. An extractive IBBCEAS instrument was developed for detecting HONO and NO_2 and had a sensitivity of about 10^{-9} cm^{-1}. This instrument participated in a major international intercomparison of HONO and NO_2 measurements held in the

EUPHORE simulation chamber in Valencia, Spain, and results from that campaign are also reported here. Issues arising from the large thermal gradients involved in the experiments compromised the stability of the IBBCEAS instrument, although the response of the system generally correlates well with large changes in the concentrations of HONO and NO_2. Suggestions for improving the instrument performance are presented. Finally, open path IBBCEAS instruments are described that were deployed in two field campaigns. These early field instruments provided useful lessons in system design for future field campaigns.

Acknowledgement

Firstly, I want to express my sincere gratitude to my supervisor Dr. Dean Venables for the opportunity to carry out this PhD research. His enthusiasm, carefulness, support and instructive guidance over the past four years will have an impact on my future career. I will always remember that he picked me up at the airport when I first arrived in Cork, which meant a lot to me. My thanks also go to the other group members, Steven Darby, Enowmbi Ashu-Ayem, and Dr. Paul Smith for their help over the last few years. I would also like to thank the members in the CRAC laboratory and the ERI for their kind assistance. I especially want to acknowledge Dr. John Wenger for allowing me to use his simulation chamber and for helpful discussions about my experiments. In my time in Cork, I have particularly appreciated the friendship of Zhou Shouming, Chen Yang, Gao Xin, Gao Min and Dai Li – I have been fortunate to know all of them.

My thanks also go to Dr. Andy Ruth for his advice and the generous loan of his optics and equipment for my experiments. I am also grateful for the members of his group, especially Dr. Ravi Varma, Dr. Stewart Vaughan, and Dr. Sophie Dixneuf for their assistance and our shared experiences in the laboratory and on field campaigns. I would also like to thank John Lucey, Christy Roche and Joe Sheehan in the Physics workshop.

I am grateful to Dr. Amalia Muñoz and Dr. Mila Ródenas Garcías of CEAM for their assistance during the experiments in the FIONA campaign and for permission to use their DOAS and chemiluminescence data in Chapter 6.

I am deeply grateful my parents who have given their love and support to me over the last three decades. Finally, to my wife, Yun, I have always known that you are the right person who will stand beside me since we met and for the rest of our lives.

To my parents and my wife

有风自南 翼彼新苗

Chapter 1

INTRODUCTION

1.1 Atmospheric photochemistry

The atmosphere, the thin and fragile envelope of air surrounding our earth, greatly affects the environment in which we live. The atmosphere contains oxygen used by most organisms for respiration, carbon dioxide used by plants, algae and cyanobacteria for photosynthesis, as well as ozone, which at high altitude protects living organisms from genetic damage by solar ultraviolet radiation. The composition of the atmosphere has a direct link to the earth's climate through the radiative forcing effect of greenhouse gases, clouds and airborne particles. Absorption of sunlight initiates photochemical processes and generates a variety of free radicals that drive the chemistry of the troposphere as well as that of the stratosphere. For example, the generation of the hydroxyl radical (OH), which is the dominant atmospheric oxidant, occurs primarily via the photolysis of O_3 in the presence of water vapour. Thus, the fundamental spectroscopy and photochemistry of atmospheric species is central to understanding the chemistry of the atmosphere (Finlayson-Pitts and Pitts, 2000).

The chemistry of the atmosphere is driven to a very large measure by light, that is, by photochemical processes. After absorbing a photon of visible or UV wavelength, a molecule is excited into an electronically excited state, from which it can undergo a number of different processes. If the excited species does not relax to the ground electronic state via radiative or non-radiative processes, it may dissociate, isomerize, rearrange, or react with another molecule. Among these various fates for the excited species, photolysis is an important removal process for atmospheric constituents. In the troposphere, only light above 290 nm is available, and the near-UV region of the spectrum (300-400 nm) is the most photochemically important. Near-UV radiation gives rise to the major atmospheric oxidants, such as OH radical via the reaction of water vapour and $O(^1D)$ produced via the photolysis of O_3. Photolysis of NO_2 is the also a major route to forming O_3 in the troposphere.

Photolysis of a molecule after absorption of light can be described as a first order

reaction. The photolysis rate constant is given by following expression:

$$j = \int \sigma(\lambda)\Phi(\lambda)F(\lambda)\mathrm{d}\lambda \qquad (1.1)$$

where j is the rate coefficient of photolysis, σ (λ) is the absorption cross-section of the species, Φ (λ) is the quantum yield of photolysis, and F (λ) is the actinic flux. The absorption cross-section σ (λ) and quantum yield depend not only on wavelength, but also on the temperature and pressure. The importance of photolysis relative to other loss processes, such as reaction with OH and O_3 can be determined by comparison with the rates of other competing degradation pathways.

Molecular absorption of light has long been a fundamental way to identify and to quantify numerous atmospheric constituents, and absorption spectroscopy has played an important role in studying the physical and chemical properties of the atmosphere. Spectroscopic studies of the earth's atmosphere date back to the late 19th century. An early landmark in atmospheric research was John Tyndall's investigation of the infrared absorption of the atmospheric gases in the 1860s, notably nitrogen, oxygen, water vapour, carbon dioxide, ozone, and methane. The Hartley band of O_3 in 1880 discovered by Sir Walter Noel Hartley. In the same year, Chappuis discovered the visible absorption bands of O_3, now named the Chappuis band. In 1890, the near-UV absorption of O_3, known today as the Huggins band, was discovered by Sir William Huggins. The Meinel bands of OH were discovered in 1950 and connected HO_x-chemistry with O_3 chemistry. Spectroscopic methods have been key to the identification and quantification of the atmospheric relevant species in these historic milestones. In the following the photochemistry of several major atmospheric constituents will be discussed.

1.1.1 Ozone

Stratospheric O_3 plays a very important role in that the Hartley band (200 - 290 nm) of O_3 has an extremely strong absorption (~$10^{-17}$$cm^2$$molecule^{-1}$). This absorption filters the sun's harmful UV radiation and was the source of much early interest in O_3 atmospheric chemistry. As a result, solar radiation below 290 nm is absorbed before reaching the earth surface. The stratospheric O_3 layer contains 90% of the atmosphere's O_3 and is thus responsible for the majority of the absorption of solar UV radiation.

Photolysis of O_2 in the 175 to 242 nm region to produce oxygen atoms is particularly important in the stratosphere because it is the only significant source of O_3:

$$O_2 + h\nu\ (175\ nm < \lambda < 242\ nm) \rightarrow 2O\ (^3P) \quad (1.2)$$

$$O_2 + 2O\ (^3P) + M \rightarrow O_3 + M \quad (1.3)$$

O_3 is removed via reaction with the oxygen atom (1.4) or via photolysis (1.5)

$$O + O_3 \rightarrow \quad O_2 + O_2 \quad (1.4)$$

$$O_3 + h\nu\ (\lambda < 336\ nm) \rightarrow O(^1D) + O_2 \quad (1.5)$$

The above reactions were first proposed by Chapman in 1930 and are known as 'the Chapman Cycle'. In these reactions, the production and destruction of O_3 leads to a steady-state level of O_3 in the stratosphere.

Detailed investigation of O_3 in the 1960s found that the Chapman mechanism overestimated O_3 concentrations (Crutzen, 1969;Bates and Hays, 1967). A group of reactions were found to catalyze the reaction of $O + O_3$ (above reaction 1.4). The general scheme is:

$$R + O_3 \rightarrow RO + O_2 \quad (1.6)$$

$$RO + O \rightarrow R + O_2 \quad (1.7)$$

The net result is:

$$O + O_3 \rightarrow O_2 + O_2 \quad (1.8)$$

The radical species Cl, Br, NO or OH were found to act as catalysts in reactions (1.6)

and (1.7) After including these catalytic reactions the model calculations were in much closer agreement with observations. A general reaction schema for stratospheric O_3 is shown in Fig.1.1.

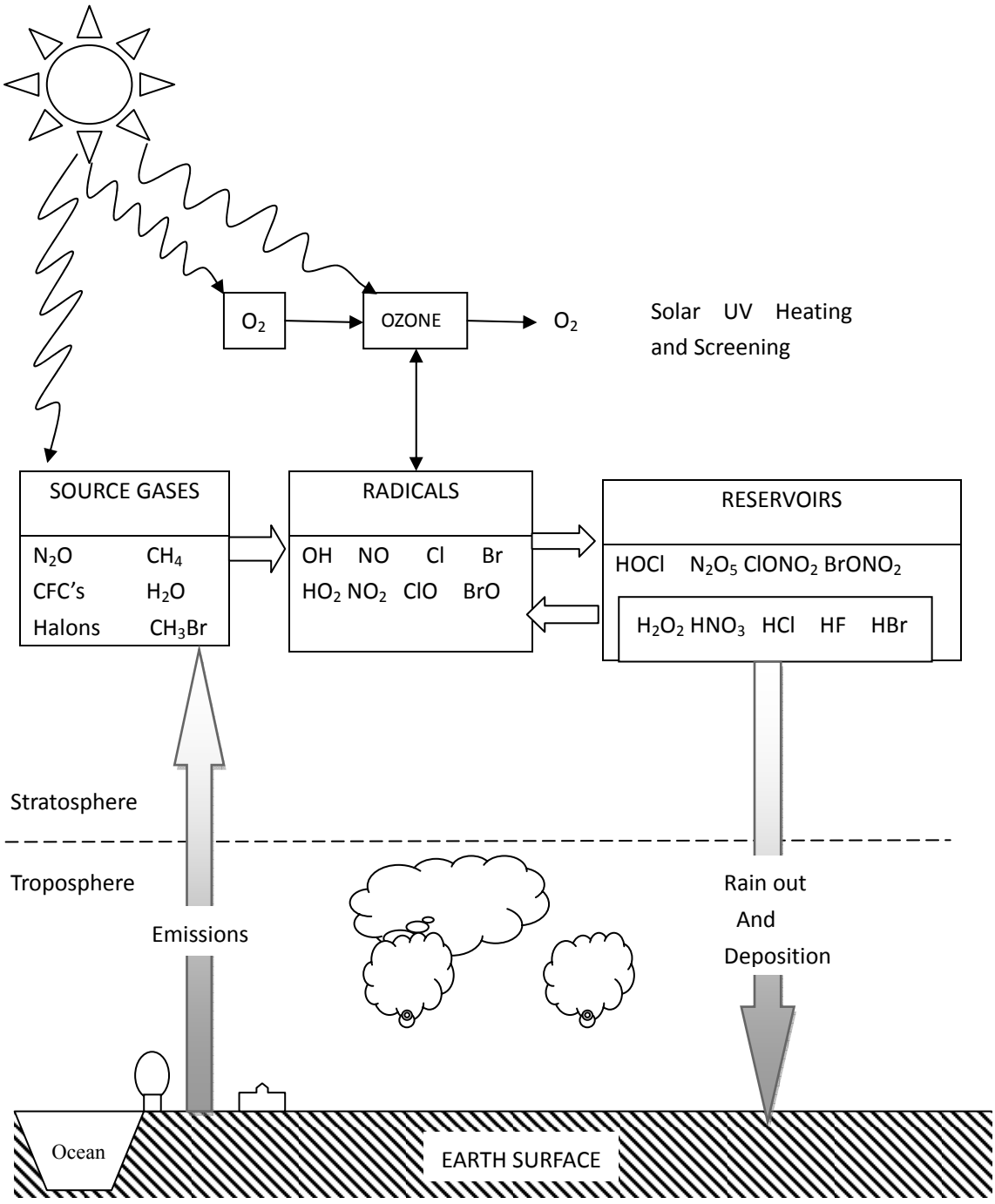


Figure 1.1 Schematic diagram of the chemistry of O_3 in the stratosphere..After Brasseur et al. 1999

1.1.2 The hydroxyl radical

The hydroxyl radical (OH) is the dominant oxidant for most chemical compounds and is particular important in terms of the atmospheric oxidation capacity. The most significant source of OH is photolysis of O_3 and subsequent reaction with H_2O:

$$O_3 + h\nu \rightarrow O_2 + O \quad (1.9)$$

$$O + H_2O \rightarrow 2OH \quad (1.10)$$

Another important source of OH is the reaction of the hydroperoxy radical (HO_2) radical with NO:

$$NO + HO_2 \rightarrow OH + NO_2 \quad (1.11)$$

In polluted air, photolysis of nitrous acid is a further source of OH:

$$HONO + h\nu \rightarrow OH + NO \quad (1.12)$$

The hydroxyl radical reacts with most oxidisable gases in the atmosphere.

OH reacts with carbon monoxide to form carbon dioxide and an H atom:

$$OH + CO \rightarrow CO_2 + H \quad (1.13)$$

which may subsequently react with molecular oxygen to form HO_2:

$$H + O_2 + M \rightarrow HO_2 + M \quad (1.14)$$

OH is also critical to the degradation of organic species, such as methane:

$$OH + CH_4 \rightarrow CH_3 + H_2O \quad (1.15)$$

$$O_2 + CH_3 + M \rightarrow CH_3O_2 + M \quad (1.16)$$

Other primary reactions of OH are the oxidation of hydrogen and formaldehyde:

$$OH + H_2 \rightarrow H + H_2O \quad (1.17)$$

$$OH + CH_2O \rightarrow CHO + H_2O \quad (1.18)$$

$$O_2 + CHO \rightarrow HO_2 + CO \quad (1.19)$$

In all the above OH reactions, HO_2 is generated and easily converted to OH. Other major reactions include reactions of OH with NO_2 and SO_2 to form acids:

$$OH + NO_2 + M \rightarrow HNO_3 + M \quad (1.20)$$

$$OH + SO_2 + M \rightarrow HSO_3 + M \quad (1.21)$$

$$HSO_3 + O_2 \rightarrow SO_3 + HO_2 \quad (1.22)$$

$$SO_3 + HO_2 + M \rightarrow H_2SO_4 + M \quad (1.23)$$

Eventually nitric acid and sulfuric acid are removed from the gas phase by various processes, such as dry deposition to the ground or rainout.

1.1.3 Nitrogen oxides

In the stratosphere, the Chapman cycle is the core mechanism in the formation of O_3. Before the 1960s it was believed that stratospheric O_3 was the only source of tropospheric O_3. Stratospheric O_3 actually contributes only a minor part of the total O_3 budget of the troposphere, whereas large amounts of O_3 are formed and destroyed in the troposphere.

Formation of tropospheric O_3 differs from that in the stratosphere. The mechanism behind the production of high concentrations of O_3 near the ground was known by the late 1960s (Weinstoc, 1969;Crutzen, 1970;Levy, 1971). Photolysis of NO_2 produces the oxygen atom O (^{3}P), which then reacts with O_2:

$$NO_2 + h\nu\ (\lambda < 420\ \text{nm}) \rightarrow NO + O(^3P) \quad (1.24)$$

$$O_2 + O\ (^3P) + M \rightarrow O_3 + M \quad (1.25)$$

The recommended absorption cross-section and wavelength-dependent quantum yield for photolysis of NO_2 are shown in Fig. 1.2, where it is clear that the quantum yield is essentially unity below 400 nm. The calculated photolysis threshold for NO_2 to form ground state NO and an O atom is only 398 nm (Okabe, 1978). The extension of the non-zero quantum yields from 398 nm to 420 nm is believed to be due to the energy acquired from the internal vibration-rotation energy and collisions between molecules.

However, NO is rapidly oxidized by O_3 back to NO_2

$$O_3 + NO \rightarrow NO_2 + O_2 \quad (1.26)$$

Reactions (1.24) and (1.25) are the only significant source of O_3 in the troposphere. Reaction (1.26) leads to a 'photo-stationary' state, in which the ratio of concentrations of O_3, NO, and NO_2 is constant:

$$\frac{[O_3][NO]}{[NO_2]} = \frac{k_{1.24}}{k_{1.26}} \quad (1.27)$$

Eq. 1.27 was first expressed by Philip in 1961 and is now known as the Leighton Relationship. The photolysis rate of reaction (1.24) under clear sky conditions at noontime is about 8×10^{-3} s^{-1} giving a lifetime about 2 minutes for NO_2 molecules (Junkermann et al., 1989). The relation between major constituents in the global troposphere is shown in Fig. 1.3 (Brasseur et al., 1999).

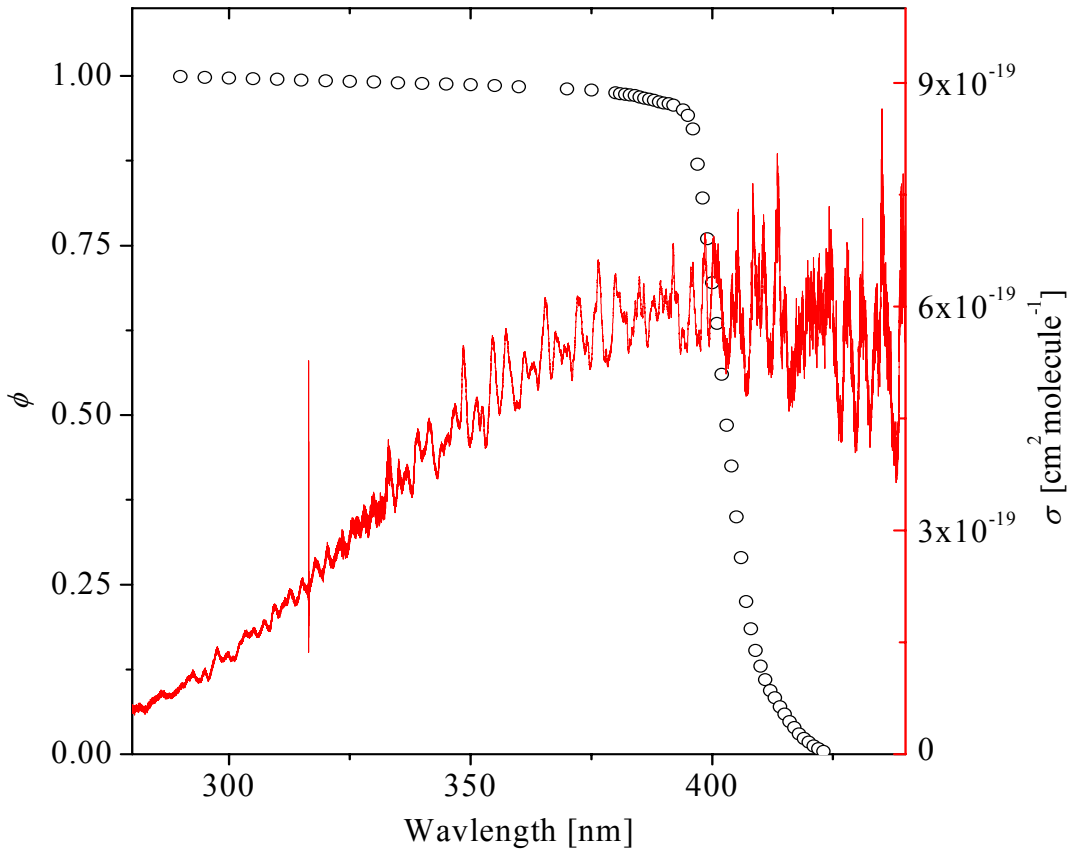


Figure 1.2 The recommended wavelength-dependent quantum yield of photolysis of NO_2 (black cycle) (DeMore et al., 1997) and absorption cross-section of NO_2 (red line) (Voigt et al., 2002)

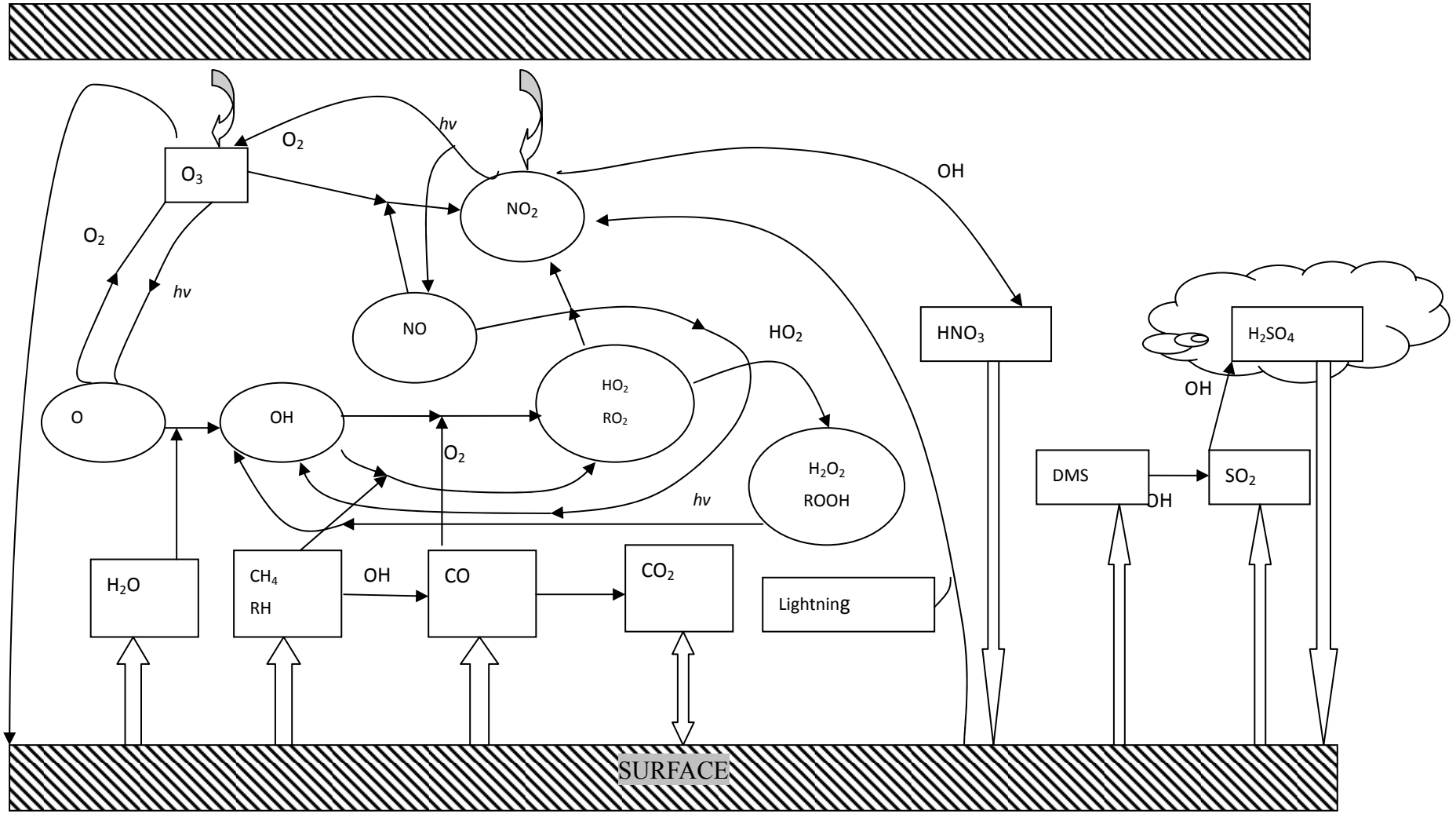


Figure 1.3 Schematic diagram of the relation between the constituents of the global troposphere. After Brasseur et. al. 1999

1.1.4 Halogens

Interest in the atmospheric chemistry of halogen compounds increased following the proposal in the early 1970s that chlorine chemistry in the stratosphere could lead to catalytic O_3 depletion (Molina and Rowland, 1974;Rowland and Molina, 1975). Such catalytic destruction of the O_3 follows the general reaction of (1.6) and (1.7), if there is a source of chlorine atoms in stratosphere:

$$2Cl + O_3 \rightarrow ClO + O_2 \quad (1.28)$$

$$ClO + O \rightarrow Cl + O_2 \quad (1.29)$$

In 1974, the inert chlorofluorocarbons (CFCs) were shown to be a source of atomic chlorine in the stratosphere via photolysis:

$$CF_2Cl_2 + h\nu \rightarrow Cl + CF_2Cl \quad (1.30)$$

In 1985, a team of British scientists reported alarmingly low levels of O_3 above Halley Bay, Antarctica, during austral springtime (Farman et al., 1985). Subsequent work indicated that the polar vortex, a relatively well-contained air mass over Antarctica, combined with heterogeneous chemistry occurring in and on the polar stratospheric clouds was the key to major changes in O_3 levels. Figure 1.4 shows satellite measurements of the dramatic reduction in springtime Antarctic O_3 levels from the 1970s to 1990s, also known as the "ozone hole". In September 1987 an international protocol was signed in Montreal, Canada, to limit the production of chlorofluorocarbons. By 2004, the chlorine loading of the stratosphere had begun to decline (Rinsland et al., 2003) and recent evidence shows that stratospheric O_3 levels have started to recover (Newchurch et al., 2003;Bodeker et al., 2005). The 1995 Nobel Prize in Chemistry was shared by Crutzen, Molina and Rowland, who established how these anthropogenic emissions in the troposphere influence the chemistry of the stratosphere (Molina and Rowland, 1974;Crutzen, 1969).

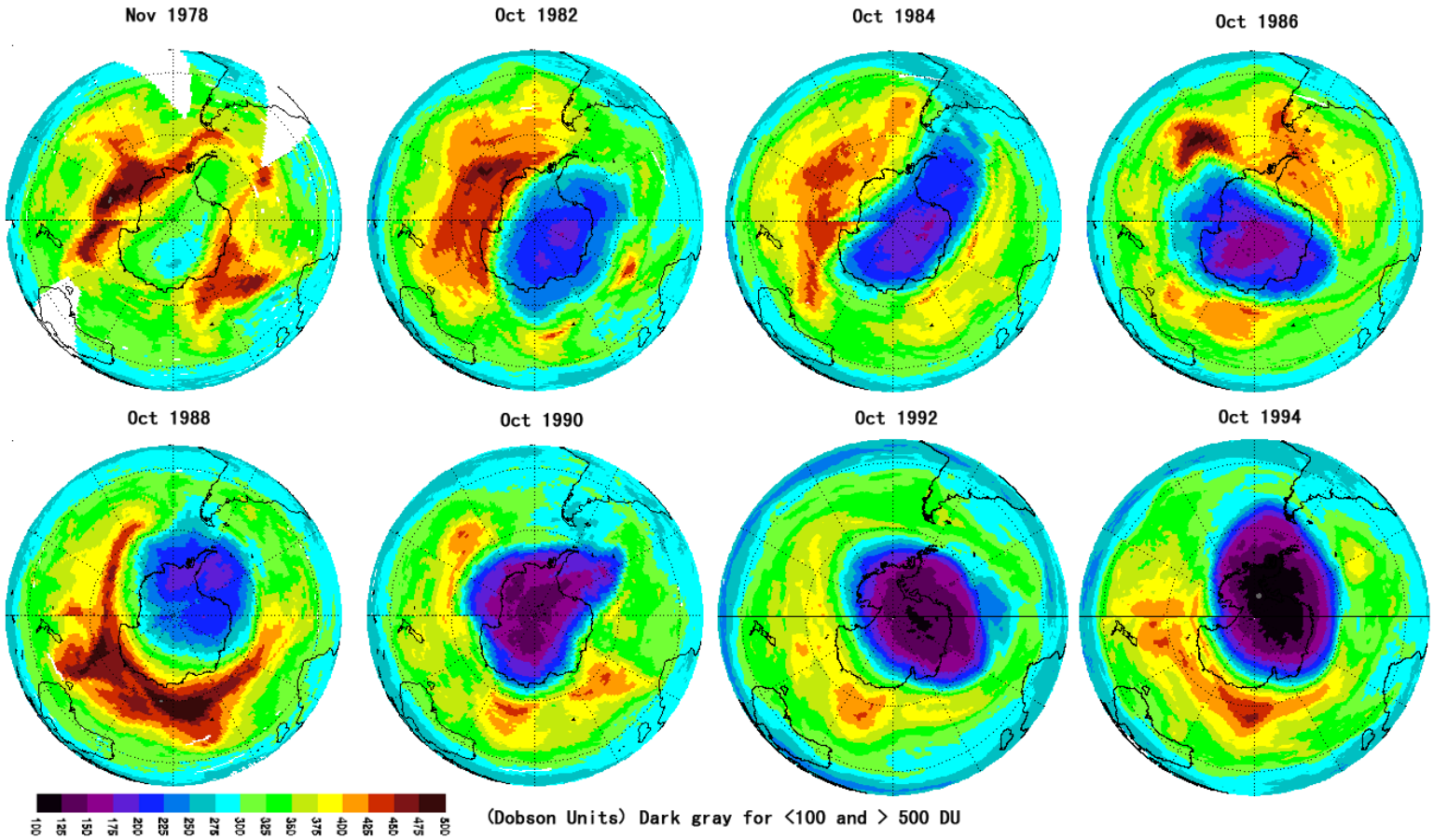


Figure 1.4 Evolution of the total ozone column abundance over the South Pole from 1978 to 1994, measured by the Solar Backscatter Ultraviolet and the Total Ozone Mapping Spectrometer (image courtesy of the NASA/Goddard Space Flight Centre).

Although the role of halogen species in the destruction of stratospheric O_3 is relatively well understood, their impact in the troposphere is much less certain (Wagner and Platt, 1998;Avallone et al., 2003). Bromine and iodine are of greater interest (Sander et al., 2003) than chlorine in the troposphere because a) the absorption cross-sections of I_2 and Br_2 are an order of magnitude larger than that of Cl_2, b) the photolysis wavelength threshold for I_2 and Br_2 is longer than that of Cl_2 and occurs where the actinic flux is greater, and c) the chlorine atom reacts readily with organic species to form hydrogen chloride, which is removed rapidly by wet or dry deposition. This reaction cycle has been reviewed in previous studies about reactive halogen species (Wayne et al., 1995;Platt and Honninger, 2003;Lehrer et al., 1997;Platt and Janssen, 1995;von Glasow et al., 2004).

Following their release halogen species are easily photolyzed to form halogen atoms which then mainly react with O_3:

$$X + O_3 \rightarrow XO + O_2 \quad (1.31)$$

Photolysis of XO regenerates the halogen atom:

$$XO + h\nu \rightarrow X + O \quad (1.32)$$

while XO also undergoes self-reaction or reaction with another halogen oxide YO:

$$XO + YO \rightarrow X + Y + O \quad (1.33)$$

$$XO + YO \rightarrow XY + O_2 \quad (1.34)$$

The net reaction is then $2O_3 \rightarrow 3O_2$.

In addition, XO reacts with NO to recycle the halogen atoms

$$XO + NO \rightarrow X + NO_2 \quad (1.35)$$

This reaction provides a shortcut in the normal tropospheric $NO/NO_2/O_3$ cycle. (reactions 1.24, 1.25 and 1.26) with additional consequences for tropospheric photochemistry and O_3 formation.(Stutz et al., 1999)

Ozone depletion events in the polar boundary layer were linked to the above catalytic reaction cycles, especially for tropospheric bromine (Barrie et al., 1988;Barrie and

Platt, 1997). In the polar regions, significant quantities of BrO have been observed in the free troposphere (McElroy et al., 1999), and large increases in BrO correlate with low O_3 episodes. However the origin and extent of elevated BrO concentrations is poorly understood (Wagner and Platt, 1998). Hence, quantitative measurements are required to identify sources and sinks of BrO (Avallone et al., 2003), clarify its atmospheric chemistry, and evaluate its impact on a regional and global scale.

1.1.5 Nitrous acid

Photolysis of nitrous acid (HONO) via reaction (1.12) is believed to be an important early morning source of OH radicals and thus initiates daytime oxidation chemistry in the polluted urban atmosphere (Platt et al., 1979;Platt et al., 1980a;Harris et al., 1982;Harrison et al., 1996;Alicke et al., 2002;Alicke et al., 2003;Zhou et al., 2002;Aumont et al., 2003;Ren et al., 2003;Kleffmann et al., 2005) as well the polar boundary layer (Li, 1993;Zhou et al., 2001). Field observations showed that the highest HONO concentrations were observed early in the morning before photolysis of HONO had started (Zhou et al., 2002). The general HONO concentration is in the range of 0-15 ppbV in highly polluted environments (Calvert et al., 1994;Lammel, 1996;Alicke et al., 2002).

The near-UV absorption of HONO extends from 300 to 400 nm (Fig. 1.5), where the photolysis quantum yield is unity below 400 nm (Cox and Derwent, 1976;Stutz et al., 2000). The HONO absorption spectrum has several clearly visible vibronic lines and unresolved rotational structure.

HONO is formed in the atmosphere by a variety of chemical mechanisms. In the gas phase, direct recombination of OH and NO occurs via a termolecular process: (Zabarnick, 1993;Pagsberg et al., 1997;Nguyen et al., 1998).

$$OH + NO (+ M) \rightarrow \quad HONO (+ M) \qquad (1.36)$$

A large urban source of HONO is the reaction of water and NO_2 (Svensson et al., 1987;Jenkin et al., 1988;Kleffmann et al., 1998;Finlayson-Pitts et al., 2003), where strong evidence shows it to be a heterogeneous process (Gutzwiller et al., 2002;Ammann et al., 2005):

$$H_2O + 2NO_2 \leftrightarrow HONO + HNO_3 \quad (1.37)$$

However, the exact heterogeneous mechanism of HONO formation is still unclear and may involve surface of organic aerosols or soot particles (Gutzwiller et al., 2002;Bröske et al., 2003). Other sources of HONO include nitrophenols and are still an active area of research (Zhou et al., 2002;Zhou et al., 2003;Trick, 2004;George et al., 2005;Stemmler et al., 2006;Bejan et al., 2006).

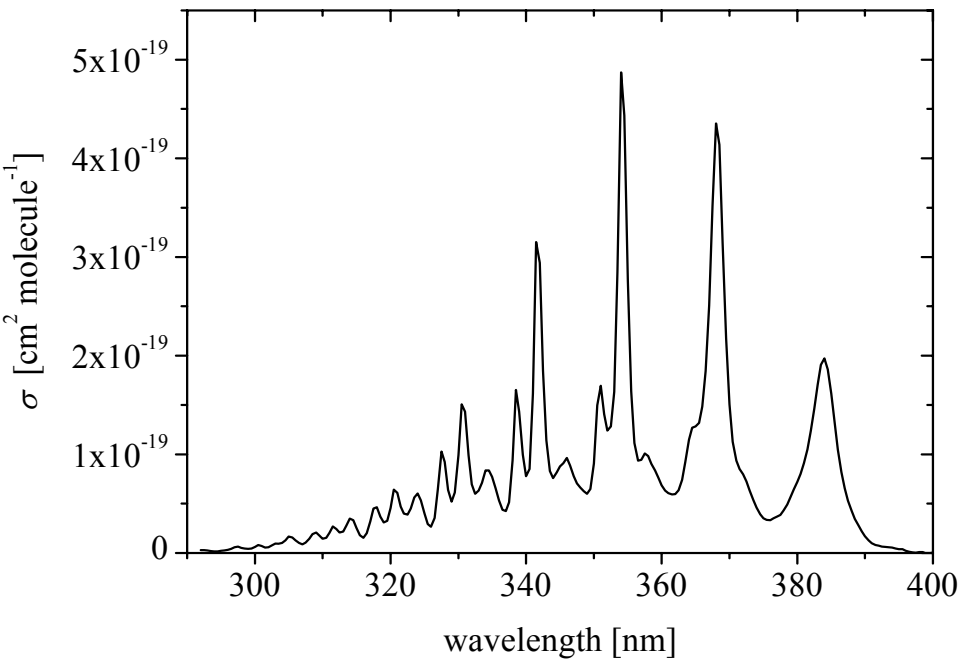


Figure 1.5 Nitrous acid absorption cross-section in the near-UV of $A^1A' \leftarrow X^1 A''$ (Stutz et al., 2000).

1.1.6 Nitrophenols

Aromatic hydrocarbons are an important class of volatile organic compounds (VOCs) and contribute approximately 25% of non-methane anthropogenic emissions (Calvert, 2002). These compounds account for 30% of photooxidants in the atmosphere (Derwent et al., 1996;Derwent et al., 1998) and contribute to secondary organic aerosol formation (Odum et al., 1996;Forstner et al., 1997;Hurley et al., 2001). Nitrophenols are a class of aromatic hydrocarbons that are largely sourced from anthropogenic emissions and have been observed in various environments including air, (Harrison et al., 2005) clouds, (Luttke et al., 1997) soil, (Voznakova et al., 1996) fog (Herterich, 1991) and snow (Kawamura and Kaplan, 1986a, b). Much of the initial interest in nitrophenols stemmed from their phytotoxic properties and potential contribution to forest decline (Rippen et al., 1987).

Bejan et al. (Bejan et al., 2006) proposed that photolysis of the gas phase nitrophenols was a gas phase source of HONO, and showed that HONO was produced from photolysis of nitrophenols in a flow tube photoreactor. Nitrophenols strongly absorb near-UV light due to the $n \rightarrow \pi^*$ transition. However, the mechanism of the photolysis of nitrophenols as a source of HONO in the atmosphere is still unclear and the absorption cross-section in the gas phase is still unknown. Bejan and coworkers also estimated the quantum yield of photolysis to form HONO, but used solution spectra due to the absence of gas phase absorption cross-sections. Measurement of gas phase absorption cross-sections of these nitrophenols is needed to refine the quantum yield values and to better understand its photochemistry.

1.2 Near-ultraviolet absorption spectroscopy methods

1.2.1 Absorption measurements in the atmosphere

Electronic transitions of molecules occur in the near-UV and visible spectral ranges. Absorption in the near-UV plays a particularly important role in atmospheric

photochemistry and is also useful in the study of atmospheric composition. Historically, UV absorption measurements by Cornu and Hartley in 1880 helped to identify O_3 in the atmosphere. The identification and quantification of various halogen free radicals, ClO, OClO and BrO, revealed the catalytic chemistry responsible for the destruction of O_3, while OH and NO_3 were also first identified by absorption spectroscopy (Perner et al., 1976;Platt et al., 1980b).

The Beer-Lambert law relates the strength of light absorption to the concentration and absorption spectrum of molecules. In many cases, measuring absorption spectra is difficult owing to the very low concentration of most atmospheric species. Detecting short-lived free radicals, for which concentrations are necessarily low, is a formidable challenge. For instance, the typical tropospheric concentrations of bromine monoxide, BrO, are extremely low – typically below 5 ppt – and at the detection limit of existing analytical methods (Sander et al., 2003;Fleischmann et al., 2004). Nevertheless, quantitative measurements are necessary to identify the sinks and sources of halogen oxides (BrO, IO) in the field. The absorption of low volatility species (below 1 mbar at 298 K) is also not easy to determine due to large wall losses as well as spectrometer and sample stability issues over the long measurement time. Nitrophenols are examples which are below the FTIR detection limit in chamber experiments (Bejan et al., 2006). In the case of weak absorption cross-sections, even O_3, arguably the most important atmospheric absorber in the visible and UV, has a near-UV spectrum that is relatively poorly characterized, with reported discrepancies up to one order of magnitude in the absorption minimum around 370 nm (Brion et al., 1998;Bogumil et al., 2003;Voigt et al., 2001). Accurate cross-sections are necessary for satellite retrievals and in calculations of the solar radiation transferred to the Earth (Burrows et al., 1999).

1.2.2 Spectroscopic methods

Spectroscopic techniques used for atmospheric observations can be broadly divided

into those approaches based on absorption and those based on emission. The absorption techniques currently and widely employed in atmospheric studies include differential optical absorption spectroscopy (including Long-Path DOAS, Multi-Axis-DOAS, etc.), multi-pass cells for absorption spectroscopy (including multi-pass FTIR), cavity ring down spectroscopy (CRDS) and cavity-enhanced absorption spectroscopy (CEAS), and tunable diode laser absorption spectroscopy (TDLAS). Others techniques like resonance fluorescence (RF), laser induced fluorescence (LIF) and chemiluminescence (CL) are based on emission. The technical criteria of absorption spectroscopic methods are mainly the arrangement of the light path (whether long-path, folded path, or optical system cavity) and the wavelength region (i.e. infra-red, visible or ultraviolet), and the light source (whether broadband or monochromatic). These differences determine the performance as well as the specificity of each technique.

Long-Path DOAS (LP-DOAS) is one of the most widely used techniques in field studies of various atmospheric species (Platt et al., 1979;Platt et al., 1980a;Platt et al., 1980b;Platt et al., 1988;Hebestreit et al., 1999). The long optical path length results in high sensitivity to small absorptions in accordance with the Beer-Lambert law. Measuring the so-called ‘differential’ absorption solved the problem of measuring the intensity of light in the absence of absorption and scattering in the open atmosphere. Satellite observations (eg., from GOME or SCIAMACHY) also employ a differential absorption spectral analysis algorithm to retrieve and map the slant column density from space (Khokhar et al., 2005). However, a drawback of long physical pathlengths is that the atmospheric composition may vary significantly across the path and these long path methods only measure the total column density of the light path (Avallone et al., 2003;Harder et al., 1997;Wayne, 1985). In fact, most DOAS applications constitute remote detection of trace gases. Hence, *in-situ* measuring trace gas at a point in space is also desirable to probe the spatial variation of atmospheric species.

There are several different configurations of multi-pass cells in use. The most common configuration is the White cell which uses a three-mirror multiple-pass cell. Multi-pass cells can extend the base path-length up to hundreds of metres or a few kilometres(Steyert et al., 2001). Major advantages of such cells are that they are relatively easy to align and folded optical paths can be obtained in moderate volumes. This is important when only small amounts of sample are available, for example, in laboratory studies, or when a fast response is needed; smaller volumes cells can be pumped out faster, giving shorter residence times in the cell. However, for incoherent light sources the optical stability is compromised by vibration and thermal expansion, especially in field settings.

The characteristics of multi-pass cells are successful exploited in tunable diode laser absorption spectroscopy (TDLAS). TDLAS uses a narrow-band, frequency variable diode laser tuned to a suitable trace gas absorption structure. The linewidths of the laser are less than 10^{-4} cm^{-1} and the coherent laser light is readily coupled into multi-pass cell. In contrast to bulk lasers, semiconductor diode lasers are easy to use, free of maintenance, rugged, and low cost. They also have very low intensity noise, which is essential for achieving high sensitivity. In addition, their wavelength can be directly tuned by varying the injection current to scan over the entire line-shape of an absorption transition. The advantages of TDLAS are increased resolution and sensitivity and high specificity to the target molecule. Unfortunately reliable diode lasers are best suited to the relatively weak vibrational overtone bands in the near-IR where the fiber telecommunication windows are located. Current commercial diode lasers are only available down to 390 nm and have limited application in the near-UV. In addition, the tunable range of diode lasers is short compared to the relatively broad spectral features of electronic transitions.

Optical cavities provide an alternative means of obtaining a long effective path-length of light through the sample, and techniques exploiting this property include cavity ring-down spectroscopy (CRDS) and cavity-enhanced absorption

spectroscopy (CEAS) (Mazurenka et al., 2005). Light path-lengths on the order of many kilometres can be obtained with a resonator of around 1 m. Such laser-based techniques are exceptionally sensitive to weak absorptions (10^{-9} cm^{-1} or better) but have some drawbacks for recording broad spectra. Because the laser must be scanned across the spectrum, the approach is limited by the stability of the absorber concentration over the duration of the measurement. Furthermore, the intrinsic high resolution of laser is compromised if measurements are taken at widely spaced intervals, as is sometimes the case (Xiang et al., 2009). The cost and experimental complexity of tuneable laser systems may also be prohibitive for UV measurements in particular.

As one of the alternatives to absorption measurements, laser-induced fluorescence (LIF) relies on the excitation of gas molecules by absorption of laser radiation, the frequency of which corresponds to a suitable transition from the molecule's ground state to an electronic excited state (Baardsen and Terhune, 1972). The number of fluorescing photons is proportional to the atmospheric species' concentration, making it a very sensitive and specific technique for detection of atmospheric trace gases. In addition, as fluorescence is spatially emitted, it is possible to image the fluorescence or to make range-resolved measurements. One of the central difficulties is separating other radiation (especially Rayleigh scattering) from the fluorescence signal. Other problems include photochemical formation (Ortgies et al., 1980;Davis et al., 1981;Shirinzadeh et al., 1987) or saturation of the transition under consideration. It is also necessary to calibrate the instrument response (Hofzumahaus et al., 1996;Schultz et al., 1995;Holland et al., 2003).

Another widely used emission technique is chemiluminescence. The similarity between chemiluminescence and LIF is that some gas molecules are also electronically excited following chemical reaction. The effective concentration of the emitting species, and hence the emitted light intensity, is again proportional to the reactant concentration. For example, chemiluminescence is a standard method for

monitoring NO and is based on the reaction of O_3 with NO to produce electronically excited NO_2:

$$O_3 + NO \rightarrow NO_2^* + O_2 \quad (1.38)$$

$$NO_2^* \rightarrow NO_2 + h\nu \quad (1.39)$$

Electronically excited NO_2 emits light extending from 590 nm to 2800 nm, a region that is relatively easily and sensitively monitored using conventional photomultipliers. However, interferences from other chemical reactions can be a big source of measurement uncertainty (Navas et al., 1997).

1.2.3 Incoherent broadband cavity enhanced absorption spectroscopy

Techniques suitable for the measurement of atmospheric trace species must fulfill two main requirements. First, a technique must be sensitive enough to detect the species at their ambient concentration levels. Second, the technique must be selective to the particular species and subject to insignificant interferences or other measurement artefacts. Other desirable characteristics are the ability to monitor multiple species simultaneously and to monitor the composition of the atmosphere over short spatial scales. *In-situ*, high spatial resolution measurements are particularly desirable owing to the high variability of the reactive species in the troposphere. Incoherent broadband cavity enhanced absorption spectroscopy (IBBCEAS), an approach that combines the simultaneous measurement of a broad spectral window with the advantage of the long effective path-length of optical cavities, provides a sensitive, *in-situ* approach to measuring several atmospherically relevant species.

IBBCEAS was first demonstrated by Fiedler and co-workers (Fiedler et al., 2003). The technique employs an optical cavity, a broadband light source (usually a Xe arc lamp or light emitting diode), and a spectrograph to cover a relatively broad spectral window with high sensitivity to weak absorptions (or other extinction processes) in

the sample. The principle of the IBBCEAS technique will be presented in Chapter 2. The technique has proved valuable for quantifying trace gases and aerosol extinction in chamber and field measurements (Venables et al., 2006;Dixneuf et al., 2009;Ball et al., 2010;Varma et al., 2009;Washenfelder et al., 2008;Thalman and Volkamer, 2010) and good agreement with other techniques has been demonstrated in the recent intercomparison between NO_2 and NO_3 measurements. (Fuchs et al., 2010;Dorn et al., in preparation, 2011.) Most IBBCEAS measurements thus far have been at visible wavelengths, with the shortest wavelength measurements between 360 nm and 380nm to quantify HONO and NO_2. (Gherman et al., 2008) Extending IBBCEAS into the UV would facilitate the study of a broader range of atmospherically important species, such as BrO and other species absorbing in the near-UV including OClO, HONO, O_3 and NO_2 (Orphal and Chance, 2003). IBBCEAS allows multiple species to be measured simultaneously and with high spatial resolution.

1.3 Aim of the work

The aim of this work is to develop and exploit the IBBCEAS technique in the near-ultraviolet. Several different experimental systems were constructed for laboratory experiments, *in-situ* chamber measurements and field observations. The approach was applied to measure the absorption spectra and cross-sections of numerous species including O_3, BrO, HONO as well as several ketones, nitrates and nitrophenols. These absorption spectra are important to evaluate their photochemistry. The system was used for trace gas measurements and some of the results were obtained in the context of two large international measurement campaigns held in Canada and Spain.

Chapter 2 describes the IBBCEAS technique and discusses the principle and the optimization of the system. A variety of methods to calibrate the system are discussed in this chapter. In Chapter 3, laboratory spectra are reported using an IBBCEAS system with a flow tube sample cell. The weak band near-UV absorption

cross-sections of SO_2, O_3, acetone, 2-pentone and 2-butanone are reported. In addition, a photoreaction experiment producing BrO radicals is described. Chapter 4 presents two IBBCEAS field instruments, one of which took part in the COBRA campaign in Hudson Bay, Canada, while the other was deployed at the Mace Head Atmosphere Research Station, Galway. In Chapter 5 an *in-situ* chamber study was carried out in a simulation chamber to measure the absorption cross-sections of alkyl nitrates, the nitrophenols and benzaldehyde. The extinction of secondary organic aerosol formed in the chamber was also investigated. Chapter 6 reports results from an extractive IBBCEAS system used in EUPHORE chamber, Valencia, in which an inter-comparison of HONO measurements was conducted. Finally, Chapter 7 summarizes the results and suggests future work.

Bibliography

Alicke, B., Platt, U., and Stutz, J.: Impact of nitrous acid photolysis on the total hydroxyl radical budget during the Limitation of Oxidant Production/Pianura Padana Produzione di Ozono study in Milan, J. Geophys. Res.-Atmos., 107, 2002.

Alicke, B., Geyer, A., Hofzumahaus, A., Holland, F., Konrad, S., Patz, H. W., Schafer, J., Stutz, J., Volz-Thomas, A., and Platt, U.: OH formation by HONO photolysis during the BERLIOZ experiment, J. Geophys. Res.-Atmos., 108, DOI**:** 10.1029/2001JD000579, 2003.

Ammann, M., Rossler, E., Strekowski, R., and George, C.: Nitrogen dioxide multiphase chemistry: Uptake kinetics on aqueous solutions containing phenolic compounds, Phys. Chem. Chem. Phys., 7, 2513-2518, 2005.

Aumont, B., Chervier, F., and Laval, S.: Contribution of HONO sources to the NOx/HOx/O_3 chemistry in the polluted boundary layer, Atmos. Environ., 37, 487-498, 2003.

Avallone, L. M., Toohey, D. W., Fortin, T. J., McKinney, K. A., and Fuentes, J. D.: In situ measurements of bromine oxide at two high-latitude boundary layer sites: Implications of variability, J. Geophys. Res.-Atmos., 108, DOI: 10.1029/2002JD002843, 2003.

Baardsen, E. L., and Terhune, R. W.: Detection of OH in Atmosphere Using a Dye Laser, Appl. Phys. Lett., 21, 209, 1972.

Ball, S. M., Hollingsworth, A. M., Humbles, J., Leblanc, C., Potin, P., and McFiggans, G.: Spectroscopic studies of molecular iodine emitted into the gas phase by seaweed, Atmos. Chem. Phys., 10, 6237-6254, 2010.

Barrie, L., and Platt, U.: Arctic tropospheric chemistry: an overview, Tellus B, 49, 450-454, 1997.

Barrie, L. A., Bottenheim, J. W., Schnell, R. C., Crutzen, P. J., and Rasmussen, R. A.: Ozone Destruction and Photochemical-Reactions at Polar Sunrise in the

Lower Arctic Atmosphere, Nature, 334, 138-141, 1988.

Bates, D. R., and Hays, P. B.: Atmospheric Nitrous Oxide, Planet Space Sci., 15, 189, 1967.

Bejan, I., Abd El Aal, Y., Barnes, I., Benter, T., Bohn, B., Wiesen, P., and Kleffmann, J.: The photolysis of ortho-nitrophenols: a new gas phase source of HONO, Phys. Chem. Chem. Phys., 8, 2028-2035, 2006.

Bodeker, G. E., Shiona, H., and Eskes, H.: Indicators of Antarctic ozone depletion, Atmos. Chem. Phys., 5, 2603-2615, 2005.

Bogumil, K., Orphal, J., Homann, T., Voigt, S., Spietz, P., Fleischmann, O. C., Vogel, A., Hartmann, M., Kromminga, H., Bovensmann, H., Frerick, J., and Burrows, J. P.: Measurements of molecular absorption spectra with the SCIAMACHY pre-flight model: instrument characterization and reference data for atmospheric remote-sensing in the 230-2380 nm region, J. Photochem. Photobiol. A, 157, 167-184, 2003.

Bröske, R., Kleffmann, J., and Wiesen, P.: Heterogeneous conversion of NO_2 on secondary organic aerosol surfaces: A possible source of nitrous acid (HONO) in the atmosphere?, Atmos. Chem. Phys., 3, 469-474, 2003.

Brasseur, G., Orlando, J. J., Tyndall, G. S., Atmospheric chemistry and global change, Topics in environmental chemistry, Oxford University Press, New York, 1999.

Brion, J., Chakir, A., Charbonnier, J., Daumont, D., Parisse, C., and Malicet, J.: Absorption spectra measurements for the ozone molecule in the 350-830 nm region, J. Atmos. Chem., 30, 291-299, 1998.

Burrows, J. P., Richter, A., Dehn, A., Deters, B., Himmelmann, S., and Orphal, J.: Atmospheric remote-sensing reference data from GOME - 2. Temperature-dependent absorption cross sections of O_3 in the 231-794 nm range, J. Quant. Spectrosc. Radiat. Transf., 61, 509-517, 1999.

Calvert, J.: The mechanisms of atmospheric oxidation of aromatic hydrocarbons, Oxford University Press, Oxford, 2002.

Calvert, J. G., Yarwood, G., and Dunker, A. M.: An Evaluation of the Mechanism of Nitrous-Acid Formation in the Urban Atmosphere, Res. Chem. Intermediat., 20, 463-502, 1994.

Cox, R. A., and Derwent, R. G.: Ultraviolet-Absorption Spectrum of Gaseous Nitrous-Acid, J. Photochem., 6, 23-34, 1976.

Crutzen, P. J.: Determination of Parameters Appearing in Dry and Wet Photochemical Theories for Ozone in Stratosphere, Tellus, 21, 368-&, 1969.

Crutzen, P. J.: Influence of Nitrogen Oxides on Atmospheric Ozone Content, Q. J. Roy. Meteor. Soc., 96, 320, 1970.

Davis, D. D., Rodgers, M. O., Fischer, S. D., and Asai, K.: An Experimental Assessment of the O_3-H_2O Interference Problem in the Detection of Natural Levels of OH Via Laser-Induced Fluorescence, Geophys. Res. Lett., 8, 69-72, 1981.

DeMore, W. B., Sander, S. P., Golden, D. M., Hampson, R. F., Kurylo, M. J., Howard, C. J., Ravishankara, A. R., Kolb, C. E., and Molina, M. J.: Chemical Kinetics and Photochemical Data for Use in Stratospheric Modeling. Evaluation No. 12, 1997.

Derwent, R. G., Jenkin, M. E., and Saunders, S. M.: Photochemical ozone creation potentials for a large number of reactive hydrocarbons under European conditions, Atmos. Environ., 30, 181-199, 1996.

Derwent, R. G., Jenkin, M. E., Saunders, S. M., and Pilling, M. J.: Photochemical ozone creation potentials for organic compounds in northwest Europe calculated with a master chemical mechanism, Atmos. Environ., 32, 2429-2441, 1998.

Dixneuf, S., Ruth, A. A., Vaughan, S., Varma, R. M., and Orphal, J.: The time dependence of molecular iodine emission from *Laminaria digitata*, Atmos. Chem. Phys., 9, 823-829, 2009.

Dorn, H. P., Apodaca, R. L., Ball, S. M., Brauers, T., Brown, S. S., Cohen, R. C., Crowley, J. N., Dubé, W. P., Fry, J. L., Fuchs, H., Häseler, R., Heitmann, U.,

Jones, R. L., Kato, S., Kajii, Y., Kiendler-Scharr, A., Labazan, I., Langridge, J. M., Matsumoto, J., Meinen, J., Nishida, S., Platt, U., Pőhler, D., Rohrer, F., Rollins, A. W., Ruth, A. A., Schlosser, E., Schuster, G., Shillings, A. J. L., Simpson, W. R., Thieser, J., Venables, D. S., Wahner, A., Wegener, R., and Wooldridge, P. J.: Intercomparison of NO_3 radical detection instruments in the Atmosphere Simulation Chamber SAPHIR, Atmos. Chem. Phys. Discuss., in preparation, 2011.

Farman, J. C., Gardiner, B. G., and Shanklin, J. D.: Large Losses of Total Ozone in Antarctica Reveal Seasonal ClO_x/NO_x Interaction, Nature, 315, 207-210, 1985.

Fiedler, S. E., Hese, A., and Ruth, A. A.: Incoherent broad-band cavity-enhanced absorption spectroscopy, Chem. Phys. Lett., 371, 284-294, 2003.

Finlayson-Pitts, B. J., and Pitts, J. N.: Chemistry of the upper and lower atmosphere : theory, experiments, and applications, Academic Press, San Diego, 2000.

Finlayson-Pitts, B. J., Wingen, L. M., Sumner, A. L., Syomin, D., and Ramazan, K. A.: The heterogeneous hydrolysis of NO_2 in laboratory systems and in outdoor and indoor atmospheres: An integrated mechanism, Phys. Chem. Chem. Phys., 5, 223-242, 2003.

Fleischmann, O. C., Hartmann, M., Burrows, J. P., and Orphal, J.: New ultraviolet absorption cross-sections of BrO at atmospheric temperatures measured by time-windowing Fourier transform spectroscopy, J. Photochem. Photobiol. A, 168, 117-132, 2004.

Forstner, H. J. L., Flagan, R. C., and Seinfeld, J. H.: Secondary organic aerosol from the photooxidation of aromatic hydrocarbons: Molecular composition, Environ. Sci. Technol., 31, 1345-1358, 1997.

Fuchs, H., Ball, S. M., Bohn, B., Brauers, T., Cohen, R. C., Dorn, H. P., Dubé, W. P., Fry, J. L., Häseler, R., Heitmann, U., Jones, R. L., Kleffmann, J., Mentel, T. F., Musgen, P., Rohrer, F., Rollins, A. W., Ruth, A. A., Kiendler-Scharr, A., Schlosser, E., Shillings, A. J. L., Tillmann, R., Varma, R. M., Venables, D. S.,

Tapia, G. V., Wahner, A., Wegener, R., Wooldridge, P. J., and Brown, S. S.: Intercomparison of measurements of NO_2 concentrations in the atmosphere simulation chamber SAPHIR during the NO_3 Comp campaign, Atmos. Meas. Tech., 3, 21-37, 2010.

George, C., Strekowski, R. S., Kleffmann, J., Stemmler, K., and Ammann, M.: Photoenhanced uptake of gaseous NO_2 on solid-organic compounds: a photochemical source of HONO?, Faraday Discuss., 130, 195-210, 2005.

Gherman, T., Venables, D. S., Vaughan, S., Orphal, J., and Ruth, A. A.: Incoherent broadband cavity-enhanced absorption spectroscopy in the near-ultraviolet: Application to HONO and NO_2, Environ. Sci. Technol., 42, 890-895, 10.1021/es0716913, 2008.

Gutzwiller, L., Arens, F., Baltensperger, U., Gaggeler, H. W., and Ammann, M.: Significance of semivolatile diesel exhaust organics for secondary HONO formation, Environ. Sci. Technol., 36, 677-682, 2002.

Harder, J. W., Williams, E. J., Baumann, K., and Fehsenfeld, F. C.: Ground-based comparison of NO_2, H_2O, and O_3 measured by long-path and in situ techniques during the 1993 tropospheric OH photochemistry experiment, J. Geophys. Res.-Atmos., 102, 6227-6243, 1997.

Harris, G. W., Carter, W. P. L., Winer, A. M., Pitts, J. N., Platt, U., and Perner, D.: Observations of Nitrous-Acid in the Los-Angeles Atmosphere and Implications for Predictions of Ozone Precursor Relationships, Environ. Sci. Technol., 16, 414-419, 1982.

Harrison, M. A. J., Barra, S., Borghesi, D., Vione, D., Arsene, C., and Olariu, R. L.: Nitrated phenols in the atmosphere: a review, Atmos. Environ., 39, 231-248, 2005.

Harrison, R. M., Peak, J. D., and Collins, G. M.: Tropospheric cycle of nitrous acid, J. Geophys. Res.-Atmos., 101, 14429-14439, 1996.

Hebestreit, K., Stutz, J., Rosen, D., Matveiv, V., Peleg, M., Luria, M., and Platt, U.: DOAS measurements of tropospheric bromine oxide in mid-latitudes,

Science, 283, 55-57, 1999.

Herterich, R.: Gas-chromatographic Determination of Nitrophenols In Atmospheric Liquid Water And Airborne-Particulates, J. Chromatogr., 549, 313-324, 1991.

Hofzumahaus, A., Aschmutat, U., Hessling, M., Holland, F., and Ehhalt, D. H.: The measurement of tropospheric OH radicals by laser-induced fluorescence spectroscopy during the POPCORN field campaign, Geophys. Res. Lett., 23, 2541-2544, 1996.

Holland, F., Hofzumahaus, A., Schafer, R., Kraus, A., and Patz, H. W.: Measurements of OH and HO2 radical concentrations and photolysis frequencies during BERLIOZ, J. Geophys. Res.-Atmos., 108, 2003.

Hurley, M. D., Sokolov, O., Wallington, T. J., Takekawa, H., Karasawa, M., Klotz, B., Barnes, I., and Becker, K. H.: Organic aerosol formation during the atmospheric degradation of toluene, Environ. Sci. Technol., 35, 1358-1366, 2001.

Jenkin, M. E., Cox, R. A., and Williams, D. J.: Laboratory Studies of the Kinetics of Formation of Nitrous-Acid from the Thermal-Reaction of Nitrogen-Dioxide and Water-Vapor, Atmos. Environ., 22, 487-498, 1988.

Junkermann, W., Platt, U., and Volzthomas, A.: A Photoelectric Detector for the Measurement of Photolysis Frequencies of Ozone and Other Atmospheric Molecules, J. Atmos. Chem., 8, 203-227, 1989.

Kawamura, K., and Kaplan, I. R.: Compositional Change of Organic-matter in Rainwater during Precipitation Events, Atmos. Environ., 20, 527-535, 1986a.

Kawamura, K., and Kaplan, I. R.: Biogenic and Anthropogenic Organic-compounds in Rain and Snow Samples Collected in Southern-California, Atmos. Environ., 20, 115-124, 1986b.

Khokhar, M. F., Frankenberg, C., Van Roozendael, M., Beirle, S., Kuhl, S., Richter, A., Platt, U., and Wagner, T.: Satellite observations of atmospheric SO_2 from

volcanic eruptions during the time-period of 1996-2002, Atmospheric Remote Sensing: Earth's Surface, Troposphere, Stratosphere and Mesosphere - I, 36, 879-887, 2005.

Kleffmann, J., Becker, K. H., and Wiesen, P.: Heterogeneous NO_2 conversion processes on acid surfaces: Possible atmospheric implications, Atmos. Environ., 32, 2721-2729, 1998.

Kleffmann, J., Gavriloaiei, T., Hofzumahaus, A., Holland, F., Koppmann, R., Rupp, L., Schlosser, E., Siese, M., and Wahner, A.: Daytime formation of nitrous acid: A major source of OH radicals in a forest, Geophys. Res. Lett., 32, 2005.

Lammel, G.: A DOAS study on the origin of nitrous acid at urban and non-urban sites - Comment, Atmos. Environ., 30, 4101-4103, 1996.

Lehrer, E., Wagenbach, D., and Platt, U.: Aerosol chemical composition during tropospheric ozone depletion at Ny Alesund/Svalbard, Tellus B, 49, 486-495, 1997.

Levy, H.: Normal Atmosphere - Large Radical and Formaldehyde Concentrations Predicted, Science, 173, 141, 1971.

Li, S. M.: Particulate and Snow Nitrite in the Spring Arctic Troposphere, Atmos. Environ. A, 27, 2959-2967, 1993.

Luttke, J., Scheer, V., Levsen, K., Wunsch, G., Cape, J. N., Hargreaves, K. J., StoretonWest, R. L., Acker, K., Wieprecht, W., and Jones, B.: Occurrence and formation of nitrated phenols in and out of cloud, Atmos. Environ., 31, 2637-2648, 1997.

Mazurenka, M., Orr-Ewing, A. J., Peverall, R., and Ritchie, G. A. D.: Cavity ring-down and cavity enhanced spectroscopy using diode lasers, Phys. Chem. C, 101, 100-142, 2005.

McElroy, C. T., McLinden, C. A., and McConnell, J. C.: Evidence for bromine monoxide in the free troposphere during the Arctic polar sunrise, Nature, 397, 338-341, 1999.

Molina, M. J., and Rowland, F. S.: Stratospheric Sink for Chlorofluoromethanes - Chlorine Atomic-Catalysed Destruction of Ozone, Nature, 249, 810-812, 1974.

Navas, M. J., Jimenez, A. M., and Galan, G.: Air analysis: Determination of nitrogen compounds by chemiluminescence, Atmos. Environ., 31, 3603-3608, 1997.

Newchurch, M. J., Yang, E. S., Cunnold, D. M., Reinsel, G. C., Zawodny, J. M., and Russell, J. M.: Evidence for slowdown in stratospheric ozone loss: First stage of ozone recovery, J. Geophys. Res.-Atmos., 108, 2003.

Nguyen, M. T., Sumathi, R., Sengupta, D., and Peeters, J.: Theoretical analysis of reactions related to the HNO_2 energy surface: OH+NO and H+NO_2, Chem. Phys., 230, 1-11, 1998.

Odum, J. R., Hoffmann, T., Bowman, F., Collins, D., Flagan, R. C., and Seinfeld, J. H.: Gas/particle partitioning and secondary organic aerosol yields, Environ. Sci. Technol., 30, 2580-2585, 1996.

Orphal, J., and Chance, K.: Ultraviolet and visible absorption cross-sections for HITRAN, J. Quant. Spectrosc. Radiat. Transf., 82, 491-504, 2003.

Ortgies, G., Gericke, K. H., and Comes, F. J.: Is UV Laser-Induced Fluorescence a Method to Monitor Tropospheric OH, Geophys. Res. Lett., 7, 905-908, 1980.

Pagsberg, P., Bjergbakke, E., Ratajczak, E., and Sillesen, A.: Kinetics of the gas phase reaction OH+NO(+M)->HONO(+M) and the determination of the UV absorption cross sections of HONO, Chem. Phys. Lett., 272, 383-390, 1997.

Perner, D., Ehhalt, D. H., Patz, H. W., Platt, U., Roth, E. P., and Volz, A.: OH - Radicals in Lower Troposphere, Geophys. Res. Lett., 3, 466-468, 1976.

Platt, U., Perner, D., and Patz, H. W.: Simultaneous Measurement of Atmospheric CH_2O, O_3, and NO_2 by Differential Optical-Absorption, J. Geophys. Res.-Atmos., 84, 6329-6335, 1979.

Platt, U., Perner, D., Harris, G. W., Winer, A. M., and Pitts, J. N.: Observations of Nitrous-Acid in an Urban Atmosphere by Differential Optical-Absorption,

Nature, 285, 312-314, 1980a.

Platt, U., Perner, D., Winer, A. M., Harris, G. W., and Pitts, J. N.: Detection of NO_3 in the Polluted Troposphere by Differential Optical-Absorption, Geophys Res Lett, 7, 89-92, 1980b.

Platt, U., Rateike, M., Junkermann, W., Rudolph, J., and Ehhalt, D. H.: New Tropospheric OH Measurements, J. Geophys. Res.-Atmos., 93, 5159-5166, 1988.

Platt, U., and Janssen, C.: Observation and role of the free radicals NO_3, ClO, BrO and IO in the troposphere, Faraday Discuss, 175-198, 1995.

Platt, U., and Honninger, G.: The role of halogen species in the troposphere, Chemosphere, 52, 325-338, 2003.

Ren, X. R., Harder, H., Martinez, M., Lesher, R. L., Oliger, A., Simpas, J. B., Brune, W. H., Schwab, J. J., Demerjian, K. L., He, Y., Zhou, X. L., and Gao, H. G.: OH and HO_2 chemistry in the urban atmosphere of New York City, Atmos. Environ., 37, 3639-3651, 2003.

Rinsland, C. P., Flaud, J. M., Perrin, A., Birk, A., Wagner, G., Goldman, A., Barbe, A., De Backer-Barilly, M. R., Mikhailenko, S. N., Tyuterev, V. G., Smith, M. A. H., Devi, V. M., Benner, D. C., Schreier, F., Chance, K. V., Orphal, J., and Stephen, T. M.: Spectroscopic parameters for ozone and its isotopes: recent measurements, outstanding issues, and prospects for improvements to HITRAN, J. Quant. Spectrosc. Radiat. Transf., 82, 207-218, 2003.

Rippen, G., Zietz, E., Frank, R., Knacker, T., and Klopffer, W.: Do Airborne Nitrophenols Contribute to Forest Decline, Environ. Technol. Lett., 8, 475-482, 1987.

Rowland, F. S., and Molina, M. J.: Chlorofluoromethanes in Environment, Rev. Geophys., 13, 1-35, 1975.

Sander, R., Keene, W. C., Pszenny, A. A. P., Arimoto, R., Ayers, G. P., Baboukas, E., Cainey, J. M., Crutzen, P. J., Duce, R. A., Honninger, G., Huebert, B. J., Maenhaut, W., Mihalopoulos, N., Turekian, V. C., and Van Dingenen, R.:

Inorganic bromine in the marine boundary layer: a critical review, Atmos. Chem. Phys., 3, 1301-1336, 2003.

Schultz, M., Heitlinger, M., Mihelcic, D., and Volzthomas, A.: Calibration Source for Peroxy-Radicals with Built-in Actinometry Using H_2O and O_2 Photolysis at 185 nm, J. Geophys. Res.-Atmos., 100, 18811-18816, 1995.

Shirinzadeh, B., Wang, C. C., and Deng, D. Q.: Pressure-Dependence of Ozone Interference in the Laser Fluorescence Measurements of OH in the Atmosphere, Appl. Optics, 26, 2102-2105, 1987.

Stemmler, K., Ammann, M., Donders, C., Kleffmann, J., and George, C.: Photosensitized reduction of nitrogen dioxide on humic acid as a source of nitrous acid, Nature, 440, 195-198, 2006.

Steyert, D. W., Sirota, J. M., Mickelson, M. E., and Reuter, D. C.: Two new long-pass cells for infrared and visible spectroscopy, Rev. Sci. Instrum., 72, 4337-4343, 2001.

Stutz, J., Hebestreit, K., Alicke, B., and Platt, U.: Chemistry of halogen oxides in the troposphere: Comparison of model calculations with recent field data, J. Atmos. Chem., 34, 65-85, 1999.

Stutz, J., Kim, E. S., Platt, U., Bruno, P., Perrino, C., and Febo, A.: UV-visible absorption cross sections of nitrous acid, J. Geophys. Res.-Atmos., 105, 14585-14592, 2000.

Svensson, R., Ljungstrom, E., and Lindqvist, O.: Kinetics of the Reaction between Nitrogen-Dioxide and Water-Vapor, Atmos. Environ., 21, 1529-1539, 1987.

Thalman, R., and Volkamer, R.: Inherent calibration of a blue LED-CE-DOAS instrument to measure iodine oxide, glyoxal, methyl glyoxal, nitrogen dioxide, water vapour and aerosol extinction in open cavity mode, Atmos. Meas. Tech., 3, 1797-1814, 10.5194/amt-3-1797-2010, 2010.

Varma, R. M., Venables, D. S., Ruth, A. A., Heitmann, U., Schlosser, E., and Dixneuf, S.: Long optical cavities for open-path monitoring of atmospheric trace gases and aerosol extinction, Appl. Opt., 48, B159-B171, 2009.

Venables, D. S., Gherman, T., Orphal, J., Wenger, J. C., and Ruth, A. A.: High sensitivity in situ monitoring of NO_3 in an atmospheric simulation chamber using incoherent broadband cavity-enhanced absorption spectroscopy, Environ. Sci. Technol., 40, 6758-6763, 10.1021/es061076j, 2006.

Voigt, S., Orphal, J., Bogumil, K., and Burrows, J. P.: The temperature dependence (203-293 K) of the absorption cross sections of O_3 in the 230-850 nm region measured by Fourier-transform spectroscopy, J. Photochem. Photobiol. A, 143, 1-9, 2001.

Voigt, S., Orphal, J., and Burrows, J. P.: The temperature and pressure dependence of the absorption cross-sections of NO_2 in the 250-800 nm region measured by Fourier-transform spectroscopy, J. Photochem. Photobiol. A, 149, 1-7, 2002.

von Glasow, R., von Kuhlmann, R., Lawrence, M. G., Platt, U., and Crutzen, P. J.: Impact of reactive bromine chemistry in the troposphere, Atmos. Chem. Phys., 4, 2481-2497, 2004.

Voznakova, Z., Podehradska, J., and Kohlickova, M.: Determination of nitrophenols in soil, Chemosphere, 33, 285-291, 1996.

Wagner, T., and Platt, U.: Satellite mapping of enhanced BrO concentrations in the troposphere, Nature, 395, 486-490, 1998.

Washenfelder, R. A., Langford, A. O., Fuchs, H., and Brown, S. S.: Measurement of glyoxal using an incoherent broadband cavity enhanced absorption spectrometer, Atmos. Chem. Phys., 8, 7779-7793, 2008.

Wayne, R. P.: Chemistry of atmospheres: an introduction to the chemistry of the atmospheres of Earth, the planets, and their satellites, Oxford University Press, Oxford 1985.

Wayne, R. P., Poulet, G., Biggs, P., Burrows, J. P., Cox, R. A., Crutzen, P. J., Hayman, G. D., Jenkin, M. E., Lebras, G., Moortgat, G. K., Platt, U., and Schindler, R. N.: Halogen Oxides - Radicals, Sources and Reservoirs in the Laboratory and in the Atmosphere, Atmos. Environ., 29, 2677-2881, 1995.

Weinstoc, B.: Carbon Monoxide - Residence Time in Atmosphere, Science, 166, 224,

1969.

Xiang, B., Zhu, C. Z., and Zhu, L.: Gas-phase absorption cross sections of 2-nitrobenzaldehyde and benzaldehyde in the 285-400 nm region, and photolysis of 2-nitrobenzaldehyde vapor at 308 and 351 nm, Chem. Phys. Lett., 474, 74-78, 2009.

Zabarnick, S.: Kinetics of the Reaction OH+NO+M = HONO+M as a Function of Temperature and Pressure in the Presence of Argon, SF_6, and N_2 Bath Gas, Chem. Phys., 171, 265-273, 1993.

Zhou, X., Civerolo, K., Dai, H., Huang, G., Schwab, J., and Demerjian, K.: Summertime nitrous acid chemistry in the atmospheric boundary layer at a rural site in New York State, J. Geophys. Res., 107, 4590, 10.1029/2001jd001539, 2002.

Zhou, X., Gao, H., He, Y., Huang, G., Bertman, S. B., Civerolo, K., and Schwab, J.: Nitric acid photolysis on surfaces in low-NOx environments: Significant atmospheric implications, Geophys. Res. Lett., 30, 2217, 10.1029/2003gl018620, 2003.

Zhou, X. L., Beine, H. J., Honrath, R. E., Fuentes, J. D., Simpson, W., Shepson, P. B., and Bottenheim, J. W.: Snowpack photochemical production of HONO: a major source of OH in the Arctic boundary layer in springtime, Geophys. Res. Lett., 28, 4087-4090, 2001.

Chapter 2

INCOHERENT BROADBAND CAVITY-ENHANCED SPECTROSCOPY

Measurements of trace gas concentrations are the experimental prerequisites for understanding physico-chemical processes in the earth's atmosphere (Platt, 1999). Optical absorption spectroscopy is widely used in atmospheric and geophysical sciences as a straightforward, non-invasive approach for the *in situ* detection of trace species concentrations and the measurement of wavelength-dependent absorption cross-sections.

In conventional optical absorption methods, the incident and transmitted intensities of the light travelling through a medium with a certain pathlength are measured. The absorption is related to the attenuation of the light expressed in terms of the Lambert–Beer law (assuming light scattering to be a negligible attenuation mechanism). In this approach the measurement of the absorption is genuinely intensity-dependent and its sensitivity depends on the optical pathlength, which is therefore maximized in most applications. The arrangement of the light path is thus a key consideration for absorption measurements. Classical schemes employ multi-pass cells according to White (White, 1976) or Herriott and Schulte (Herriott and Schulte, 1965). An alternative approach, using a high finesse optical cavity for sensitive absorption measurements, was first demonstrated a little over two decades ago with the development of cavity ring-down spectroscopy (CRDS) (Ramponi et al., 1988).

The type of the light source is another important experimental consideration. Narrow band diode-lasers can be tuned (Reid et al., 1978;Werle, 1998) in terms of amplitude or frequency modulation spectroscopy (Bjorklund, 1980;Hall et al., 1981), which achieves sensitivity for detection of several atmospheric trace gases. Spectrally broad light sources, whose emission is dispersed before or after passing the sample, are also used in most differential optical absorption spectroscopy (DOAS) applications. A

broadband light source is particularly suited to detection of multiple species based on their spectral signature.

In this chapter, a novel spectroscopic method which combines an optical cavity with a broadband light source (Incoherent Broadband Cavity-Enhanced Spectroscopy) will be introduced. The performance and calibration of the instrument, as well as the analysis procedure will be presented and discussed.

2.1 Prior cavity absorption methods

"Classical" cavity spectroscopy has undergone rapid development since the mid-1990s. Various types of cavity-enhanced methods have been established based on pulsed (Engeln and Meijer, 1996;O'Keefe and Deacon, 1988;Crosson et al., 1999) and continuous wave laser excitation (Romanini et al., 1997), and summaries can be found in a number of reviews (Wheeler et al., 1998;Berden et al., 2000;Berden and Engeln, 2009). Among continuous wave cavity-enhanced techniques, significant improvements were made in recent years using diode-lasers (Ye et al., 1998), whereby exceptional sensitivities were achieved in applications such as NICE-OHMS (Ma et al., 1999) or heterodyne CRDS (Ye and Hall, 2000). However, the refinement of the spectral resolution better than 1 MHz with cavity-enhanced sensitivity was achieved at the expense of experimental simplicity. In many applications, mode-locking of the cavity is necessary, which requires fast optical switches and feedback electronics, as well as Faraday rotators to avoid optical feedback into the laser diode. In diode-laser-based cavity-enhanced absorption spectroscopy (CEAS), as described by Engeln (Engeln et al., 1998), cavity transmission is extensively averaged, similar to pulsed integrated cavity spectroscopy output (ICOS) demonstrated by O'Keefe. These methods retain a measure of experimental simplicity as well as high sensitivity.

Although CEAS with diode lasers is promising in terms of robustness and spectral resolution, it cannot be flexibly applied in a wide spectral region as there are no commercial available diode lasers below 390 nm. Mode-hops in diode lasers are also a practical drawback, especially if high resolution is not required and a large spectral region is to be studied. Several pulsed laser applications have been developed (Scherer, 1998;Czyzewski et al., 2001;Ball et al., 2001), besides more established intracavity absorption methods (Romanini, 1995;Cheskis, 1999). Excepting Fourier transform phase shift CRDS (Hamers et al., 2002), previous cavity-enhanced absorption techniques were laser-based. In atmospheric applications where several compounds are to be monitored simultaneously or species with broad absorption bands are to be detected, techniques covering wide spectral absorption regions are required, rather than high spectral resolution. Therefore, combined with the multiplexing capabilities of modern spectrographs, the development of broadband cavity-enhanced methods appears very attractive.

Incoherent Broad Band Cavity-Enhanced Absorption Spectroscopy (IBBCEAS) is a technique that combines cavity enhancement of absorption with a broadband spectral light source. The broad simultaneous spectral coverage allows interfering species to be accounted for, which is an important practical consideration. The sensitivity of this approach is comparable to that of cavity ring down or conventional long path methods, but it is experimentally simpler and therefore suitable for laboratory and field observations of atmospherically relevant trace gases. The approach was first demostrated by Fiedler et al. (Fiedler et al., 2003b). Subsequently, the technique was applied to a wide variety of atmospherically relevant trace species, including NO_2, NO_3, I_2, IO, OIO, HONO, O_3, glyoxal, O_4, H_2O, BrO and ketones. A summary of previous broadband cavity studies for atmospheric species is given in Table 2.1.

Table 2.1 Summary of prior broadband cavity enhanced studies.

Light source	Mirror reflectivity	Spectral range [nm]	Detected species	Author's study
Xe Arc	0.9999	630-670	O_2, azulene	(Fiedler et al., 2003a)
LED	0.99995	645-705	O_2, H_2O, NO_3, NO_2, I_2	(Ball et al., 2004)
	0.9999	530-580		
LED	0.99976	441-462	NO_2, O_4 dimer	(Langridge et al., 2006)
Xe Arc	0.99775	630-700	NO_3, NO_2, O_3, H_2O	(Venables et al., 2006)
Xe Arc	0.996	612-712	O_2, H_2O	(Ruth et al., 2007)
Xe Arc	0.997	1550-1650	CO_2, OCS, $HD^{18}O$	(Orphal and Ruth, 2008)
LED	0.9999	630-680	NO_2, H_2O, NO_3	(Langridge et al., 2008)
LED	0.9985	360-380	HONO, NO_2	(Gherman et al., 2008)
Xe Arc	0.9999	525-560	I_2, OIO and IO	(Vaughan et al., 2008)
	0.9998	427-450		
Xe Arc	0.999966	440-465	CHOCHO, NO_2, H_2O	(Washenfelder et al., 2008)
Xe Arc	0.999	630-690	NO_2, NO_3	(Varma et al., 2009)
LED	0.9955	450-490	NO_2	(Wu et al., 2009)
Xe Arc	0.9998	530-553	I_2	(Dixneuf et al., 2009)
LED	0.999985	620-700	NO_3, O_3	(Meinen et al., 2010)
LED	0.99955	520-555	I_2	(Ball et al., 2010)
LED	0.99996	420-490	CHOCHO, CH_3COCHO, IO, NO_2,O_4,H_2O	(Thalman and Volkamer, 2010)
LED	0.9999	631-670	NO_3, H_2O	(Benton et al., 2010)

2.2 Principle of measurement

An IBBCEAS system is shown in Fig 2.1. Light from a broadband light source, such as a short-arc Xe-lamp or LED, is transmitted through an optically stable resonator composed of two highly reflective mirrors. Light in the cavity is reflected back and forth between the high reflective dielectric mirrors and slowly leaks out to the detector. This results in a long photon residence time and hence a very long effective pathlength for photons in the cavity. The long effective pathlength is the source of the absorption sensitivity of the technique. The light transmitted through the cavity is coupled into and dispersed by a grating spectrograph and detected with a sensitive CCD detector. Usually a combination of filters is necessary for removing stray light which would otherwise have a serious influence on the weak cavity transmission. The IBBCEAS technique can be used with a sample cell enclosing the cavity (closed path) or without the sample cell entirely (open path). Each configuration has advantages and disadvantages. The sample cell provides a rigid structure for the stable cavity, but inlet and sample losses to the wall surfaces may be important. The open path configuration avoids wall effects, but long term stability can be more difficult to maintain. Ultimately, the selection of the cavity structure depends on the stability of the target species and the application.

IBBCEAS combines the simplicity and robustness of standard non-invasive optical absorption spectroscopy with the absorption enhancement achieved in cavity ring-down spectroscopy.

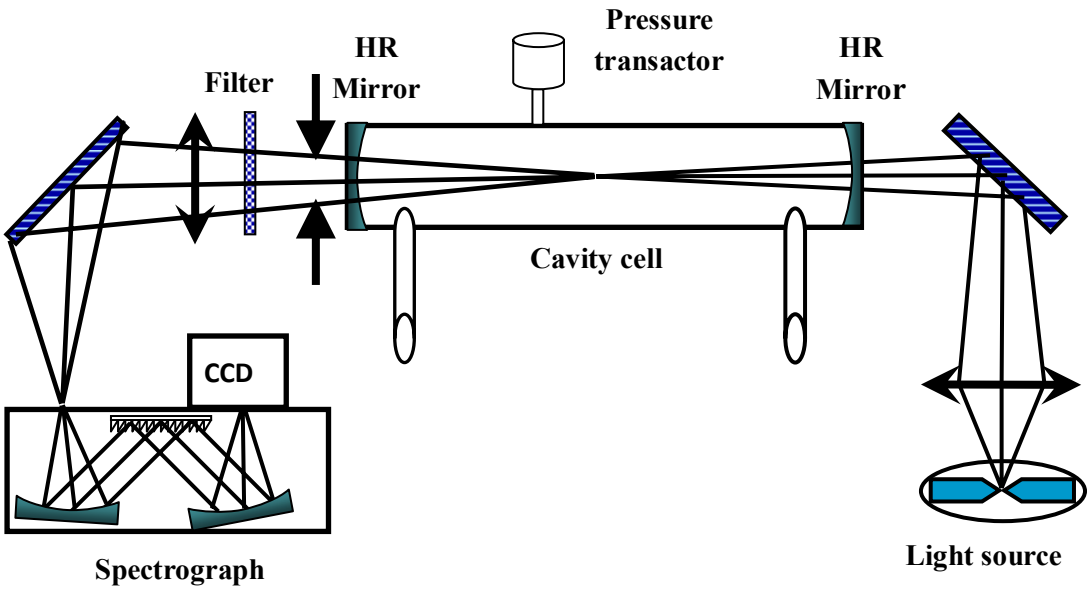


Figure 2.1 Schematic of an incoherent broadband cavity-enhanced spectroscopy system

The retrieval of the extinction coefficient in the cavity with broad-band incoherent light is based on the superposition principle (Lehmann and Romanini, 1996). It is assumed that nonlinear effects are negligible and that the bandwidth $\Delta\nu$ of the detector is sufficiently large (i.e, $\Delta\nu$> free spectral range of the cavity), so that the influence of the eigenmode structure of the resonator on the variation of the intensity is too small to be detected.

Following the analysis of Fielder et al. (2003a) we assume an optically stable cavity of length d, formed by two mirrors of reflectivity R. The cavity is continuously excited with incoherent light of intensity $I_{in.}$ The intensity of the light transmitted through the entrance mirror is thus $I= I_{in}$ (1-R), where (1-R) indicates the imperfect mirror reflectivities. As the cavity is subject to additional losses per pass, L, arising from sample absorption or extinction, the intensity reflected back at the 2nd exit mirror is $I=I_{in}(1-R)(1-L)R$, while the transmitted intensity is $I=I_{in}(1-R)^2(1-L)$. After an odd

number of passes, I can then be described by the superposition of the light, leading to the following infinite sum:

$$\begin{aligned} I &= I_{in}(1-R)^2(1-L)+ \\ &I_{in}(1-R)^2R^2(1-L)^3+....+I_{in}(1-R)^2R^{2n}(1-L)^{2n+1}+... \\ &= I_{in}(1-R)^2(1-L)\sum_{n=0}^{\infty}R^{2n}(1-L)^{2n} \end{aligned} \tag{2.1}$$

Since $R < 1$ and $L < 1$ this geometric series converges and Eq. (2.1) can be written in the form:

$$I = I_{in}\frac{(1-R)^2(1-L)}{1-R^2(1-L)^2} \tag{2.2}$$

For an empty resonator with $L = 0$, the time integrated transmitted intensity, I_0, is given by $I_0 = I_{in}(1\text{-}R)(1+R)^{-1}$, and the fractional losses per pass can then be expressed as a function of the ratio of intensities measured without and with losses:

$$(1-L) = \sqrt{\frac{1}{4}\left(\frac{I_0}{I}\frac{(1-R^2)}{R^2}\right)^2+\frac{1}{R^2}}-\frac{1}{2}\left(\frac{I_0}{I}\frac{(1-R^2)}{R^2}\right) \tag{2.3}$$

Assuming the losses per pass to be solely due to Lambert–Beer absorption with which $1 - L = \exp(-\varepsilon d)$, the molar extinction coefficient, ε , can be written in the general form:

$$\varepsilon = \frac{1}{d}\left|\ln\left(\frac{1}{2R^2}\left(\sqrt{4R^2+\left(\frac{I_0}{I}(R^2-1)\right)^2}+\frac{I_0}{I}(R^2-1)\right)\right)\right| \tag{2.4}$$

For small losses per pass and high reflectivities of the mirrors, $L\rightarrow 0$, $R\rightarrow 1$, and the extinction coefficient in Eq. (2.4) can be approximated by:

$$\varepsilon \approx \frac{1}{d}\left(\frac{I_0}{I}-1\right)(1-R) \tag{2.5}$$

The validity regime of the Eq. 2.5 depends on losses per pass and reflectivities Equation 2.5 starts to strongly deviate from Eq. 2.4 at 25% losses per pass when the R equals 0.995 (Fiedler et al., 2003a). Therefore for small absorptions in the atmosphere Eq. 2.5 is a reasonable approximation.

2.3 Components of the spectrometer

2.3.1 The light source

The light source is a key component of the IBBCEAS approach and influences the performance of the whole system. As the name of technique suggests, the light source used is both broadband and incoherent. The spectral output of the light source should cover the absorption spectra of the species to be investigated. Desirable characteristics are a high radiance in the spectral region of interest and stable intensity over the duration of measurement. Although most light sources do not meet these requirements, both Xenon arc lamps and high power light emitting diodes (LEDs) are stable, high radiance devices that are widely used in IBBCEAS systems.

Xenon arc lamps have a wide thermal emission spectrum covering the ultraviolet, visible, and near-infrared wavelength regions (approximately 180–2000 nm). A typical xenon arc lamp has a very high radiance that allows efficient imaging of light into the optical cavity. The brightest emission of the arc lamp usually comes from a spot within 1 mm of the lamp electrodes. Modifications of the arc lamp performance are possible under some circumstances, including a special short arc lamp running in so-called hot spot mode. The hot spot source differs from the conventional diffuse mode arc lamp in that the spot of the light is much smaller (~ 150 μm), with extremely high radiance. A hot spot with spectral radiance of 18 W cm^{-2} sr^{-1} nm^{-1} at 400 nm, which is about one to two orders of magnitude higher than in the diffuse mode, is formed close to the cathode surface (Fig. 2.2) (Welz et al., 2006b). Lamp intensity

variations affect the measured extinction coefficients and are another point to be considered. The long term dimming and short-term variation of a 75 W Xe arc lamp are shown in Fig. 2.3. The lamp output is highly stable, with short-term fluctuations of 0.2% and a further dimming of 0.27% per hour. This stability is likely to be worse for lamps nearing the end of their life.

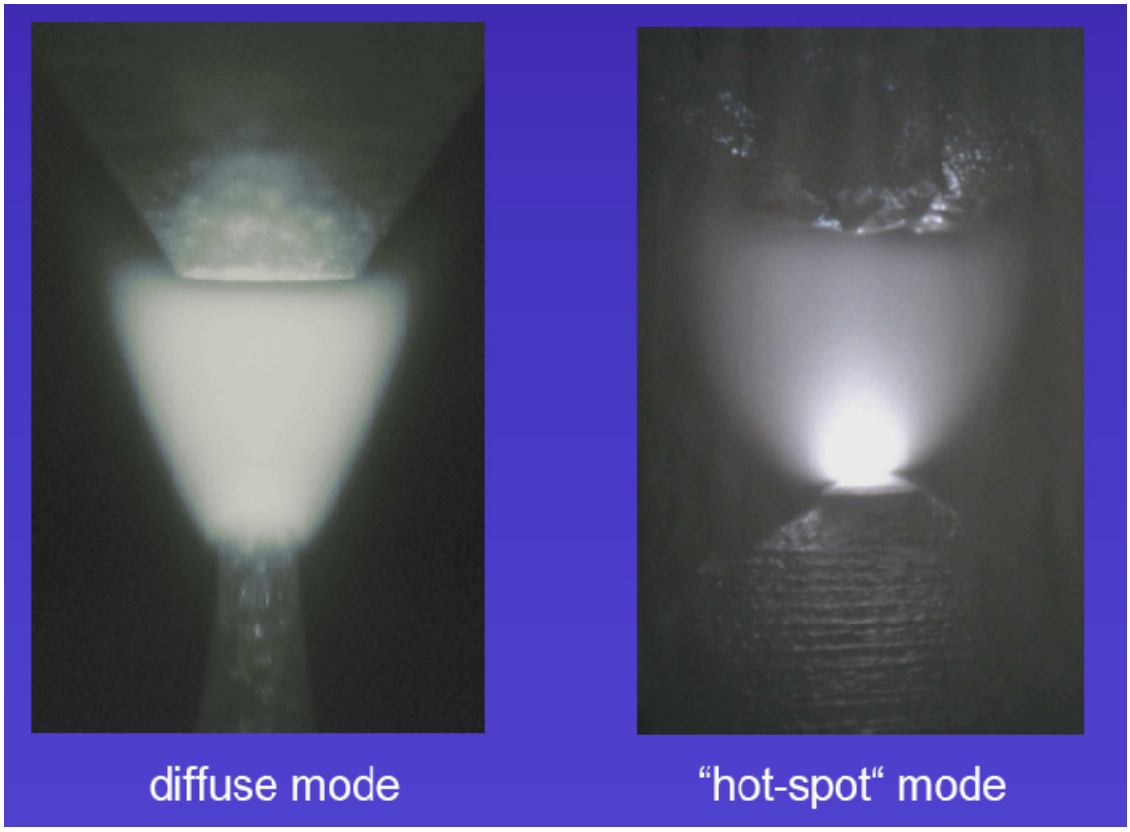


Figure 2.2 Hot Spot of the Arc Lamp. Comparison between the brightness of the normal Xe arc lamp (left) and that of the “hot-spot” mode lamp (right) showing the very bright spot near the cathode (Welz et al., 2006a)

However, the arc lamp has disadvantages as well. a) The xenon gas has some emission lines which vary depending on the temperature and pressure inside the bulb and may produce spectral artefacts. b) Transmission of the broadband emission (especially in the IR range) into the spectrometer greatly increases stray light levels. Stringent filtering is required to attenuate this background signal to sufficiently low levels. c)

The life time of xenon arc lamp bulbs varies from 4-12 weeks, and effort and expense is needed to replace the bulb. d) Only a small portion (usually 5%) of the isotropic emission of the xenon arc lamp is collected (Kern et al., 2006).

Owing to these drawbacks of the arc lamp, high power LEDs have been adopted as convenient and cost effective alternative light sources for IBBCEAS (Ball et al., 2004). Compared to Xe arc lamps, LEDs are compact, efficient, and often have higher peak spectral radiances than arc lamps. In the near-UV range, where high power LEDs only extend down to 365 nm, the Xe arc lamp remains the better light source for measuring spectra below 360 nm.

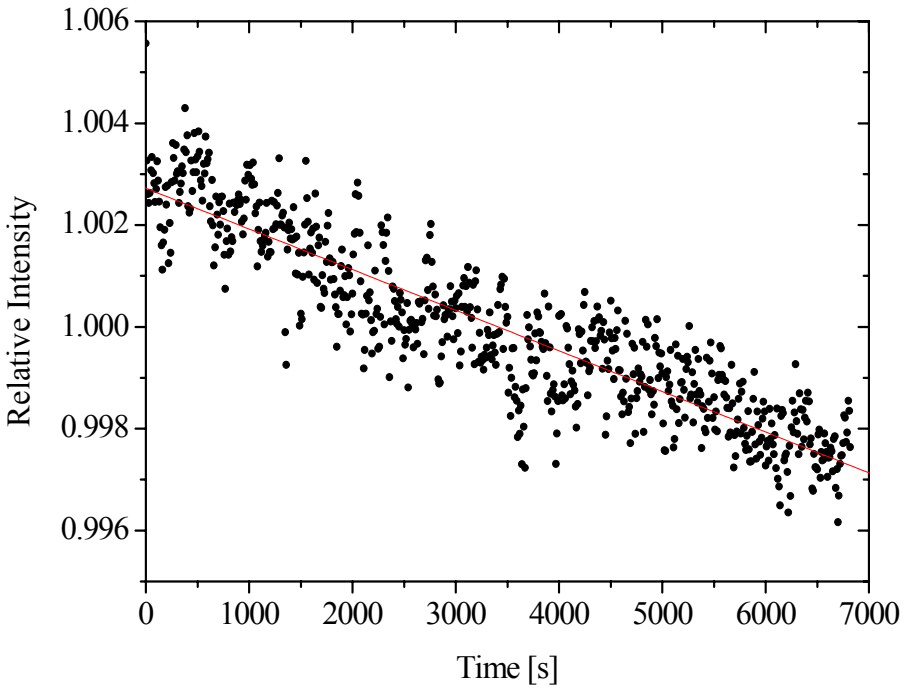


Figure 2.3 Temporal dependence of the intensity of the arc lamp output at 355 nm. The long term trend is given by a slope of 0.27% per hour and the short term fluctuations from the trend line are approximately 0.2%. The measurement plot of pixel at 355 nm was based on a 1 s integration time over 6820 s.

2.3.2 Spectral filtering

As an incoherent source, a Xe arc lamp produces spectral output from around 180 nm to 2000 nm. The highly reflective mirrors of the optical cavity function as a highly efficient band rejection filter. On the other hand, light outside of the cavity mirror range is transmitted very efficiently through the cavity. Coupling all transmitted light into the spectrograph would cause serious stray light problems and possibly saturate the CCD detector. In addition, the background light would vary with absorption outside the cavity spectral region. In the current work focusing on near-UV spectroscopy this problem is more acute because the UV output of the arc lamp is weaker than in the visible range. In addition, there are fewer standard optical elements and filters in the UV. Hence, obtaining a small spectral region in the near-UV (320 nm to 380 nm) to match that of the cavity proved to be challenging. Nevertheless, a combination of several bandpass filters, dielectric mirrors, and short-pass filters allowed reasonable control of the spectral output.

Fig. 2.4 shows the transmission of three filters: a band pass filter centred at 357 nm (Semrock), a short pass Schott UG11 filter, and an IR absorbing filter (KG1). Combining these three filters achieved a spectral window located within the high reflectivity range of the cavity mirror and reduced stray light to an acceptable level.

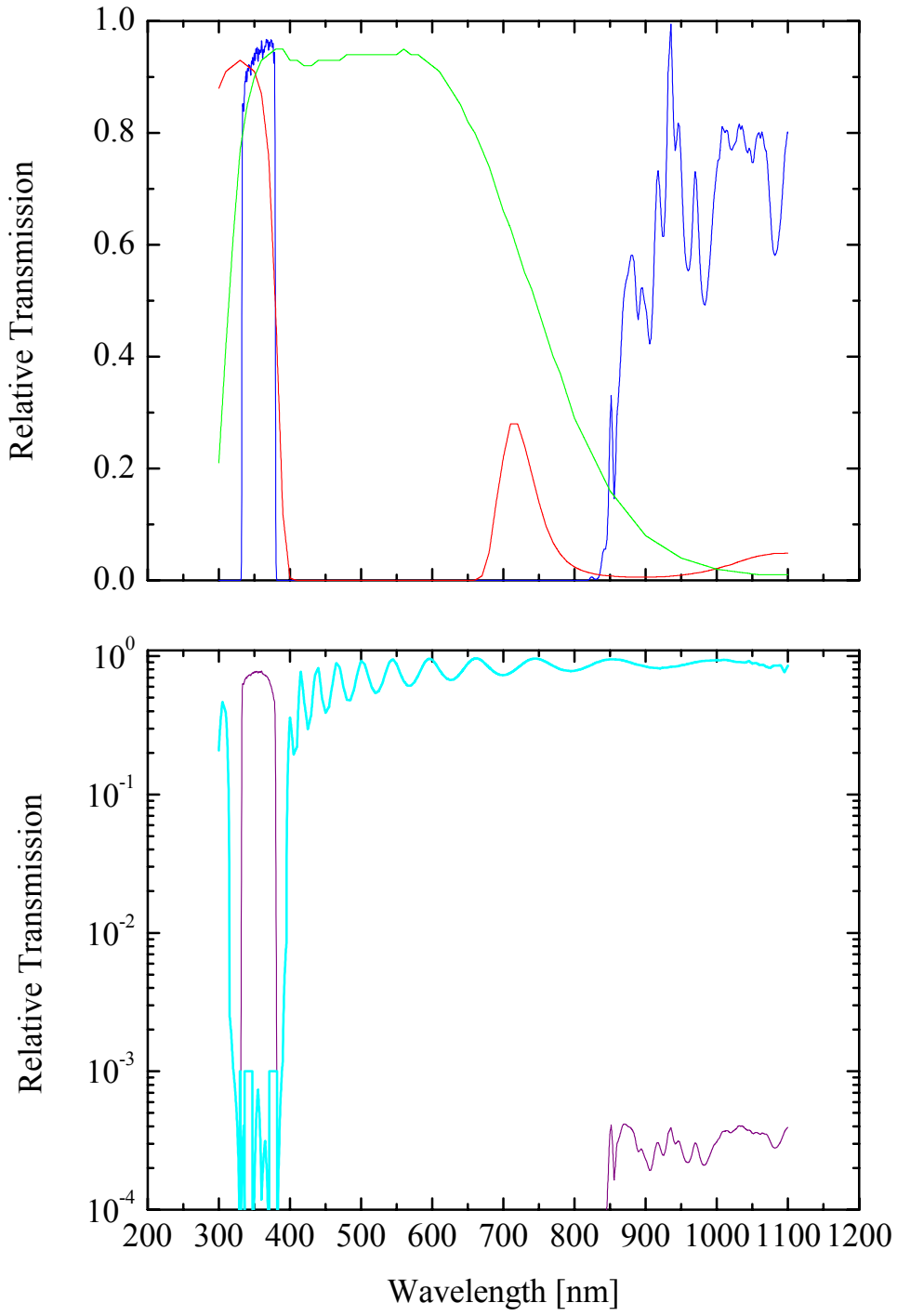


Figure 2.4 TOP: Filter transmission curves of Semrock 357 (blue), UG11 (red) and KG1 (green). BOTTOM: Calculated filter transmission curve of all three filters (purple) as well as the transmission curve of the optical cavity (cyan).

2.3.3 Detector

With low light levels reaching the CCD, it is essential that the detector be highly sensitive over the whole spectral range monitored. The quantum efficiency (QE), which indicates the conversion efficiency of photon to electrons, determines the sensitivity of the detector. A higher relative QE of the CCD at the wavelength of interest will give a larger signal and a more sensitive spectrometer. Conventional CCD detectors have at most 30% QE in the near-UV range. However, back-thinned CCD detectors are more efficient in the UV range. Combining this detector with an anti-reflection coating, the detector selected for our system (Andor DV420-BU) has an average 80% QE from 300 to 400 nm (90% at 400 nm and 60% at 300 nm). Different integration times of 200, 400, 600, 800 and 1000 ms were measured and indicated that the detector displayed good linearity (Fig. 2.5).

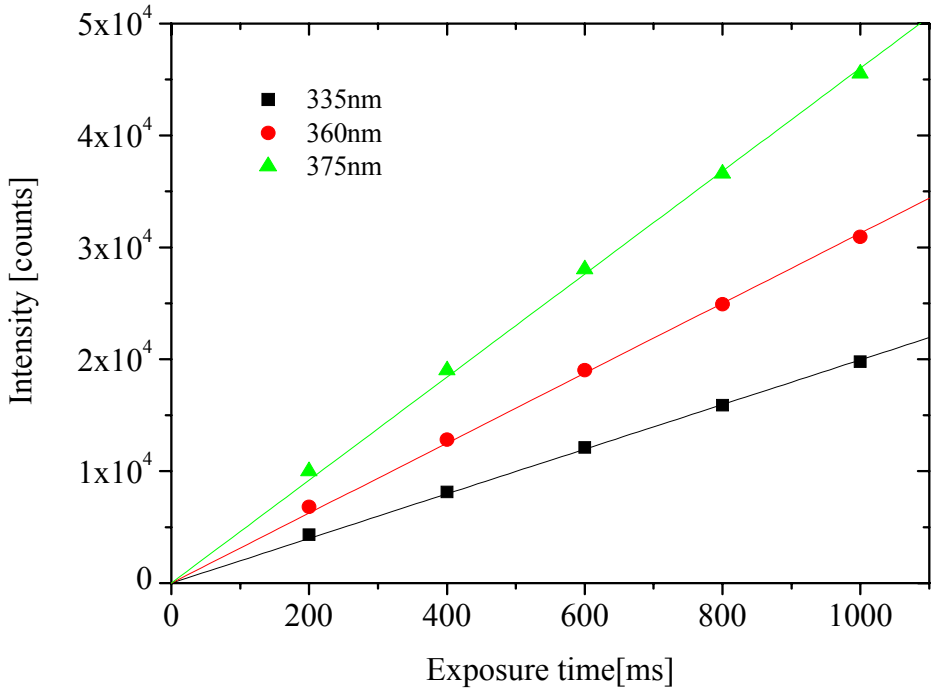


Figure 2.5 Linearity of the detector response to different integration times for several wavelengths.

2.4 Instrument performance

2.4.1 Allan variance study

The Allan variance is often used to study the stability and sensitivity of a measuring device (Werle et al., 1993;Weibring et al., 2006;Wu et al., 2008). The IBBCEAS spectra within the mirror range can be used for estimating the entire system's stability and sensitivity, thereby identifying the optimum averaging time to give a maximum signal-to-noise ratio. In the current case, the intensity of the cavity signal was recorded over 200 consecutive 2.5 s spectra (500 ms integration time averaged 5 times) in an evacuated cavity. The following calculation was carried out: the N elements of the recorded cavity light intensity $Y_{p,n}$ were divided into M groups containing K data points (p=1,2,…370 the pixel number within the mirror range 330 - 370 nm), and n=1,2,…200 the N elements) and then averaged within the groups as follows:

$$X_{p,i}(K) = \frac{1}{K}\sum_{m=1}^{K} Y_{p,ik+m} \qquad i = 0,1,2,\ldots,M\,;\, M = \frac{N}{K}\text{-}1 \tag{2.6}$$

The Allan variance can be then calculated using:

$$\sigma_A^2(p,K)=\frac{1}{2M}\sum_{i=1}^{M}\left(X_{p,i+1}(K)\text{-}X_{p,i}(K)\right)^2 \tag{2.7}$$

and the averaged Allan variance of all the pixels was determined from:

$$\overline{\sigma_A^2(K)}=\frac{1}{P}\sum_{p=1}^{P}\sigma_A^2(p,K) \tag{2.8}$$

The results are plotted in Fig. 2.6 and extend to 100 s averaging time for 370 pixels. Regarding to the optimization of the detector, the minimum Allan variance appears around 55 s and can be used as a reference for this detector in future experiments.

Other acquisition intervals, such as 30 or 60 seconds, may be more convenient for experimental purposes while still displaying good signal-to-noise characteristics.

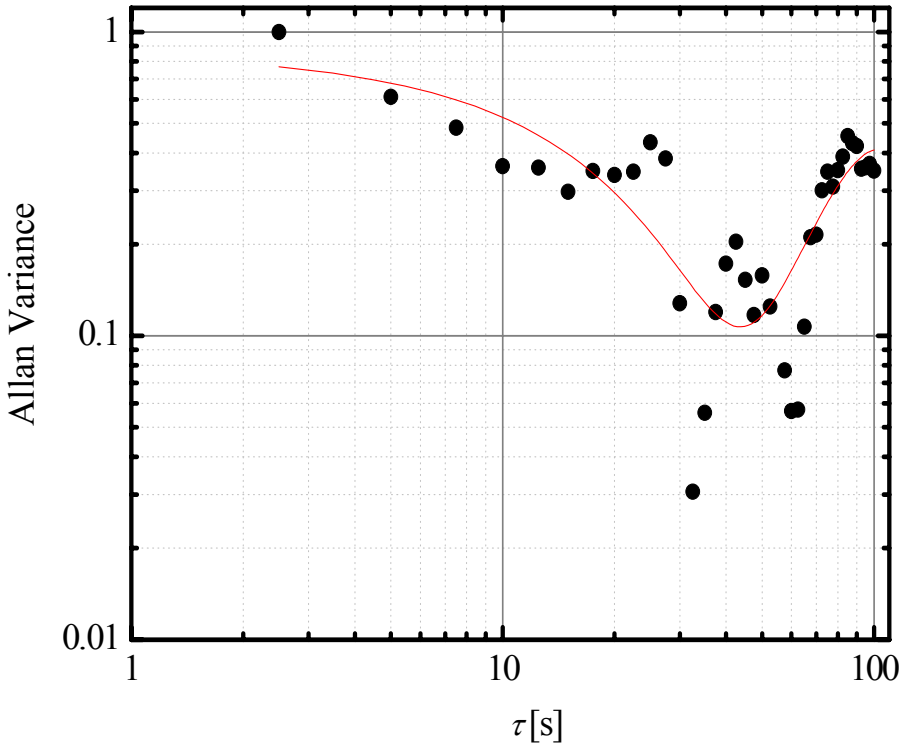


Figure 2.6 Allan variance of the integrated spectrometer intensity from 330 and 370 nm as a function of the averaging time. At the average time τ = 55 s the Allan variance showed a minimum.

2.4.2 Sensitivity

The sensitivity of IBBCEAS can be compared to that of conventional single pass absorption spectroscopy using Eq. (2.5). Approximating $(I_0\text{-}I)/I_0 \approx (I_0\text{-}I)/I \approx ln\,{}^{I_0}/_{I}$ in the case of small absorptions, the minimum detectable absorption coefficient, $\varepsilon_{\min}$, can be expressed as:

$$\varepsilon_{\min} = \frac{1}{d}\left(1 - \frac{I_{\min,\,sp}}{I_{0,sp}}\right) \tag{2.9}$$

for single pass measurements, and as:

$$\varepsilon_{\min} = \frac{1}{d}\left(1 - \frac{I_{\min}}{I_0}\right)(1 - R) \tag{2.10}$$

for IBBCEAS measurements. Here $I_{\min;sp}$ and $I_{\min}$ are the minimum detectable intensities, while $I_{0;sp}$ and I_0 are the background intensities (without any analyte) for single pass and IBBCEAS measurements respectively. The right-hand side of Eq. (2.10) represents the minimum detectable fractional absorption in IBBCEAS and follows directly from Eq. (2.5). The above equation demonstrates that the IBBCEAS technique is generally $(1\text{-}R)^{-1}$ times more sensitive than a conventional single pass absorption method (Eq. 2.9), assuming that the ratios of minimum detectable intensity to background intensity are comparable for both approaches. This is always the case, as the optical cavity significantly reduces the measured intensity.

In practice, the sensitivity of an IBBCEAS system to atmospheric trace species can be estimated by dividing the maximum absorption coefficient by the root mean square of the fitting residual to give an estimate of the sensitivity of the instrument. Table 2.2, lists the sensitivity of an IBBCEAS spectrometer in the near-UV for several atmospheric trace species with a 60 s acquisition time (Chen and Venables, 2010).

Table 2.2 Measured sensitivity of an IBBCEAS spectrometer (in a 60 s acquisition time, cavity length L = 198 cm) to several trace gases. The estimated sensitivity to OClO is.shown in italics.

Species	σ [10^{-17}cm^2]	R	Sensitivity [ppbV]
NO_2	0.05 (368 nm)	0.999	0.28
HONO	0.04 (368 nm)	0.999	0.23
BrO	2.5 (340 nm)	0.996	0.02
OClO	*1.3 (345 nm)*	*0.996*	*0.04*

2.4.3 Effect of flow rate and pressure on the cavity signal

Although an *in situ* measurement at low pressures is one of the advantages of the IBBCEAS technique, the flow rate may influence the transmitted light intensity. An experiment was designed to vary the flow rate and pressure of the system to determine how these factors affected the IBBCEAS signal. Fig. 2.12 shows the temporal dependence of the intensity and pressure during the experiment. The flow rate of pure N_2 was increased using a mass flow controller from 0.2 L min^{-1} to 1 L min^{-1}, after which the system pressure was increased by 3 mbar for 20 minutes by placing the gas exhaust under a few centimetres of water. The pressure was then decreased while maintaining the same flow rate at 1 L min^{-1}, and eventually the original slow flow rate was restored. Changing the flow rate had a significant (15%) influence on the signal. Increasing the flow rate also raised the pressure by about 0.2 mbar, but isolating the influence of the pressure showed that pressure changes caused a much smaller and temporary variation in the intensity. The effect of the flow rate on the system signal probably arises from turbulence in the cavity. As a consequence: (a) the flow rate should be kept as stable as possible throughout the experiment; (b) slight

changes in pressure do not affect the system signal significantly, which means that simple misalignment of the cavity mirrors by a pressure effect associated with higher flow rates can be excluded; and (c) as turbulence could affect the effective path length of the system, calibration of the mirror reflectivity should be carried out under the same flow conditions as subsequent measurements.

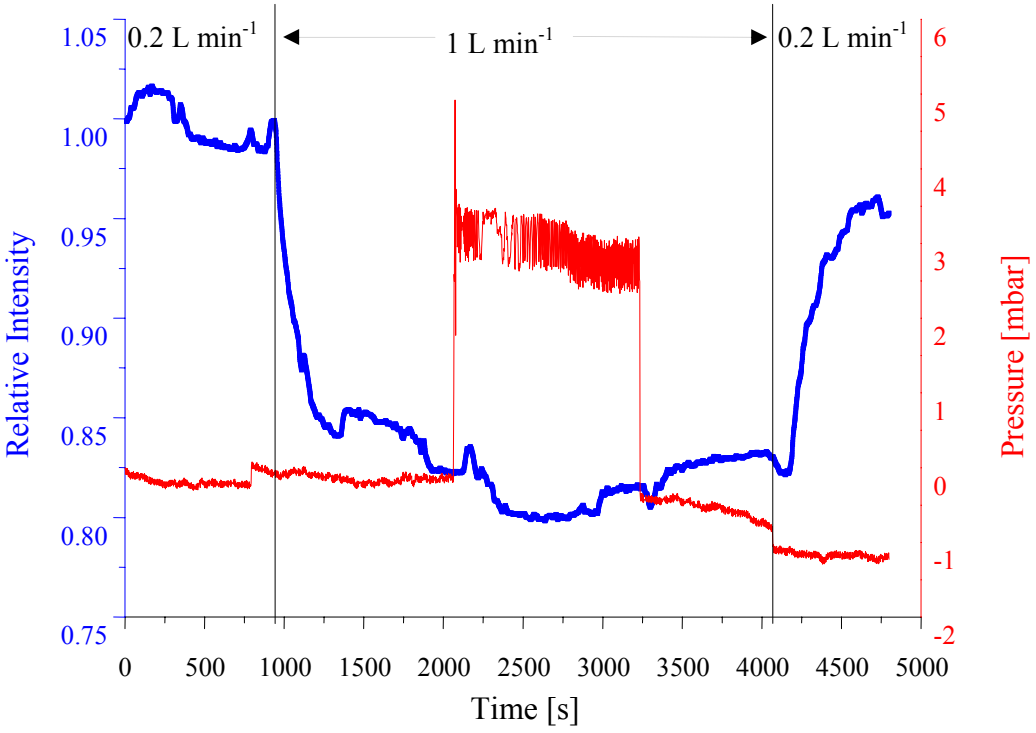


Figure 2.12 Relative intensity variations at 355 nm (blue) at different flow rates and pressures (red). The noise at high pressure is associated with bubbling from the submerged sample gas outlet.

2.5 Calibration of the instrument

2.5.1 Spectrograph wavelength and resolution

The wavelength scale and instrument line shape must be calibrated so that literature absorption cross-sections can be convoluted to match the measured spectrum. A HgNe pencil lamp (Newport) was used as an atomic emission line source for the

calibration. Several strong Hg emission lines are visible between 280 nm and 410 nm (Fig. 2.7a). A 3rd order polynomial function was fitted to the pixel-wavelength mapping of several strong emissions (Fig. 2.7b). The uncertainty between the polynomial fitting and observed points was about 0.02 nm. The spectrometer resolution was calculated from the FWHM of a Gaussian fit an mercury emission lines (Fig. 2.7c). With a 25 micron slit and 1200 line/mm grating, the resolution of the spectrometer was 0.27 nm at 334 nm. Several other emission lines gave similar results.

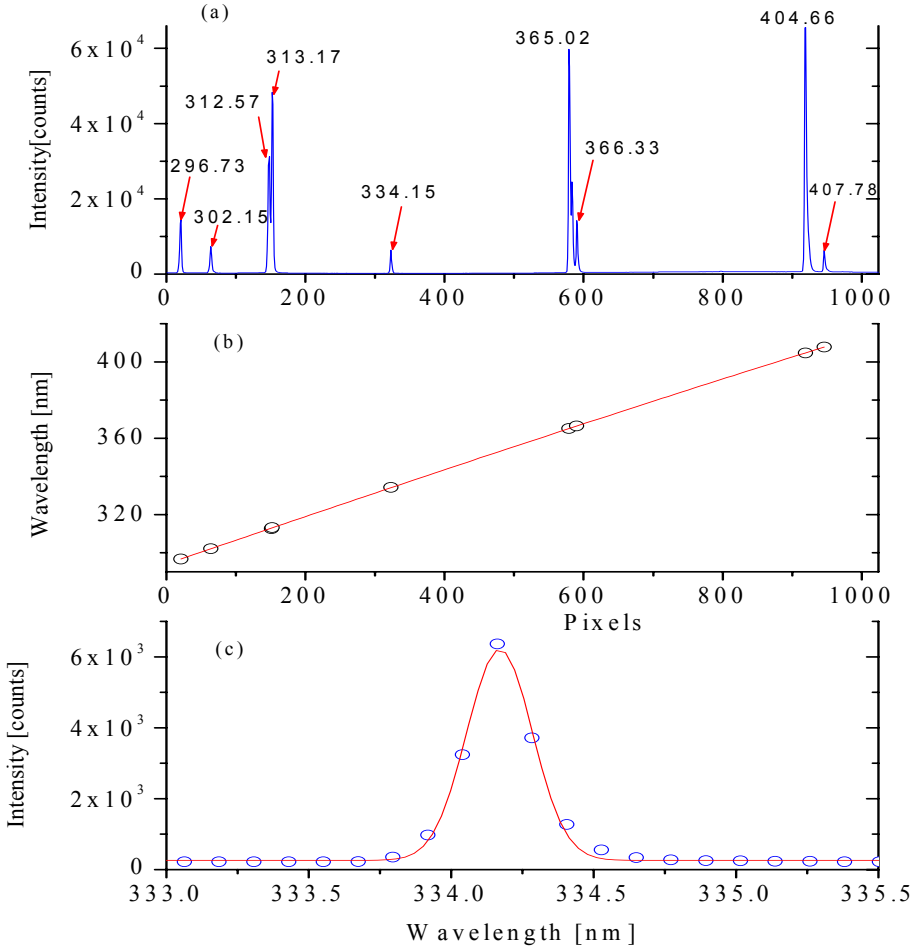


Figure 2.7 (a) A near-UV spectrum of the HgNe penray lamp as recorded by the spectrograph. (b) A 3rd order polynomial fit of the wavelength to the pixels. The uncertainty is about 0.02 nm. (c) A Gaussian fit to the 334.15 nm mercury emission line showing a FWHM of 0.27 nm.

2.5.2 Calibration of the mirror reflectivity

Quantitative measurements using IBBCEAS require the mirror reflectivity, R, as derived in Eq. (2.5). The mirror reflectivity can be calibrated using several methods: (a) by the absorption spectrum of a known concentration of gas, (b) by the difference in Rayleigh scattering of two gases, or (c) with a calibrated low-loss optic. Each approach is described below.

Calibration from a known absorption

This approach requires a gas absorbing in the wavelength range of interest. Although any such gas may be used, NO_2 is particularly convenient as it is readily available and has a broad absorption across the near-UV and visible ranges. The method is based on Eq. (2.5). The mirror reflectivity requires a known concentration of NO_2 and hence a known absorption coefficient; the mirror reflectivity can then be derived from the measured absorption (Gherman et al., 2008).

There are several ways to quantify NO_2 in the cavity: (a) In vacuum the number density can be determined by measuring the pressure directly. (b)With a known mass of NO_2 in a cell or chamber of known volume, the real number density of NO_2 is readily calculated. (c) Another calibrated instrument, such as the chemiluminescent NO_x detector, can be used to measure the NO_2 concentration. Very low concentrations of NO_2 (tens of ppbV) are required for suitable absorptions. Losses to the walls of the glass bulb or sample cell can occur, especially where the surface-to-volume ratio is large. These effects increase the uncertainty in the calibration. Another disadvantage of this method is that the measured absorption spectrum does not exactly match the literature absorption cross sections convoluted to

the instrumental function, leaving some residual structures in the reflectivity curve (Fig. 2.8). Some form of smoothing or a polynomial fit could remove these features.

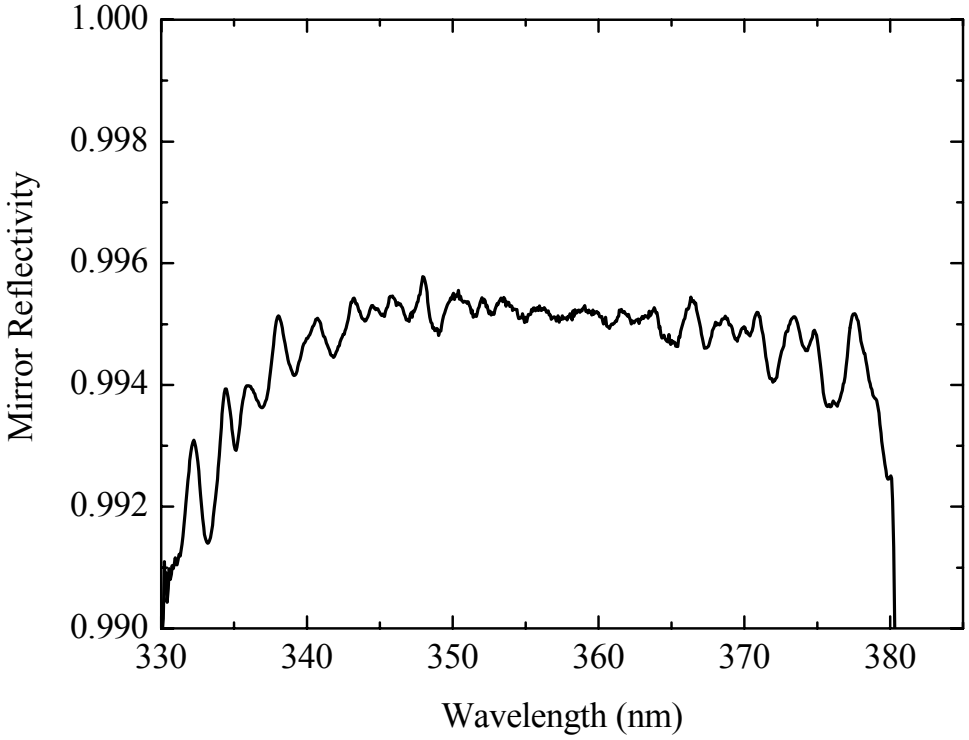


Figure 2.8 Mirror reflectivity calibrated by NO_2 in a low pressure system. Residual structures are evident in the reflectivity spectrum.

Rayleigh scattering of two gases

In some circumstances, it is not possible to work under vacuum, especially in flow systems or in open path configurations in the field. Alternative approaches to calibrate the mirror reflectivity besides a known absorption of gas are desirable. Nitrogen and carbon dioxide are two unreactive gases that have a big difference in their Rayleigh scattering cross sections (Naus and Ubachs, 2000;Sneep and Ubachs, 2005), suggesting that Rayleigh scattering could be used to determine the mirror reflectivity (Langridge et al., 2008;Thalman and Volkamer, 2010). After taking a

measurement of the cavity signal filled with CO_2, the sample gas was switched to N_2 and a further measurement was taken (Fig. 2.9). The observed extinction of each gas is then:

$$\varepsilon_{co_2} = n\sigma_{co_2}^{rayl} = \left(\frac{I_0}{I_{co_2}} - 1\right)\frac{(1-R)}{L} \tag{2.11}$$

And

$$\varepsilon_{N_2} = n\sigma_{N_2}^{rayl} = \left(\frac{I_0}{I_{N_2}} - 1\right)\frac{(1-R)}{L} \tag{2.12}$$

Based on Eq. (2.11) and Eq. (2.12) the two unknowns, R and I_0, can be calculated. The reflectivity is then given by:

$$\frac{(1-R(\lambda))}{d} = \frac{I_{N_2}(\lambda)N_{N_2}\sigma_{N_2}^{rayl}(\lambda) - I_{CO_2}(\lambda)N_{CO_2}\sigma_{CO_2}^{rayl}(\lambda)}{I_{CO_2}(\lambda) - I_{N_2}(\lambda)} \tag{2.13}$$

The advantage of this calibration approach is that the Rayleigh scattering is a broad, smooth extinction, as opposed to structured absorption of NO_2. The results of the NO_2 and Rayleigh scattering calibrations are shown in Fig. 2.10. However, the uncertainty of the Rayleigh scattering cross sections (~10 %) is larger than that of NO_2 (less than 5%). As the intensity changes are small (Fig. 2.9), drifts in the lamp output add to the calibration uncertainty. Therefore, Rayleigh scattering is better used as a relative calibration of the mirror and then scaled to an absolute value determined at a single wavelength.

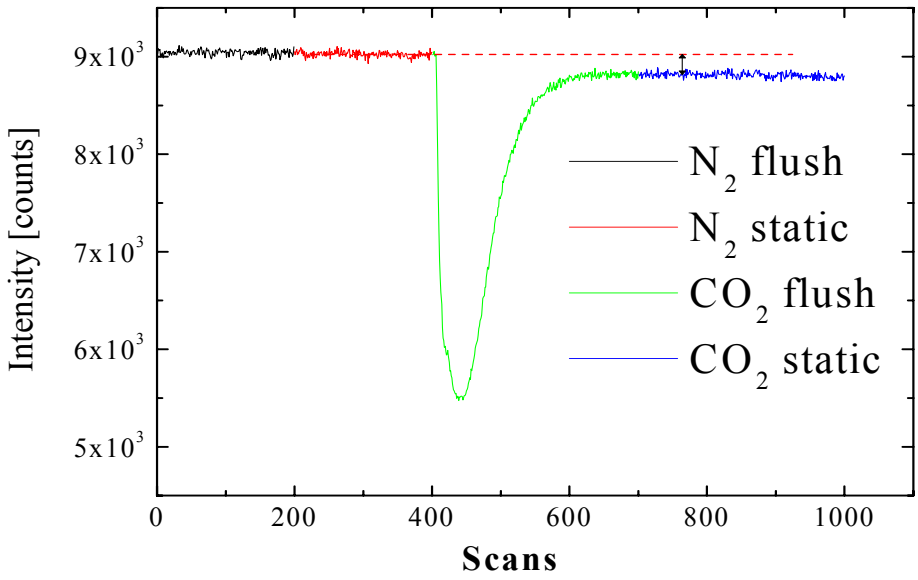


Figure 2.9 The calibration of the mirror reflectivity based on the different Rayleigh scattering of N_2 and CO_2.

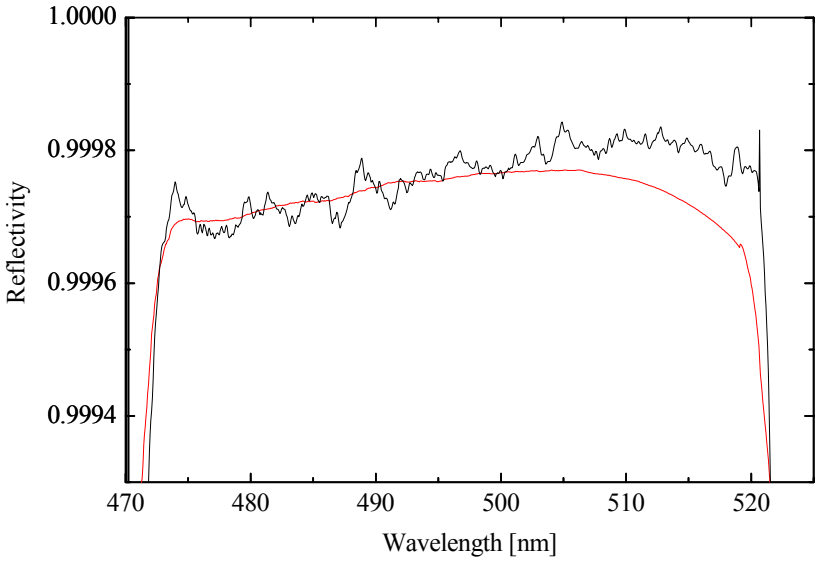


Figure 2.10 Comparison of the same mirror reflectivity calibrated by NO_2 (top black) and by Rayleigh scattering (red bottom)

Single wavelength absorption

As shown above, Rayleigh scattering calibration gives a smooth mirror reflectivity curve, but the relatively small signal can be susceptible to drifts in lamp intensity, thereby introducing a systematic error. Therefore the Rayleigh scattering calibration of the mirror reflectivity was scaled to match the known absorption of a gas at a single wavelength. In this case, after calibration by Rayleigh scattering, the reflectivity curve was scaled, based on the O_4 dimer absorption at 360.5 nm. The accuracy of the mirror calibration is limited to the literature absorption cross-section standard deviation at 360.5 nm (Greenblatt et al., 1990;Dianov-Klokov, 1964;Volkamer, 1996;Salow and Steiner, 1936), as well as the uncertainty in the gas concentration. Other single wavelength calibrations are also possible based on O_3 or O_2 absorption.

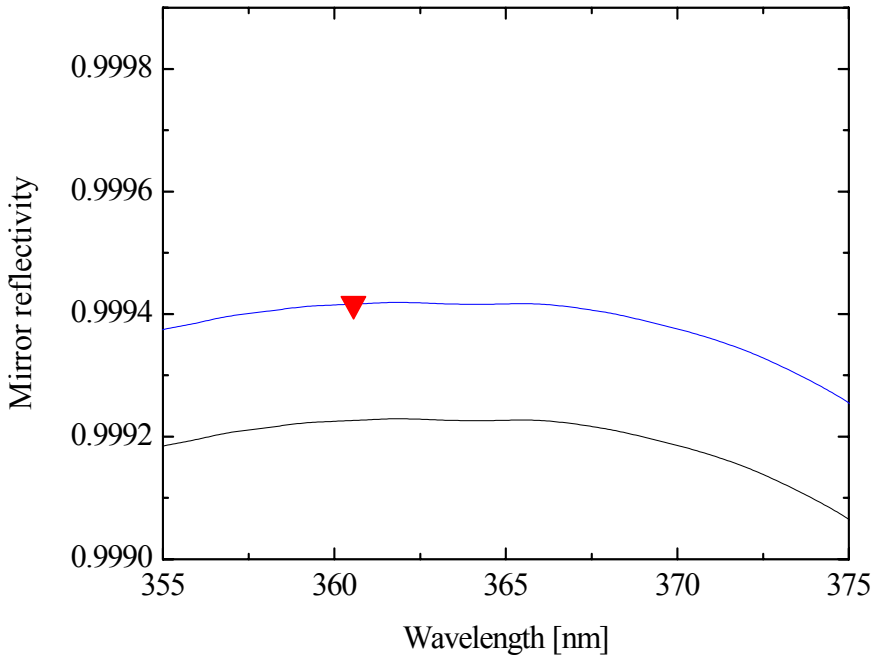


Figure 2.11 The mirror reflectivity calibrated by Rayleigh scattering (black line). The blue line shows the mirror reflectivity scaled to the value determined by the O_4 dimer absorption at 360.5 nm (red triangle)

Low loss optics

In all the above cases, a known loss was used to calibrate the mirror reflectivity. By using an anti-reflection coated optical substrate of known loss, $L(\lambda)$, instead of a calibration gas, the mirror reflectivity can also be determined (Varma et al., 2009). In this case, the losses of the substrate must be very low (< 0.01%) otherwise the intensity reduction would be too great to be used within the cavity regime. This method, which involves inserting the low loss optic substrate into the optical cavity, is especially convenient for open path configurations. In this case the reflectivity $R(\lambda)$ can be calibrated as follows:

$$R(\lambda) = 1 - \left(\frac{I_{LLS}(\lambda)}{I_0(\lambda) - I_{LLS}(\lambda)} L(\lambda) \right) \tag{2.14}$$

In Eq. (2.14) the $I_0(\lambda)$ and $I_{LLS}(\lambda)$ are the cavity transmission intensity with and without the low loss optics in the cavity. However, drawbacks of this method are that the loss, L, has to be calibrated before the experiment and that custom optics with sufficiently low losses are costly. The calibration of $L(\lambda)$ can be determined by cavity ring-down methods as below:

$$L(\lambda) = \frac{d}{c} \left(\frac{1}{\tau_2(\lambda)} - \frac{1}{\tau_1(\lambda)} \right) \tag{2.15}$$

This method has first reported by Varma et. al. but has not been widely adopted, probably because calibrating the low loss optic itself is not straightforward and the low loss optics itself is expensive. However, it is a feasible method to calibrate the mirror reflectivity for open path configurations and may be valuable in harsh conditions.

2.6 Spectral Analysis

The IBBCEAS extinction spectrum can be analyzed either based on the absolute or on the differential absorption. In this section, quantification based on the absolute absorption of the sample will be introduced first, followed by a discussion of the use of the differential absorption method. Lastly, retrieval of the aerosol extinction will be addressed.

2.6.1 Absolute absorption

The measured extinction $\varepsilon(\lambda)$, if only arising from gas phase absorption, can be described as followed:

$$\varepsilon(\lambda) = \sum_i \sigma_i(\lambda) \cdot N_i = \frac{1}{d}\left(\frac{I_0(\lambda)}{I(\lambda)} - 1\right)\left(1 - R(\lambda)\right) \qquad (2.16)$$

where $\sigma_i(\lambda)$ and N_i represents the absorption cross-section and number density of species i respectively. The number density can be retrieved by a linear least square fitting procedure if each absorption cross section of species i is known (Press et al., 2007):

$$\varepsilon(\lambda) = N_1\sigma_1(\lambda) + N_2\sigma_2(\lambda) + ... + N_i\sigma_i(\lambda) + a_0 + a_1\lambda + a_2\lambda^2 \qquad (2.17)$$

The polynomials are included as a baseline to compensate for the apparent extinction arising from lamp fluctuations. This approach was previously adopted in several studies (Dixneuf et al., 2009;Gherman et al., 2008;Varma et al., 2009;Vaughan et al., 2008;Venables et al., 2006).

2.6.2 Differential absorption

Under atmospheric conditions, the extinction coefficient also includes Rayleigh scattering by gas molecules as well as the Mie scattering by particles. The Rayleigh extinction coefficient, $\varepsilon_{\mathrm{Rayl}}$, describes elastic scattering of photons by air molecules and is proportional to λ^{-4}. The Rayleigh scattering cross section of air, σ_R^{air}, is about 4.4×10^{-16} cm^2 nm^4. The Mie extinction coefficient, $\varepsilon_{\mathrm{Mie}}$, describes elastic scattering processes by aerosols and largely depends on the aerosol size distribution and chemical composition. Therefore the extinction coefficient of Eq. (2.17) can be generalised as follows:

$$\varepsilon(\lambda) = \sum_i \sigma_i(\lambda) \cdot N_i + \varepsilon_{Rayl}(\lambda) + \varepsilon_{Mie}(\lambda)$$

In the real atmosphere, molecular absorbers are always present and Rayleigh and Mie scattering are also inevitable, so the atmospheric spectrum I_0 cannot be obtained free of any extinction. Instead, differential absorption methods can be used if the absorption spectrum of the species of interest contains marked structure within a fairly narrow wavelength range (typically 10 nm or less). These structured features in the spectrum can be used as a "fingerprint" of the molecular species.

In differential absorption spectrum analysis, the absorption cross-section $\sigma(\lambda)$ is separated into a "slow" component $\sigma^s(\lambda)$ and "fast" (highly structured) component $\sigma'(\lambda)$ (Platt and Perner, 1984;Plane and Nien, 1989). The example of the SO_2 absorption cross-section is shown in Fig. 2.12 where it is split into a rapid and a slow component after fitting to a 5th order polynomial. In the extinction spectrum, a broad variation arises from $\varepsilon_{Raly}(\lambda)$ and $\varepsilon_{Mie}(\lambda)$ as well as the slowly varying absorption from gas molecules. Then the differential extinction, $\varepsilon'(\lambda)$, can be defined as:

$$\varepsilon'(\lambda) = \varepsilon(\lambda) - \sum_i \sigma_i^s(\lambda) \cdot N_i - \varepsilon_{Raly}(\lambda) - \varepsilon_{Mie}(\lambda) \quad (2.19)$$

Thus, by using the polynomial representing the "slow" variations in the spectrum, Eq. (2.19) can be written as:

$$\varepsilon'(\lambda) = \sum_i \sigma_i'(\lambda) \cdot N_i + a_0 + a_1\lambda + \ldots + a_n\lambda^{n-1} \quad (2.20)$$

Hence, the number density of a trace gas, N_i, is now obtained by fitting the differential absorption cross-section, $\sigma'(\lambda)$, to the differential extinction, $\varepsilon'(\lambda)$.

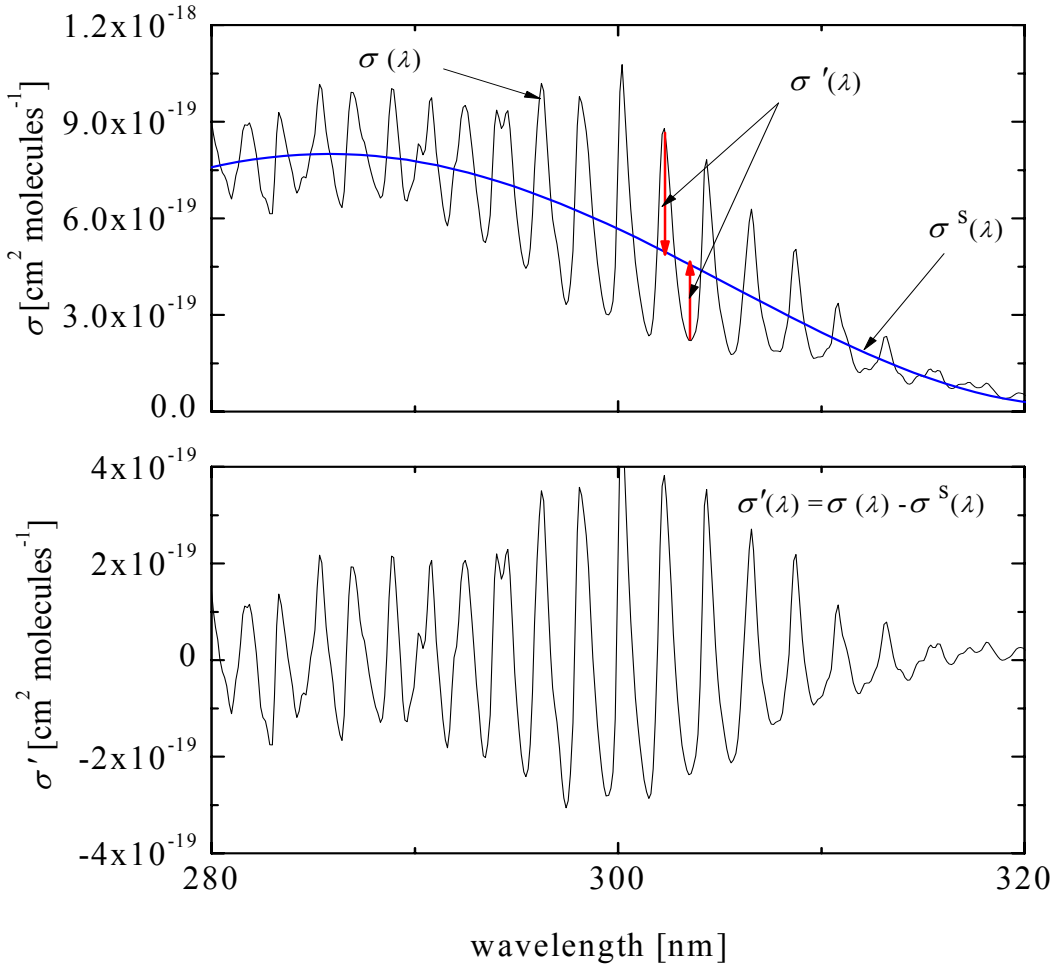


Figure 2.12 TOP: The absorption cross-section, $\sigma(\lambda)$, composed of a broadband (slow) component, $\sigma^s(\lambda)$, and a differential (fast) component, $\sigma'(\lambda)$, in the case of SO_2 (Bogumil et al.,

2003) BOTTOM: The differential absorption cross-sections of SO_2.

2.6.3 Aerosol extinction

Although the polynomial represents slow variations in the differential absorption method, the broad extinction spectrum $\varepsilon_B(\lambda)$ can be assigned to aerosol extinction as long as other contributions from molecular absorbers and instrumental artefacts have been accounted for. Unfortunately, the aerosol extinction is very sensitive to I_0 in Eq. (2.5), and long term dimming of the lamp is difficult to separate from the aerosol extinction. An alternative approach is to retrieve the aerosol extinction based on a known concentration of the fractional absorption, α_{abs}^{K}.

Figure 2.13 illustrates the calculation procedure. There are three different intensities transmitted through the cavity associated with different cavity extinctions, (a) Intensity without any sample extinction can be defined as I_0 (that is $\varepsilon = 0$). (b) Intensity with only spectrally broad and unstructured extinction can be defined as I_B ($\varepsilon = \varepsilon_B$). (c) Intensity in the general case in which there is both broad extinction as well as some (structured) sample absorption can be defined as I.

Assuming $I_0 > I_B > I$, with $\Delta I_B = I_0 - I_B$ attributed to the background extinction, and $\Delta I_A = I_B - I$ arising from structured absorption, the known fractional absorption, α_{abs}^{K}, can be deduced as follows:

$$\begin{aligned} \alpha_{abs}^{K} &= \varepsilon - \varepsilon_B \\ &= \left(\frac{\Delta I_B + \Delta I_A}{I}\right)\left(\frac{1-R}{L}\right) - \left(\frac{\Delta I_B}{I_B}\right)\left(\frac{1-R}{L}\right) \\ &= \frac{\Delta I_A}{I}\left(\left(\frac{1-R}{L}\right) + \varepsilon_B\right) \end{aligned} \tag{2.21}$$

Hence with a known absorption, α_{abs}^{K}, such as the O_2 B-band absorption which is

known in the atmosphere, we can retrieve the aerosol extinction as:

$$\varepsilon_B = \alpha_{abs}^K \left(\frac{I}{\Delta I_A}\right) - \left(\frac{1-R}{L}\right) \tag{2.22}$$

This method to retrieve the aerosol extinction based on a known fractional absorption was reported by Varma et al. (2009) and Thalman et al. (2010) and shown to correlate well with specific aerosol instruments (Varma et al., 2009;Thalman and Volkamer, 2010).

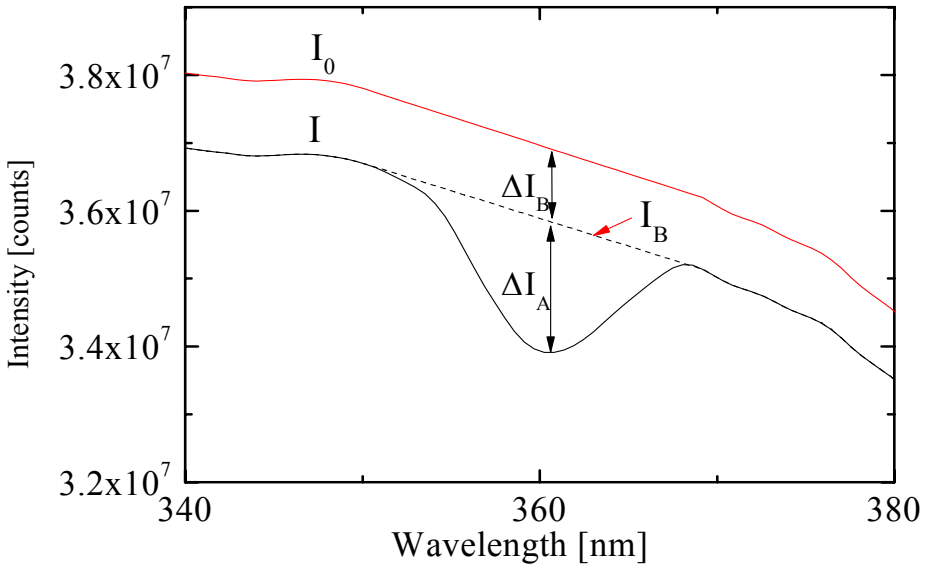


Figure 2.13 Calculation of the aerosol extinction based on a known structured absorption feature.

Bibliography

Ball, S. M., Povey, I. M., Norton, E. G., and Jones, R. L.: Broadband cavity ringdown spectroscopy of the NO_3 radical, Chem. Phys. Lett., 342, 113-120, 2001.

Ball, S. M., Langridge, J. M., and Jones, R. L.: Broadband cavity enhanced absorption spectroscopy using light emitting diodes, Chem. Phys. Lett., 398, 68-74, 10.1016/j.cplett.2004.08.144, 2004.

Ball, S. M., Hollingsworth, A. M., Humbles, J., Leblanc, C., Potin, P., and McFiggans, G.: Spectroscopic studies of molecular iodine emitted into the gas phase by seaweed, Atmos. Chem. Phys., 10, 6237-6254, 2010.

Benton, A. K., Langridge, J. M., Ball, S. M., Bloss, W. J., Dall'Osto, M., Nemitz, E., Harrison, R. M., and Jones, R. L.: Night-time chemistry above London: measurements of NO_3 and N_2O_5 from the BT Tower, Atmos. Chem. Phys., 10, 9781-9795, 10.5194/acp-10-9781-2010, 2010.

Berden, G., Peeters, R., and Meijer, G.: Cavity ring-down spectroscopy: Experimental schemes and applications, Int. Rev. Phys. Chem., 19, 565-607, 2000.

Berden, G., and Engeln, R.: Cavity ring-down spectroscopy : techniques and applications, Wiley, Chichester, U.K., 2009.

Bjorklund, G. C.: Frequency-Modulation Spectroscopy - New Method for Measuring Weak Absorptions and Dispersions, Opt. Lett., 5, 15-17, 1980.

Bogumil, K., Orphal, J., Homann, T., Voigt, S., Spietz, P., Fleischmann, O. C., Vogel, A., Hartmann, M., Kromminga, H., Bovensmann, H., Frerick, J., and Burrows, J. P.: Measurements of molecular absorption spectra with the SCIAMACHY pre-flight model: instrument characterization and reference data for atmospheric remote-sensing in the 230-2380 nm region, J. Photochem. Photobiol. A, 157, 167-184, 2003.

Chen, J., and Venables, D. S.: A broadband optical cavity spectrometer for measuring

weak near-ultraviolet absorption spectra of gases, Atmos. Meas. Tech., 4, 425-436, 10.5194/amt-4-425-2011, 2011.

Cheskis, S.: Quantitative measurements of absolute concentrations of intermediate species in flames, Prog. Energy Combust. Sci., 25, 233-252, 1999.

Crosson, E. R., Haar, P., Marcus, G. A., Schwettman, H. A., Paldus, B. A., Spence, T. G., and Zare, R. N.: Pulse-stacked cavity ring-down spectroscopy, Rev. Sci. Instrum., 70, 4-10, 1999.

Czyzewski, A., Chudzynski, S., Ernst, K., Karasinski, G., Kilianek, L., Pietruczuk, A., Skubiszak, W., Stacewicz, T., Stelmaszczyk, K., Koch, B., and Rairoux, P.: Cavity ring-down spectrography, Opt. Commun., 191, 271-275, 2001.

Dianov-Klokov, V. I.: Absorption spectrum of oxygen at pressues from 2 to 35 atm in the region from 12600 to 3600 Å, Opt. Spectrosc., 16, 224-227, 1964.

Dixneuf, S., Ruth, A. A., Vaughan, S., Varma, R. M., and Orphal, J.: The time dependence of molecular iodine emission from *Laminaria digitata*, Atmos. Chem. Phys., 9, 823-829, 2009.

Engeln, R., and Meijer, G.: A Fourier transform cavity ring down spectrometer, Rev. Sci. Instrum., 67, 2708-2713, 1996.

Engeln, R., Berden, G., Peeters, R., and Meijer, G.: Cavity enhanced absorption and cavity enhanced magnetic rotation spectroscopy, Rev. Sci. Instrum., 69, 3763-3769, 1998.

Fiedler, S. E., Hese, A., and Ruth, A. A.: Incoherent broad-band cavity-enhanced absorption spectroscopy, Chem. Phys. Lett., 371, 284-294, 2003a.

Fiedler, S. E., Hoheisel, G., Ruth, A. A., and Hese, A.: Incoherent broad-band cavity-enhanced absorption spectroscopy of azulene in a supersonic jet, Chem. Phys. Lett., 382, 447-453, 2003b.

Gherman, T., Venables, D. S., Vaughan, S., Orphal, J., and Ruth, A. A.: Incoherent

broadband cavity-enhanced absorption spectroscopy in the near-ultraviolet: Application to HONO and NO_2, Environ. Sci. Technol., 42, 890-895, 2008.

Greenblatt, G. D., Orlando, J. J., Burkholder, J. B., and Ravishankara, A. R.: Absorption Measurements of Oxygen Between 330 and 1140 nm, J. Geophys. Res., 95, 18577-18582, 10.1029/JD095iD11p18577, 1990.

Hall, J. L., Hollberg, L., Baer, T., and Robinson, H. G.: Optical Heterodyne Saturation Spectroscopy, Appl. Phys. Lett., 39, 680-682, 1981.

Hamers, E., Schram, D., and Engeln, R.: Fourier transform phase shift cavity ring down spectroscopy, Chem. Phys. Lett., 365, 237-243, 2002.

Herriott, D. R., and Schulte, H. J.: Folded Optical Delay Lines, Appl. Opt., 4, 883-889, 1965.

Kern, C., Trick, S., Rippel, B., and Platt, U.: Applicability of light-emitting diodes as light sources for active differential optical absorption spectroscopy measurements, Appl. Opt. , 45, 2077-2088, 2006.

Langridge, J. M., Ball, S. M., and Jones, R. L.: A compact broadband cavity enhanced absorption spectrometer for detection of atmospheric NO_2 using light emitting diodes, Analyst, 131, 916-922, 2006.

Langridge, J. M., Ball, S. M., Shillings, A. J. L., and Jones, R. L.: A broadband absorption spectrometer using light emitting diodes for ultrasensitive, in situ trace gas detection, Rev. Sci. Instrum., 79, 14, 10.1063/1.3046282, 2008.

Lehmann, K. K., and Romanini, D.: The superposition principle and cavity ring-down spectroscopy, J. Chem. Phys., 105, 10263-10277, 1996.

Ma, L. S., Ye, J., Dube, P., and Hall, J. L.: Ultrasensitive frequency-modulation spectroscopy enhanced by a high-finesse optical cavity: theory and

application to overtone transitions of C_2H_2 and C_2HD, J. Opt. Soc. Am. B-Opt. Phys., 16, 2255-2268, 1999.

Meinen, J., Thieser, J., Platt, U., and Leisner, T.: Technical Note: Using a high finesse optical resonator to provide a long light path for differential optical absorption spectroscopy: CE-DOAS, Atmos. Chem. Phys., 10, 3901-3914, 2010.

Naus, H., and Ubachs, W.: Experimental verification of Rayleigh scattering cross sections, Opt. Lett., 25, 347-349, 2000.

O'Keefe, A., and Deacon, D. A. G.: Cavity Ring-Down Optical Spectrometer for Absorption-Measurements Using Pulsed Laser Sources, Rev. Sci. Instrum., 59, 2544-2551, 1988.

Orphal, J., and Ruth, A. A.: High-resolution Fourier-transform cavity-enhanced absorption spectroscopy in the near-infrared using an incoherent broad-band light source, Opt. Express, 16, 19232-19243, 2008.

Plane, J. M. C., and Nien, C. F.: Measurements of NO_3 in the Marine Troposphere by Differential Optical-Absorption Spectroscopy, Am. Chem. S, 198, 19, 1989.

Platt, U., and Perner, D.: An Instrument for the Spectroscopic Measurement of Trace Substances in the Atmosphere, Fresen. Z. Anal. Chem., 317, 309-313, 1984.

Platt, U.: Modern methods of the measurement of atmospheric trace gases, Phys. Chem. Chem. Phys., 1, 5409-5415, 1999.

Press, W., Teukolsky, S., Vetterling, W., and Flannery, B.: Numerical Recipes 3rd Edition: The Art of Scientific Computing, Cambridge University Press, Cambridge, 2007.

Ramponi, A. J., Milanovich, F. P., Kan, T., and Deacon, D.: High-Sensitivity

Atmospheric Transmission Measurements Using a Cavity Ringdown Technique, Appl. Opt., 27, 4606-4608, 1988.

Reid, J., Garside, B. K., Shewchun, J., Elsherbiny, M., and Ballik, E. A.: High Sensitivity Point Monitoring of Atmospheric Gases Employing Tunable Diode-Lasers, Appl. Opt., 17, 1806-1810, 1978.

Romanini, D.: High-performance quantitative absorption spectroscopy: Cavity ring down and intracavity laser absorption, Ann. Phys.-Paris, 20, 665-674, 1995.

Romanini, D., Kachanov, A. A., Sadeghi, N., and Stoeckel, F.: CW cavity ring down spectroscopy, Chem. Phys. Lett., 264, 316-322, 1997.

Ruth, A. A., Orphal, J., and Fiedler, S. E.: Fourier-transform cavity-enhanced absorption spectroscopy using an incoherent broadband light source, Appl. Opt., 46, 3611-3616, 2007.

Salow, H., and Steiner, W.: Die durch Wechselwirkungskräfte bedingten Absorptionsspektra des Sauerstoffes, I. Die Absorptionsbanden des (O_2-O_2) Moleküls, Z. Physik, 99, 137-158, 1936.

Scherer, J. J.: Ringdown spectral photography, Chem. Phys. Lett., 292, 143-153, 1998.

Sneep, M., and Ubachs, W.: Direct measurement of the Rayleigh scattering cross section in various gases, J. Quant. Spectrosc. Radiat. Transf., 92, 293-310, 2005.

Thalman, R., and Volkamer, R.: Inherent calibration of a blue LED-CE-DOAS instrument to measure iodine oxide, glyoxal, methyl glyoxal, nitrogen dioxide, water vapour and aerosol extinction in open cavity mode, Atmos. Meas. Tech., 3, 1797-1814, 10.5194/amt-3-1797-2010, 2010.

Varma, R. M., Venables, D. S., Ruth, A. A., Heitmann, U., Schlosser, E., and Dixneuf, S.: Long optical cavities for open-path monitoring of atmospheric trace

gases and aerosol extinction, Appl. Opt., 48, B159-B171, 2009.

Vaughan, S., Gherman, T., Ruth, A. A., and Orphal, J.: Incoherent broad-band cavity-enhanced absorption spectroscopy of the marine boundary layer species I_2, IO and OIO, Phys. Chem. Chem. Phys., 10, 4471-4477, 10.1039/b802618a, 2008.

Venables, D. S., Gherman, T., Orphal, J., Wenger, J. C., and Ruth, A. A.: High sensitivity in situ monitoring of NO_3 in an atmospheric simulation chamber using incoherent broadband cavity-enhanced absorption spectroscopy, Environ. Sci. Technol., 40, 6758-6763, 2006.

Volkamer, R.: Absorption von Sauerstoff im Herzberg I System und Anwendungen auf die Aromatenmessungen am EUropran PHOto REactor (EUPHORE), Diploma thesis, Univ. of Heidelberg, Germany, 1996.

Washenfelder, R. A., Langford, A. O., Fuchs, H., and Brown, S. S.: Measurement of glyoxal using an incoherent broadband cavity enhanced absorption spectrometer, Atmos. Chem. Phys., 8, 7779-7793, 2008.

Weibring, P., Richter, D., Fried, A., Walega, J. G., and Dyroff, C.: Ultra-high-precision mid-IR spectrometer II: system description and spectroscopic performance, Appl. Phys. B-Lasers Opt., 85, 207-218, 10.1007/s00340-006-2300-4, 2006.

Welz, B., Becker-Ross, H., Florek, S., and Heitmann, U.: High-Resolution Continuum Source AAS, Wiley-VCH, Darmstadt, 2006a.

Welz, B., Becker-Ross, H., Florek, S., and Heitmann, U.: Special Features of HR-CS AAS, Wiley-VCH, Darmstadt, 2006b.

Werle, P., Mucke, R., and Slemr, F.: The limits of signal averaging in atmospheric trace-gas monitoring by tunable diode-laser absorption-spectroscopy (TDLAS), Appl. Phys. B-Lasers Opt., 57, 131-139, 1993.

Werle, P.: A review of recent advances in semiconductor laser based gas monitors, Spectroc. Acta. A-Molec. Biomolec. Spectr., 54, 197-236, 1998.

Wheeler, M. D., Newman, S. M., Orr-Ewing, A. J., and Ashfold, M. N. R.: Cavity ring-down spectroscopy, J. Chem. Soc.-Faraday Trans., 94, 337-351, 1998.

White, J. U.: Very Long Optical Paths in Air, J. Opt. Soc. Am., 66, 411-416, 1976.

Wu, T., Zhao, W. X., Li, J. S., Zhang, W. J., Chen, W. D., and Gao, X. M.: Incoherent Broadband Cavity Enhanced Absorption Spectroscopy Based on LED, Spectrosc. Spectr. Anal., 28, 2469-2472, 10.3964/j.issn.1000-0593(2008)11-2469-04, 2008.

Wu, T., Zhao, W., Chen, W., Zhang, W., and Gao, X.: Incoherent broadband cavity enhanced absorption spectroscopy for in situ measurements of NO_2 with a blue light emitting diode, Appl. Phys. B-Lasers Opt., 94, 85-94, 10.1007/s00340-008-3308-8, 2009.

Ye, J., Ma, L. S., and Hall, J. L.: Ultrasensitive detections in atomic and molecular physics: demonstration in molecular overtone spectroscopy, J. Opt. Soc. Am. B-Opt. Phys., 15, 6-15, 1998.

Ye, J., and Hall, J. L.: Cavity ringdown heterodyne spectroscopy: High sensitivity with microwatt light power, Phys. Rev. A, 6106, 2000.

Chapter 3

FLOW CELL SPECTROMETER

3.1 Introduction

Whereas large absorption cross-sections of atmospheric species are generally well established, weak absorption spectra are often poorly known. Accurate absorption cross-sections are important in atmospheric observations, laboratory work, and studies of fundamental molecular properties. The near-ultraviolet (300 nm to 400 nm) absorption spectra of gases are particularly relevant for understanding and modelling the chemistry of the atmosphere, since light in this spectral region drives most tropospheric photochemistry.

Weak absorptions, which occur when molecular absorption cross-sections are small or when the concentration of the species of interest is low, are a challenge to measure. In ozone, for instance, the absolute absorption cross-section drops to about 10^{-23} cm^2 $molecule^{-1}$ between the Chappuis and the Huggins bands (around 370 nm). Despite its prominent role in atmospheric chemistry, even recent O_3 absorption cross-sections differ by almost an order of magnitude in this region.(Brion et al., 1998;Bogumil et al., 2003;Voigt et al., 2001). The low concentrations associated with short-lived species also result in weak absorption. Bromine monoxide, BrO, exemplifies this case: although the absorption cross-section of BrO is large (about 1.5×10^{-17} cm^2 $molecule^{-1}$ at 338.5 nm)(Fleischmann et al., 2004), the tropospheric mixing ratio is typically only a few ppt.(Honninger and Platt, 2002;Peters et al., 2005;Wagner et al., 2007;Mahajan et al., 2009). At a high atmospheric concentration of 10 pptv, the maximum absorption of BrO would be only about 4×10^{-9} cm^{-1}, making it extremely difficult to measure. Even in the laboratory, low concentrations of BrO are inevitable owing to its fast self-reaction.(Fleischmann et al., 2004) Lastly, low gas concentrations are found also for substances with low vapour pressures; as a result,

the ultraviolet spectra of many low volatility organic species of atmospheric interest have yet to be determined. This includes the large group of compounds with carbonyl or nitro functional groups, for which the $n \rightarrow \pi$ transition occurs in the near-ultraviolet.

The aim in this chapter is to demonstrate an IBBCEAS instrument for measuring weak absorption spectra of gases over the wavelength range 335 to 375 nm. We do so by first showing the comparability of SO_2 absorption spectra measured by the instrument with literature spectra. The technique is then applied to obtain moderate resolution spectra of several molecules for which the absorption cross-section is poorly known in this spectral region, namely ozone, the O_4 dimer, and the small ketones acetone, 2-butanone, and 2-pentanone. Moreover, as weak absorption spectra are often used to quantify sample constituents, we also demonstrate the measurement of a radical, BrO, from a background of Br_2 and O_3.

3.2 Experimental

3.2.1 The flow cell IBBCEAS system

The IBBCEAS system is shown schematically in Fig. 3.1. Light from a 75 W arc Xe lamp was focused into the centre of a 198 cm long optical cavity formed by two high reflectivity dielectric mirrors (Layertec). The mirrors had a maximum reflectivity of ca. 99.8% at 365 nm and a 5 m radius of curvature. Focusing the beam into the cavity centre improved the cavity quality and minimised dispersion losses. (Fiedler et al., 2007;Wu et al., 2008) Light exiting the cavity was focussed into a Czerny-Turner spectrograph (Andor SR-163) with a 163 cm focal length and a 1200 l/mm, 300 nm blaze grating. The spectrum was recorded using a back-illuminated

CCD (Andor 420A-BU) optimized for the near-UV and cooled to -40℃ to reduce the dark current. The wavelength scale of the spectrograph was calibrated by fitting several emission lines of a Hg/Ne lamp to a second-order polynomial function. The uncertainty of the wavelength calibration was about 0.02 nm and the resolution of the instrument was 0.31 nm (25μm silt width) and 0.55 nm (100 μm slit width) as determined from emission lines at 334 nm and 365 nm. The lamp output was highly stable: the short term intensity fluctuation of 1 s duration scans was below 0.1% and dimming of around 0.4% was observed over a 2 hour period.

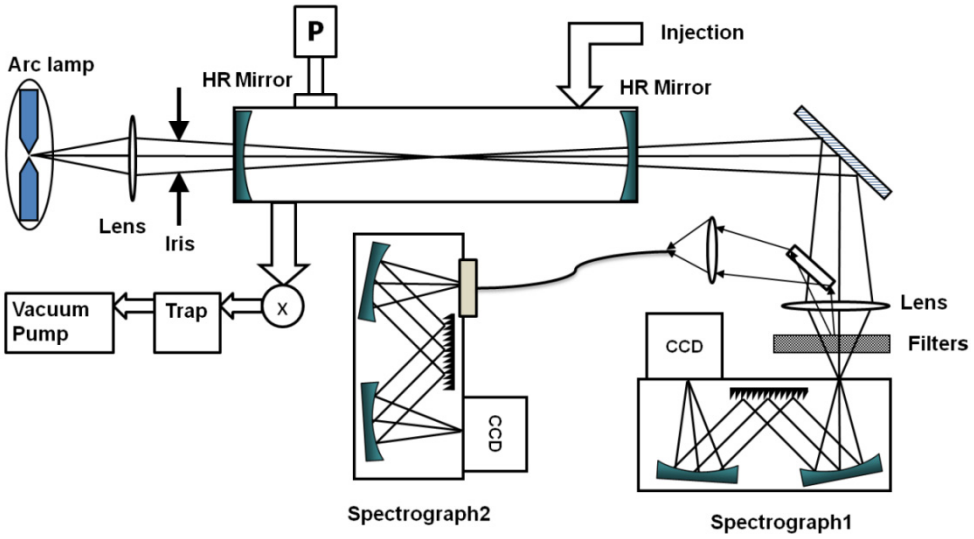


Figure 3.1 Schematic diagram of the IBBCEAS instrument. Spectrograph 1 recorded the IBBCEAS spectra, while spectrograph 2 recorded single-pass spectra outside of the cavity mirror reflectivity range.

One of the practical challenges with IBBCEAS systems employing Xe arc lamps is to filter the extremely broadband light (200 nm to 2000 nm) to the high reflectivity region of the cavity mirrors. The cavity mirrors act as a band rejection filter but

longer and shorter wavelengths are efficiently transmitted into the spectrograph, thereby adding to the background signal. A Schott UG11 band pass filter (270 to 380 nm) removed most visible and near-IR light in our system, while a heat-absorbing filter (Schott KG1) rejected wavelengths above 900 nm. A final band-pass filter (Semrock FF01-357/44-25) placed in front of the spectrograph provided a final, close match of the filter transmission to the high reflectivity range of the cavity mirrors and a usable spectral region from 335 nm to 375 nm.

The concentration of absorber must be known to calculate the absorption cross-section. Although any analytical method could be used to quantify the concentrations of O_3 and the ketones, here we exploit the single-pass absorption at 320.1 nm to determine the concentration of the absorber. At this wavelength, which falls outside of the high reflectivity region of the optical cavity mirrors, most light traverses the sample once (a pathlength of 2 m); in contrast, the spectrometer is dramatically more sensitive at the reflectivity maximum and the effective pathlength of light though the sample is given by $d/(1 - R)$, where d is the mirror separation and R is the mirror reflectivity. In the system employed here, the effective pathlength in the IBBCEAS region (335 to 375 nm) is about 0.5 km for weak absorptions and therefore about two orders of magnitude more sensitive than the 320 nm (single-pass) measurement. These species have moderate absorption cross-sections (10^{-20} cm^2 $molecule^{-1}$) at 320 nm and literature spectra agree closely (Meyrahn et al., 1986;Hynes et al., 1992;Martinez et al., 1992;Brion et al., 1998;Gierczak et al., 1998;Burrows et al., 1999;Mu and Mellouki, 2000;Wollenhaupt et al., 2000;Voigt et al., 2001;Bogumil et al., 2003). The absorption was determined by measuring a small portion of the light reflected by the Semrock filter, transmitted through an Andover 320 nm band-pass filter, and recorded in another spectrograph (Andor SR-303). As

the cavity mirrors have a reflectivity of 42% at 320 nm, about 20% of the light makes two or more passes through the sample. To account for multiple passes, the absorption coefficient was therefore determined from the general cavity equation, Eq. (4), in (Fiedler et al., 2003).

3.2.2 Mirror calibration

The extinction (or absorption) spectrum of a sample in the cavity is given by:(Fiedler et al., 2003)

$$\varepsilon(\lambda) = \sum_i \sigma_i(\lambda) \cdot N_i = \frac{1}{d}\left(\frac{I_0(\lambda)}{I(\lambda)} - 1\right)\left(1 - R(\lambda)\right) \qquad (3.1)$$

where I and I_0 are respectively the intensities transmitted through the optical cavity in the presence and absence of an absorber, d is the distance between the cavity mirrors, R is the mirror reflectivity, and σ_i (cm^2 $molecule^{-1}$) and N_i (molecules cm^{-3}) are the absolute absorption cross section and number density of species i. Equation (3.1) implies that the lamp intensity must be stable between the measurement of I_0 and I, and that the mirror reflectivity is known. The reflectivity spectrum of the mirrors was calibrated in two steps. In the first step, the shape of the reflectivity spectrum was determined based on the difference in Rayleigh scattering of N_2 and CO_2. The cavity was successively flushed with CO_2 and N_2 at about 1 L min^{-1} for an hour each until the transmitted intensity attained a stable value. The sample was kept at 1013 mbar and 293 K. The observed extinction, ε_i, arising from Rayleigh scattering of gas i is related to the mirror reflectivity according to:

$$\alpha_i(\lambda) = N_i \sigma_i^{Rayl}(\lambda) = \left(\frac{I_0(\lambda)}{I_i(\lambda)} - 1 \right) \frac{\left(1 - R(\lambda)\right)}{d} \qquad (3.2)$$

In Eq. (3.2), I_0 represents the (unmeasured) intensity of a non-scattering medium (that is, equivalent to the evacuated cavity) and σ^{Rayl} is the Rayleigh scattering cross-section of species *i*. Rayleigh scattering cross-sections were based on those of Naus, et al. (2000), Sneep, et al. (2005) and Sutton, et al. (2004). The mirror reflectivity is thus related to the measured intensity through both CO_2 and N_2 by:

$$\frac{\left(1 - R(\lambda)\right)}{d} = \frac{I_{N_2}(\lambda) N_{N_2} \sigma_{N_2}^{rayl}(\lambda) - I_{CO_2}(\lambda) N_{CO_2} \sigma_{CO_2}^{rayl}(\lambda)}{I_{CO_2}(\lambda) - I_{N_2}(\lambda)} \qquad (3.3)$$

Although Rayleigh scattering gives a smooth mirror reflectivity spectrum (Fig 3.2(b)), the relatively small extinction can be susceptible to drifts in lamp intensity, thereby introducing a systematic error. The second step of the mirror calibration therefore scaled the reflectivity to match the absorption of O_3 in the cavity to the literature absorption cross-section at 353 nm. The cross-section used was the average of four literature cross-sections convoluted to our instrumental function (Brion, Chakir et al. 1998; Burrows, Richter et al. 1999; Voigt, Orphal et al. 2001; Bogumil, Orphal et al. 2003). Figure 3.2(a) shows the linear dependence of the fractional absorption with O_3 concentration, where the slope equals $\sigma_{O3}d/(1 - R)$, as indicated by Eq. (1). The scaled mirror reflectivity is rather flat over this spectral range (Fig. 3.2(b)). The accuracy of the mirror calibration at 353 nm is limited by the 7% standard deviation of the cross-sections at 353 nm, as well as the uncertainty in the individual cross-sections and the regression slope. The uncertainty in the reflectivity at other wavelengths is expected to be somewhat higher further away from 353 nm but cannot be explicitly quantified. Nevertheless, spectra generally agree closely with literature spectra, with some suggestion of a small overestimation

of the mirror reflectivity below 340 nm in the ketone spectra.

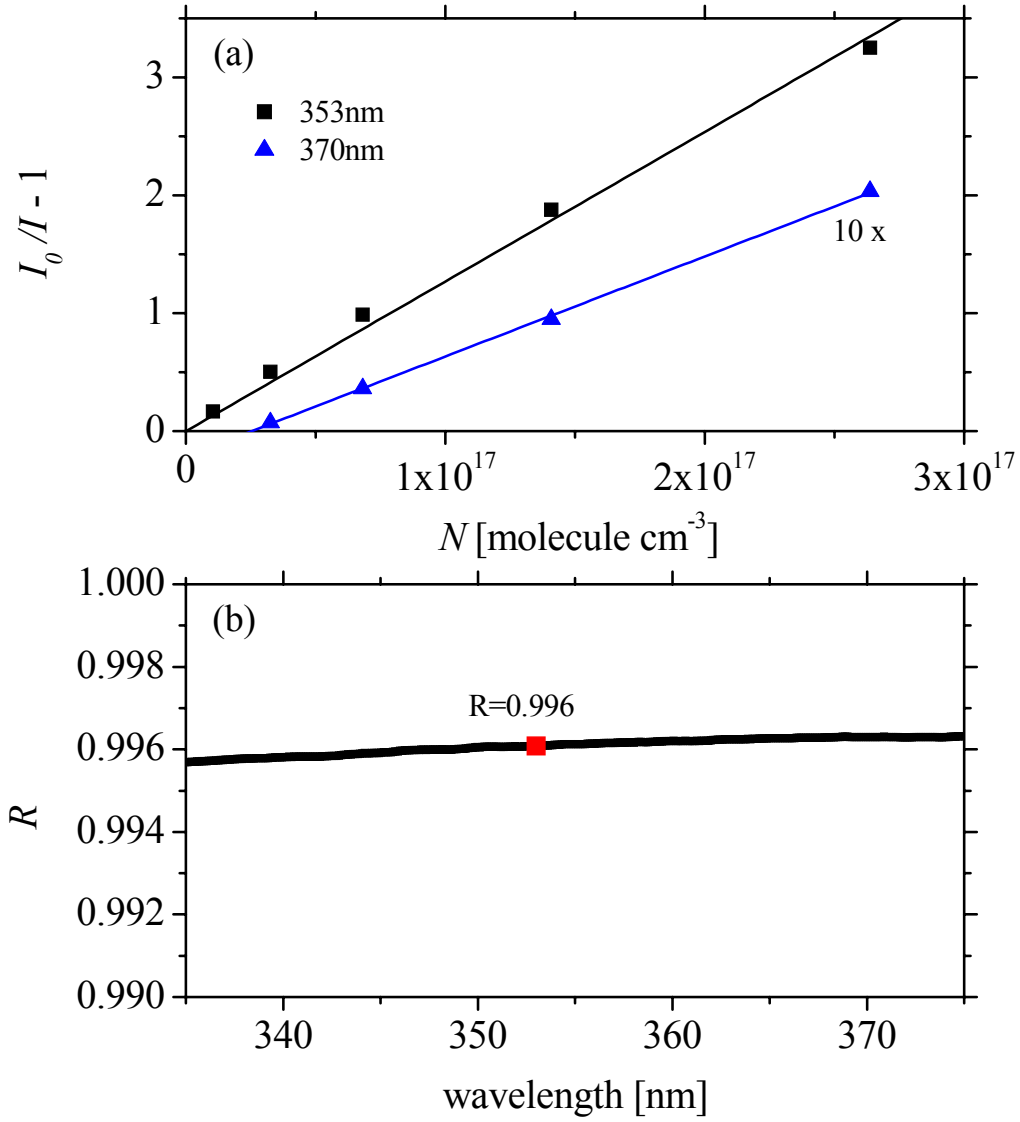


Figure 3.2 (a) Fractional absorption of O_3 at 353nm and 370 nm. The slope of the graph, $\sigma_{O3}d/(1-R)$, was used to determine R based on the literature absorption cross-section at 353 nm. (b) Mirror reflectivity scaled to give the literature cross-section of O_3 absorption at 353 nm.

3.2.3 Uncertainty of cross-sections

The uncertainty of the absorption cross-sections was estimated using standard uncertainty propagation. The uncertainty in the extinction coefficient, $\Delta\varepsilon$, was common to all spectra and was evaluated from Eq. (3.1):

$$\Delta\varepsilon^2 = \left|\frac{\partial\varepsilon}{\partial d}\right|^2 \Delta d^2 + \left|\frac{\partial\varepsilon}{\partial(1-R)}\right|^2 \Delta(1-R)^2 + \left|\frac{\partial\varepsilon}{\partial I_F}\right|^2 \Delta I_F{}^2 \qquad (3.4)$$

where Δd, $\Delta(1–R)$, and ΔI_F are the uncertainties in the mirror separation, the mirror reflectivity term, and the fractional change in intensity ($I_F \equiv I_0/I$ -1). A more intuitive expression of the uncertainty, in which the uncertainties are expressed in relative terms, can be derived from Eq. (3.4):

$$\left(\frac{\Delta\varepsilon}{\varepsilon}\right)^2 = \left(\frac{\Delta d}{d}\right)^2 + \left(\frac{\Delta(1-R)}{1-R}\right)^2 + \left(\frac{\Delta I_F}{I_F}\right)^2 \qquad (3.5)$$

The relative uncertainties (see above) are 7% for $(1 – R)$ at 353 nm, about 0.5% for d, and about 0.4% for I_F (depending on the duration of the experiment). The overall uncertainty in the extinction measurement at 353 nm is therefore around 7% and is clearly dominated by the uncertainty in the mirror reflectivity. The uncertainty in the absorption cross-sections must furthermore account for the uncertainty in the concentration of each species (ΔN):

$$\left(\frac{\Delta\sigma}{\sigma}\right)^2 = \left(\frac{\Delta\varepsilon}{\varepsilon}\right)^2 + \left(\frac{\Delta N}{N}\right)^2 \qquad (3.6)$$

We have estimated ΔN from the standard deviation of the literature cross-sections at 320 nm, together with a 1.1% uncertainty in the single-pass absorption measurement. The uncertainties of the concentrations are 3% for O_3, 4% for acetone, 3% for 2-butanone and 3% for 2-pentanone. The overall uncertainties in absorption

cross-sections are thus 8% (O_3), 8% (acetone), 10% (2-butanone) and 8% (2-pentanone).

We emphasise that this uncertainty applies to the absorption cross-section at 353 nm and is necessarily a lower limit. The uncertainty is larger at other wavelengths, and particularly at the long and short wavelength limits of the IBBCEAS spectrum. Some of the spectra following suggest that our absorption cross-sections are underestimated towards the short wavelength limit. The uncertainty will therefore be revisited in the section 3.5 to place a more conservative estimate on the overall uncertainty on the absorption cross-section.

3.3 Near UV absorption spectra

3.3.1 Sulfur dioxide

SO_2 (BOC 99.9%) has a relatively weak absorption band from 345 to 420 nm arising from the spin-forbidden $a^3B_1–X^1A_1$ transition. Since recent spectra agree closely,(Vandaele et al., 2009;Bogumil et al., 2003) and because SO_2 is stable and easily handled, the absorption of SO_2 in this region served as a convenient test of the spectrometer performance.

SO_2 was introduced into the spectrometer from a 500 μL gas-tight syringe into a stream of N_2 (0.5 L min^{-1}) at ambient temperature (296 K) and pressure (1013 mbar). The SO_2 flowed through the optical cavity as a short plug of gas with a relatively constant total column density. The sample absorption rose to a maximum for a short period before subsiding as the SO_2 was flushed from the chamber. Diffusion of gas into the dead volumes near the cavities mirrors resulted in a relatively long residence time of about 6 min. Measurements were based on the maximum absorption in the

cell. The integrated absorption from 350 to 375 nm increased linearly with volume of SO_2 (Fig. 3.3(a)). The small, negative intercept may have arisen from residual SO_2 in the chamber from one injection to another. Repeatability was good, with a standard deviation of 5% at the absorption peak at 370.2 nm found for five successive injections of 500 µL SO_2 (Fig. 3.3(b)).

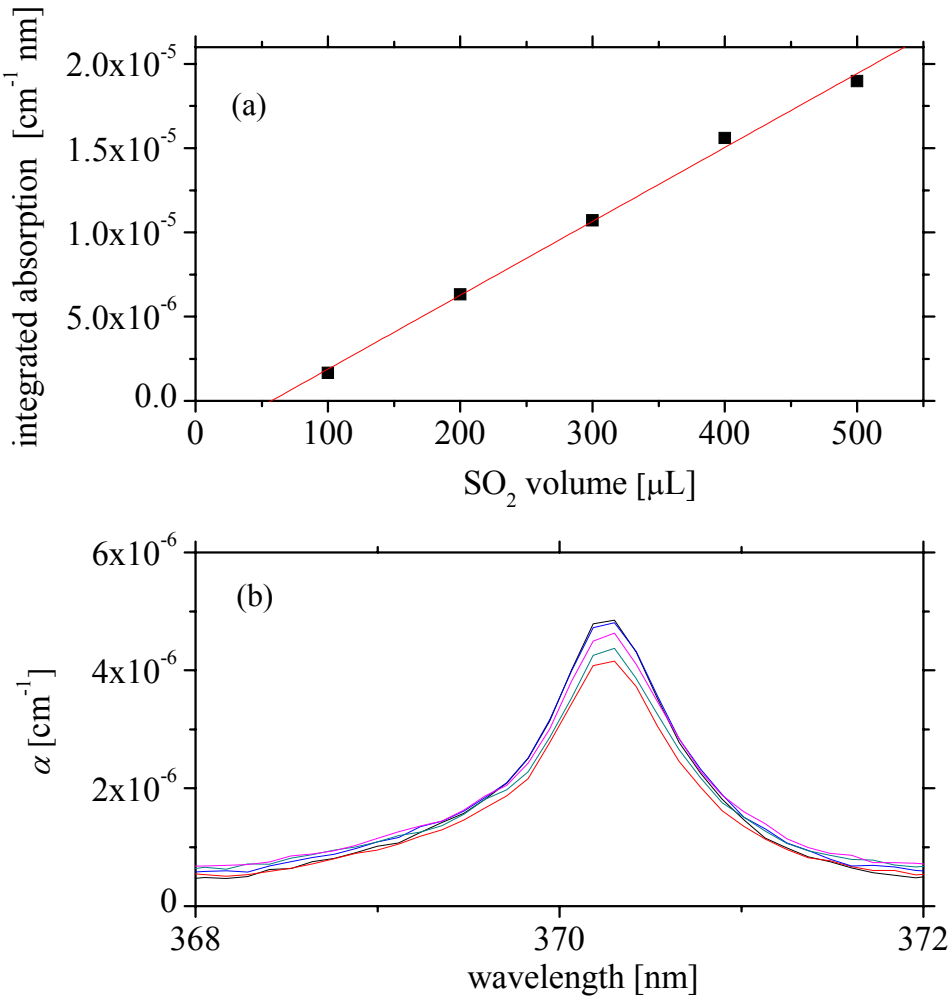


Figure 3.3 (a) Dependence of the SO_2 integrated absorption on the volume of SO_2 introduced into the inlet stream. The correlation coefficient of the linear regression is R^2 = 0.9961. (b) Repeatability of five successive injections of 500 μL SO_2 into the inlet stream. The standard deviation is 5% at the absorption peak at 370.2 nm.

The average absorption cross-section of SO_2 from the five samples is shown in Fig. 3.4. The number density was calculated from the volume of the SO_2 injected and the volume of the sample cell. Figure 3.4 also displays the spectra of Bogumil et al. (2003) and Vandaele et al. (2009) at resolutions of 0.26 nm and 0.032 nm, respectively, as well as magnitudes of the absorption maxima convoluted to our instrument resolution. The magnitudes of the five largest absorption features above 350 nm were 28% larger than the average literature cross-sections, although around half of the difference (8.2×10^{-23} cm^2 average) can be explained by the generally higher baseline (4.2×10^{-23} cm^2 higher on average). Nevertheless, the agreement between the spectrum reported here and the literature spectra is generally good over this region, which includes changes in absorption coefficient of about an order of magnitude. Together with the absorption linearity and repeatability, these data thus provide evidence of the reliability of the spectra reported here.

A comparison of the experimental parameters illustrates the sensitivity of our instrument (Table 3.1). The overall concentration of SO_2 is about 0.039% in our spectrometer compared to pure SO_2 and 1% SO_2 in N_2 of Vandaele and Bogumil respectively. Furthermore, the total measurement of 360 s for the averaged spectra (including the measurement of I_0) was similar to that of the Bogumil spectra (320 s), but much shorter than the acquisition time of ca. 1 hour that Vandaele and co-workers used for several pressure measurements. On the other hand, the lower resolution of our instrument would tend to improve the signal-to-noise of the measurement over the much higher resolution of the Vandaele and Bogumil spectra. Despite these differences, the noise apparent in the absorption minima is comparable to or smaller than that in the literature spectra.

Table 3.1 Instrumental parameters of literature absorption cross sections

Author (Year)	Temp. [K]	Wavelength range [nm]	Resolution [nm]
This work	295	335-375	0.55
	Sulfur dioxide		
Bogumil et al. (2003)	293	239-395	0.26
Vandaele et al. (2009)	298	227-420	0.03
	Ozone		
Bogumil et al. (2003)	293	230-1075	0.26
Voigt et al. (2001)	293	230-851	0.027
Burrows et al. (1999)	293	230-794	0.2-0.4
Brion et al. (1998)	295	350-830	0.01
	Acetone		
Yujing et al. (2000)	298	240-350	0.04
Wollenhaupt et al. (2000)	296	220-346	0.16
Gierczak et al. (1998)	298	215-349	0.5
Martinez et al. (1992)	300	202-355	0.5
Hynes et al. (1992)	298	253.7-360	2
Meyrahn et al. (1986)	298	275-368	1.8
	2-Butanone		
Yujing et al. (2000)	298	240-350	0.04
Martinez et al. (1992)	300	202-355	0.5
	2-Pentanone		
Horowitz et al. (1999)	298	210-360	0.07
Martinez et al. (1992)	300	202-354	0.5

This absorption band of SO_2 has some practical potential. The structured absorption features in this region have recently been used in DOAS measurements of SO_2 column densities (Bobrowski et al., 2010). For a broadband optical cavity spectrometer, injection of small volumes of SO_2 would also be a convenient approach to calibrate mirror reflectivities since the small absorption cross-section results in moderate, easily measurable absorptions. Strongly absorbing gases such as NO_2 must be highly diluted to low levels or no light will be transmitted through the optical cavity. In addition this absorption band of SO_2 may be useful in satellite retrieval (Bogumil et al., 2003).

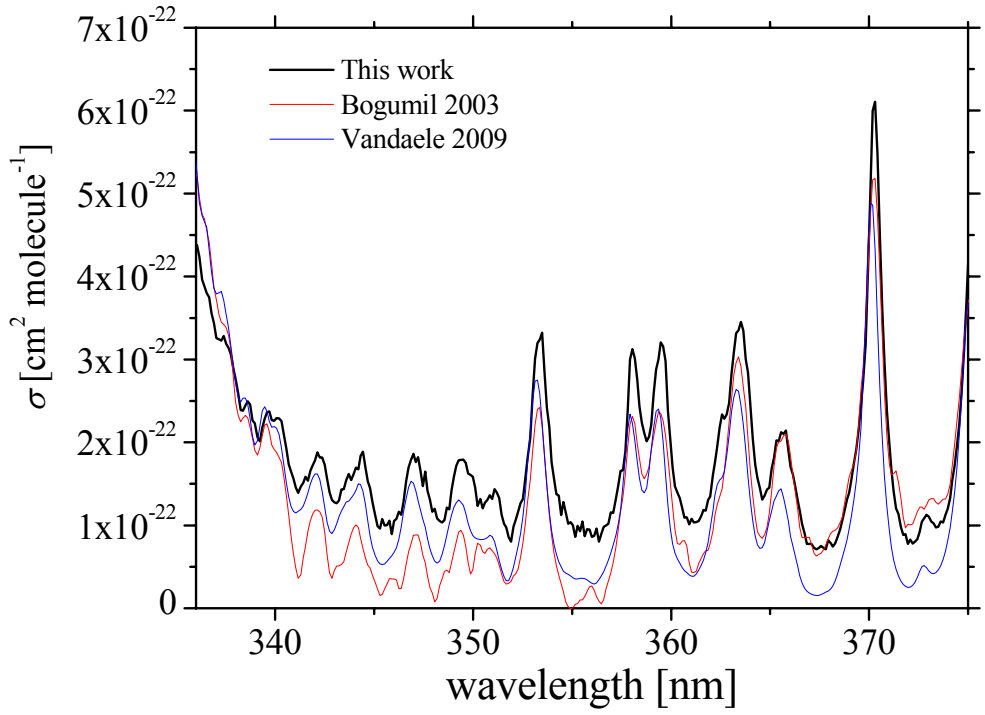


Figure 3.4 SO_2 absorption cross-sections spectra from this work (black), Vandaele (red) and Bogumil (blue). The lines are spectra of the respective literature convoluted to our spectrograph resolution.

3.3.2 Ozone

In contrast to the SO_2 absorption cross-sections, relatively poor agreement exists between reported cross-sections of O_3 in the minimum between the Huggins and Chappuis bands.(Bogumil et al., 2003;Burrows et al., 1999;Voigt et al., 2001;Brion et al., 1998) Although various workers report similar absorption features, the absorption cross-sections differ enormously around 370 nm (Fig. 3.5). Agreement above 360 nm is poor owing to the very weak absorption and the relatively modest concentrations of O_3 in samples. With the long effective pathlength of our instrument, we report an improved estimate of ozone absorption cross-section in this region.

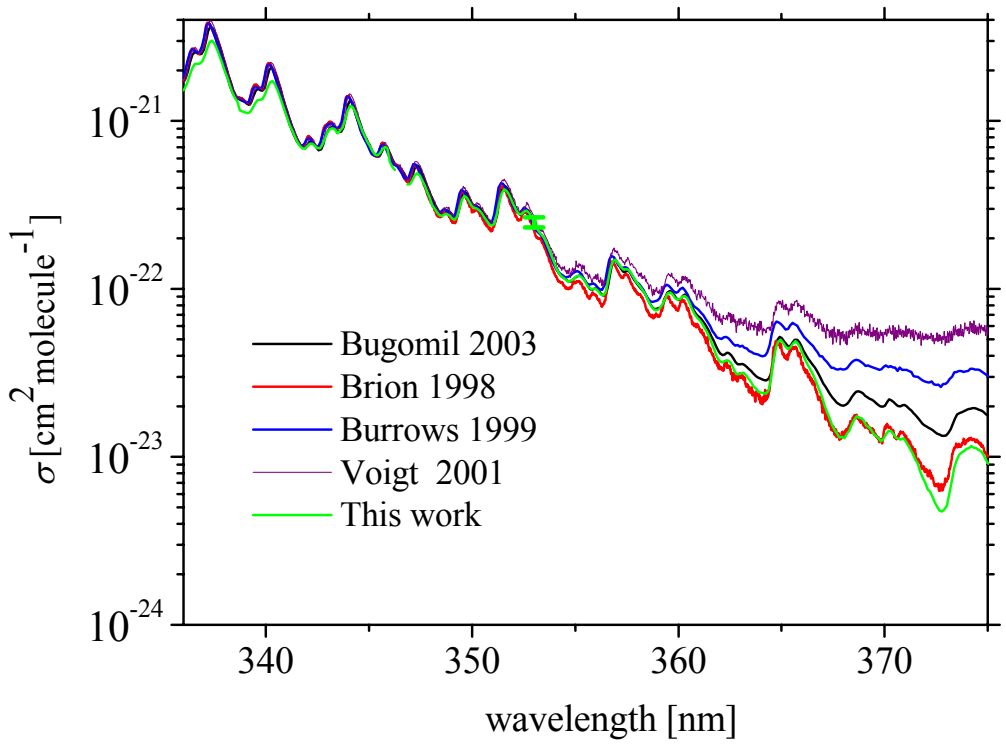


Figure 3.5 O_3 absorption cross-sections from this work, Voigt et al. (2001), Burrows et al. (1999), Bogumil et al. (2003), and Brion et al. (1998).

Intensity spectra of around 1% O_3 in O_2 were recorded with a 5 minute averaging time and at a resolution of 0.26 nm. The ozone concentration in the cavity was quantified from the absorption at 320 nm. The absorption cross-section and literature spectra are shown in Fig. 3.5. Of the literature spectra, Brion et al. (1998) and Voigt et al. (2001) employed FTS, while the data from Burrows and co-workers (1999) and from Bogumil et. al. (2003) employed monochromators developed for satellite monitoring. The IBBCEAS spectrum was corrected for the weak collision-induced absorption of the O_4 dimer at 360 nm (see below). (Note that the magnitude of the absorption cross-section at 353 nm is fixed to the average literature cross-section by the calibration of the mirror reflectivity.) Below 340 nm, the cross-sections are 10 to 20% smaller than the literature values, probably because the mirror reflectivity is overestimated at short wavelengths. At longer wavelengths, the spectra diverge, with the IBBCEAS spectrum agreeing closely with the Brion spectrum. Remarkably little noise is apparent in the IBBCEAS spectrum, and linear absorption behaviour with concentration is apparent even at 370 nm where the absorption is weak (Fig. 3.2(a)). Hence the spectrum reported here provides good evidence that the O_3 absorption in this region is even weaker than most previous reports suggest.

The collision-induced absorption of the O_4 dimer ($^1\Sigma_g^+ + {}^1\Sigma_g^+$ (v=1) $\leftarrow {}^3\Sigma_g^- + {}^3\Sigma_g^+$) contributes marginally to the O_3 absorption spectrum at 360.5 nm. The cross-section of the dimer was determined by comparing the sample extinction of pure O_2 versus that of N_2. Differences between the Rayleigh scattering cross-sections of N_2 and O_2 are small and contribute only a small baseline offset to the extinction. The observed absorption feature was fitted to a Gaussian line shape on a sloping baseline (Fig. 3.6). The magnitude of the Gaussian maximum was 4.0×10^{-46} cm^5 molecule^{-2} at 360.1 nm with a FWHM of 4.3 nm, in satisfactory

agreement with the careful measurements of Greenblatt and co-workers (4.10×10^{-46} cm^5 molecule^{-2} at 360.5 nm with a FWHM of 4.0 nm) and other work (Greenblatt et al., 1990;Volkamer, 1996;Salow and Steiner, 1936;Dianov-Klokov, 1964). Nevertheless, our signal-to-noise ratio is small despite the relatively long effective pathlength of our system ($L_{eff} = d/(1 - R) \approx 500$ m) in pure O_2: the spectrum of Greenblatt taken at 55 atm O_2 is to be preferred to our results. More precise estimates of the absorption cross-section would be feasible with higher mirror reflectivities or at higher O_2 pressures.

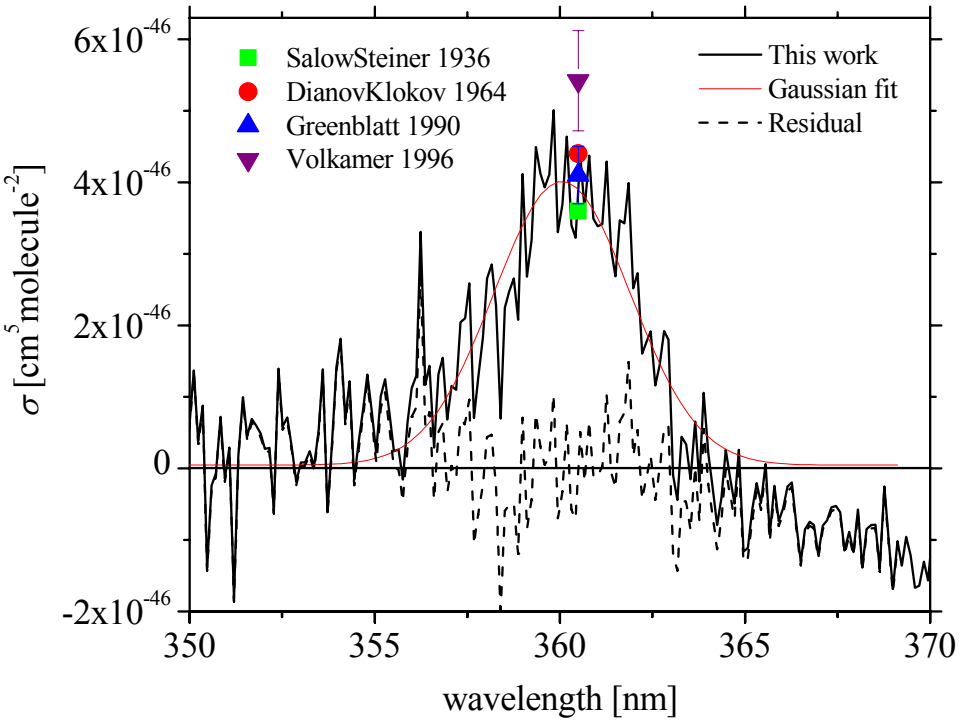


Figure 3.6 Experimental spectrum (black) and Gaussian fit (red) of the collision-induced absorption of the O_4 dimer. Literature maxima shown are those of Salow and Steiner (green square), Greenblatt (blue triangle), Dianov-Klokov (red circle), and Volkamer (purple triangle). Our measured spectrum was shifted downwards by the Gaussian offset of 1.1×10^{-46} cm^5 molecule^{-2} to facilitate comparison with the literature maxima.

3.3.3 Ketone spectra

Spectra of acetone (Aldrich 99.9%), 2-pentanone (Aldrich 99%), and 2-butanone (Aldrich 99%) were measured from 335 to 355 nm. The ketones were introduced via a N_2 stream (0.5 L min^{-1}) into the cavity and quantified from the literature absorption cross-sections at 320 nm. The acetone cross-sections used were those of Gierczak et al. and the 2-pentanone and 2-butanone cross-sections were taken from Martinez and co-workers.(Gierczak et al., 1998;Martinez et al., 1992) The acetone concentration was further diluted to check the linearity of the absorption measurement. The absorption of acetone increased linearly with concentration at 340 nm and 350 nm, where the absorption differs by over an order of magnitude (Fig. 3.7(a)). For acetone, the absorption cross-section was derived from the slope of the linear regression of the three concentrations; Fig. 3.7(b) shows the resulting spectrum. The lamp stability would increasingly influence the measurement of progressively weaker absorption at longer wavelengths.

The resulting absorption cross-section of acetone compares favourably with the available literature spectra. Most literature spectra are evidently close to their detection limits for such weak absorptions and agreement is poor even at the shortest wavelengths (largest absorption) in Fig. 3.7(b). Of the spectra, those of Mu and Mellouki, Wollenhaupt, Martinez, and Gierczak exhibit the lowest discernable measurement noise.(Mu and Mellouki, 2000;Wollenhaupt et al., 2000;Martinez et al., 1992;Gierczak et al., 1998) Our spectrum is reasonable agreement with these spectra. At wavelengths shorter than 340 nm our measured absorption increases less strongly than other spectra, possibly indicating an overestimation of the mirror reflectivity at the short wavelength limit of the spectrometer. On the other hand, the

linear dependence of the absorption with concentration at 340 nm, and particularly at 350 nm, provides strong evidence for the reliability of these cross-sections at these and similar wavelengths. Small undulations are visible in the IBBCEAS absorption spectra and probably correspond to vibronic transitions. Such absorption structures have been known for a long time (Noyes et al., 1956).

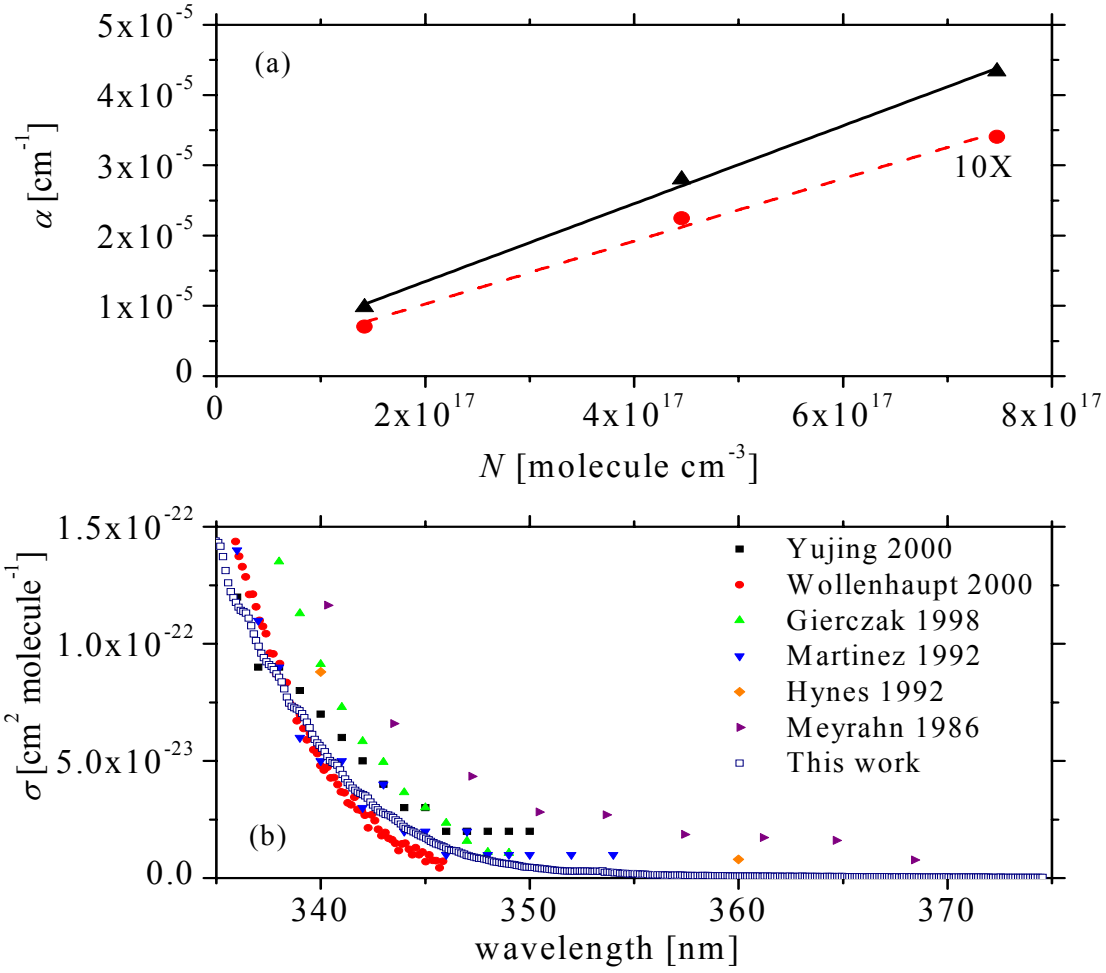


Figure 3.7 (a) Dependence of absorption coefficient on the acetone concentration at 340 nm (black triangles) and at 350 nm (red circles). Correlation coefficients are 0.996 and 0.987, respectively. (b) Acetone absorption cross-section of this work and of several literature spectra.

Spectra of 2-butanone and 2-pentanone are shown in Fig. 3.8. These spectra were determined from the absorption at a single concentration (2.07×10^{17} molecule cm^{-3} for 2-butanone and 1.05×10^{17} molecule cm^{-3} for 2-pentanone). Cross-sections from this work agree with earlier spectra at the shortest wavelengths; again, lower noise is evident, especially at longer wavelengths. The spectrum of 2-butanone clearly agrees closely with that of Martinez and co-workers to 355 nm. For 2-pentanone, the IBBCEAS spectrum is higher than either the spectrum of Martinez or that of Horowitz. In the case of Horowitz's data, the negative values probably signify some measurement artefact.(Horowitz, 1999) In like manner, the IBBCEAS spectrum does not fall to zero at longer wavelengths (as would be expected); this result is ascribed to a small decrease in the lamp output over the duration of the measurement, thereby giving rise to an apparent absorption.

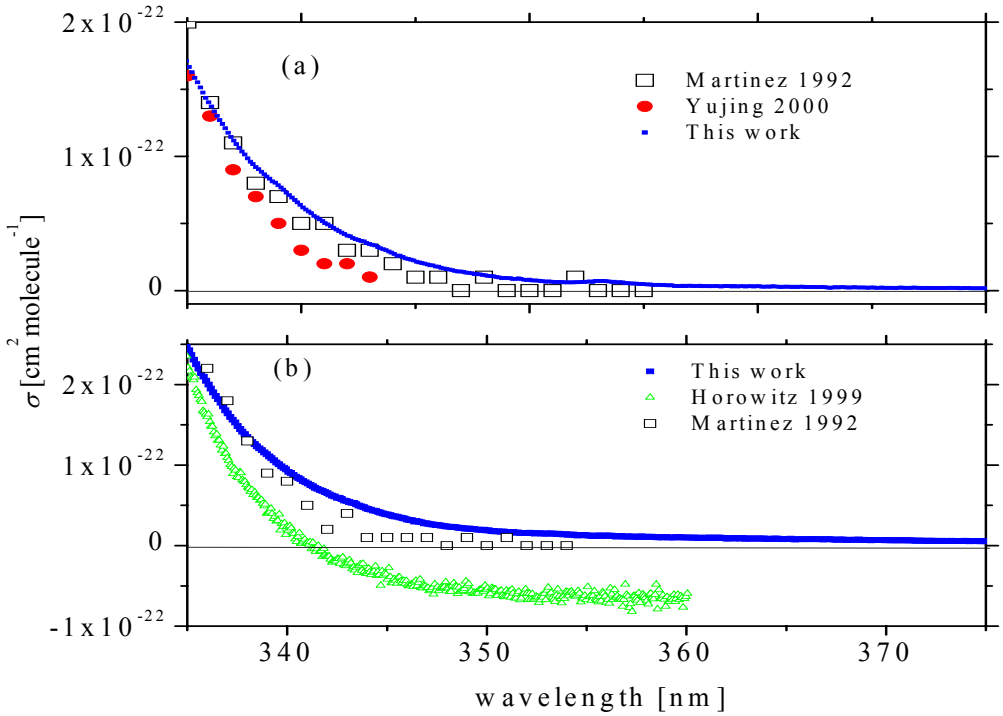


Figure 3.8 Absorption cross-sections of (a) 2-butanone and (b) 2-pentanone.

3.4 The spectrum of bromine monoxide

3.4.1 Generation of bromine monoxide

The sample cell and optical cavity were enclosed in a vacuum tight system with the middle of the cell enclosed by a 100 cm glass tube. The outlet was connected to a foreline trap and rotary vane pump. The system pressure was monitored with a Leybold CTR 90 capacitance manometer and samples were studied at atmospheric pressure (ca. 1013 mbar) and under moderate vacuum. Bromine (Aldrich reagent grade) was used as received. Samples were introduced into the chamber at well-defined flow rates via MKS mass flow controllers (Fig.3.9). Br_2 was introduced into a stream of N_2 via a trap assembly. To reduce the Br_2 concentration to below 10^{-13} cm^{-3}, the trap was cooled to around -30°C in an alcohol/liquid nitrogen cooling bath and the Br_2/N_2 stream diluted further in a higher flow-rate N_2 stream. Ozone was produced in a flow of oxygen by an ozone generator (OzoneLab OL80W).

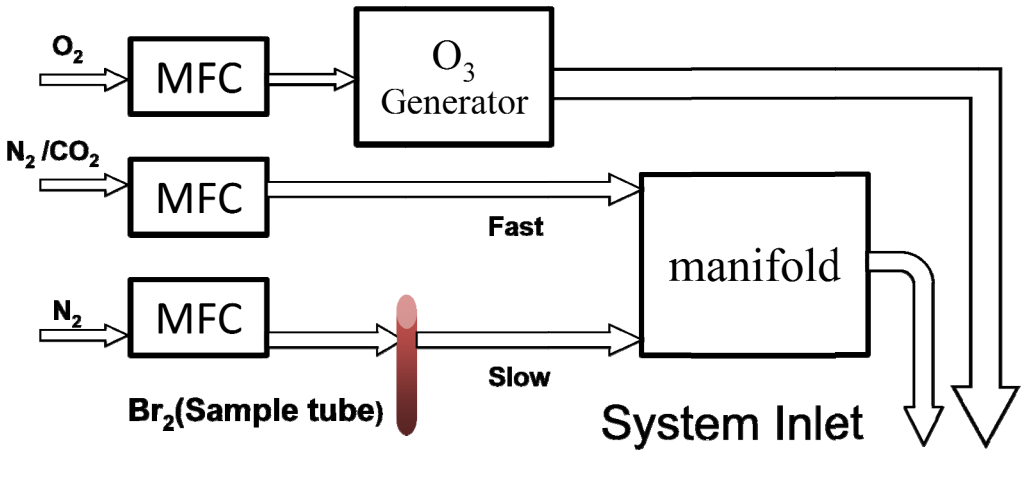


Figure 3.9 Gas sample handling line

With a broad spectral window, the concentrations of several species can be determined concurrently. We illustrate this application of the instrument by quantifying the composition of a sample comprising Br_2, O_3, and the short-lived species BrO. BrO was produced inside the cavity at reduced pressures (3 to 18 mbar) by photolysing Br_2 in the presence of O_3:

$$Br_2 + h\nu \rightarrow Br + Br \quad (3.7)$$

$$O_3 + Br \rightarrow BrO + O_2 \quad (3.8)$$

Molecular bromine, Br_2, has a broad absorption band from 200 to 510 nm with a maximum at 420 nm and unity photolysis quantum efficiency (Atkinson, 2007). With filters placed behind the cavity, Br_2 is readily photolysed by residual light in the cavity. Under these conditions BrO formation is prompt. Nevertheless, rapid self-reaction suppresses the BrO concentration in the cavity:

$$BrO + BrO \rightarrow Br_2 + O_2 \quad (3.9)$$

$$BrO + BrO \rightarrow 2Br + O_2 \quad (3.10)$$

BrO is readily identified by the $A^2\Pi_{3/2} \leftarrow X^2\Pi_{3/2}$ transition, with the (7, 0), (6, 0), (5, 0) and (4, 0) vibrational bands falling within the spectral range of our spectrometer (Fig. 3.10(b)). The large absorption cross-section of this transition permits sensitive retrieval of even very low concentrations of BrO.

3.4.2 Spectral analysis and quantification of BrO, Br_2, and O_3

The number densities of O_3, Br_2, and BrO were retrieved by least squares fitting their literature cross-sections to the measured absorption coefficient and including a linear offset:

$$\alpha(\lambda) = N_{BrO}\,\sigma_{BrO}(\lambda) + N_{O_3}\sigma_{O_3}(\lambda) + N_{Br_2}\sigma_{Br_2}(\lambda) + a + b(\lambda) \quad (3.11)$$

Literature cross-sections were those of Fleischmann et al. (2004) for BrO, the IUPAC recommendation for Br_2 (Atkinson, 2007) and Voigt et al. (2001) for O_3 and were convoluted with our instrument function. As the composition of the sample is probably non-uniform in the sample cell, the fitted number densities represent pathlength-integrated concentrations or column densities. A typical absorption spectrum of the sample and fit of the literature spectra over the range 336 nm to 358 nm is shown in Fig. 3.10. The absorption features of BrO and O_3 are readily evident against the monotonically increasing absorption of Br_2 with wavelength. The fitted curve closely matches the experimental absorption and the residual is small (RMS of 1.8×10^{-8} cm^{-1}). The fitted concentration values were little affected by extending the fitting window to 370 nm (a maximum change of 8% was found for N_{Br2}). Excluding parameters *a* and *b* influenced the fit result more, with the value of N_{Br2} decreasing by 31%. In this case, *a* and *b* most likely compensate for a nominal offset in the absorption arising from a slow decline in the lamp intensity. A comparison of fitting results using different fitting window and baseline parameters is presented in Table 3.2.

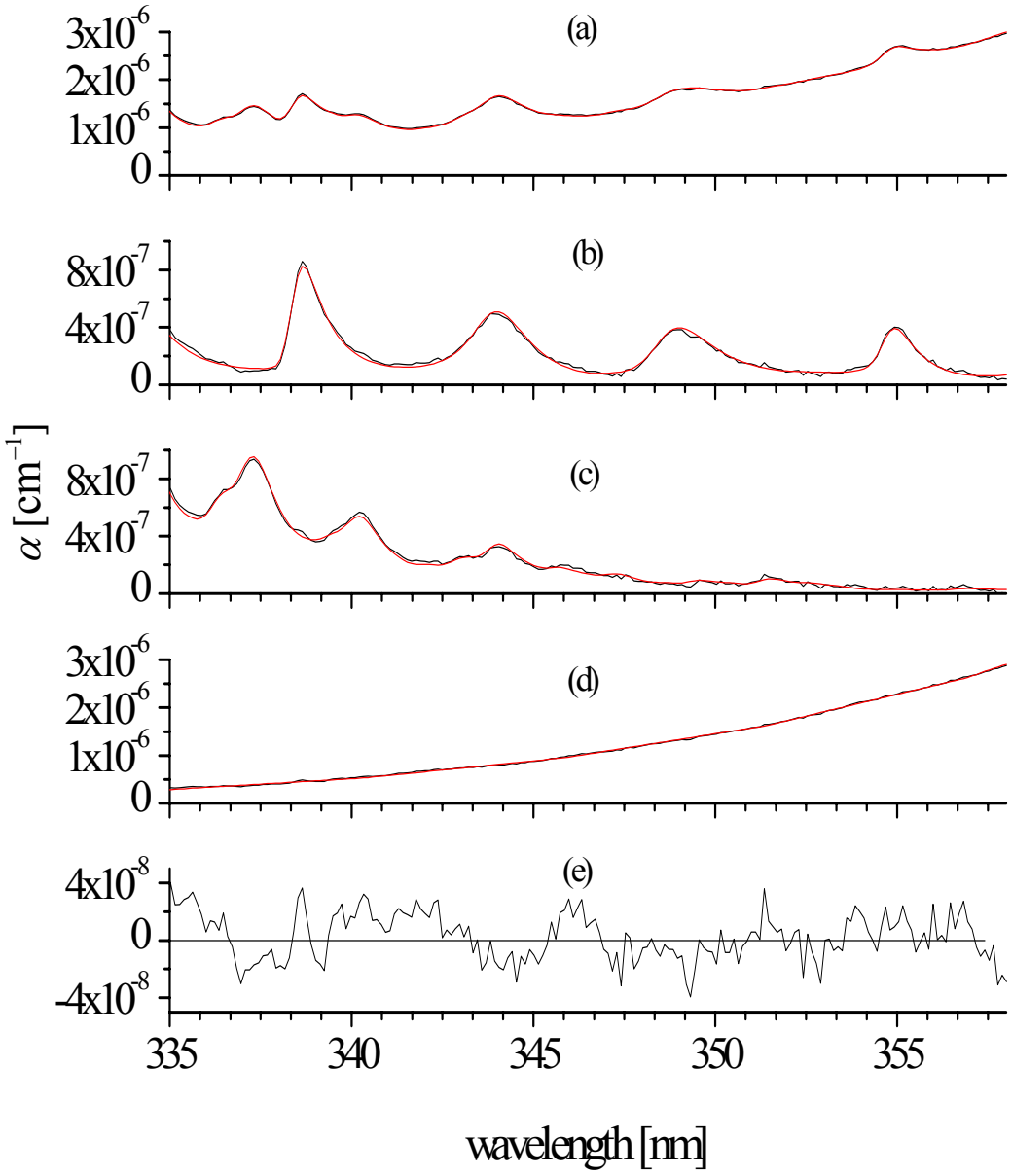


Figure 3.10 Absorption and fitted spectra for the Br_2, O_3, and BrO system. (a) Measured spectrum (black) and fitted result (red). The individual components of the spectrum are (b) BrO, (c) O_3, and (d) Br_2. (e) Residual of the fit.

Table 3.2 The influence of fitting window and the linear baseline on the retrieved concentrations from the spectral fit.

Fitting window(nm)	N_{BrO} **(10^{10}molecule cm^{-3})**	N_{Ozone} **(10^{14}molecule cm^{-3})**	$N_{Bromine}$ **(10^{13}molecule cm^{-3})**	***a*** **(10^{-7} cm^{-1})**	***b*** **(10^{-9}cm^{-1} nm^{-1})**	**RMS residual**
336 to 358	**6.09 ± 0.04**	**3.86 ± 0.01**	**4.81 ±0.005**	**0**	**0**	**1.74E-8**
336 to 370	7.88 ± 0.15	3.91 ± 0.06	3.81± 0.005	0	0	6.84E-8
336 to 358	6.22 ± 0.05	3.59 ± 0.02	3.79 ± 0.01	1.35± 0.06	0	1.96E-8
336 to 370	5.91 ± 0.08	3.26 ± 0.03	3.60± 0.005	2.32± 0.06	0	3.05E-8
336 to 358	6.24 ± 0.05	3.72 ± 0.05	3.66 ± 0.04	-17.02±5.9	5.38±1.7	1.91E-8
336 to 370	6.22 ± 0.06	3.90 ± 0.04	3.38 ± 0.01	-51.40±3.4	15.49±0.9	2.23E-8

(1) Zero values for a and b imply that these parameters were not included in the fit. (2) Bold values are from the fit shown in Fig. 3.10

The concentration of BrO in the flow cell was investigated as a function of reactant concentration (Fig. 3.11). The O_3 concentration in the input stream was increased at points A, C, and E by ramping up the O_3 generator output. Br_2 was introduced at time B by flowing N_2 over Br_2 in a liquid nitrogen/alcohol cooling bath initially at –30°C. As expected, photolysis of Br_2 in the presence of O_3 results in the immediate appearance of BrO; the BrO concentration increases with both Br_2 and O_3 concentration. The temperature of the cooling bath rose about 10°C over the course of the experiment, causing a gradual rise in the Br_2 and BrO concentrations. After the Br_2 source was stopped at time F, both Br_2 and BrO concentrations dropped off sharply, whereas the O_3 concentration rose by about a third as Br-catalysed O_3 loss is progressively choked off. The BrO concentration also rose at time D, when the Br_2 photolysis rate was increased by shining a high power 465 nm LED diagonally across the transparent centre of the flow tube.

The observed behaviour of the concentration of each species is in sensible agreement with known chemistry. Under stable inlet conditions, minimal scan-to-scan variation is observed. The precision of each concentration measurement was estimated based on the standard deviation from a seven-point running average between 49 and 65 min. Values of 1.2×10^{-12}, 4.5×10^{-10}, and 1.6×10^{-8} molecules cm^{-3} were found for O_3, Br_2, and BrO, respectively, which are comparable to the statistical uncertainties of the fit (respective averages of 2.1×10^{-12}, 9.0×10^{-10}, and 4.3×10^{-8} molecules cm^{-3}). We note in passing that whereas our measurements were obtained under steady-state conditions with low BrO concentrations, previous BrO measurements have recorded the absorption of higher BrO concentrations, either by using a microwave discharge or with short-time observations following flash lamp or laser photolysis of Br_2.(Fleischmann et al., 2004;Wahner et al., 1988;Sander and Friedl, 1989;Basco and

Dogra, 1971;Friedl and Sander, 1989;Gilles et al., 1997;Wilmouth et al., 1999;Laszlo et al., 1997;Cox et al., 1982;Orlando et al., 1991)

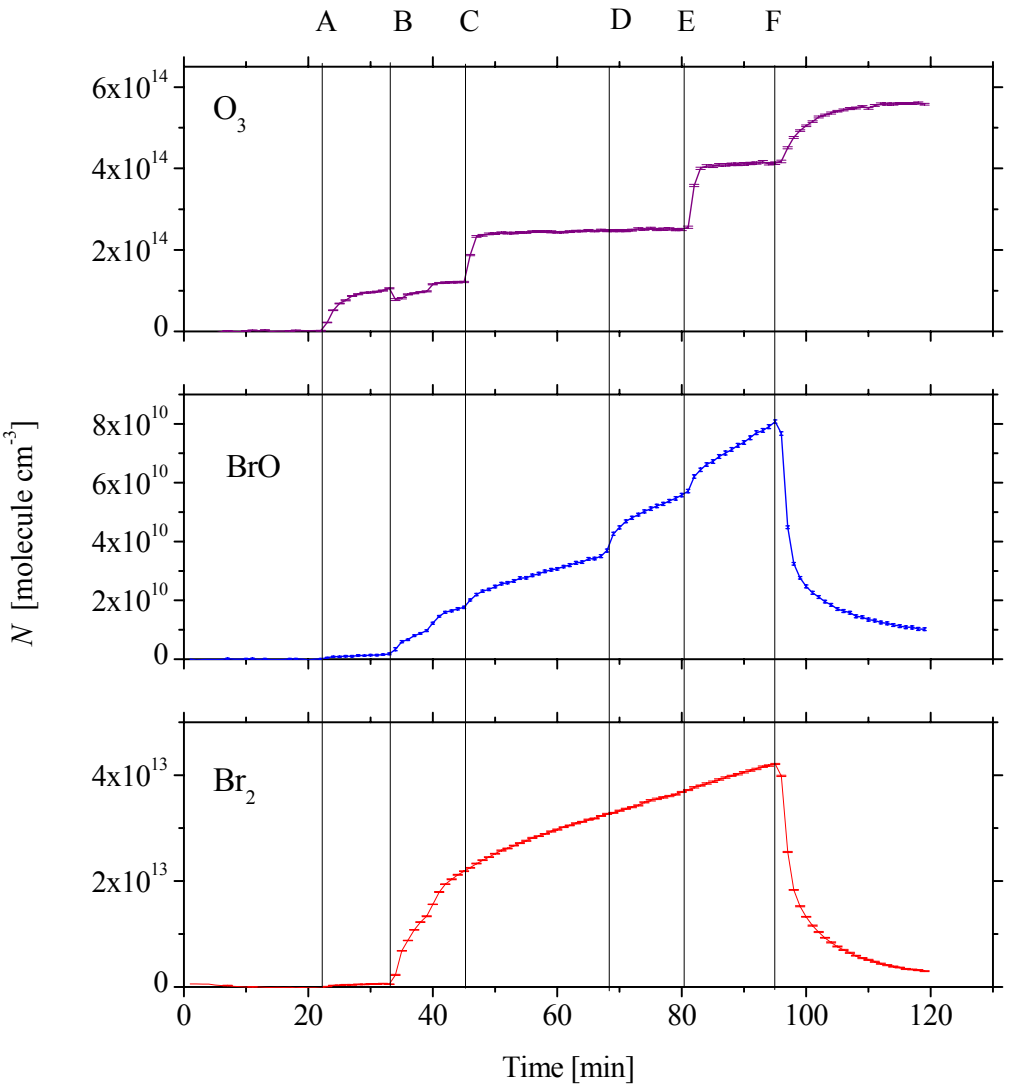


Figure 3.11 Temporal dependence of the number density of O_3, BrO, and Br_2 in the flow cell. Points A – F indicate changes in either the input concentrations or photolysis rate.

3.5 Discussion

The results above show the potential of the IBBCEAS system for retrieving weak absorption spectra in the near-UV at moderate resolution. The instrument performance is affected by several factors which we discuss below.

Whereas earlier near-UV IBBCEAS systems employed a 365 nm LED, in this study a Xe arc lamp was used as the light source. The high radiance of LEDs at 365 nm is attractive for monitoring several species over a narrow spectral window, but the spectral output falls rapidly from the maximum and has a typical FWHM of only about 10 nm. High power LEDs are not yet available below 365 nm. In contrast, the Xe arc-lamp spectrum is relatively unstructured in this spectral range and better suited to retrieving reference spectra. Xe arc lamps also have useful output at even shorter wavelengths and can be used for relatively broad spectral coverage (greater than 100 nm with appropriate cavity mirrors), which we have demonstrated in recent chamber studies of low volatility organic species (Chen et al., in preparation 2011). Notwithstanding these advantages, arc-lamps (and other very broadband sources) require stringent filtering to minimise stray light levels.

The sensitive absorption of this spectrometer (ca. 2×10^{-8} cm^{-1}) is with mirrors of only modest reflectivity. Although adequate for the purposes of this study, the sensitivity of the instrument could be improved with higher reflectivity mirrors. Higher reflectivity mirrors also lower the cavity transmission and the signal-to-noise ratio, so a balance must be struck between these competing factors. The reflectivity of the dielectric mirrors must be calibrated. In this study, we used a combination of the Rayleigh scattering and the well-established absorption of O_3 at 353 nm to determine the overall reflectivity. The mirror reflectivity is mostly flat across the spectral window determined by the filters. Any uncertainty in the mirror reflectivity –

or, more accurately, in the $(1 - R)$ term in Eq. (3.1) – contributes linearly to the overall uncertainty in the absorption coefficient. In the results here, this uncertainty is 8% to 10% at 353 nm but increases towards the long and short-wavelength limits of the spectra owing to the uncertainty in the $(1 - R)$ term. Below 340 nm, the spectra were 10 to 20% lower than previously reported absorption cross-sections, suggesting that the mirror reflectivity was overestimated at the short wavelength limit and that our spectra are less accurate in this region. Taking the wavelength-dependence of the uncertainty into account, we estimate the uncertainty in our cross-sections above 340 nm to range from 10 to 15%, which is acceptable for many applications and in line with the uncertainty in prior IBBCEAS studies. This work has also demonstrated that transmission of the windows outside of the high reflectivity range can be exploited to quantify components of the sample based on absorption in other spectral regions. In the results above, the small uncertainty of the (larger) absorption cross-sections of O_3 and ketones allows direct in situ quantification of these species. Sample losses elsewhere in the system can therefore be ignored.

In comparison to numerous literature spectra, the IBBCEAS spectra have significantly lower noise and also display linear absorption behaviour for weak absorptions. In these regions, where large variations between literature data are found, we believe that the spectra reported here are to be preferred to most prior spectra. Two caveats are in order, however. Firstly, even with long effective pathlengths, lamp intensity variations and gradual lamp dimming gives rise to apparent weak absorptions. This is evident in the small positive offset in the length wavelength limit of the 2-pentanone spectrum and implicitly in the linear offset of the fitting parameters of the BrO, O_3, and Br_2 spectrum. Secondly, the ketone absorptions below 340 nm did not rise as quickly as reported in numerous literature spectra. (A similar effect was also observed in the O_3 spectrum). This effect is

modest (probably less than 20% at 330 nm) and presumably arises from a small overestimation of the mirror reflectivity.

3.6 Conclusions

A near-UV IBBCEAS instrument has been developed for measuring weak absorption spectra from 335 to 375 nm. Spectra of SO_2 measured with the instrument show good agreement with literature spectra. The instrument has been used to retrieve revised absorption cross-sections of O_3, acetone, 2-butanone, and 2-pentanone, for which previously reported values diverge widely. The IBBCEAS spectra showed linear absorption behaviour and low spectral noise and provide revised estimates for the long-wavelength tail of these spectra. Concurrent retrieval of the concentrations of BrO, Br_2, and O_3 in a steady-state flow system has been demonstrated.

Bibliography

Atkinson, R.: Evaluated kinetic and photochemical data for atmospheric chemistry: Volume III - gas phase reactions of inorganic halogens, Atmos. Chem. Phys., 7, 981-1191, 2007.

Basco, N., and Dogra, S. K.: Reactions of halogen oxides studied by flash photolysis .3. production and reactions of BrO and ClO radicals in halogen-sensitized decomposition of chlorine dioxide, Proceedings of the Royal Society of London Series A-Mathematical and Physical Sciences, 323, 417, 1971.

Bobrowski, N., Kern, C., Platt, U., Hörmann, C., and Wagner, T.: Novel SO_2 spectral evaluation scheme using the 360-390 nm wavelength range, Atmos. Meas. Tech., 3, 879-891, 10.5194/amt-3-879-2010, 2010.

Bogumil, K., Orphal, J., Homann, T., Voigt, S., Spietz, P., Fleischmann, O. C., Vogel, A., Hartmann, M., Kromminga, H., Bovensmann, H., Frerick, J., and Burrows, J. P.: Measurements of molecular absorption spectra with the SCIAMACHY pre-flight model: instrument characterization and reference data for atmospheric remote-sensing in the 230-2380 nm region, J. Photochem. Photobiol. A, 157, 167-184, 2003.

Brion, J., Chakir, A., Charbonnier, J., Daumont, D., Parisse, C., and Malicet, J.: Absorption spectra measurements for the ozone molecule in the 350-830 nm region, J. Atmos. Chem., 30, 291-299, 1998.

Burrows, J. P., Richter, A., Dehn, A., Deters, B., Himmelmann, S., and Orphal, J.: Atmospheric remote-sensing reference data from GOME - 2. Temperature-dependent absorption cross sections of O_3 in the 231-794 nm range, J. Quant. Spectrosc. Radiat. Transf., 61, 509-517, 1999.

Chen, J., J.C.Wenger, and D.S.Venables: Near-ultraviolet absorption cross-sections of nitrophenols and their potential influence on tropospheric oxidation

capacity, J. Phys.Chem. A, revision submitted 2011.

Cox, R. A., Sheppard, D. W., and Stevens, M. P.: Absorption-coefficients and kinetics of the BrO radical using molecular modulation, J. Photochem., 19, 189-207, 1982.

Dianov-Klokov, V. I.: Absorption spectrum of oxygen at pressures from 2 to 35 atm in the region from 12600 to 3600 Å, Opt. Spectrosc., 16, 224-227, 1964.

Fiedler, S. E., Hese, A., and Ruth, A. A.: Incoherent broad-band cavity-enhanced absorption spectroscopy, Chem. Phys. Lett., 371, 284-294, 2003.

Fiedler, S. E., Hese, A., and Heitmann, U.: Influence of the cavity parameters on the output intensity in incoherent broadband cavity-enhanced absorption spectroscopy, Rev. Sci. Instrum., 78, 7, 073104,10.1063/1.2752608, 2007.

Fleischmann, O. C., Hartmann, M., Burrows, J. P., and Orphal, J.: New ultraviolet absorption cross-sections of BrO at atmospheric temperatures measured by time-windowing Fourier transform spectroscopy, J. Photochem. Photobiol. A, 168, 117-132, 2004.

Friedl, R. R., and Sander, S. P.: Kinetics and Product Studies of the Reaction ClO + BrO Using Discharge-Flow Mass-Spectrometry, J. Phys. Chem., 93, 4756-4764, 1989.

Gierczak, T., Burkholder, J. B., Bauerle, S., and Ravishankara, A. R.: Photochemistry of acetone under tropospheric conditions, Chem. Phys., 231, 229-244, 1998.

Gilles, M. K., Turnipseed, A. A., Burkholder, J. B., Ravishankara, A. R., and Solomon, S.: Kinetics of the IO radical .2. Reaction of IO with BrO, J. Phys. Chem. A, 101, 5526-5534, 1997.

Greenblatt, G. D., Orlando, J. J., Burkholder, J. B., and Ravishankara, A. R.: Absorption Measurements of Oxygen Between 330 and 1140 nm, J. Geophys. Res., 95, 18577-18582, 10.1029/JD095iD11p18577, 1990.

Honninger, G., and Platt, U.: Observations of BrO and its vertical distribution during surface ozone depletion at Alert, Atmos. Environ., 36, 2481-2489, 2002.

Horowitz, A.: Absorption cross sections of 2-pentanone, 3-pentanone, and 3-hexanone, Personal communication of unpublished data of the Max-Planck-Institut für Chemie, Mainz (1999). 1999.

Hynes, A. J., Kenyon, E. A., Pounds, A. J., and Wine, P. H.: Temperature-Dependent Absorption Cross-Sections for Acetone and Normal-Butanone - Implications for Atmospheric Lifetimes, Spectrochim. Acta. A, 48, 1235-1242, 1992.

Laszlo, B., Huie, R. E., Kurylo, M. J., and Miziolek, A. W.: Kinetic studies of the reactions of BrO and IO radicals, J. Geophys. Res.-Atmos, 102, 1523-1532, 1997.

Mahajan, A. S., Oetjen, H., Lee, J. D., Saiz-Lopez, A., McFiggans, G. B., and Plane, J. M. C.: High bromine oxide concentrations in the semi-polluted boundary layer, Atmos. Environ., 43, 3811-3818, 2009.

Martinez, R. D., Buitrago, A. A., Howell, N. W., Hearn, C. H., and Joens, J. A.: The near UV absorption-spectra of several aliphatic-aldehydes and ketones at 300K, Atmo. Enviro. A, 26, 785-792, 1992.

Meyrahn, H., Pauly, J., Schneider, W., and Warneck, P.: Quantum Yields for the Photodissociation of Acetone in Air and an Estimate for the Life Time of Acetone in the Lower Troposphere, J. Atmos. Chem., 4, 277-291, 1986.

Mu, Y. J., and Mellouki, A.: The near-UV absorption cross sections for several ketones, J. Photochem. Photobiol. A, 134, 31-36, 2000.

Naus, H., and Ubachs, W.: Experimental verification of Rayleigh scattering cross sections, Opt. Lett., 25, 347-349, 2000.

Noyes, W. A., Porter, G. B., and Jolley, J. E.: The Primary Photochemical Process in Simple Ketones, Chem. Rev., 56, 49-94, 1956.

Orlando, J. J., Burkholder, J. B., Bopegedera, A. M. R. P., and Howard, C. J.: Infrared measurements of BrO ($X^2\Pi_{3/2}$), J. Mol. Spectrosc., 145, 278-289, 1991.

Peters, C., Pechtl, S., Stutz, J., Hebestreit, K., Honninger, G., Heumann, K. G., Schwarz, A., Winterlik, J., and Platt, U.: Reactive and organic halogen species in three different European coastal environments, Atmos. Chem. Phys., 5, 3357-3375, 2005.

Salow, H., and Steiner, W.: Die durch Wechselwirkungskräfte bedingten Absorptionsspektra des Sauerstoffes, I. Die Absorptionsbanden des O_2-O_2 Moleküls, Z. Physik, 99, 137-158, 1936.

Sander, S. P., and Friedl, R. R.: Kinetics and Product Studies of the Reaction ClO + BrO Using Flash Photolysis-Ultraviolet Absorption, J. Phys. Chem., 93, 4764-4771, 1989.

Sneep, M., and Ubachs, W.: Direct measurement of the Rayleigh scattering cross section in various gases, J. Quant. Spectrosc. Radiat. Transf., 92, 293-310, 2005.

Sutton, J. A., and Driscoll, J. F.: Rayleigh scattering cross sections of combustion species at 266, 355, and 532 nm for thermometry applications, Opt. Lett., 29, 2620-2622, 2004.

Vandaele, A. C., Hermans, C., and Fally, S.: Fourier transform measurements of SO_2 absorption cross sections: II. Temperature dependence in the 29 000-44 000 $cm^{(-1)}$ (227-345 nm) region, J. Quant. Spectrosc. Radiat. Transf., 110, 2115-2126, 2009.

Voigt, S., Orphal, J., Bogumil, K., and Burrows, J. P.: The temperature dependence (203-293 K) of the absorption cross sections of O_3 in the 230-850 nm region measured by Fourier-transform spectroscopy, J. Photochem. Photobiol. A, 143, 1-9, 2001.

Volkamer, R.: Absorption von Sauerstoff im Herzberg I System und Anwendungen auf die Aromatenmessungen am EUropran PHOto REactor (EUPHORE), Diploma thesis, Univ. of Heidelberg, Germany, 1996.

Wagner, T., Ibrahim, O., Sinreich, R., Friess, U., von Glasow, R., and Platt, U.: Enhanced tropospheric BrO over Antarctic sea ice in mid winter observed by MAX-DOAS on board the research vessel Polarstern, Atmos. Chem. Phys., 7, 3129-3142, 2007.

Wahner, A., Ravishankara, A. R., Sander, S. P., and Friedl, R. R.: Absorption cross section of BrO between 312 and 385 nm at 298 and 223 K, Chem. Phys. Lett., 152, 507-512, 1988.

Wilmouth, D. M., Hanisco, T. F., Donahue, N. M., and Anderson, J. G.: Fourier transform ultraviolet spectroscopy of the $A^2\Pi_{3/2}$ <- $X^2\Pi_{3/2}$ transition of BrO, J. Phys. Chem. A, 103, 8935-8945, 1999.

Wollenhaupt, M., Carl, S. A., Horowitz, A., and Crowley, J. N.: Rate coefficients for reaction of OH with acetone between 202 and 395 K, J. Phys. Chem. A, 104, 2695-2705, 2000.

Wu, T., Zhao, W. X., Li, J. S., Zhang, W. J., Chen, W. D., and Gao, X. M.: Incoherent Broadband Cavity Enhanced Absorption Spectroscopy Based on LED, Spectrosc. Spectr. Anal., 28, 2469-2472, 10.3964/j.issn.1000-0593(2008)11-2469-04, 2008.

Chapter 4

FIELD OBSERVATIONS

In Chapter 3, an incoherent broadband cavity-enhanced absorption spectroscopy (IBBCEAS) instrument was applied to laboratory measurements. Using the instrument, new absorption cross-sections of O_3, acetone, 2-butanone, and 2-pentanone were measured in the near-UV. The application of the instrument to quantifying low concentrations of the short-lived radical, BrO, was also demonstrated. These studies notwithstanding, one of the key drivers of the technique is its potential for field observations. IBBCEAS is in several respects similar to long path-DOAS (LP-DOAS), an established and sensitive field method for a wide range of atmospheric species. However, one of the advantages of IBBCEAS compared to LP-DOAS is its higher spatial resolution which is especially important for reactive halogens with potentially small-scale sources.

The IBBCEAS approach has already been used at the SAPHIR atmospheric simulation chamber with a 20 m long cavity as well as in an open path configuration at a weather observing station (Roches Point, Co. Cork) for the retrieval of aerosol extinction (Varma et al., 2009;Fuchs et al., 2010). These studies showed that IBBCEAS can be used with an open path configuration as well as with large mirror separations for improved sensitivity. Other groups have also carried out several IBBCEAS field observations recently (Ball et al., 2010;Benton et al., 2010). This chapter reports on the use of the IBBCEAS approach in two field campaigns. The first campaign COBRA (=*Impact of combined iodine and bromine release on the Arctic atmosphere*) was a major international campaign that took place at Hudson Bay, Canada, in Spring 2008 as part of the International Polar Year (IPY). In Autumn 2009, a second campaign to investigate reactive halogen compounds was undertaken at Mace Head Atmospheric Research Station. In this chapter, both campaigns will be introduced and the field instruments developed for them will be presented. Ultimately neither campaign produced useful data owing to the difficult

meteorological conditions experienced. Nevertheless, as the group's first major deployments of the technique in the field, these campaigns provide valuable lessons on the instrument's performance and design issues for future field work.

4.1 COBRA Campaign

4.1.1 Motivation

During late winter and spring, sudden ozone depletion events (ODEs) occur in the polar boundary layer (PBL).This phenomenon has been observed since the 1980s (Barrie et al., 1988;Bottenheim et al., 1986). In these episodes, oxidation chemistry in the PBL shifts from being dominated by ozone photochemistry to being dominated by halogen chemistry, and especially by reactive bromine chemistry (Simpson et al., 2007). The events have been linked to the exchange of halogen species between the snowpack or sea-ice and the overlying atmosphere, and subsequent catalytic reaction of bromine atoms with ozone to produce bromine oxide is believed to be the primary loss process for ozone in this region (Piot and von Glasow, 2008).

$$Br_2 + h\nu \rightarrow 2Br \quad (4.1)$$

$$HOBr + h\nu \rightarrow Br + OH \quad (4.2)$$

Then,

$$2Br + 2O_3 \rightarrow 2BrO + 2O_2 \quad (4.3)$$

$$BrO + BrO \rightarrow 2Br + O_2 \quad (4.4)$$

Net:

$$2O_3 \rightarrow 3O_2 \quad (4.5)$$

However, questions still remain as to the source of the bromine: do these species evolve from frost flowers (crystalline structures that form on new sea ice), open leads in the ice, or from the ice or snow itself; are they released steadily with time or in

'bromine explosions'; what is the temporal and spatial variation of BrO relative to the source; and is there recycling of BrO on the snowpack/ice?

Since tropospheric ozone is not only an important greenhouse gas, but it also has significant consequences for the oxidative capacity of this region, it is imperative to develop the quantitative understanding of relevant chemical interactions so that the future states of the Arctic and Antarctic atmosphere can be better predicted. Accurate observations of BrO during polar ODEs are critical for this task. Current data have been obtained using methods – for instance, LP-DOAS – that rely on performing measurements across several kilometres and thus have unavoidably been limited in their ability to follow the spatial variation of BrO.

A newly build field instrument based on IBBCEAS would allow sensitive monitoring of BrO over just a few metres, thus providing excellent spatial and temporal versatility. Furthermore, there has been great interest in the possibility that iodine-related species could play a significant role in Arctic chemistry following the recent observations of iodine oxides in the Antarctic atmosphere (Frieß et al.); in this context and based on the previous experiments in the laboratory the IBBCEAS approach looked promising for monitoring BrO during the COBRA campaign.

The COBRA campaign took place at a research site near Kuujjuarapik on Hudson Bay from 7 February to 7 March 2008 (Fig. 4.1). Research groups from several UK research institutions (Universities of York, Leeds, Manchester, East Anglia, Cambridge and Leicester and the British Antarctic Survey), and international bodies (Universities of Bremen, Montreal and Battelle, and Environment Canada) also participated in the campaign. In spring, the sea in this region is covered with about 1 m of ice, with open leads and frost-flower formation in some areas near the research site. Hence, ODEs and subsequent generation of BrO was expected during the

campaign. The group's objective in the campaign was to install the IBBCEAS instrument at various sites near frost flowers and open leads to investigate the evolution of BrO and iodine-containing species.

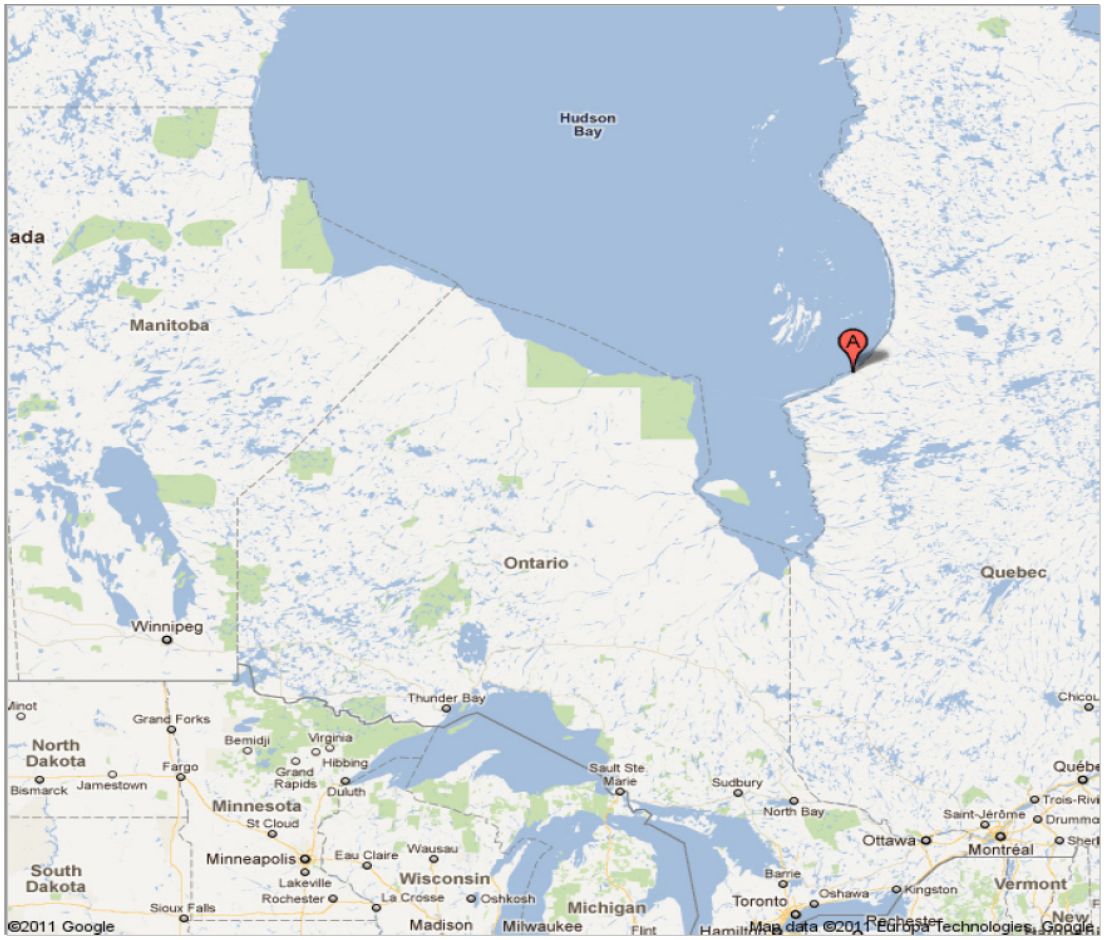


Figure 4.1 Kuujjuarapik (marked A), the research site of the COBRA campaign.

4.1.2 Spectrometer description

An IBBCEAS spectrometer, designed specifically for cold-temperature conditions, was developed at University College Cork in collaboration with the Ruth group (Department of Physics). The structure was based on the NO_3 Jülich campaign instrument (Varma et al., 2009), but had to be portable, easy to align, and thermally stable in the extremely cold conditions of the campaign.

The instrument was designed for near-UV measurements and consisted of a transmitter unit and a receiver unit, each housing one of the cavity mirrors (Fig. 4.2). Delrin, an engineering thermoplastic, was used for the body of the instrument. The advantages of Delrin are its high stiffness, low friction, excellent dimensional stability and low thermal conductivity (0.31 W m^{-1} K^{-1}), which is critical to reduce heat losses. The two units could be separated by any arbitrary distance in an open-path configuration. The instrument for BrO targeted its strong $A^2\Pi_{3/2} \leftarrow X^2\Pi_{3/2}$ electronic transition which has a maximum at 338.5 nm.

A short Xe arc lamp, running in the "hot spot" mode, was used as a light source. This lamp had very high power radiance but required water cooling, a disadvantage in the field. The direction of the light emitted from the source was controlled by a piezo-mounted mirror and feedback loop linked to a quadrant detector. Two parabolic mirrors were used to transmit and focus the light onto an iris. A short pass filter was placed before the focal point. The light transmitted through the iris was imaged by a telescope into the centre of the cavity. Two highly reflective mirrors composed the optical resonator. The cavity mirrors (Layertec) each had a reflectivity centred at 355 nm, a 5 m radius of curvature, and were 40 cm in diameter. Transmission of the light from the cavity was collected by a fused silica lens and coupled into a fibre bundle. Fibres were vertically arranged to match the entrance slit of the spectrograph (Andor SR-163 and 420A-BU CCD camera). Both transmitter and receiver units were mounted on heavy duty tripods (Hercules Series, Quick Set Inc.) which allowed the height to be adjusted. A He-Ne laser was installed in the transmitter to align the optical resonator. The alignment laser beam was directed from the transmitter to the receiver via pinholes on both platforms to give coarse alignment of the height of both units. During alignment of the cavity mirrors, an aluminium mirror on a pre-located magnetic base reflected the alignment beam back

through the optical cavity. After aligning the optical resonator, the mirror was removed to avoid blocking the cavity transmission.

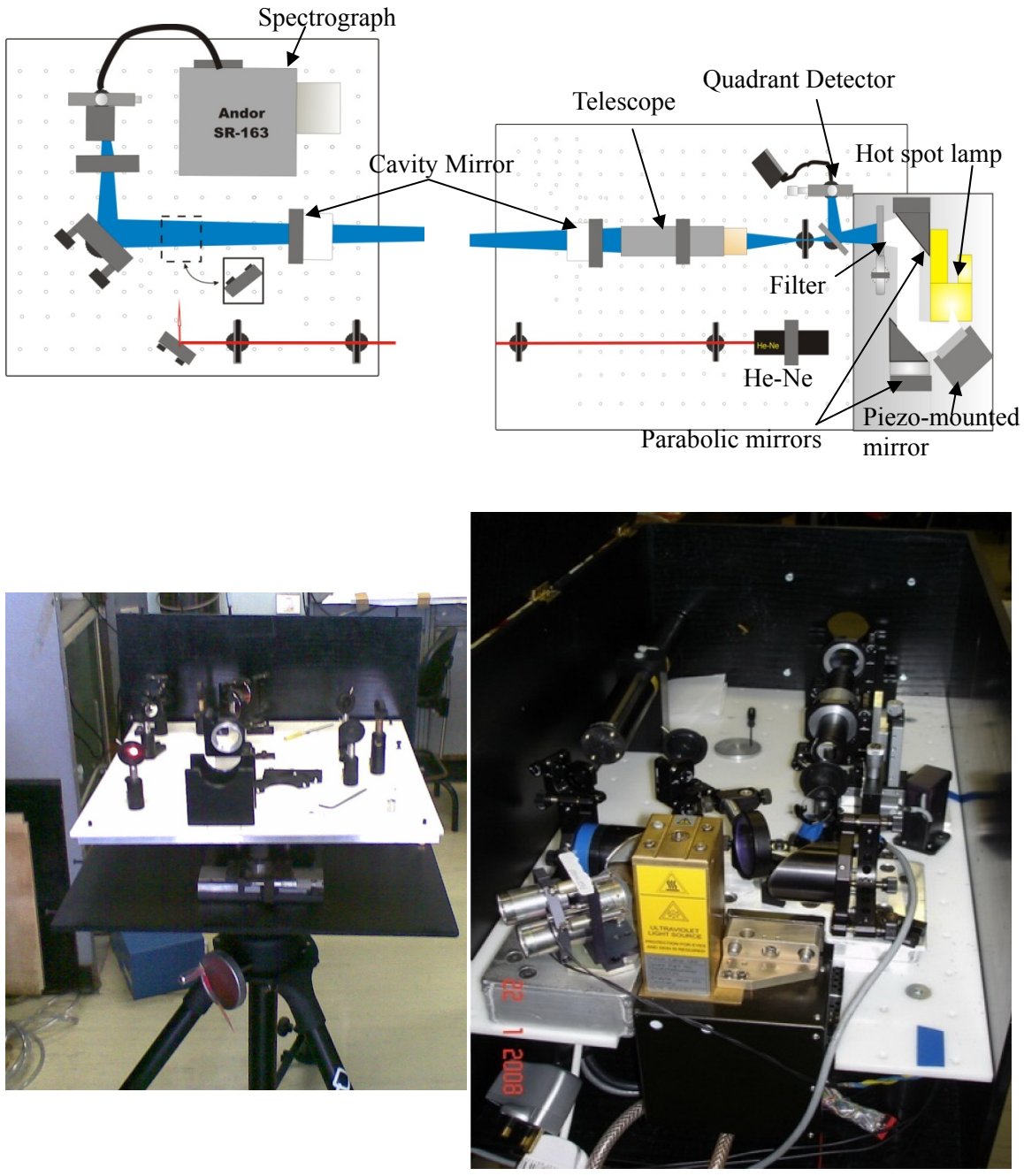


Figure 4.2 TOP: Schematic of the open path field IBBCEAS instrument for the COBRA campaign. BOTTOM: Photographs of the inside of both units (receiver on the left and transmitter on right)

4.1.3 Campaign results

The extreme environmental conditions at the site posed a number of technical challenges for instrument design. Daytime temperatures were regularly below -20°C, falling on occasion to below -30°C at night, and the temperature could vary by as much as 30°C over a 24 hour period. Thus, the instrument contained controllers, heaters and thermostats to maintain the internal temperature above 0°C. Gusting winds were frequent, and could reach 70 km/hr, so the use of windbreaks was essential. Optimization of the optical components of the instrument was necessarily delayed during periods of snow precipitation. In fact, all work at the research site had to be halted for at least two days because of a blizzard. Even during optimal conditions, aligning the system was difficult because the optics had to be manipulated through thick winter gloves. In addition the alignment beam was difficult to observe because of the very bright snowpack.

Unfortunately, the IBBCEAS system was critically impaired by the unforeseeable breakdown of the light sources, without which the instrument could not operate. This was caused by the overnight malfunction of the generator that powered the research site and which led to the burn-out of the Xe short-arc lamp, probably because the cooling liquid froze. Due to the remote locality of the research site (Kuujjuarapik is over 1000 km from the nearest major city), the lamp could not be repaired at the site. A high-power light-emitting diode (LED) with strong emission in the ultra-violet (previously used for the detection of HONO) was substituted for the broken lamp unit. However, for unknown reasons, the LED also stopped functioning on the first night that measurements were being recorded and could not be repaired. Thus, our participation in the campaign eventually had to be aborted.

Although our participation in the campaign did not produce any new data to explain

the behaviour of BrO and iodo-species in the Arctic troposphere, there were several positive aspects resulting from participation in the COBRA campaign. For instance, this was the first field deployment of an IBBCEAS spectrometer in the field outside Ireland. Had the light sources not failed, the instrument could have yielded important scientific data and information. The campaign also provided the group and campaign participants with valuable experience of fieldwork in extreme and very difficult environments. Finally, the presence of the international scientific community allowed for a significant transfer of knowledge and expertise, as well as generating important contacts between UCC and other researchers that are leading experts in their field.

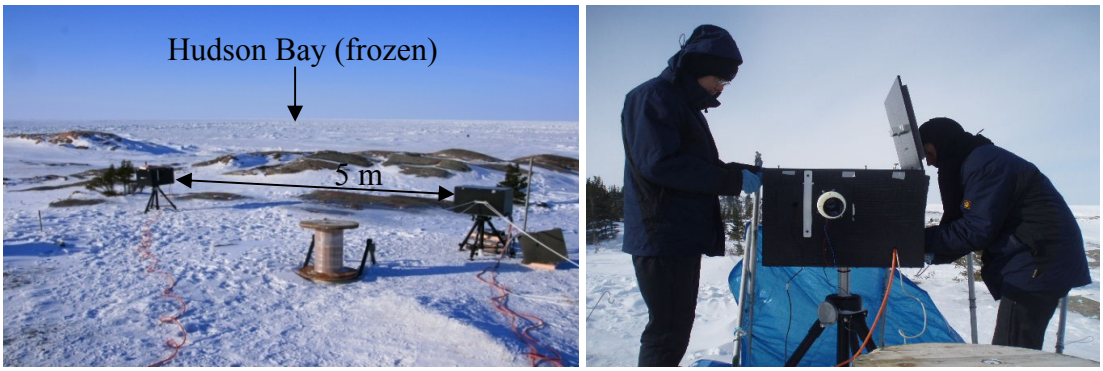


Figure 4.3 Campaign site (left) showing the IBBCEAS system with Hudson Bay in the background. Author and Dr. S. Vaughan aligning the IBBCEAS system (right).

4.2 Mace Head Campaign

4.2.1 Motivation

Reactive halogen compounds not only play an important role in stratospheric chemistry (Molina and Rowland, 1974), but also in the troposphere via catalytic depletion of ozone (von Glasow et al., 2004). BrO was identified in the Arctic and Antarctic (Tuckermann et al., 1997), in which it contributes to ozone depletion

(Barrie et al., 1988). However, BrO was also found at low concentrations in the marine boundary layer (MBL) (Leser et al., 2003;Saiz-Lopez et al., 2004). This reactive bromine can have a significant influence on the chemistry in the MBL. It can destroy ozone, change the NO/NO_2 and the OH/HO_2 ratios and oxidise dimethylsulfide (DMS) (Simpson et al., 2007). Heterogeneous reactions might also play a role in the release of bromine compounds in the MBL (Usher et al., 2003).

Iodine chemistry in ozone depletion events and marine aerosol formation has also received considerable attention recently. Molecular iodine is probably the dominant source of atmospheric iodine in certain coastal regions, as suggested by recent field observations and laboratory studies. High concentrations of I_2 have been measured during a previous campaign at Mace Head, County Galway (Saiz-Lopez and Plane, 2004). During daylight, I_2 molecules in the atmosphere are photolyzed to I atoms which then react with O_3 to form iodine oxide (IO).

$$I_2 + h\nu \rightarrow 2I \quad (4.6)$$

$$I + O_3 \rightarrow IO + O_2 \quad (4.7)$$

An anti-correlation between IO and tidal height and a correlation between IO and solar irradiation were also observed at Mace Head (Carpenter et al., 2001;Saiz-Lopez et al., 2006). The self-reaction of IO is thought to result in the formation of higher iodine oxides like OIO or I_2O_4 and eventually leads to new particle formation (Hoffmann et al., 2001;O'Dowd and Hoffmann, 2005;Pirjola et al., 2005;Plane et al., 2010). However, the exact mechanism of particle formation has not been fully established and probably involves reactions of IO and OIO (Himmelmann et al., 1996), which is formed via:

$$IO + IO \rightarrow OIO + I \quad (4.8)$$

Biogenic emission of I_2 by macroalgae has been suggested to be one of the most important processes responsible for the observed tropospheric iodine levels in coastal

locations (McFiggans et al., 2004;Palmer et al., 2005). Iodine is accumulated in macroalgae (e.g., *Laminaria digitata*) in the form of iodide and can react with O_3 when the plants are exposed to the ambient air at low tide, leading to the direct release of I_2 into the atmosphere (Küpper et al., 2008). Emission of organic iodine was not thought to be as important due to the relative low photolysis rate of these species. The time dependence of I_2 emission from *Laminaria digitata* was previously investigated by the IBBCEAS method (Dixneuf et al., 2009). Hence, to study both bromine and iodine chemistry in the marine boundary layer it is desirable to develop an instrument that can measure both BrO and IO simultaneously. Another motivation for monitoring both species is that iodine seems to enhance the bromine-catalyzed destruction of ozone (Vogt et al., 1999). The LP-DOAS and MAX-DOAS methods have previously been used to measure these species, but do give information about their spatial distribution which is important especially for halogen chemistry in the MBL. To address these issues, a dual cavity instrument measuring both BrO and IO was designed and setup at the Mace Head Atmospheric Research Station (Fig 4.4). The campaign took place from 19 to 27 August 2009, which was chosen to coincide with a spring tide during which the macroalgae would be exposed and relatively high iodine emissions were expected.



Figure 4.4 The dual cavity IBBCEAS instrument in the campaign site at Mace Head (green covers), and the tripod-mounted IBBCEAS instrument of the Ruth group (red covers)

4.2.2 The Dual Cavity Spectrometer

The spectrometer was designed to quantify BrO and IO concentrations. The open path configuration was also used in this spectrometer. The transmitter and receiver platforms were made from aluminium and were separated by 4 m. Both units were mounted and connected to each other on Bosch aluminium profile structures for rigidity.

Inside the transmitter unit (Fig 4.5), the hot spot lamp provides about 20 times the brightness compared to ordinary diffuse arcs, but the spot tended to wander around the cathode. This arc wandering was compensated by stabilizing the image of the hot spot with a feedback loop between the quadrant detector and a piezo-mounted plane mirror placed between the lamp and the first parabolic mirror. A fraction of the light was focused onto the quadrant detector while the main beam was imaged in the plane of an iris in a similar manner to the COBRA instrument. The light was separated into two bands (320-410 nm and 410-575 nm) with a beam splitter (Semrock FF409) before entering each cavity. The spot on the iris aperture was imaged at the centres of both the near-UV and blue open-path cavities using two telescopes. One of the telescopes was made from fused silica lenses to optimize the transmission of light into the near-UV cavity.

The receiver unit housed the other cavity mirrors. Light transmitted through the cavity was filtered with two different filter combinations. Filters for the UV cavity included a short-pass filter (UG11 Schott glass), a bandpass interference filter (Semrock FF01-357/44) and an IR cutoff filter (KG1 Schott glass). The blue cavity filters included a 460 nm centred band-pass filter (Semrock FF01-440/40) and an IR cutoff filter (KG1 Schott glass) to ensure that light outside the mirror reflectivity range was eliminated. After filtering, both beams were focused into a 2-way fibre.

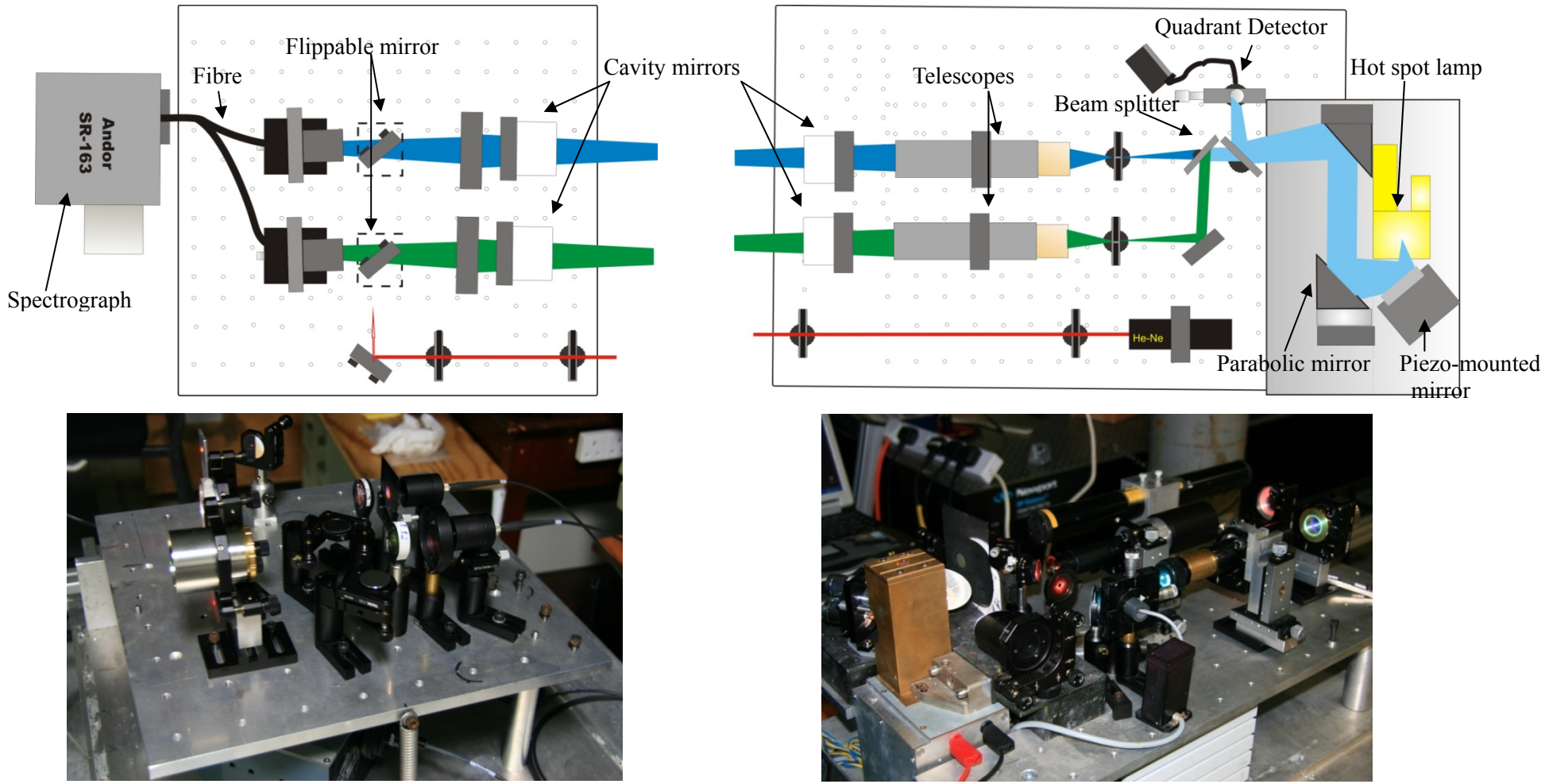


Figure 4.5 Schema (top) and photograph (bottom) of the dual cavity IBBCEAS instrument. The transmitter platform is shown on the right and receiver on the left.

The fibre output bundle formed a 25 µm width vertical arrangement at the slit of the spectrograph (Andor SR-163 with 1200 l/mm grating) that had a CCD detector (Andor 420A-BU) attached to it. Two aluminium mirrors were placed between the cavity mirrors and filters using flippable mirror mounts. These mirrors were used to reflect the aligning beam back to the transmitter during the alignment of the optical cavities. Both cavity signals are shown in Fig. 4.6 along with the absorption cross-sections of BrO and IO. The windows extended from 330 to 380 nm and from 420 to 450 nm and covered major vibronic peaks of both species. Much more light was transmitted through the blue cavity than the near-UV cavity, which would reduce the relative magnitude of photon noise and improve sensitivity to small absorptions in the blue cavity. From laboratory measurements of BrO, the sensitivity of the field instrument can be conservatively estimated as about 10^{-8} cm^{-1}, equivalent to the absorption of 20 ppt of BrO and 10 ppt of IO respectively.

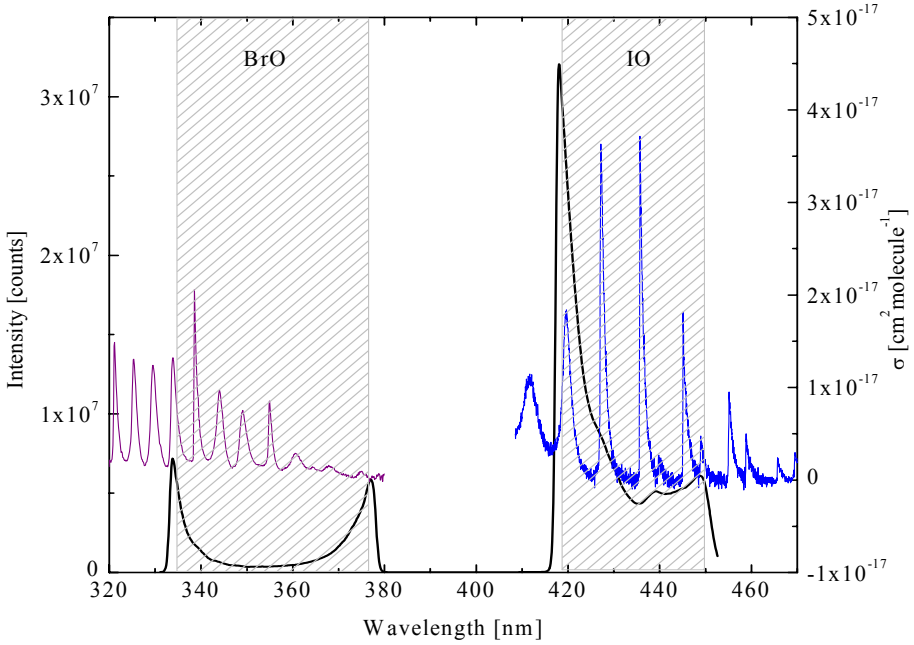


Figure 4.6 The dual cavity intensity (black) from 320 to 460 nm after 60 s acquisition time. The spectral windows of each cavity (diagonal lines) and the BrO (purple) and IO (blue) absorption cross-sections are also shown (Fleischmann et al., 2004;Spietz et al., 2005) .

4.2.3 Campaign results

The dual cavity spectrometer was set up outside the Mace Head Atmospheric Research Station on uneven coastal grassland (Fig. 4.4). Maintaining a stable cavity was a challenge as the wind was frequent with the gusts of up to 100 km/hr. Although the profiles were firmly tied down on the ground, the high wind speeds resulted in vibrations in the system giving a rather unstable cavity signal (Fig. 4.7). Furthermore, open path optical instruments are limited by weather conditions, and precipitation occurred regularly during the campaign. For these reasons, measurements during that time resulted in no useful data. Another IBBCEAS system for I_2 measurements mounted on tripods was operated by colleagues from the Ruth group also shown in (Fig. 4.4). This system was based on the platform from the COBRA campaign, except that a super-continuum source substituted for the arc lamp. Unfortunately, this system also was not sufficiently mechanically stable and with the intermittent rain also did not produce any results during the campaign.

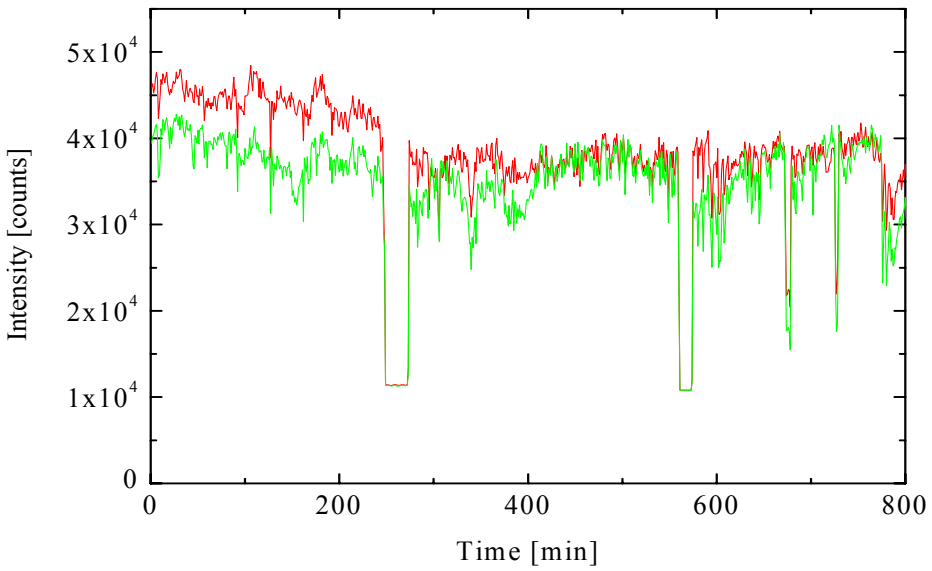


Figure 4.7 The cavity intensity measured at 370 nm (green) and 430 nm (red) on 20 Aug 2009. The intensity drops around 250 min and 550 min correspond to calibration of the system.

Although the campaign did not produce useful data, the basic instrumental design of the dual cavity system proved to be feasible and was replicated for chamber studies. In conclusion, for field observations IBBCEAS requires a very stable platform for the optical cavity and further work on the design of such a platform is necessary. The dual cavity configuration has been implemented on the halogen atmosphere simulation chamber in the Environmental Research Institute (Fig. 4.8). Two pairs of cavity mirrors were installed on a flange mounted on the wall of the chamber. The mirrors were pushed from the back side onto a compressible silica O-ring to provide adjustment. The mirrors can be purged from the edge of the flange to prevent degradation. The IBBCEAS instrument coupled on the halogen chamber has a blue (420 to 460 nm) and a green (490 to 550 nm) window for monitoring species such as I_2, IO and OIO.

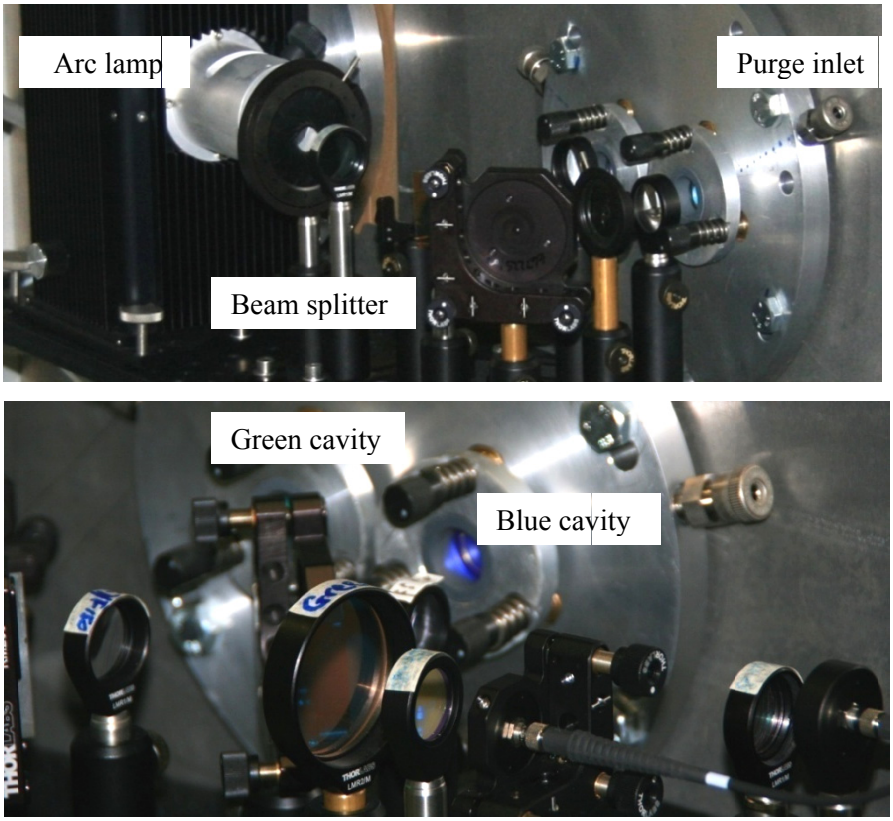


Figure 4.8 Dual cavity IBBCEAS instrument coupled onto the chamber in the Environmental Research Institute, Cork. The transmitter side with arc lamp (top) and the receiver side (bottom).

Bibliography

Ball, S. M., Hollingsworth, A. M., Humbles, J., Leblanc, C., Potin, P., and McFiggans, G.: Spectroscopic studies of molecular iodine emitted into the gas phase by seaweed, Atmos. Chem. Phys., 10, 6237-6254, 2010.

Barrie, L. A., Bottenheim, J. W., Schnell, R. C., Crutzen, P. J., and Rasmussen, R. A.: Ozone Destruction and Photochemical-Reactions at Polar Sunrise in the Lower Arctic Atmosphere, Nature, 334, 138-141, 1988.

Benton, A. K., Langridge, J. M., Ball, S. M., Bloss, W. J., Dall'Osto, M., Nemitz, E., Harrison, R. M., and Jones, R. L.: Night-time chemistry above London: measurements of NO_3 and N_2O_5 from the BT Tower, Atmos. Chem. Phys., 10, 9781-9795, 10.5194/acp-10-9781-2010, 2010.

Bottenheim, J. W., Gallant, A. G., and Brice, K. A.: Measurements of NO_Y Species and O_3 at 82-Degrees-N Latitude, Geophys. Res. Lett., 13, 113-116, 1986.

Carpenter, L. J., Hebestreit, K., Platt, U., and Liss, P. S.: Coastal zone production of IO precursors: a 2-dimensional study, Atmos. Chem. Phys., 1, 9-18, 2001.

Dixneuf, S., Ruth, A. A., Vaughan, S., Varma, R. M., and Orphal, J.: The time dependence of molecular iodine emission from *Laminaria digitata*, Atmos. Chem. Phys., 9, 823-829, 2009.

Fleischmann, O. C., Hartmann, M., Burrows, J. P., and Orphal, J.: New ultraviolet absorption cross-sections of BrO at atmospheric temperatures measured by time-windowing Fourier transform spectroscopy, J Photochem. Photobiol. A, 168, 117-132, 2004.

Frieß, U., Deutschmann, T., Gilfedder, B. S., Weller, R., and Platt, U.: Iodine monoxide in the Antarctic snowpack, Atmos. Chem. Phys., 10, 2439-2456, 10.5194/acp-10-2439-2010,

Fuchs, H., Ball, S. M., Bohn, B., Brauers, T., Cohen, R. C., Dorn, H. P., Dubé, W. P., Fry, J. L., Häseler, R., Heitmann, U., Jones, R. L., Kleffmann, J., Mentel, T.

F., Musgen, P., Rohrer, F., Rollins, A. W., Ruth, A. A., Kiendler-Scharr, A., Schlosser, E., Shillings, A. J. L., Tillmann, R., Varma, R. M., Venables, D. S., Tapia, G. V., Wahner, A., Wegener, R., Wooldridge, P. J., and Brown, S. S.: Intercomparison of measurements of NO_2 concentrations in the atmosphere simulation chamber SAPHIR during the NO_3 Comp campaign, Atmos. Meas. Tech., 3, 21-37, 2010.

Himmelmann, S., Orphal, J., Bovensmann, H., Richter, A., LadstatterWeissenmayer, A., and Burrows, J. P.: First observation of the OIO molecule by time-resolved flash photolysis absorption spectroscopy, Chem. Phys. Lett., 251, 330-334, 1996.

Hoffmann, T., O'Dowd, C. D., and Seinfeld, J. H.: Iodine oxide homogeneous nucleation: An explanation for coastal new particle production, Geophys. Res. Lett., 28, 1949-1952, 2001.

Küpper, F. C., Carpenter, L. J., McFiggans, G. B., Palmer, C. J., Waite, T. J., Boneberg, E.-M., Woitsch, S., Weiller, M., Abela, R., Grolimund, D., Potin, P., Butler, A., Luther, G. W., Kroneck, P. M. H., Meyer-Klaucke, W., and Feiters, M. C.: Iodide accumulation provides kelp with an inorganic antioxidant impacting atmospheric chemistry, Proceedings of the National Academy of Sciences, 105, 6954-6958, 10.1073/pnas.0709959105, 2008.

Leser, H., Honninger, G., and Platt, U.: MAX-DOAS measurements of BrO and NO_2 in the marine boundary layer, Geophys. Res. Lett., 30, DOI: 10.1029/2002GL015811, 2003.

McFiggans, G., Coe, H., Burgess, R., Allan, J., Cubison, M., Alfarra, M. R., Saunders, R., Saiz-Lopez, A., Plane, J. M. C., Wevill, D. J., Carpenter, L. J., Rickard, A. R., and Monks, P. S.: Direct evidence for coastal iodine particles from Laminaria macroalgae - linkage to emissions of molecular iodine, Atmos. Chem. Phys., 4, 701-713, 2004.

Molina, M. J., and Rowland, F. S.: Stratospheric Sink for Chlorofluoromethanes -

Chlorine Atomic-Catalysed Destruction of Ozone, Nature, 249, 810-812, 1974.

O'Dowd, C. D., and Hoffmann, T.: Coastal new particle formation: A review of the current state-of-the-art, Environ. Chem, 2, 245-255, 10.1071/en05077, 2005.

Palmer, C. J., Anders, T. L., Carpenter, L. J., Kupper, F. C., and McFiggans, G. B.: Iodine and halocarbon response of *Laminaria digitata* to oxidative stress and links to atmospheric new particle production, Environ. Chem, 2, 282-290, 10.1071/en05078, 2005.

Piot, M., and von Glasow, R.: The potential importance of frost flowers, recycling on snow, and open leads for ozone depletion events, Atmos. Chem. Phys., 8, 2437-2467, 2008.

Pirjola, L., O'Dowd, C. D., Yoon, Y. J., and Sellegri, K.: Modelling iodine particle formation and growth from seaweed in a chamber, Environ. Chem, 2, 271-281, 10.1071/en05075, 2005.

Plane, J. M. C., Saunders, R. W., Kumar, R., Martin, J. C. G., Mahajan, A. S., and Murray, B. J.: Studies of the Formation and Growth of Aerosol from Molecular Iodine Precursor, Zeitschrift Fur Physikalische Chemie-International Journal of Research in Physical Chemistry & Chemical Physics, 224, 1095-1117, 2010.

Saiz-Lopez, A., and Plane, J. M. C.: Novel iodine chemistry in the marine boundary layer, Geophys. Res. Lett., 31, 2004.

Saiz-Lopez, A., Plane, J. M. C., and Shillito, J. A.: Bromine oxide in the mid-latitude marine boundary layer, Geophys. Res. Lett., 31, DOI: 10.1029/2003GL018956, 2004.

Saiz-Lopez, A., Shillito, J. A., Coe, H., and Plane, J. M. C.: Measurements and modelling of I_2, IO, OIO, BrO and NO_3 in the mid-latitude marine boundary layer, Atmos. Chem. Phys., 6, 1513-1528, 2006.

Simpson, W. R., von Glasow, R., Riedel, K., Anderson, P., Ariya, P., Bottenheim, J., Burrows, J., Carpenter, L. J., Friess, U., Goodsite, M. E., Heard, D., Hutterli, M., Jacobi, H. W., Kaleschke, L., Neff, B., Plane, J., Platt, U., Richter, A., Roscoe, H., Sander, R., Shepson, P., Sodeau, J., Steffen, A., Wagner, T., and Wolff, E.: Halogens and their role in polar boundary-layer ozone depletion, Atmos. Chem. Phys., 7, 4375-4418, 2007.

Spietz, P., Martin, J. C. G., and Burrows, J. P.: Spectroscopic studies of the I_2/O_3 photochemistry - Part 2. Improved spectra of iodine oxides and analysis of the IO absorption spectrum, J. Photochem. Photobiol. A, 176, 50-67, 2005.

Tuckermann, M., Ackermann, R., Golz, C., LorenzenSchmidt, H., Senne, T., Stutz, J., Trost, B., Unold, W., and Platt, U.: DOAS-observation of halogen radical-catalysed arctic boundary layer ozone destruction during the ARCTOC-campaigns 1995 and 1996 in Ny-Alesund, Spitsbergen, Tellus B, 49, 533-555, 1997.

Usher, C. R., Michel, A. E., and Grassian, V. H.: Reactions on mineral dust, Chem. Rev., 103, 4883-4939, 10.1021/cr020657y, 2003.

Varma, R. M., Venables, D. S., Ruth, A. A., Heitmann, U., Schlosser, E., and Dixneuf, S.: Long optical cavities for open-path monitoring of atmospheric trace gases and aerosol extinction, Appl. Opt., 48, B159-B171, 2009.

Vogt, R., Sander, R., Von Glasow, R., and Crutzen, P. J.: Iodine chemistry and its role in halogen activation and ozone loss in the marine boundary layer: A model study, J. Atmos. Chem., 32, 375-395, 1999.

von Glasow, R., von Kuhlmann, R., Lawrence, M. G., Platt, U., and Crutzen, P. J.: Impact of reactive bromine chemistry in the troposphere, Atmos. Chem. Phys., 4, 2481-2497, 2004.

Chapter 5

SIMULATION CHAMBER MEASUREMENTS

5.1 Introduction

The application of incoherent broadband cavity-enhanced absorption spectroscopy (IBBCEAS) to flow tube measurement of weak absorptions was presented in Chapter 3. A good sensitivity of *ca*. 10^{-8} cm^{-1} was achieved in the near-ultraviolet. IBBCEAS may also be applied in simulation chambers, which have advantages over flow tubes configuration for certain types of experiments. Simulation chambers have low surface-to-volume ratios to minimize wall losses. Combined with the large volumes of typical chambers, this is advantageous for determining the absorption cross-sections of low volatility compounds. Owing to their low vapour pressures, these compounds are usually difficult to detect in the gas phase. Nevertheless, the gas phase spectra of many low vapour pressure compounds are important in atmospheric photochemistry modelling. The characteristics of simulation chambers are also suited to study the formation of secondary organic aerosol (SOA) and its subsequent aging over several hours. The large volume of such chambers allow the installation of several instruments, such as scanning mobility particle sizers (SMPS), to provide multiple measurements during each experiment. Simulation chambers also allow studies at concentrations more closely resembling those in the real atmosphere.

The IBBCEAS technique has previously been successfully applied to chamber studies of NO_3 and HONO (Venables et al., 2006;Gherman et al., 2008). A 20 m long cavity has been setup up in the SAPHIR atmospheric simulation chamber for a NO_3 measurement campaign (Varma et al., 2009). However, previous chamber work has not yet applied the IBBCEAS technique to recording reference spectra in the near-UV. In addition, the spectral ranges in prior IBBCEAS work have been relatively modest (usually less than 60 nm), whereas broader coverage would be

better suited to recording reference spectra.

The aims of the experiments carried out in the simulation chamber of the Centre for Research into Atmospheric Chemistry (CRAC) were the following. 1) To demonstrate the application of an IBBCEAS system with a very wide spectral range and to extend the range to the shortest wavelengths yet demonstrated. 2) To develop a robust and simple mirror calibration procedure in the chamber. 3) To record reference absorption cross-sections of several gas phase species, including those of several alkyl nitrites, benzaldehyde and several nitrophenols. 4) To carry out a preliminary investigation of the short-wavelength optical properties of anthropogenic and biogenic SOA.

5.2 Experimental

5.2.1 IBBCEAS chamber setup

The CRAC chamber comprised a cylindrically-shaped fluorine-ethene-propene (FEP) bag. It was surrounded by 36 UV-visible fluorescence lamps (Philips TUV and TL05) for photochemical experiments (Clifford et al., 2005;Thuner et al., 2004). The chamber was 4.1 m long with a diameter of 1.1 m, giving a volume of approximately 3.91 m^3. The chamber's surface-to-volume ratio was *ca*. 0.24 m. It was operated at atmospheric pressure and ambient laboratory temperature (*ca.* 21 ºC). Between experiments the chamber was flushed by dry clean air at 200 L min^{-1} for 3 to 12 hours.

The IBBCEAS instrument attached to the simulation chamber is shown schematically in Fig. 5.1. Two highly reflective mirrors (Layertec) with maximum reflectivity of 99.6% and 5 m radius of curvature were separated across the length of

the chamber. Mirrors were mounted in sealed flexible mounts that were attached to the walls of the chamber. The mirrors were purged with purified air at 0.5 L min^{-1} to keep the mirrors clean. Light from a 75 W arc Xe lamp was focussed into the centre of the optical cavity formed by the two high reflectivity mirrors. After passing the cavity, light was focussed into a Czerny-Turner spectrograph (Andor SR-303) with a 303 mm focal length and a 150 l/mm grating and 500 nm blaze. A back-illuminated CCD (Andor 420A-BU), optimized for the near-UV, was cooled to -40 ºC to reduce the dark current. Spectra were recorded with a 1 min integration time. Wavelength calibration was carried out using a HgAr calibration source (Ocean Optics) and had a 0.11 nm uncertainty when fitted by a second order polynomial function. This uncertainty is not unexpected given the broad spectral coverage from 200 to 800 nm. With the motorized slit set to 50 μm, the resolution of the instrument (FWHM) was *ca*. 2.2 nm based on the 365 nm mercury emission line. In an earlier study , the short-term fluctuations of the arc lamp was measured to be 0.1% (Chen and Venables, 2011). For the experiments in this chapter the lamp was near the end of its life and had a significantly higher dimming rate.

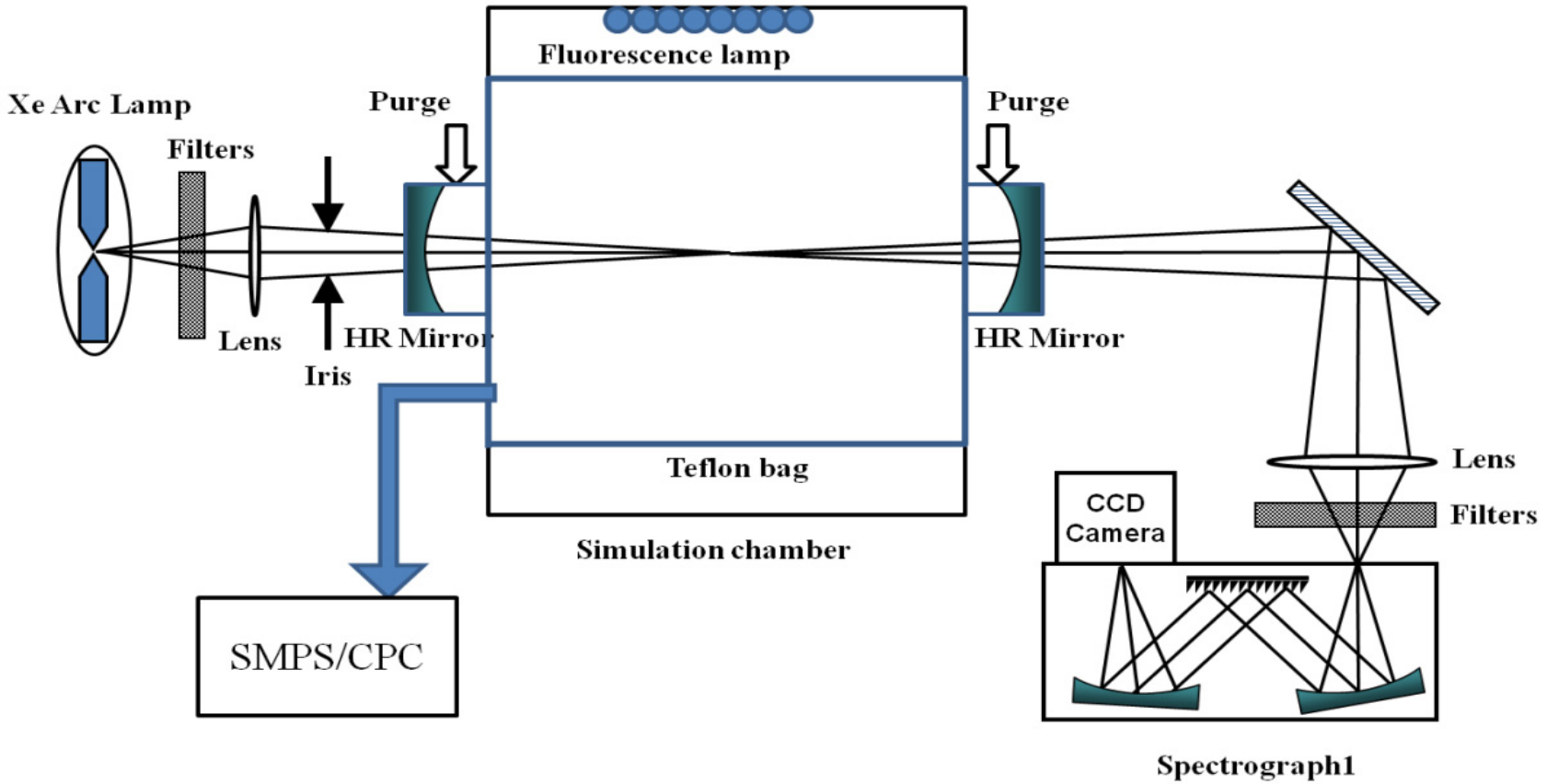


Figure 5.1 Schematic diagram of the IBBCEAS *in-situ* chamber setup.

As the high reflectivity range of the mirror acts as a band rejection filter, the broad Xe arc output must be filtered. A Schott BG 3 glass filter was used to filter the window from 315 to 445 nm to within the high reflectivity range of the cavity mirrors. Another BG 40 short pass filter removed wavelengths longer than 715 nm. However, the transmission of the BG40 filter falls off quickly below 335 nm, reducing the measured intensity at short wavelengths. As the BG3 filter is still partially transmitting above 450 nm, the detector saturated from about 460 to 500 nm. The effect of filters on the cavity intensity is shown in Fig. 5.2. For the SOA experiment a TSI scanning mobility particle sizer (SMPS) with a condensation particle counter (CPC) was used to measure the particle size distribution. The SMPS sampled chamber air at 1 L min^{-1}. The particle size range of the SMPS extended from 10 to 500 nm.

Samples of 2-nitrophenol (Fluka 99%), 3-methyl-2-nitrophenol (Fluka 99%), 4-methyl-2-nitrophenol (Fluka 99%), Benzaldehyde (Aldrich 99%) T-butyl nitrite (Aldrich 90%), Isobutyl nitrite (Aldrich 95%), Butyl nitrite (Aldrich 95%), and Iso-pentyl nitrite (Aldrich 96%) were used as received. Weighed samples were introduced into the chamber via an impinger connected to a stream of purified compressed air. The samples were volatilized into the air stream by gentle heating with a heat gun. Depending on the volatility of the compound, the heating took place over a period of a few minutes.

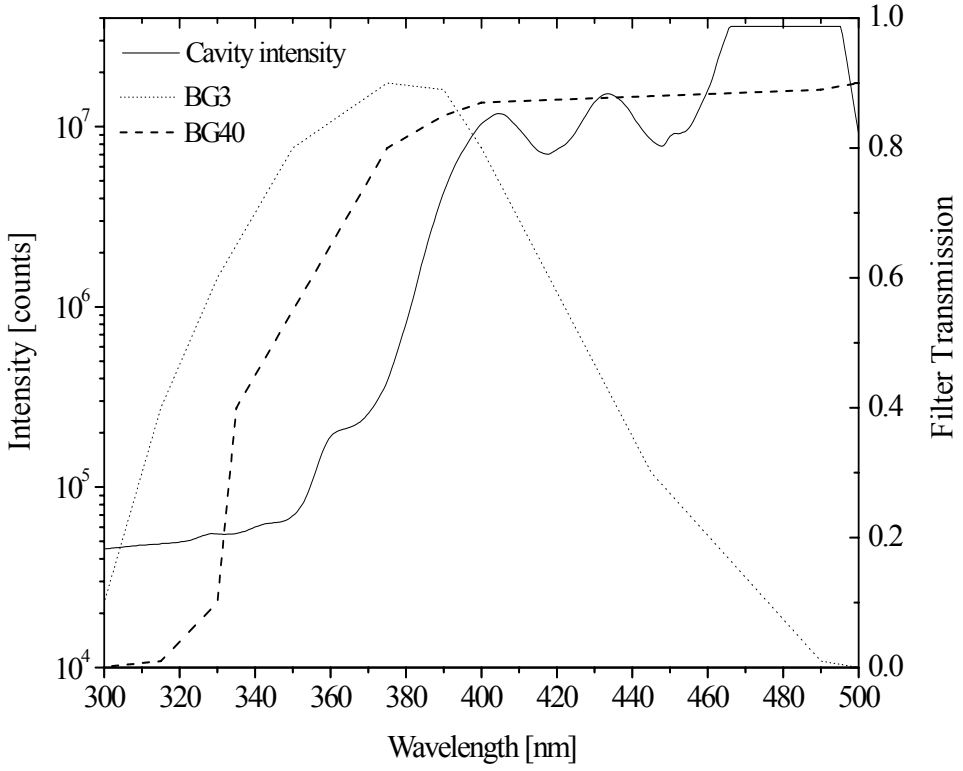


Figure 5.2 Cavity intensity (solid line) of the IBBCEAS chamber system and transmission of the BG3 (dash dot) and BG40 (dot) filters. The intensity around 300 nm represents the background signal level.

5.2.2 Instrument Calibration

The extinction (or absorption) spectrum of a sample in the cavity is given by:(Fiedler et al., 2003)

$$\varepsilon(\lambda) = \sum_i \sigma_i(\lambda) \cdot n_i / V = \frac{1}{d}\left(\frac{I_0(\lambda)}{I(\lambda)} - 1\right)\left(1 - R(\lambda)\right) \quad (5.1)$$

where I and I_0 are respectively the intensities transmitted through the optical cavity in the presence and absence of an absorber, d is the distance between the cavity mirrors, R is the mirror reflectivity, and σ_i (cm^2 $molecule^{-1}$) and n_i (molecules) are

the absolute absorption cross section and molecules of species *i*. *V* (cm^{-3}) is the volume of the chamber.

Because the FEP bag was flexible and subject to significant pressure fluctuations during purging, the chamber volume was slightly variable from experiment to experiment. Furthermore, the path length through the actual sample was affected by the slow purge of the cavity mirror. Therefore, instead of directly calibrating the reflectivity *R(λ)*, the overall system response to a given number of absorbing molecules in the chamber was calibrated. This was done in a two step process by first using NO_2 for a relative calibration and then determining an absolute value by reference to the absorption of MVK.

NO_2, a broadband absorbing gas, was used to obtain the broad overall shape of the mirror transmission spectrum:

$$K_{NO2}(\lambda) = \sigma_{NO_2}(\lambda) \cdot n_{NO_2} \Big/ \left(\frac{I_0(\lambda)}{I(\lambda)} - 1 \right) = \frac{V}{d}\left(1 - R(\lambda)\right) \quad (5.2)$$

As shown in Fig. 5.3.b, the $K_{NO2}(\lambda)$ curve extends from 320 to 450 nm covering most of the near-UV and part of the visible spectrum. The reflectivity curve demonstrates a usable 130 nm band which is about twice that of previous IBBCEAS applications (Table 2.1). Unlike most optical cavity mirrors which have a relatively flat transmission minimum over the short range of high reflectivity, the transmission spectrum of the cavity mirrors has significant undulations. These are in good agreement with the manufacturer's scaled transmission spectra of the mirrors. Although these structures in the mirror spectrum are readily apparent in Fig. 5.3.a, no evidence was found that these features led to artefacts in the spectra reported below.

Although NO_2 provides a suitably broad absorption for calibrating the system, without an accurate measurement of the NO_2 concentration, the calibration is only a relative one. Unfortunately, during the experiment reported here, the chamber chemiluminescence NO_x detector was not working. Therefore, the absorption of a known mass of methyl vinyl ketone (MVK) was used to establish the absolute calibration (Eq. 5.2). MVK has several advantages: (a) it has a broad absorption below 390 nm (Gierczak et al., 1997); (b) the strength of the absorption cross-section is moderate (*ca*. 7×10^{-20} $cm^2 molecule^{-1}$) and suitable for calibrating the IBBCEAS instrument; and (c) MVK is relatively stable and easily added into the chamber.

The linearity of the instrument response to the MVK absorption was first tested (Fig. 5.3.a). Masses of 4, 9, 15, 22, 32, and 41 mg of MVK were weighted into a glass impinger. N_2 was used as a carrier gas to introduce the sample into the chamber. The corresponding absorption of MVK showed good linearity from 340 to 370 nm ($R^2 > 0.997$). The small positive offset of the regression probably arose from slight dimming of the lamp, particularly at short wavelengths. The MVK absorption at 360 nm was chosen to establish the absolute calibration based on the Gierczak cross-sections (Gierczak et al., 1997). The difference between literature cross-sections at 360 nm is 5% and overall agreed to within 10% (Gierczak et al., 1997;Barker, 1995). With a 0.1% uncertainty in the mass measurement, the uncertainty of calibration is therefore around 5%.

The rest of the spectral calibration was relative to the 360 nm value and was scaled accordingly:

$$K(\lambda) = K_{NO_2}(\lambda) \cdot K_{MVK}(\lambda_{360}) / K_{NO_2}(\lambda_{360}) \qquad (5.3)$$

A small mass of MVK (typically 15 mg) was introduced for calibration before each experiment to provide a daily calibration of the system.

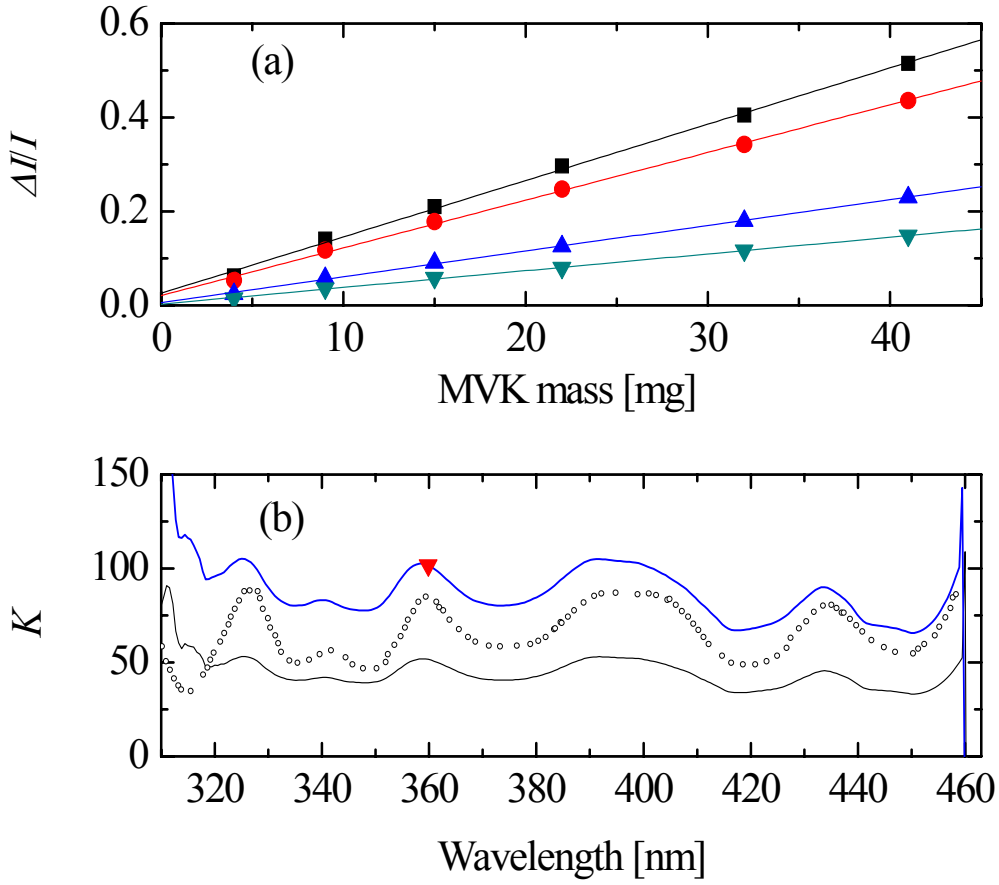


Figure 5.3 Calibration of the IBBCEAS simulation chamber instrument (a) Fractional absorption of MVK at 340 nm (black squares), 350 nm (red dots), 360 nm (blue triangles) and 370 nm (cyan triangles); linear regressions are also shown (R^2_{340nm}= 0.9976, R^2_{350nm}= 0.9982, R^2_{360nm}= 0.9988, R^2_{370nm}= 0.9989; y-intercepts are 0.026 at 340 nm, 0.020 at 350 nm, 0.006 at 360 nm and 0.003 at 370 nm). (b) The relative calibration from 320 to 450 nm using NO_2 (black line), and the absolute calibration at 360 nm after scaling to the reflectivity obtained from MVK (red triangle). The final scaled calibration is shown (blue line) along with the scaled transmission from the manufacturer's data (black dots).

5.2.3 Standard addition method

The long purge time of the atmosphere simulation chamber – a minimum of several hours – imposed practical constraints on using the chamber for recording spectra. However, if the absorption is monitored continuously and no rapid changes occur in the absorption of the sample (such as rapid deposition to chamber surfaces or reactions within the chamber), it is possible to carry out multiple absorption measurements per experiment in the chamber using a variation of the standard addition method.

In practice, the intensity reduction observed after several analyte injections will be nonlinear. Earlier studies (Platt et al., 2009) have shown that the effective path length of the spectrometer is related to the concentration of the absorbing species. We therefore quantified the extinction based on the difference in intensity between before and after each addition of the sample. Consider the time-dependent absorption coefficient of the sample in the chamber:

$$\alpha(t)=\left(\frac{I_0\text{-}I(t)}{I(t)}\right)\left(\frac{1\text{-}R}{L}\right) \tag{5.4}$$

where I_0 is the intensity transmitted through the clean chamber. Adding an absorbing compound to the chamber changes the overall sample absorption, and we define $\Delta\alpha$ as the difference between the sample absorption before (α_{OLD}) and after (α_{NEW}) addition of the absorber:

$$\Delta\alpha = \alpha_{NEW}\text{-}\alpha_{OLD} \tag{5.5}$$

If I_{OLD} and I_{NEW} are the corresponding intensities measured before and after addition of sample, the change in absorption associated with the addition of sample is readily determined:

$$\Delta\alpha = \left[\left(\frac{I_0 - I_{NEW}}{I_{NEW}}\right) - \left(\frac{I_0 - I_{OLD}}{I_{OLD}}\right)\right]\left(\frac{1-R}{L}\right) = \left[\frac{I_0}{I_{NEW}} - \frac{I_0}{I_{OLD}}\right]\left(\frac{1-R}{L}\right)$$

It is necessary that I_0 must reasonably approximate the transmitted intensity of the clean chamber at the time of both measurements, implying that normalisation is needed if the lamp output varies with time.

5.3 Gas phase spectra

5.3.1 Benzaldehyde

Benzaldehyde is released during the manufacture of pesticides and from plants. It is also formed during the OH-initiated oxidation of anthropogenic species such as toluene, xylenes and trimethylbenzenes (Klotz et al., 1998;Smith et al., 1998;Clifford et al., 2005). Its structured absorption between 320 and 360 nm arises from a dipole forbidden *n*-π* electronic transition of the carbonyl group. Determining the atmospheric photolysis rates from the near-UV absorption cross-section of these compounds is important. In addition, the absorption cross-section is required for *in-situ* detection of these species in the atmosphere based on absorption spectroscopy (Trost et al., 1997;Etzkorn et al., 1999). The UV absorption spectra of benzaldehyde have been determined previously by different groups and literature spectrum from 300 to 400 nm agree to within 45% (Etzkorn et al., 1999;Trost et al., 1997;Xiang et al., 2009;Zhu and Cronin, 2000;Noziere et al., 1994;Thiault et al., 2004).

The absorption spectrum of benzaldehyde was recorded for benzaldehyde masses of 3.8, 5.7, 8.8, and 12.6 mg introduced into the chamber, where each addition corresponded to approximate concentration increases of 0.22, 0.34, 0.52, and 0.74 ppm in the chamber. As with the MVK calibration of the mirror reflectivity

spectrum, the absorption of benzaldehyde increased linearly with the total amount of benzaldehyde in the chamber. The absorption cross-section of benzaldehyde recorded in the chamber is shown in Fig. 5.4. The absorption extends to around 380 nm and several diffuse bands with maxima at 339 nm (29.5×10^3 cm^{-1}), 354 nm (28.3×10^3 cm^{-1}), and 371 nm (27.0×10^3 cm^{-1}) are apparent in the spectrum and in good agreement with earlier high resolution studies.(Ohmori et al., 1988;Imanishi et al., 1952) These features are separated by 1250 to 1300 cm^{-1} and form part of a vibrational progression of the excited state carbonyl stretching mode.(Ohmori et al., 1988) A small offset of about 3×10^{-21} cm^2 $molecule^{-1}$ is visible in our spectrum beyond 380 nm and probably arises from lamp dimming. The absorption cross-section was extended into the visible in these measurements. The standard deviation varied depending on wavelength: it was about 2.4×10^{-22} cm^{-2} at 320 nm, 2.1×10^{-21} cm^{-2} at 340 nm, 7.7×10^{-22} cm^{-2} at 370 nm and 5.4×10^{-22} cm^{-2} at 380 nm. The uncertainty of the (1-*R*) value is 6%, that of the lamp intensity fluctuation is about 1%, and with a 5% standard deviation between measured values, the overall uncertainty in the absorption cross-section is about 8%.

The chamber spectrum is in broad agreement with the spectra of Thiault et al. and Xiang et al., also shown in Fig. 5.4 (Xiang et al., 2009;Thiault et al., 2004). Thiault et al. used an elevated temperature and multipath cell arrangement to record spectra of benzaldehyde and tolualdehyde from 252 to 368 nm. In contrast, Xiang and co-workers used a cavity ringdown system in a vacuum cell to record spectra from 285 to 400 nm at 5 nm intervals. The results of these studies agree fairly well below 340 nm (within 5%), but the spectra diverge significantly at longer wavelengths.

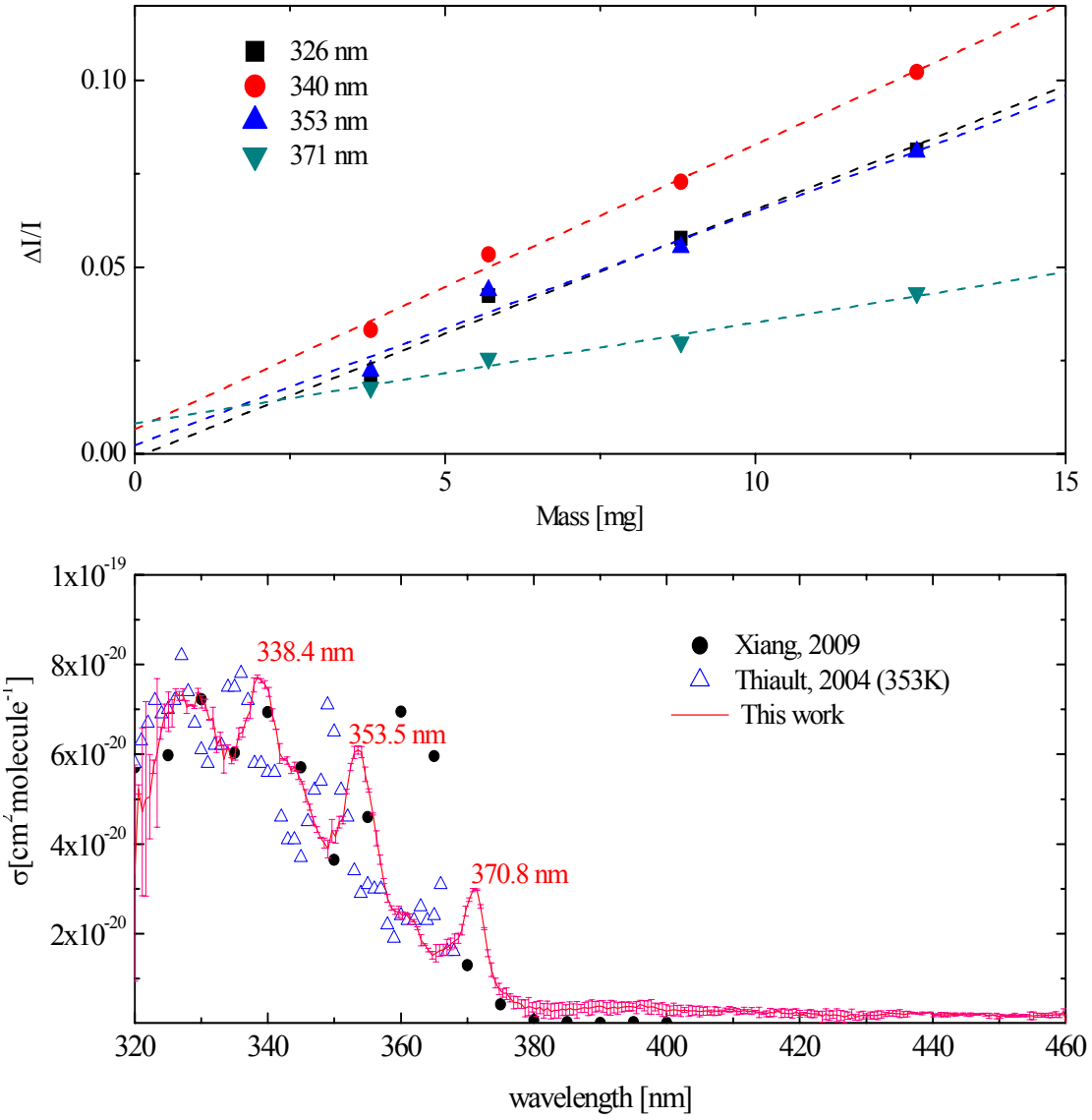


Figure 5.4 Top: Changes in the fractional absorption with increasing mass of benzaldehyde. Bottom: The benzaldehyde absorption cross-section and associated variation between different additions (error bars). Literature spectra covering the near-UV are also shown.

The spectrum of Thiault et al. has a similar magnitude and structure to that reported here; they also observed additional fine structure that our system could not resolve. Surprisingly, however, the spectra appear to be shifted about 4 nm relative to each

other, with our spectrum found at longer wavelengths. The reason for the apparent shift in wavelength is unclear. But, as the wavelength calibration was checked both at the start of the experiment (HgNe calibration lamp) and against the convoluted NO_2 absorption at the end of the experiment, we are confident that our wavelength calibration is accurate. Thiault and co-workers observed no significant temperature dependence of the spectra (303–363K), nor did they see any concentration dependence to suggest formation of dimers. We also rule out dimer formation in our experiments based on the significantly lower concentrations compared to their work (up to 1052 ppm, 0.8 Torr) and the absence of any deviation from linearity with increasing concentration. We conclude that Thiault wavelength scale is incorrect.

Xiang et al. determined absorption cross-sections every 5 nm using a cavity ring-down approach at low pressures. Fine structure is thus precluded from their spectrum. Their reported absorption cross-sections are similar in magnitude to our values below 360 nm and from 375 nm and above. Three points from their spectrum between 360 and 370 nm are two to three times larger than either our results or those of Thiault and co-workers. The reason for this divergence between the spectra is unclear, but probably does not lie in the poorer signal-to-noise of the French groups as Xiang and co-workers suggest, because our results are quite similar to those of Thiault et al. We therefore suggest that either our spectrum or that of Thiault is better for estimating the photolysis rate of benzaldehyde in the atmosphere than those of Xiang et al. The slight difference between our spectra and literature spectra would only marginally affect the photolysis rate. This difference is relatively small: the integrated cross-sections of our work and the shifted Thiault spectrum are both ca. 10% lower than the cavity-ringdown spectrum of Xiang and colleagues and within the reported uncertainties of the three spectra. These minor

differences aside, we conclude that our broadband cavity approach across a simulation chamber produces results in generally good agreement with the literature.

5.3.2 Alkyl nitrites

Alkyl nitrites are volatile, photolabile compounds that have been the subject of many photochemical studies. These compounds are also of interest in air pollution and organic synthesis (Leighton., 1961). The main primary photochemical process for alkyl nitrites is fission to nitric oxide and an alkoxy radical, for which they are a convenient experimental source (Christie and Hetherington, 1976):

$$\text{R-O-N-O} + h\nu \rightarrow \text{R-O} + \text{NO} \qquad (5.7)$$

where the alkoxy radical is typically a precursor to PAN formation. Alkyl nitrites absorb strongly in the near-UV from the $n \rightarrow \pi^*$ transition associated with the lone-pair of the nitrite oxygen. The band structure arises from the N-O vibrational stretch and has a separation of about 1100 cm^{-1} between the two lowest vibrational levels of the excited state.

Although the above information on the alkyl nitrite spectra has been established for several decades, and the photophysics of these compounds have been the subject of long-standing attention (Raff and Finlayson-Pitts, 2010), there is nevertheless a surprising absence of high quality absorption cross-sections for these species. Indeed, the standard reference spectra of methyl nitrite and t-butyl nitrite are those from the Calvert and Pitts text (McMillan, 1962;Taylor et al., 1980;Calvert and Pitts, 1966) and much less work has focussed on other butyl or larger alkyl nitrites. As reaction 5.7 is useful in simulation chamber studies, high quality reference spectra of these species would be valuable in experiments where the spectrum is also being monitored. In this context, revisiting the near-UV cross-sections of these species is

warranted. Such a survey also serves as an additional test of the chamber spectrometer for volatile species and for those with structured absorption spectra. In the following we report the absorption cross-sections of the two primary nitrites (n-butyl nitrite and iso-pentyl nitrite), one secondary nitrite (isobutyl nitrite), and the tertiary nitrite t-butyl nitrite.

T-butyl nitrite, isobutyl nitrite, butyl nitrite and iso-pentyl nitrite were measured in the chamber. Absorption cross-sections from 320 to 450 nm were determined from single additions of each compound. The absorption cross-sections are shown in Fig. 5.5, where diffuse vibrational bands are apparent below 410 nm (Thompson and Dainton, 1937). The mass of alkyl nitrites injected into chamber and the peak positions of these alkyl nitrites is listed in Table 5.1. There is only one absorption cross-section spectrum of t-butyl nitrite in the literature (McMillan, 1962) which is in agreement with our spectrum. The magnitude of our absorption cross-section is larger than that of McMillan et al. which may be due to a slight offset apparent in our spectrum. This difference is relatively small, however, and comparable to the overall uncertainty in the measurement of about 10%. The absorption of isobutyl nitrite, n-butyl nitrite, and isopentyl nitrites have very similar peak positions (Table 5.1), whereas t-butyl nitrite is red-shifted by about 12 nm compared to the other spectra. It is probably as a result of steric effects.

Table 5.1 Alkyl nitrite mass and peak positions

Compound	Mass [mg]	Concentration[ppm]	Peak positions [nm]
Tert-butyl nitrite	12.5	0.75	339.4, 351.7, 365.7, 380.8, 398.1
Isobutyl-nitrite	12.1	0.71	331.6, 342.2, 354.5, 368.5,(384.1)
Butyl-nitrite	12.1	0.71	331.6, 342.8, 354.5, 369.0,(384.6)
Isopentyl-nitrite	14.0	0.74	332.1, 342.8, 355.1, 369.0,(383.5)

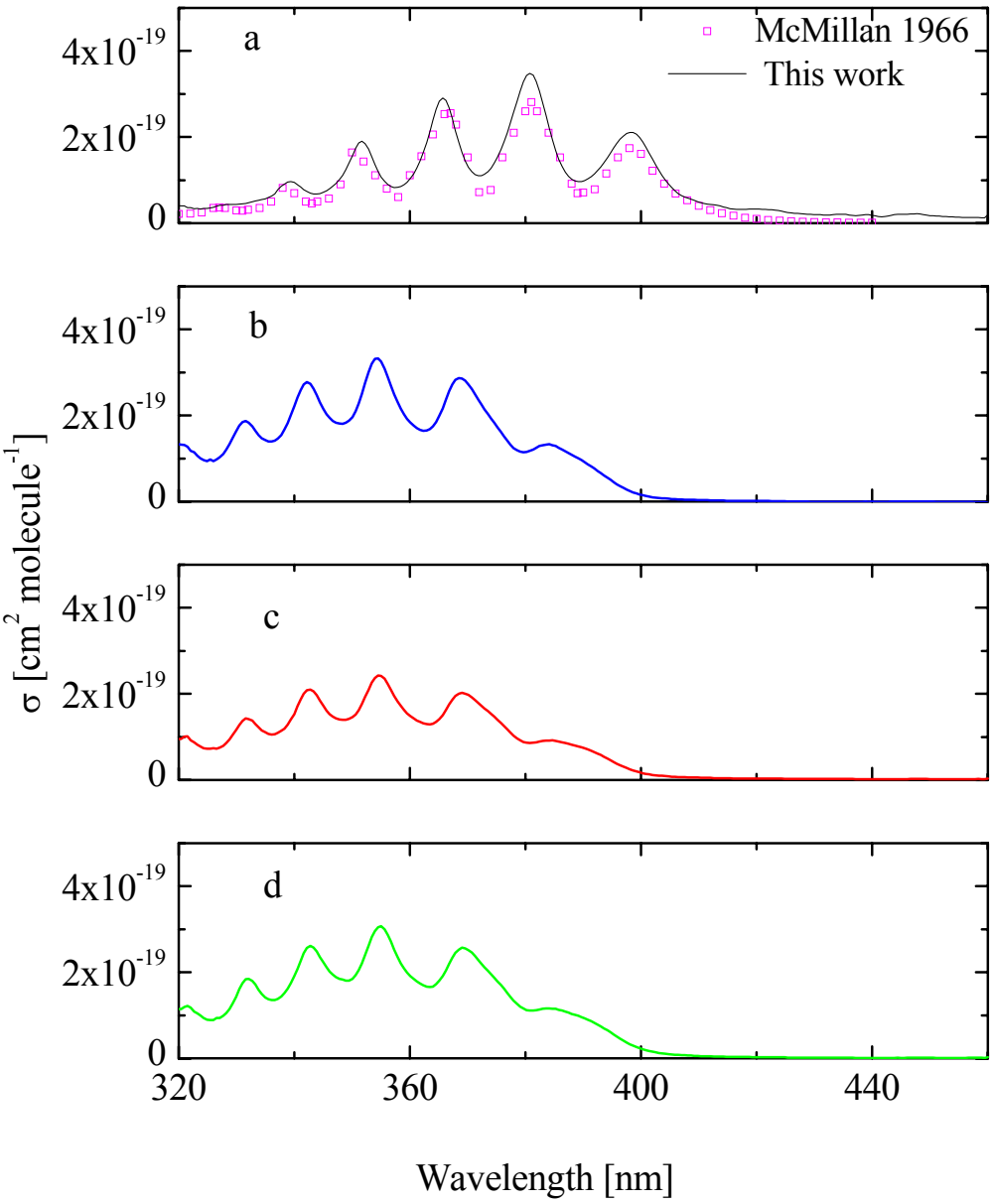


Figure 5.5 Absorption cross-sections of some alkyl nitrites from 320 to 460 nm (a) tert-butyl nitrite (this work in black line) with the McMillan 1966 spectrum (in pink squares) (b) iso-butyl nitrite (c) butyl nitrite (d) iso-pentyl nitrite.

5.3.3 Nitrophenol and methyl nitrophenol spectra

Nitrophenols are directly emitted to the atmosphere from vehicle emissions;(Tremp et al., 1993) they are also formed from tropospheric reactions of mono-aromatic compounds with the hydroxyl radical, OH, and nitrogen oxides. The photochemistry of nitrophenol has recently received much attention, particularly since the formation of nitrous acid (HONO) and the nitrite ion has been observed during the photolysis of nitrophenols in the gas phase (Bejan et al., 2006), liquid phase (Harrison et al., 2005;Ishag and Moseley, 1977;Alif et al., 1991) and in ice (Dubowski and Hoffmann, 2000).

Nitrophenols absorb strongly in the near-UV range, (Harrison et al., 2005;Ishag and Moseley, 1977;Alif et al., 1991) corresponding to the π (benzene ring) $\rightarrow \pi^*$ (nitro group) transition (Wang et al., 2006). Despite interest in their photochemistry, no near-UV gas phase absorption cross-sections have been reported. Here the near-UV gas phase absorption cross-sections of 2-nitrophenol (2NP), 3-methyl-2-nitrophenol (3M2NP), 4-methyl-2-nitrophenol (4M2NP) and 3-nitrophenol (3NP) are reported. Although photolysis rates have been measured in atmosphere simulation chamber experiments, the quantum efficiencies of photolysis have only been estimated from solution spectra. On the basis of gas phase spectra, we report an average quantum efficiency for photolysis to HONO.

2NP was introduced stepwise into the chamber. The time-varying intensity at 340 nm is shown in Fig. 5.6, where successive additions of the absorbing sample are evident as stepwise drops in the intensity. The quantities added to the chamber correspond to increases in the mixing ratio of 9, 18, 27, and 36 ppbV respectively. The transmitted intensity drops by over 50% at 0.1 ppmV of 2NP. The intensity

stabilises within a minute or two of adding the sample. From the observed intensity before adding any sample to the chamber, there is a linear dimming of the lamp. A linear fit was applied to normalize the intensity (dashed line in Fig 5.6). Note that the normalization is wavelength-dependent and that the lamp spectrum itself is gradually changing. The normalised intensity is relatively constant before the first addition, but losses to chamber surfaces are manifest as an increasingly positive slope as the concentration of 2NP increases. Each separate addition was used to calculate a spectrum of 2NP. As the measurement of $\Delta\alpha$ is taken shortly before and shortly after adding (within 2 min) the sample, minimal loss of sample to the walls is expected over this short period.

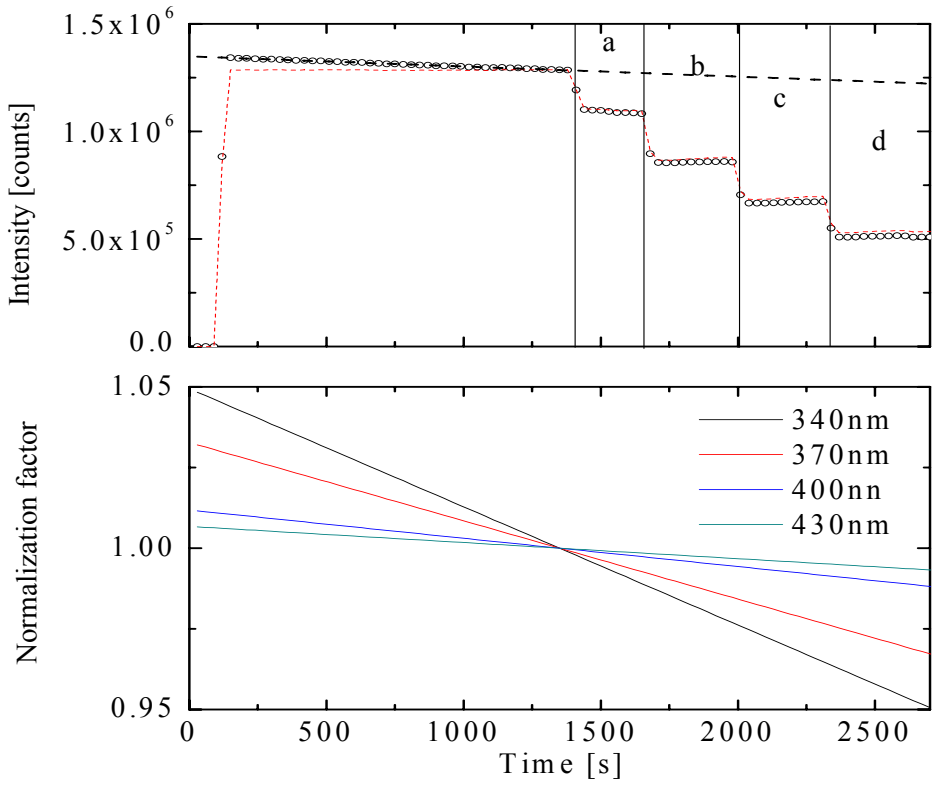


Figure 5.6 Top: The intensity at 340 nm as a function of time for several additions of 2-nitrophenol solution. Bottom: Normalization factors at 340 nm (black), 370 nm (red), 400 nm (blue) and 430 nm, (cyan) nm based on the fitted slope before 1350 s.

The absorption of nitrophenols increased linearly with the amount added in the chamber (Fig 5.7). 3M2NP was added into the chamber with increases in the mixing ratio of 4.1 ppbV, 8.2 ppbV, 12.4 ppbV, and 16.5 ppbV. 4M2NP was added into the chamber with increases in the mixing ratio of 4.3 ppbV, 8.6 ppbV, 12.8 ppbV, and 17.1 ppbV.

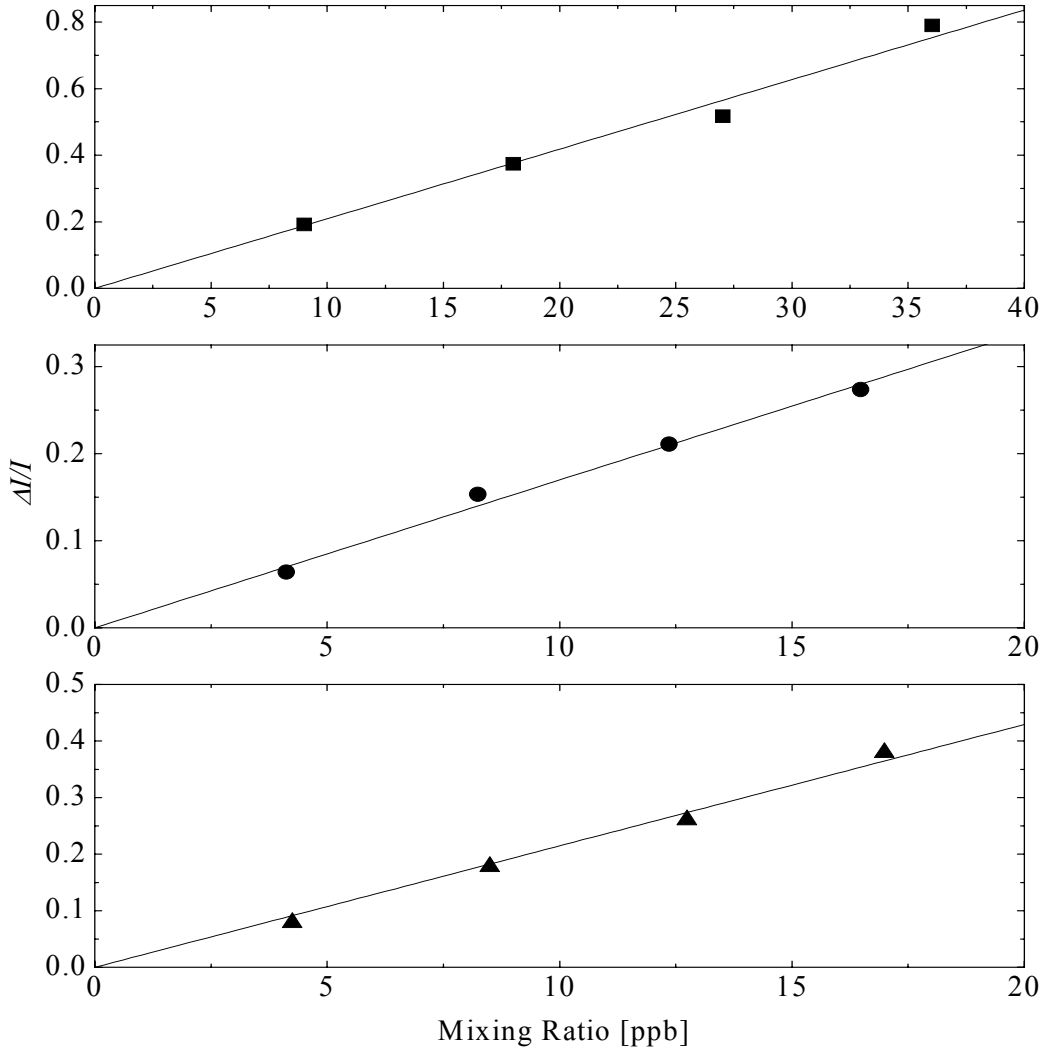


Figure 5.7 Linearity of the absorption with the nitrophenol concentration in the chamber. Top: 2-nitrophenol absorption at 335 nm. Middle: 3-methyl-2-nitrophenol absorption at 337 nm. Bottom: 4-methyl-2-nitrophenol absorption at 345 nm.

The spectrum obtained from averaging each of the four individual additions of 2NP is shown in Fig. 5.8(a): The standard deviation of the four spectra is ±5% at the absorption maxima. The absorption peaks at 335 nm with a very large absorption cross-section of 1.8×10^{-17} cm^2 $molecule^{-1}$. The absorption band has an apparent half-width of around 40 nm and the long wavelength tail extends to around 390 nm. The short-wavelength limit of the spectrum extends slightly beyond the peak maximum, where the absorption appears to fall more rapidly than at longer wavelengths.

Spectra of the 3- and 4- methyl-substituted isomers of 2-nitrophenol are also shown in Fig. 5.8(b) and (c). The peak of the absorption cross-section of 3M2NP was occurred at 339 nm and was about 8.9×10^{-18} cm^2 which is smaller than that of 2NP and shifted slightly to longer wavelengths by about 2 nm. The absorption band tail extended to about 420 nm. There is a standard deviation of about 6% at the absorption maximum of 339 nm for the measurements. The peak of 4M2NP of the absorption cross-section was at 345 nm (about 1.03×10^{-17} cm^2) and the absorption tail extended to 410 nm. There is a 5% standard deviation between the measurements at the peak.

These gas phase spectra are readily compared to the corresponding solution spectra, also shown in Fig. 5.8. The solution spectra were recorded in acetonitrile, although there little difference was observed between spectra in acetonitrile, methanol, or propanol (Bardini, 2006). The gas and solution spectra are broadly similar in shape and magnitude for 2NP. The maximum of the solution spectrum is red-shifted to 352 nm and the absorption tail also extends about 20 nm further into the visible. The peak of the 3M2NP solution spectrum was also red-shifted (to 356 nm) but without

much extension of the absorption tail. The peak of 4M2NP solution spectra occurred at 368 nm and was also red-shifted by 20 nm compared to the gas phase spectra. The solution spectra have comparable magnitudes to the gas phase spectra.

We also attempted to measure the absorption spectra of 3- and 4- nitrophenol. Sample handling was much more problematic for these compounds because their vapour pressures are markedly lower than that of 2-nitrophenol. The lower volatility of the 3- and 4-isomers stems from intermolecular hydrogen bonding, which is partially suppressed by the formation of an intra-molecular hydrogen bond in the case of 2-nitrophenol. Extensive, vigorous heating of the samples in the air stream resulted in some thermal decomposition and particle formation. Once in the chamber, these isomers also attached much more rapidly to the chamber walls. Nevertheless, we include a spectrum of 3-nitrophenol in Fig. 5.8.(c): given the uncertainties arising from sample handling, this spectrum should be regarded as indicative only. Referring to the solution spectra, the magnitude of the gas phase absorption was scaled to present the general shape of the spectrum. The gas phase 3NP spectrum is shifted to shorter wavelengths compared to the spectrum of 2NP. 4-nitrophenol was even less volatile than the 3-isomer and we were not able to determine an absorption spectrum with any certainty.

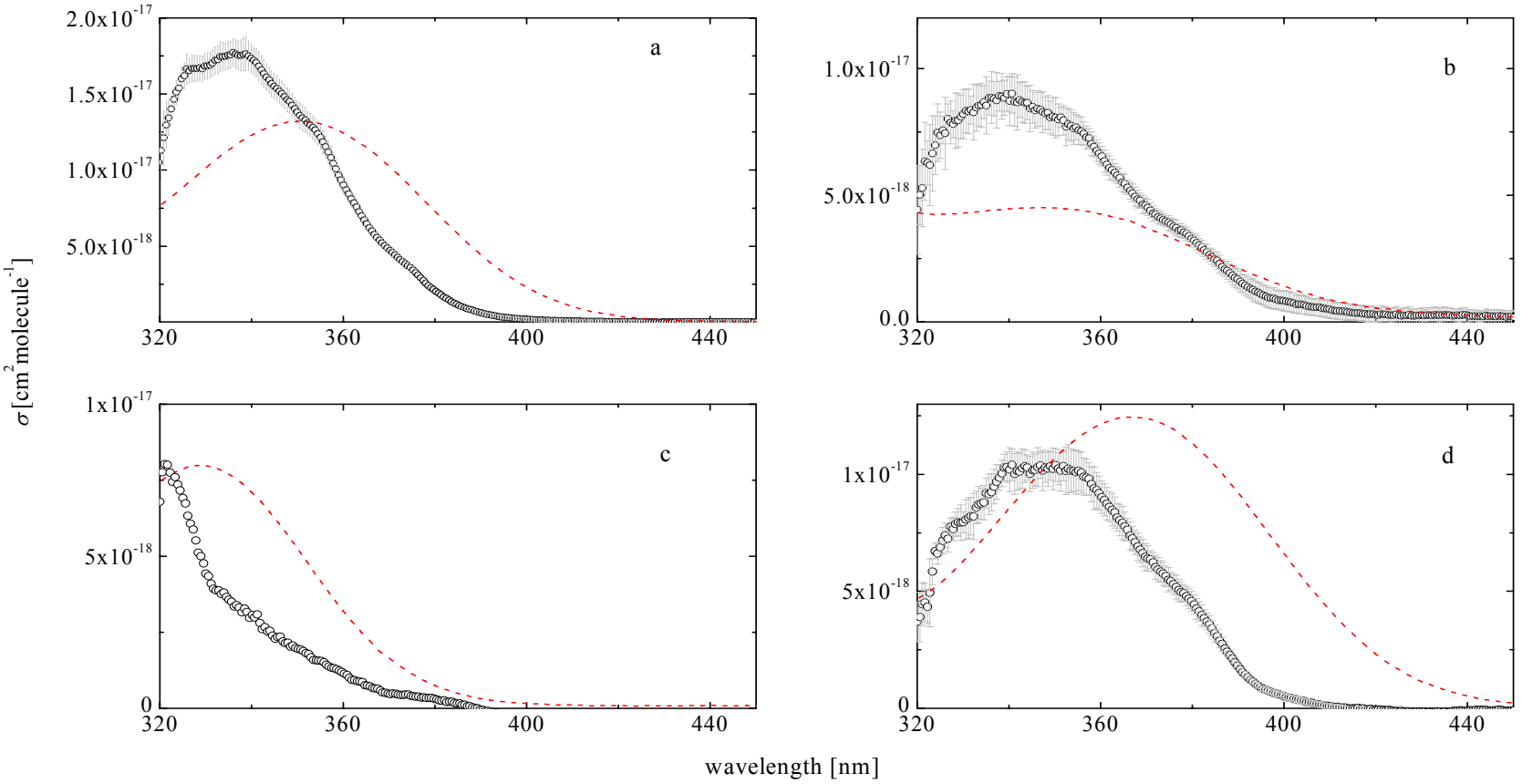


Figure 5.8 Nitrophenol absorption cross-sections in the gas phase (black cycle) with standard deviation (gray) and in acetonitrile solution (red dashes): a) 2-nitrophenol b) 3-methyl-2-nitrophenol c) 3-nitrophenol (arbitrarily scaled for the gas phase absorption) d) 4-methyl-2-nitrophenol.

5.3.4 Quantum yield of photolysis

The rate coefficient at which a species undergoes photolysis is evaluated by the following expression:

$$j = \int \sigma(\lambda)\Phi(\lambda)F(\lambda,\theta)d\lambda \qquad (5.8)$$

where j is the rate coefficient of photolysis, σ (λ) is the absorption cross-section, Φ (λ) is the quantum yield of the photolysis, and F (λ,θ) is the actinic flux.

As shown above, 2-nitrophenol and its methylated isomers have large absorption cross-sections in the near-UV. Photolysis is likely the dominant atmospheric loss process for the nitrophenols and is about 3 times faster than reaction with the OH radical (Bejan et al., 2007). Previous research showed that photolysis of 2-nitrophenol could be a new gas phase source of HONO (Bejan et al., 2006). Earlier work by the group has reported photolysis rates of 2NP ($0.63 \pm 0.03 \times 10^{-4}$ s^{-1}) in the EUPHORE (Bardini, 2006). The photolysis rate coefficient in the photoreactor was measured and scaled to be 7.1×10^{-4} $s^{-1}$of 3M2N and 3.8×10^{-4} of 4M2N for clear sky conditions (Bejan et al., 2007). The Bejan et al. study used the liquid phase absorption cross-sections as a proxy for the gas absorption to estimate an average quantum yield of $\Phi = 1.5 \times 10^{-4}$ for HONO formation.

The new absorption cross-sections allow the average photolysis quantum yield to be recalculated as $1.1\pm0.05\times10^{-4}$ for 2-nitrophenol, which is around 25% less than Bejan's earlier estimation. The actinic flux data are those of Madronich and reported in Finlayson-Pitts and Pitts (Finlayson-Pitts and Pitts, 2000) for the earth's surface as a function of zenith angle assuming a "best estimate" surface albedo. The quoted

photolysis rate *j* included a 2σ uncertainty, which was propagated to Φ. We note that the photolysis rates of 3M2NP and 4M2NP from Bejan et al. (Bejan et al., 2007) are larger than the measurements in the EUPHORE chamber by Bardini and that further work is required to more accurately measure the photolysis rate. However, the estimation of the quantum yields under atmospheric actinic flux conditions depend on the precise atmospheric photolysis rates. Nevertheless, based on the estimation of the quantum yields, the photolysis rate at different solar zenith angles can be derived.

5.4 Optical properties of secondary organic aerosol

Optical cavities provide enormously enhanced sensitivity to atmospheric extinction and are particularly promising as they allow multiple absorbing species, as well as the aerosol extinction, to be retrieved in a single measurement. An approach has already been developed to retrieve the extinction based on changes in a known absorption feature (Varma et al., 2009) and has been practically demonstrated in the NO_3 intercomparison campaign in the SAPHIR chamber (Varma et al., 2009). The intercomparison of aerosol extinction measurement showed good agreement between optical cavity systems (Varma et al., In preparation 2011).

Isoprene (2-methyl-1,3-butadiene) is largely emitted from vegetation and is the most abundant non-methane volatile organic compound (VOC) emitted into the atmosphere. It comprises 34% to 51% of non-methane volatile organic compound emissions (Guenther et al., 1995). Because of its source strength and high reactivity to atmospheric oxidants (OH, O_3, and NO_3), isoprene play a major role in the chemistry of the troposphere and strongly influences tropospheric O_3 and aerosol burdens and distributions (Chameides et al., 1988;Thornton et al., 2002;Henze and

Seinfeld, 2006;Wu et al., 2007). Recent field studies have indicated the existence of isoprene oxidation products in ambient aerosol (Gómez-González et al., 2008;Surratt et al., 2008). Photochemical oxidation of isoprene has been shown in chamber studies to produce aerosol with small mass yields (1–3%) compared to yields from other biogenic VOC's (Kroll et al., 2005, 2006). Nevertheless owing to the source strength of isoprene, it is probably the single most significant source of secondary organic aerosol (SOA) on Earth. (Ng et al., 2008;Henze and Seinfeld, 2006;Zhang et al., 2007)

In a preliminary study, the ability of the IBBCEAS approach to measure the optical properties of SOA formed by early stage photochemical oxidation of isoprene by OH under high NO_x conditions was investigated. HONO and NO_2 were simultaneously measured by the IBBCEAS instrument, while a SMPS monitored the particle size distribution during the experiment After calibrating the mirror with MVK, 12 mg isoprene was then introduced into the chamber. HONO/NO/NO_2 was introduced into the chamber several minutes later. These compounds were produced by the reactions:

$$Na_2NO_2 + H_2SO_4 \rightarrow 2HONO + Na_2SO_4$$

$$HONO \rightarrow OH + NO$$

$$O_2 + 2\ OH \rightarrow 2HO_2$$

$$HO_2 + NO \rightarrow NO_2 + OH$$

30% sulfuric acid was added dropwise into a 1% sodium nitrite solution. HONO, NO and NO_2 were carried by a stream of N_2 to the chamber.

UV fluorescent lamps were turned on to initiate photochemical oxidation of isoprene shortly thereafter. The lamps were switched off after 2 hours and the chamber was flushed.

Assuming only two gaseous absorbers, NO_2 and HONO, the total concentrations of these compounds can be determined from least squares fitting:

$$\varepsilon\ (\lambda) = \sigma_{NO2}(\lambda) \cdot n_{NO2} + \sigma_{HONO}\ (\lambda) \cdot n_{HONO}\ + a + b \cdot \lambda \quad (5.13)$$

Absorption cross-sections of σ_{NO2} and σ_{HONO} were taken from the literature and convoluted to our spectrograph resolution (Voigt et al., 2002;Stutz et al., 2000).

Assuming a chamber volume of 3.91×10^3 L, the mixing ratios (ppb) of HONO and NO_2 were calculated and are shown in Fig. 5.9. The HONO concentration decreased from 830 to 270 ppb after turning on the lamps, whereas NO_2 increased from 980 to 1260 ppb as a result of photolysis of HONO and subsequent oxidation of NO. It then decreased to 275 ppb due to NO_2 photolysis, the oxidation chemistry of isoprene and wall losses. Particle formation was delayed by several minutes after initiating photooxidation, while the number concentration of particles increased rapidly between 45 and 60 min. As the particles continued to grow through coagulation and condensation processes, the number concentration then gradually decreased. The mean size of the aerosol grew from 10 nm (the lower limit of the SMPS) to 120 nm by the end of the experiment. The aerosol extinction at 354 nm increased as the particle grew to optically relevant sizes. However, this calculation of the aerosol extinction did not fully account for the molecular absorption of NO_2 and HONO, and the apparent rise after the addition of oxidants and after initiating photolysis is not real.

In previous studies, the retrieval of the aerosol extinction was based on a known absorption, such as the B-band of O_2 or the O_4 dimer (Varma et al., 2009;Thalman and Volkamer, 2010). It is also possible to calculate the aerosol extinction directly by subtracting the gaseous species absorption from the total extinction:

$$\varepsilon_{aerosol}(\lambda) = \varepsilon(\lambda) - \sigma_{NO2}(\lambda) \cdot n_{NO2} - \sigma_{HONO}(\lambda) \cdot n_{HONO} \quad (5.14)$$

In this approach, accurately accounting for molecular absorption is important, otherwise these molecular features will be observed in the retrieved aerosol extinction. The aerosol extinction spectrum was smoothed to remove residual features of the fit and was plotted for times 45, 55, 70, 115 min (Fig. 5.10). When the particle number concentration dramatically increased from 45 to 70 min, the short wavelength extinction increased more rapidly than that at longer wavelengths extinction which was relatively unchanged. Shorter wavelengths would be more sensitive to scattering by smaller particles. As time progressed and the mean size of the aerosol increased considerably, the aerosol extinction increased over the whole measurement range and cannot be ascribed merely to changes in the concentration of gaseous absorbers.

The correlation between the aerosol extinction at 354 nm and the mean size of the aerosol is shown in Fig. 5.11. Data were mostly from 45 min and later when the aerosol particles formed and grew. Two approximately linear ranges were observed between sizes of 20 to 55 nm and 55 to 110 nm. The early investigation thus showed the potential of the approach to monitor aerosol extinction in the near-UV, although some care will be necessary to remove molecular absorption features from the resulting extinction spectra.

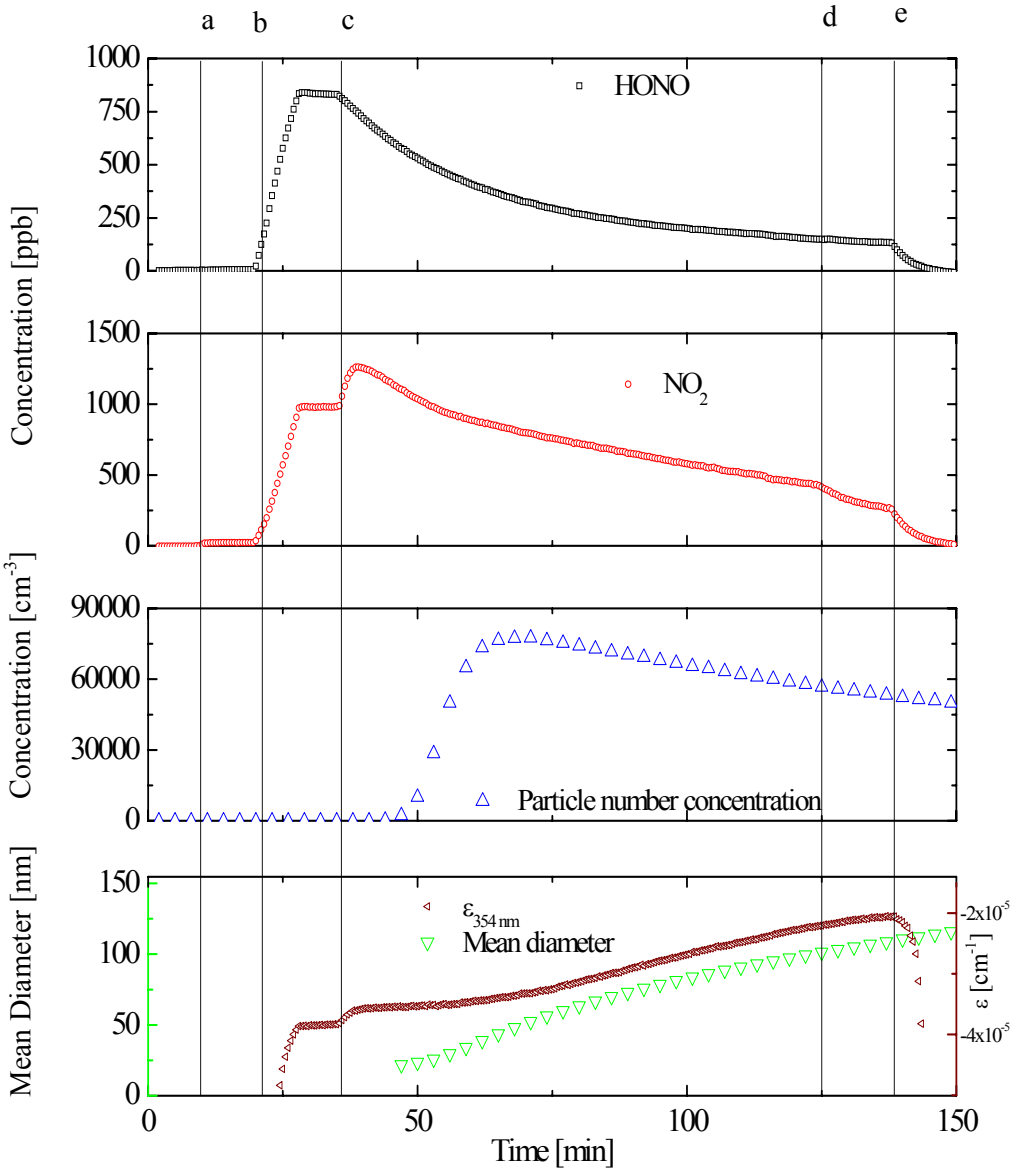


Figure 5.9 Temporal dependence of the concentrations of HONO, NO_2, and total particle number concentration as well as the mean aerosol aerodynamic diameter and the aerosol extinction at 354 nm. Points (a) – (d) indicate changes in either the input concentrations or photolysis rate: (a) Addition of isoprene, (b) Introduction of HONO/NO/NO_2, (c) Lamps switched on d) Lamps switched off, e) Flushing of chamber started.

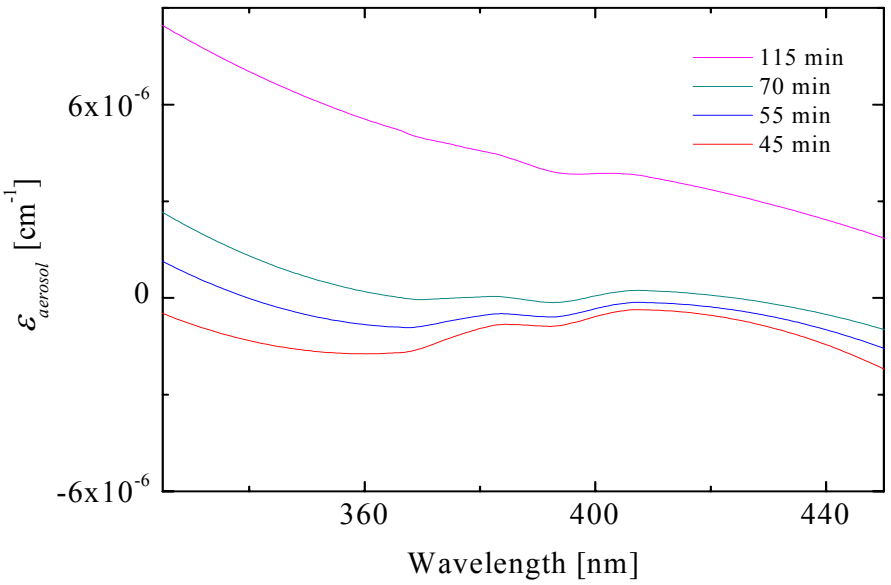


Figure 5.10 Wavelength-dependence of the aerosol extinction at different times

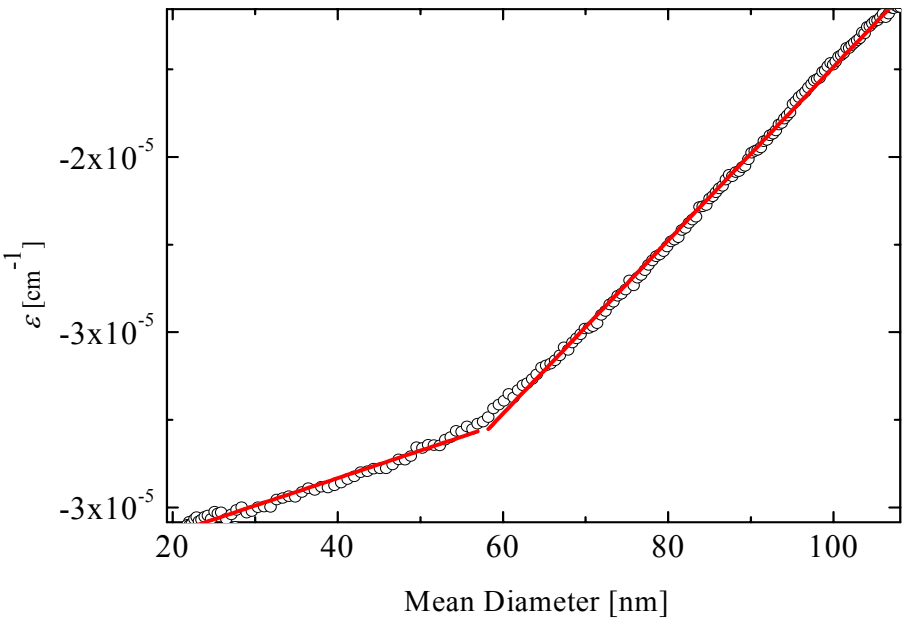


Figure 5.11 Correlation between the aerosol extinction at 354 nm and the mean diameter of the particles ($R^2 = 0.97$ < 50 nm and $R^2 = 0.979$ > 50 nm).

Bibliography

Alif, A., Pilichowski, J. F., and Boule, P.: Photochemistry and Environment .13. Phototransformation of 2-Nitrophenol in Aqueous-Solution, J. Photochem. Photobiol. A, 59, 209-219, 1991.

Bardini, P.: Atmospheric chemistry of dimethylphenols and nitrophenols, Ph.D. Thesis, Chemistry department, Univerisity College Cork, Cork, 2006.

Barker, J. R.: Progress and problems in atmospheric chemistry, Advanced series in physical chemistry, World Scientific, Singapore ; River Edge, N.J., 1995.

Bejan, I., Abd El Aal, Y., Barnes, I., Benter, T., Bohn, B., Wiesen, P., and Kleffmann, J.: The photolysis of ortho-nitrophenols: a new gas phase source of HONO, Phys. Chem. Chem. Phys., 8, 2028-2035, 2006.

Bejan, I., Barnes, I., Olariu, R., Zhou, S. M., Wiesen, P., and Benter, T.: Investigations on the gas-phase photolysis and OH radical kinetics of methyl-2-nitrophenols, Phys. Chem. Chem. Phys., 9, 5686-5692, 2007.

Calvert, J. G., and Pitts, J. N.: Photochemistry, Wiley, London, 1966.

Chameides, W. L., Lindsay, R. W., Richardson, J., and Kiang, C. S.: The Role of Biogenic Hydrocarbons in Urban Photochemical Smog - Atlanta as a Case-Study, Science, 241, 1473-1475, 1988.

Chen, J., and Venables, D. S.: A broadband optical cavity spectrometer for measuring weak near-ultraviolet absorption spectra of gases, Atmos. Meas. Tech., 4, 425-436, 10.5194/amt-4-425-2011, 2011.

Christie, M. I., and Hetherington, P. M.: The photolysis of t-butyl, isopropyl and ethyl nitrites at 254 nm, J. Photochem., 6, 285-295, 1976.

Clifford, G. M., Thuner, L. R., Wenger, J. C., and Shallcross, D. E.: Kinetics of the gas-phase reactions of OH and NO_3 radicals with aromatic aldehydes, J. Photoch. Photobio. A, 176, 172-182, 2005.

Dubowski, Y., and Hoffmann, M. R.: Photochemical transformations in ice: Implications for the fate of chemical species, Geophys. Res. Lett., 27, 3321-3324, 2000.

Etzkorn, T., Klotz, B., Sorensen, S., Patroescu, I. V., Barnes, I., Becker, K. H., and Platt, U.: Gas-phase absorption cross sections of 24 monocyclic aromatic hydrocarbons in the UV and IR spectral ranges, Atmos. Environ., 33, 525-540, 1999.

Fiedler, S. E., Hese, A., and Ruth, A. A.: Incoherent broad-band cavity-enhanced absorption spectroscopy, Chem. Phys. Lett., 371, 284-294, 2003.

Finlayson-Pitts, B. J., and Pitts, J. N.: Chemistry of the upper and lower atmosphere : theory, experiments, and applications, Academic Press, San Diego, 2000.

Gómez-González, Y., Surratt, J. D., Cuyckens, F., Szmigielski, R., Vermeylen, R., Jaoui, M., Lewandowski, M., Offenberg, J. H., Kleindienst, T. E., Edney, E. O., Blockhuys, F., Van Alsenoy, C., Maenhaut, W., and Claeys, M.: Characterization of organosulfates from the photooxidation of isoprene and unsaturated fatty acids in ambient aerosol using liquid chromatography/(-) electrospray ionization mass spectrometry, J. Mass. Spectrom., 43, 371-382, 2008.

Gherman, T., Venables, D. S., Vaughan, S., Orphal, J., and Ruth, A. A.: Incoherent broadband cavity-enhanced absorption spectroscopy in the near-ultraviolet: Application to HONO and NO_2, Environ. Sci. Technol., 42, 890-895, 2008.

Gierczak, T., Burkholder, J. B., Talukdar, R. K., Mellouki, A., Barone, S. B., and Ravishankara, A. R.: Atmospheric fate of methyl vinyl ketone and methacrolein, J. Photoch. Photobio. A, 110, 1-10, 1997.

Guenther, A., Hewitt, C. N., Erickson, D., Fall, R., Geron, C., Graedel, T., Harley, P.,

Klinger, L., Lerdau, M., Mckay, W. A., Pierce, T., Scholes, B., Steinbrecher, R., Tallamraju, R., Taylor, J., and Zimmerman, P.: A Global-Model of Natural Volatile Organic-Compound Emissions, J. Geophys. Res.-Atmos., 100, 8873-8892, 1995.

Harrison, M. A. J., Barra, S., Borghesi, D., Vione, D., Arsene, C., and Olariu, R. L.: Nitrated phenols in the atmosphere: a review, Atmos. Environ., 39, 231-248, 2005.

Henze, D. K., and Seinfeld, J. H.: Global secondary organic aerosol from isoprene oxidation, Geophys. Res. Lett., 33, DOI: 10.1029/2006GL025976, 2006.

Imanishi, S., Semba, K., Ito, M., and Anno, T.: The near Ultraviolet Absorption Spectra of Acetophenone and Benzophenone Vapors and the Long Wave-Lengths Absorption System of Benzaldehyde Vapor, B Chem. Soc. Jpn., 25, 150-153, 1952.

Ishag, M. I. O., and Moseley, P. G. N.: Effects of UV Light on Dilute Aqueous-Solutions of Meta-Nitrophenol and Para-Nitrophenol, Tetrahedron, 33, 3141-3144, 1977.

Klotz, B., Sorensen, S., Barnes, I., Becker, K. H., Etzkorn, T., Volkamer, R., Platt, U., Wirtz, K., and Martin-Reviejo, M.: Atmospheric oxidation of toluene in a large-volume outdoor photoreactor: In situ determination of ring-retaining product yields, J. Phys. Chem. A, 102, 10289-10299, 1998.

Kroll, J. H., Ng, N. L., Murphy, S. M., Flagan, R. C., and Seinfeld, J. H.: Secondary organic aerosol formation from isoprene photooxidation under high-NOx conditions, Geophys. Res. Lett., 32, DOI: 10.1029/2005GL023637, 2005.

Kroll, J. H., Ng, N. L., Murphy, S. M., Flagan, R. C., and Seinfeld, J. H.: Secondary organic aerosol formation from isoprene photooxidation, Environ. Sci. Technol., 40, 1869-1877, 2006.

McMillan, G. R.: Photolysis of Alkyl Nitrites. I. tert-Butyl Nitrite, J. Am. Chem. Soc., 84, 4007-4011, 1962.

Ng, N. L., Kwan, A. J., Surratt, J. D., Chan, A. W. H., Chhabra, P. S., Sorooshian, A., Pye, H. O. T., Crounse, J. D., Wennberg, P. O., Flagan, R. C., and Seinfeld, J. H.: Secondary organic aerosol (SOA) formation from reaction of isoprene with nitrate radicals (NO_3), Atmos. Chem. Phys., 8, 4117-4140, 2008.

Noziere, B., Lesclaux, R., Hurley, M. D., Dearth, M. A., and Wallington, T. J.: A Kinetic and Mechanistic Study of the Self-Reaction and Reaction with HO_2 of the Benzylperoxy Radical, J. Phys. Chem., 98, 2864-2873, 1994.

Ohmori, N., Suzuki, T., and Ito, M.: Why Does Intersystem Crossing Occur in Isolated Molecules of Benzaldehyde, Acetophenone, and Benzophenone, J. Phys. Chem., 92, 1086-1093, 1988.

Platt, U., Meinen, J., Pohler, D., and Leisner, T.: Broadband Cavity Enhanced Differential Optical Absorption Spectroscopy (CE-DOAS) - applicability and corrections, Atmos. Meas. Tech., 2, 713-723, 2009.

Raff, J. D., and Finlayson-Pitts, B. J.: Hydroxyl Radical Quantum Yields from Isopropyl Nitrite Photolysis in Air, Environ. Sci. Technol., 44, 8150-8155, 10.1021/es102218d, 2010.

Smith, D. F., McIver, C. D., and Kleindienst, T. E.: Primary product distribution from the reaction of hydroxyl radicals with toluene at ppb NO_X mixing ratios, J. Atmos. Chem., 30, 209-228, 1998.

Stutz, J., Kim, E. S., Platt, U., Bruno, P., Perrino, C., and Febo, A.: UV-visible absorption cross sections of nitrous acid, J. Geophys. Res.-Atmos., 105, 14585-14592, 2000.

Surratt, J. D., Gomez-Gonzalez, Y., Chan, A. W. H., Vermeylen, R., Shahgholi, M.,

Kleindienst, T. E., Edney, E. O., Offenberg, J. H., Lewandowski, M., Jaoui, M., Maenhaut, W., Claeys, M., Flagan, R. C., and Seinfeld, J. H.: Organosulfate formation in biogenic secondary organic aerosol, J. Phys. Chem. A, 112, 8345-8378, 2008.

Taylor, W. D., Allston, T. D., Moscato, M. J., Fazekas, G. B., Kozlowski, R., and Takacs, G. A.: Atmospheric Photo-Dissociation Lifetimes for Nitromethane, Methyl Nitrite, and Methyl Nitrate, Int. J. Chem. Kinet., 12, 231-240, 1980.

Thalman, R., and Volkamer, R.: Inherent calibration of a blue LED-CE-DOAS instrument to measure iodine oxide, glyoxal, methyl glyoxal, nitrogen dioxide, water vapour and aerosol extinction in open cavity mode, Atmos. Meas. Tech., 3, 1797-1814, 10.5194/amt-3-1797-2010, 2010.

Thiault, G., Mellouki, A., Le Bras, G., Chakir, A., Sokolowski-Gomez, N., and Daumont, D.: UV-absorption cross sections of benzaldehyde, ortho-, meta-, and para-tolualdehyde, J. Photochem. Photobiol. A, 162, 273-281, 2004.

Thompson, H. W., and Dainton, F. S.: The photochemistry of alkyl nitrites. III, Transactions of the Faraday Society, 33, 1546-1555, 1937.

Thornton, J. A., Wooldridge, P. J., Cohen, R. C., Martinez, M., Harder, H., Brune, W. H., Williams, E. J., Roberts, J. M., Fehsenfeld, F. C., Hall, S. R., Shetter, R. E., Wert, B. P., and Fried, A.: Ozone production rates as a function of NOx abundances and HOx production rates in the Nashville urban plume, J. Geophys. Res.-Atmos., 107, DOI: 10.1029/2001JD000932, 2002.

Thuner, L. P., Bardini, P., Rea, G. J., and Wenger, J. C.: Kinetics of the gas-phase reactions of OH and NO_3 radicals with dimethylphenols, J. Phys. Chem. A, 108, 11019-11025, 2004.

Tremp, J., Mattrel, P., Fingler, S., and Giger, W.: Phenols and Nitrophenols as Tropospheric Pollutants - Emissions from Automobile Exhausts and Phase-Transfer in the Atmosphere, Water Air Soil Poll., 68, 113-123, 1993.

Trost, B., Stutz, J., and Platt, U.: UV-absorption cross sections of a series of monocyclic aromatic compounds, Atmos. Environ., 31, 3999-4008, 1997.

Varma, R. M., Venables, D. S., Ruth, A. A., Heitmann, U., Schlosser, E., and Dixneuf, S.: Long optical cavities for open-path monitoring of atmospheric trace gases and aerosol extinction, Appl. Opt., 48, B159-B171, 2009.

Varma, R. M., Venables, D. S., Ruth, A. A., Heitmann, U., Thieser, J., Meinen, J., Platt, U., and Ball, S. M.: An intercomparison of aerosol extinction measurements, In preparation 2011.

Venables, D. S., Gherman, T., Orphal, J., Wenger, J. C., and Ruth, A. A.: High sensitivity in situ monitoring of NO_3 in an atmospheric simulation chamber using incoherent broadband cavity-enhanced absorption spectroscopy, Environ. Sci. Technol., 40, 6758-6763, 2006.

Voigt, S., Orphal, J., and Burrows, J. P.: The temperature and pressure dependence of the absorption cross-sections of NO_2 in the 250-800 nm region measured by Fourier-transform spectroscopy, J. Photochem. Photobiol. A, 149, 1-7, 2002.

Wang, Y. Q., Wang, H. G., Zhang, S. Q., Pei, K. M., Zheng, X. M., and Phillips, D. L.: Resonance Raman intensity analysis of the excited state proton transfer dynamics of 2-nitrophenol in the charge-transfer band absorption, J. Chem. Phys., 125, 2006.

Wu, S. L., Mickley, L. J., Jacob, D. J., Logan, J. A., Yantosca, R. M., and Rind, D.:

Why are there large differences between models in global budgets of tropospheric ozone?, J. Geophys. Res.-Atmos., 112, DOI: 10.1029/2006JD007801, 2007.

Xiang, B., Zhu, C. Z., and Zhu, L.: Gas-phase absorption cross sections of 2-nitrobenzaldehyde and benzaldehyde in the 285-400 nm region, and photolysis of 2-nitrobenzaldehyde vapor at 308 and 351 nm, Chem. Phys. Lett., 474, 74-78, 2009.

Zhang, Y., Huang, J. P., Henze, D. K., and Seinfeld, J. H.: Role of isoprene in secondary organic aerosol formation on a regional scale, J. Geophys. Res.-Atmos., 112, DOI: 10.1029/2007JD008675, 2007.

Zhu, L., and Cronin, T. J.: Photodissociation of benzaldehyde in the 280-308 nm region, Chem. Phys. Lett., 317, 227-231, 2000.

Chapter 6

FORMAL INTERCOMPARISON OF OBSERVATIONS OF NITROUS ACID

6.1 Introduction

Nitrous acid plays an important role as a source of the OH radical in the troposphere. OH is the primary oxidant in the atmosphere and OH reactions may lead to ozone formation and "photochemical smog" in polluted urban areas. Photolysis of HONO is considered the largest source of OH radicals shortly after sunrise and significantly enhances photo-oxidation processes during that time (Harrison et al., 1996):

$$HONO + h\nu \rightarrow NO + OH \qquad (6.1)$$

Recent studies have indicated that HONO remains a significant contributor to OH formation throughout the day and can account for up to 60% of OH production even in the middle of the day (Kleffmann et al., 2003;Kleffmann and Wiesen, 2005;Ren et al., 2003;Zhou et al., 2002). It is accepted that most HONO is formed mainly by heterogeneous processes involving anthropogenic emissions of nitrogen oxide, typically from combustion emissions:

$$4NO_2 + 2H_2O + M \rightarrow 4HONO + O_2 + M \qquad (6.2)$$

There are still several outstanding questions about the chemistry of HONO in the atmosphere, particularly the possible sources of HONO and how important HONO is as a precursor for the OH radical. In order to improve air pollution models, many of which currently do not include HONO production mechanisms, a better understanding of HONO in the atmosphere is still desirable.

The aim of this chapter is to describe the development of an extractive IBBCEAS instrument for measuring HONO. In May 2010, this instrument took part in the Formal Intercomparison of Observations of Nitrous Acid (FIONA) campaign held in the EUPHORE atmospheric simulation chamber. An additional goal of the chapter is

to report the results of the extractive-IBBCEAS measurement from the campaign and compare them to the results of other techniques.

6.2 The extractive IBBCEAS system

6.2.1 Spectrometer design

A photograph of the extractive IBBCEAS system is shown Fig. 6.1 with a further schematic of the system shown as an inset. The cavity of the extractive IBBCEAS instrument was formed by two highly reflective mirrors (M_1, M_2) separated by 198 cm. Each mirror was purged by 0.5 L min^{-1} pure N_2 (grade 5). The sample cell was made from a 1.8 m long Teflon tube of 35 mm internal diameter and 45 mm outer diameter. Teflon was chosen as the body material to minimize chemical deposition and heterogeneous reactions. Two Bosch aluminium profiles formed a support rail above which the Teflon tube was mounted. The light source was a 250 mW LED (Nichia NCSU033A) with maximum output at 365 nm. The temperature of the LED was passively stabilized by holding the LED in a lens tube with a large heat sink. The LED was driven by a maximum 700 mA current controller (LEDD1 Thorlabs). Short term fluctuations of the LED intensity were about 0.1% and long term fluctuations were about 1% over 3 hours (Fig. 6.2). Light was collected by a fused silica lens and focused into the centre of the cavity. Light leaking out the cavity was collected by another fused silica lens after passing through a band pass filter (Semrock 365/44), and then coupled into one end of a high UV transmission optical fibre. Although the LED was very weak above 385 nm and below 350 nm, the transmission of the cavity at these limits was several orders of magnitude greater due to the sharp drop in the cavity mirror reflectivity. In order to reduce the stray light coupled into the spectrograph, a band pass filter was placed in front of the fibre input. To normalize fluctuations in the LED intensity, the other end of the optical fibre was mounted near the LED to measure fluorescence from a piece of paper at longer wavelengths.

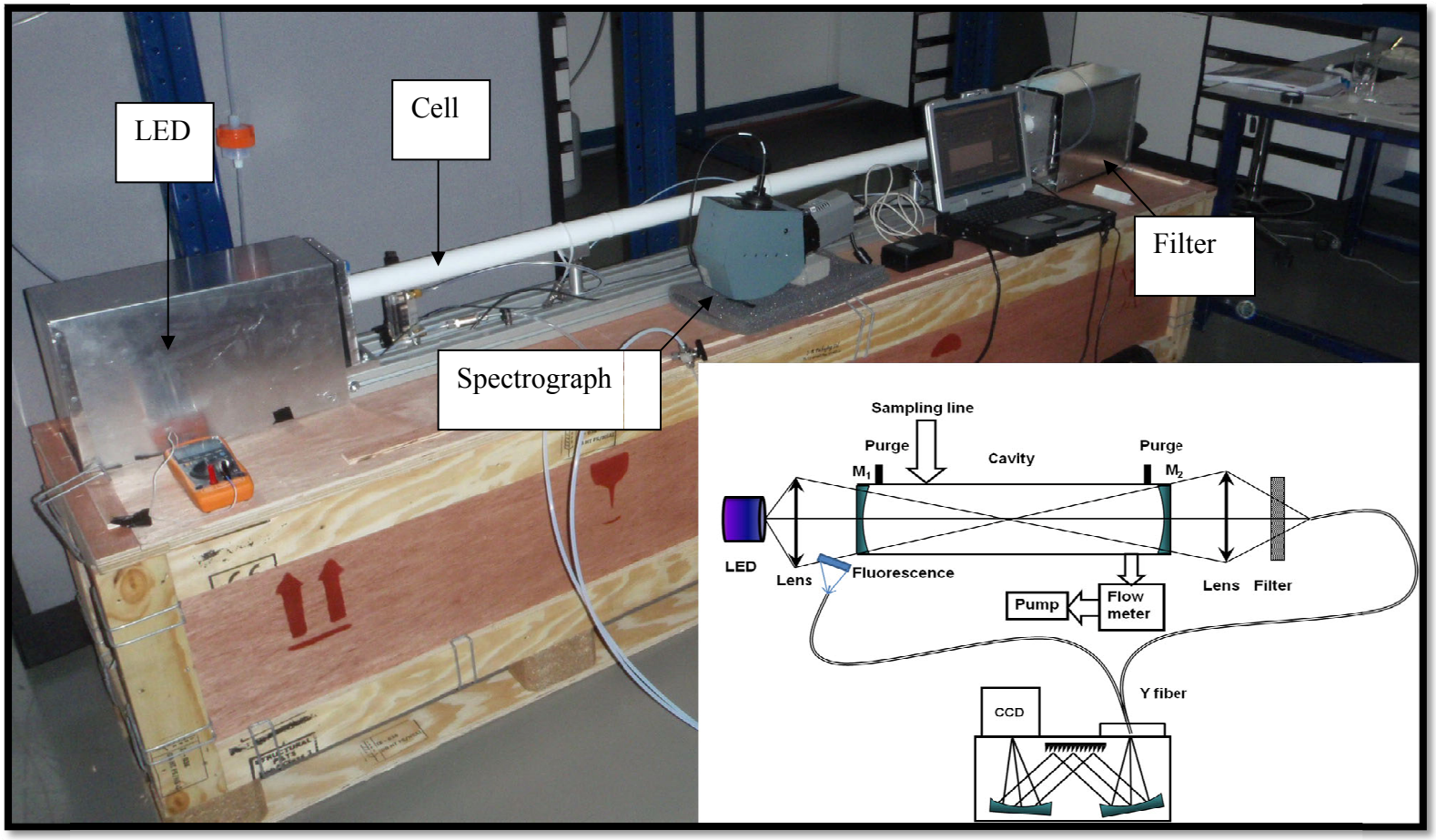


Figure 6.1 A photograph of the extractive IBBCEAS instrument during experiments in the EUPHORE Chamber. The inset shows a schema of the experimental system

A long pass filter was placed in front of the LED side fiber to exclude shorter wavelengths from coupling into the spectrograph. The cavity intensity spectrum is shown in Fig. 6.3. An 1800 line/mm grating with a 25 μm slit vertical fiber bundle was used in the 163 mm focal length Czerny-Turner spectrograph (Andor SR-163), giving a resolution of 0.3 nm at 365 nm. The wavelength scale of the spectrograph was calibrated twice each day during the FIONA experiments and was based on a second order polynomial fit to four intense emission lines from a Hg/Ar penray lamp. The average uncertainty of the wavelength calibration during the campaign was 0.01 nm. The temperature of the CCD camera was stabilized by a peltier cooler down to -40 ºC in order to minimize the dark current.

Extinction coefficients were retrieved based on the equation:

$$\varepsilon(\lambda) = \sum_i \sigma_i(\lambda) \cdot N_i = \frac{1}{d}\left(\frac{I_0(\lambda)}{I(\lambda)} - 1\right)\left(1 - R(\lambda)\right) \qquad (6.3)$$

where I_0 is the intensity when sampling clean air, I is the intensity when sampling chamber air, R is the mirror reflectivity, and d is the mirror separation.(Fiedler et al., 2003)

The mirror reflectivity was calibrated in two steps (Chen and Venables, 2010). In the first stage, the overall shape of the relative reflectivity spectrum was determined from the difference in Rayleigh scattering between N_2 and He from 350 nm to 380 nm as in Chapter 3:

$$\frac{\left(1 - R(\lambda)\right)}{d} = \frac{I_{N_2}(\lambda) N_{N_2} \sigma_{N_2}^{rayl}(\lambda) - I_{He}(\lambda) N_{He} \sigma_{He}^{rayl}(\lambda)}{I_{He}(\lambda) - I_{N_2}(\lambda)} \qquad (6.4)$$

In the second step, the absorption of the O_4 dimer at 360.5 nm was measured in a stream of pure O_2 (5 grade) and used to scale the reflectivity spectrum to the value of Wagner et al. (2002). The maximum reflectivity was ca. 0.9992 compared to the manufacturer's specification of 0.9995. Calibration procedures were carried out at the start and end of each day's experiment. Background spectra with the LED

blocked were also recorded over 5 minutes. The intensity spectrum of clean synthetic air was taken over 20 minutes to record I_0 at the start and end of each experiment as well as in the middle of selected experiments.

A diaphragm pump drew the sample through the system and the flow rate was restricted by a ball flowmeter to 2 L min^{-1}. By injecting 500 μL SO_2, the residence time was determined to be about 160 seconds at a 2 L min^{-1} extraction rate (Fig. 6.4). The repeatability of five additions was excellent with a 3% standard deviation in the retrieved concentrations. Based on the residence time of the instrument and the mixing time of the EUPHORE chamber (about 1 minute), the data acquisition time was set to 60 s.

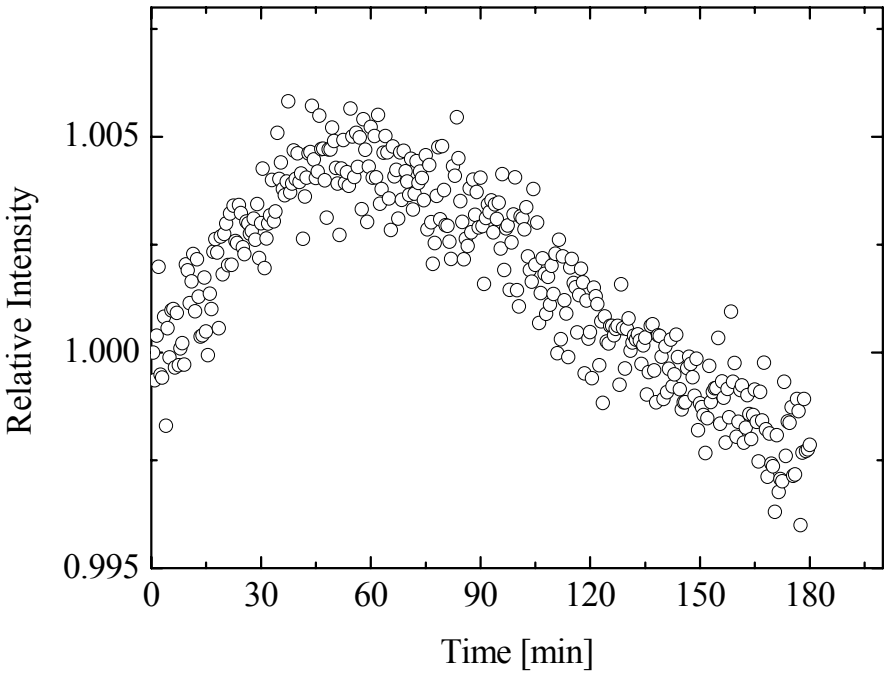


Figure 6.2 Variation of LED intensity at 367 nm over 3 hours, 30 s acquisition time.

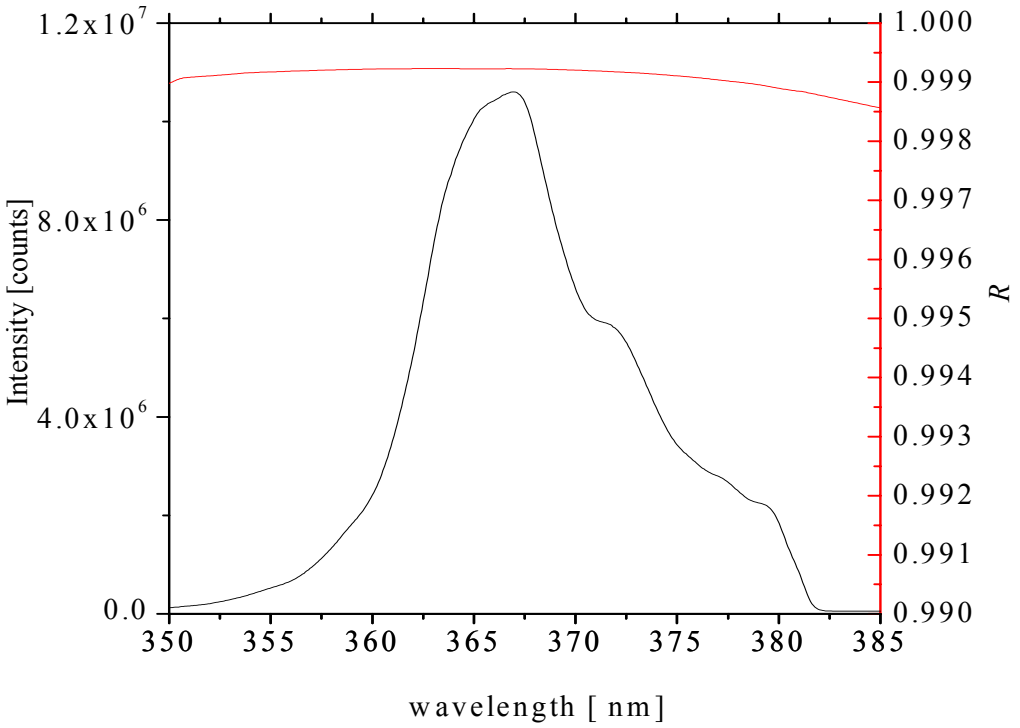


Figure 6.3 Cavity intensity and mirror reflectivity curve from 350 to 385 nm.

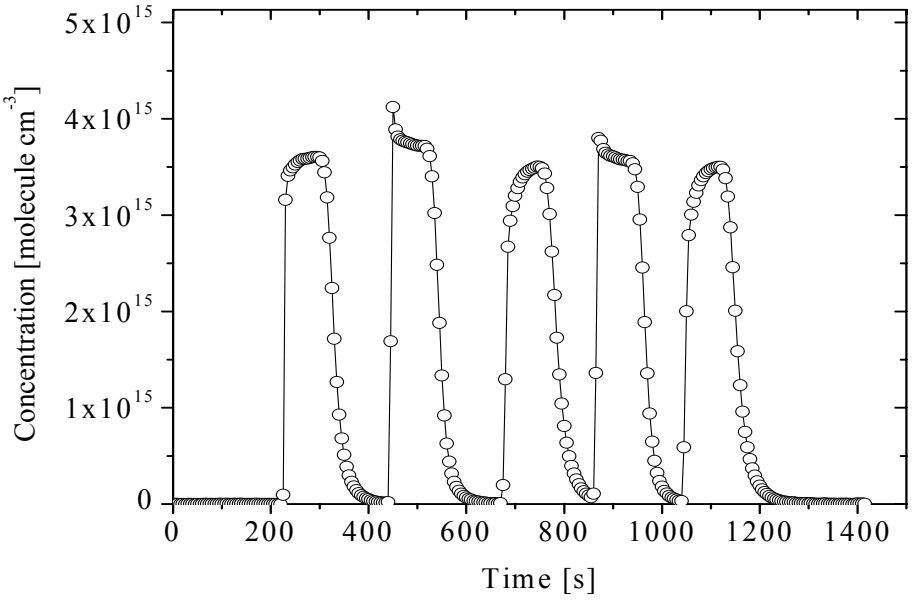


Figure 6.4 Residence time and repeatability of the extractive IBBCEAS instrument from five successive injections of 500 µL SO_2.

6.2.2 Laboratory test

To test the instrument, the spectra of HONO and NO_2 were measured with an integration time of 30 s and the number density of HONO and NO_2 were retrieved. HONO and NO_2 were produced in the same way as in Chapter 5.

Based on least square fittings, the number densities of HONO and NO_2 were evaluated from the followed equation:

$$\varepsilon\ (\lambda) = \sigma_{NO\,2}(\lambda) \cdot n_{NO\,2} + \sigma_{HONO}\ (\lambda) \cdot n_{HONO}\ + \varepsilon_{polynomial}\ (\lambda)$$

The absorption cross-sections, σ_{NO2} and σ_{HONO}, were respectively those of Voigt et al. and Stutz et al. (Voigt et al., 2002;Stutz et al., 2000). These cross-sections were convoluted to our spectrograph resolution. The baseline extinction, $\varepsilon_{\text{polynomial}}$, was included to compensate for slight changes in the intensity during the experiment and for broadband extinction processes.

The overall absorption coefficient is shown in Fig. 6.5(a), with the above two absorber parameterization giving a good match to the measured spectrum. The individual contributions to the overall absorption coefficient are also shown in Fig. 6.5 along with the fit residual. The number densities of HONO and NO_2 found in this fitting were $2.24 \pm 0.06 \times 10^{11}$ and $2.21 \pm 0.02 \times 10^{12}$ molecules cm^{-3} corresponding to 8.9 ppb and 88.4 ppb at ambient pressure and temperature. Uncertainties represent fit statistical uncertainties only.

The fit residual shows a slow variation with wavelength. Because the emission spectrum of the LED depends on the forward current as well as the temperature of the die, these slow changes in the residual probably relate to small shifts in the spectrum of the LED. These residual structures are much more obvious in the FIONA results where large environmental temperature variations were experienced. Their influence on retrieved concentrations of HONO and NO_2 will be discussed in Section 6.4 and 6.5. As a measure of the sensitivity of the instrument, the ratio of the noise to the absorption cross-section peak height was used. From the residual

spectrum we find an rms value of 3×10^{-9} cm^{-1}, which was divided by the peak absorption cross-sections. The corresponding average sensitivity of HONO and NO_2 are 0.27 ppb and 0.22 ppb respectively. Longer integration times such as 1 min would also improve the system sensitivity.

The concentrations of HONO and NO_2 were quantified based on the differential optical absorption using the DOASIS spectral analysis package. The wavelength shift and squeeze was limited to ± 0.1 nm during the fitting. Spectra were analyzed over the window from 352 to 373 nm and the wavelength scale was allowed to shift by ±0.1 nm. A 3rd order polynomial function was fitted to the featureless broadband absorption. Although narrower fitting windows would improve the residual spectrum, the cross-sensitivity between HONO and NO_2 contributes significantly close to the detection limit of the target species. A wider fitting window was therefore adopted. Other absorbers were included in the fit if they were introduced into the chamber during that day's experiment. The absorption of SO_2 was too small to influence the results in any experiment and was not included in the fits.

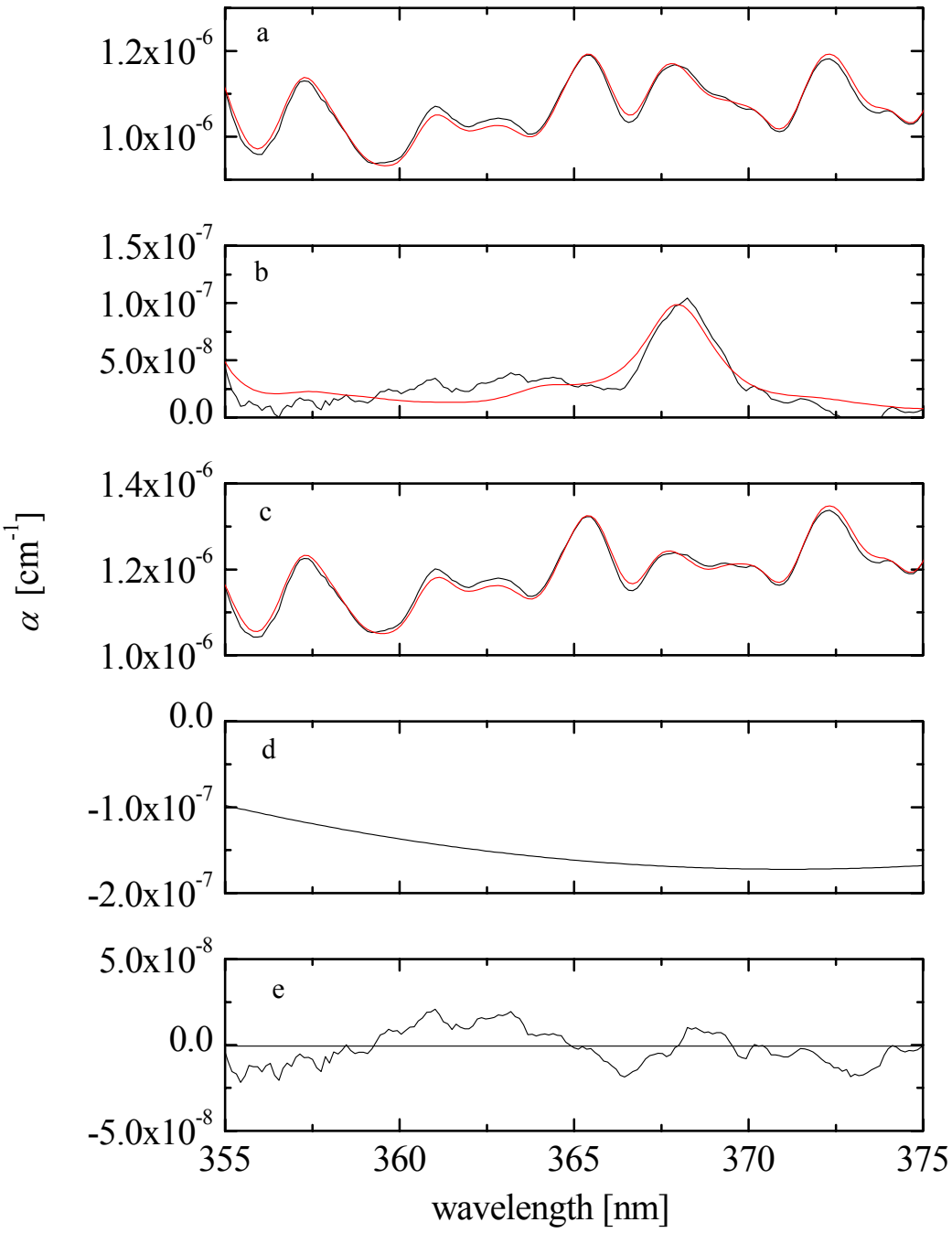


Figure 6.5 Experimental spectrum of HONO and NO_2 (black) as well as the fit result (red) The contribution of (b) HONO, (c) NO_2, and (d) the polynomial base line are shown, as is the fitting residual in (e).

The uncertainty of the retrieved number densities was estimated using standard uncertainty propagation. The uncertainty in the extinction coefficient, $\Delta\varepsilon$, was evaluated from Eq. (6.3)

$$\Delta\varepsilon^2 = \left|\frac{\partial\varepsilon}{\partial d}\right|^2 \Delta d^2 + \left|\frac{\partial\varepsilon}{\partial(1-R)}\right|^2 \Delta(1-R)^2 + \left|\frac{\partial\varepsilon}{\partial I_0}\right|^2 \Delta I_0{}^2 \quad (6.6)$$

in which the fractional uncertainties of the parameters are estimated to be 9% for $(1 - R)$, 0.5% for the cavity length d, and 3% for I_0. The overall uncertainty in the measured absorption extinction is about 10% and is dominated by the absolute uncertainty in the calibration of the mirror reflectivity.

The uncertainty in the retrieved number densities must furthermore account for the uncertainty in the absorption cross-section of each species ($\Delta\sigma$):

$$\left(\frac{\Delta N}{N}\right)^2 = \left(\frac{\Delta\varepsilon}{\varepsilon}\right)^2 + \left(\frac{\Delta\sigma}{\sigma}\right)^2 \quad (6.7)$$

With the 15% uncertainty in the HONO cross-sections and the 4% uncertainty in the NO_2 cross-sections, the overall uncertainty in the retrieved HONO number density is 17%, while NO_2 has a 10% uncertainty.

6.3 FIONA campaign

6.3.1 Introduction

Although HONO is important in the atmosphere, the difficulty of measuring HONO means that there are still large uncertainties associated with observed HONO levels, which are usually higher than model calculations suggest. HONO has been measured by a number of techniques, such as LP-DOAS, LIF, LOPAP, and IBBCEAS (Platt et al., 1980;Hanst et al., 1982;Ferm and Sjodin, 1985;Febo and Perrino, 1995;Febo et al., 1993;Wang and Zhang, 2000;Schiller et al., 2001;Huang et al., 2002;Kleffmann et al., 2002;Gherman et al., 2008). The limitations of various techniques such as detection limits, sampling approach, and interferences have cast doubt on observed

levels of HONO. Therefore, evaluation of the various techniques under simulated conditions is desirable to better determine the accuracy and precision of each instrument. For these reasons, the FIONA campaign was carried out to inter-compare numerous techniques and instruments under a range of scenarios accounting for typical urban and semi-rural conditions. Measurements during the campaign aimed to evaluate the reliability of each instrument and method under various physical and chemical conditions and to determine potential interferences in each system. Comparing modeled results to the measured concentrations also aided interpretation of the results.

6.3.2 Campaign objectives and participants

The FIONA campaign has three main objectives which are: (a) an inter-comparison of HONO measurement techniques, (b) a study of interferences on the measurements, and (c) to investigate potential sources of HONO. The inter-comparison of HONO measurements from different instruments was carried out under typical urban and semi-rural conditions to emphasize both the chemistry and potential interferences on the methodologies. Secondly, the various techniques were susceptible to potential interferences such as aerosols, nitrates, and NO_2. Evaluating the different approaches under appropriate controlled conditions aimed to further understanding of each approach. Lastly, observed daytime HONO concentrations are still suspiciously high. Potential HONO sources such as nitrophenols and VOCs from combustion emissions (Bejan et al., 2006;Gutzwiller et al., 2002;Kurtenbach et al., 2001) were also investigated during the experiments.

A total of 19 instruments from 17 institutions participated in the FIONA campaign. The participating instruments can be categorized as either spectroscopic, wet chemical or denuder systems. Table 6.1 summarizes the specifications and detection limits of each instrument.

Table 6.1 List of HONO monitoring instrumental parameters for FIONA participants

INSTITUTION	INSTRUMENT	TIME RESOLUTION	ACCURACY	PRECISION	RANGE	DETECTION LIMIT
UCC (Ireland) **FZJ Jülich (Germany)**	Open path-IBBCEAS	1-10 min	200 ppt	50 ppt	0.2-100 ppb	0.2 ppb
UCC (Ireland)	Extractive-IBBCEAS	1-10 min	17%	200 ppt	0.5-100 ppb	0.3 ppb
U.Leicester **U.Cambridge (UK)**	BBCEAS	15 s	HONO Cross Section	150 ppt	>100 ppt	100ppt
Georgia Tech (USA)	PF-LIF	1 min	0.3 ppt	0.15 ppt	0-2 ppb	1 ppt
CEAM (Spain)	DOAS	1-2 min	4%	7.5 %	0.4-200 ppb	0.4 ppb
CEAM (Spain)	FTIR	5-10 min	10 %	10 %	1.5-200 ppb	1.5-2 ppb
U.Houston (USA)	LOPAP	3-5 min	7 %	1 %	5ppt-200ppb	5 ppt
BUW (Germany)	LOPAP	3-5min	7 %	1 %	5ppt-200ppb	5 ppt
CNRS-ICARE(France)	LOPAP	0.1 s	10 %	1 %	2ppb-2ppm	2ppb
U. Jülich (Germany)	LOPAP	0.1 s	10 %	1 %	1ppt-200ppb	2ppb
CEAM (Spain)	LOPAP	3-5 min	10%	1%	30ppt-150ppb	2ppt

Continued

INSTITUTION	INSTRUMENT	TIME RESOLUTION	ACCURACY	PRECISION	RANGE	DETECTION LIMIT
LISA (France)	Nitromac:SANED	10 min	5-10 %	5-10 %	35 ppb	5-20 ppt
U.Manchester (UK)	CIMS	1 s	15 %	10 %	1ppt-10ppb	1 ppt
DLR (Germany)	CIMS	1-3 s	15 %	3 %	15ppt-20ppb	15ppt
U.New Hampshire. Durham (USA)	Mist Chamber/Ion Chromatography	2-20 min	N.A	< 15%	ppt - several ppb	ppt level
Inst. Analytical Chem. (Czetch Rep.)	Wet denuder Chemluminescent FIA	3 min	4.5%	4.5%	15ppt-45ppb	15ppt
Wadsworth Center and Sunny (USA)	Coil/azo dye derive/long pass flow cell spectrometry with denuder	1 min	< 15% at > 100 ppt	<10% at >100 ppt	3ppt-20ppb	3ppt
CEAM (Spain)	HPLC	4 min	7.5 %	10 %	100 ppt - few ppb	100 ppt
Swedish Envi. Res. Inst.(Sweden)	Volumetric Sampling with filter pack	2-3 filter a day	-	-	-	-

6.3.3 Experimental details

The campaign includes mainly three types of experiments a) calibrations, b) simulation of polluted urban sites, c) interferences in HONO measurements such as aerosols or inorganic nitrates, small aldehydes, and so on. There were a total of nine experiments in the campaign, which are listed in Table 6.2 along with summaries of each experiment's conditions. Detailed experimental conditions are given with the results in Section 6.4.

Table 6.2 List of the experimental conditions during FIONA

Expt.No.	Date	Blind	Conditions
1	17/05/2010	No	Pure conditions, simple system: HONO formation in the dark and sunlit chamber.
2	18/05/2010	No	Clean conditions: HONO / NO / NO_2 in dark and sunlit chamber.
3	25/05/2010	Yes	Low HONO at high NO / NO_2 / NO_3 / N_2O_5
4	19/05/2010	Yes	Ambient air and interference by phenols and NO_2
5	20/05/2010	Yes	Isoprene nitrates in gas phase and heterogeneous phase
6	24/05/2010	Yes	Photolysis of nitrophenols
7	26/05/2010	Yes	Methylglyoxal as PAN source
8	27/05/2010	Yes	Photo-smog scenario with diesel exhaust
9	21/05/2010	Yes	Repeat part of experiment 1 / 2

6.4 Intercomparison results

During the FIONA campaign, the following experimental protocol was adopted for the extractive IBBCEAS system: (a) the cavity alignment was optimized, (b) the spectrograph wavelength scale was calibrated, (c) a 5 minute background spectrum was recorded, (d) the mirror reflectivity was calibrated with N_2, He and O_2, (e) a 20 minutes blank scan in synthetic air, I_{ob}, was recorded, (f) sampling from the chamber was started and spectra recorded, (g) additional mirror calibrations were carried on periodically as needed, (h) at the end of the experiment, another 20 min blank scan in synthetic air, I_{oe}, was recorded, and (i) the wavelength was calibrated. The number densities of HONO and NO_2 were retrieved using the DOASIS spectra analysis procedure as described above.

The HONO results included a precision value for each measured number density, which was estimated from the variation, taken as the standard deviation of 10 points, of measured values from a 20-point running average. This method gives a more conservative value for the precision than do the fit uncertainties, which do not take instrumental noise into account. The method will necessarily over-predict measurement variability near abrupt changes in the concentration, and precision values have been omitted where rapid changes occur.

Unfortunately, the extractive IBBCEAS results were compromised by two noteworthy problems during the FIONA campaign: Firstly, vibrations on the platform immediately below the chamber resulted in unstable system performance and gradual misalignment of the optical system. This problem was solved by moving the instrument to ground level before the start of the campaign experiments; however, a much longer inlet line (4 to 5 m) was required and may have led to higher sampling artefacts than other instrumentation during the experiments.

Secondly, a more significant consideration was the thermal stability of the optical system over the large temperature changes occurring during the experiments. Thermal expansion visibly affected the cavity alignment, thereby reducing the effective pathlength of our system and the amount of light coupled into and out of the

cavity. These changes affected the accuracy of our measurement of the sample absorption, and hence quantisation of absorbing species, on each day of the campaign. To partly compensate for these changes values of I_0 and R over the course of the experiment were calculated by linear interpolation. Although the assumption of a linear variation of I_0 and R is likely to be inaccurate, the actual variation of these parameters was not experimentally accessible and is consequently a large source of uncertainty in our measurements. The influence of cavity misalignment on the accuracy of our HONO and NO_2 values is evaluated in the discussion.

In the following we present our results from the campaign. Measurements started from the second experiment due to delays in setting up the instrument. Experiment two was also non-blind, allowing the measurements of different instruments to be compared with each other. The remaining experiments were blind. Owing to the difficulties outlined above, the results presented below will focus on an initial comparison of the measurement results and an assessment of the performance of the extractive IBBCEAS system. To evaluate the performance of our instrument, CEAM kindly give us permission to show their HONO (DOAS) and NO_2 (chemiluminescence detector) results. A comprehensive comparison of the measurement results of other campaign participants will be published later. A detailed analysis of the chamber chemistry awaits modelling results and will also not be discussed here.

6.4.1 Experiment 2 on 18/05/2010

In order to calibrate all the instruments, 15 ppb HONO was first introduced into the flushed dry chamber, and then diluted in steps. The chamber roof was then opened to photolytic conversion of HONO. In the afternoon, 50 ppb methyl nitrite was added after increasing the relative humidity to 50% to test formation of HONO from hydrolysis on wet surfaces. Finally, isopropyl nitrate was added as a potential interfering compound.

The results of our measurements, DOAS results and CL NO_2 results are shown in Fig 6.6 with spectral fits in Appendix A.1 (07:30) and A.2 (09:30). The HONO results show good agreement with DOAS measurements. There is about a 5% difference immediately after the initial introduction of HONO and the HONO absorption is clearly evident at 07:30 with a close fit by the reference spectra. Compared to the open path configuration of the DOAS system inside the chamber, it is not surprising that the longer sampling line has some losses. However, the two NO_2 measurements differ when HONO is added or diluted. IBBCEAS NO_2 seems to be correlated with the HONO concentrations. This is likely to arise from a cross-sensitivity in the spectral fit and from the much larger differential cross-section of HONO compared to NO_2 (Fig. 6.7). In addition similar residual structures to those in Fig. 6.5 are evident – they are reduced by increasing the NO_2 component of the fit. However, at 9:30, when the concentrations of HONO and NO_2 are low, the spectrum appears to show real NO_2 absorption features (A.2).

The correlation of the measurements from IBBCEAS with the DOAS and CL results is shown in Fig. 6.7. The HONO measurements are in excellent agreement (R^2= 0.99) and with a slope of 1.10. On the hand, NO_2 results are mostly uncorrelated. Neither the IBBCEAS nor DOAS observed any effect from adding methyl nitrite or isopropyl nitrate to the chamber.

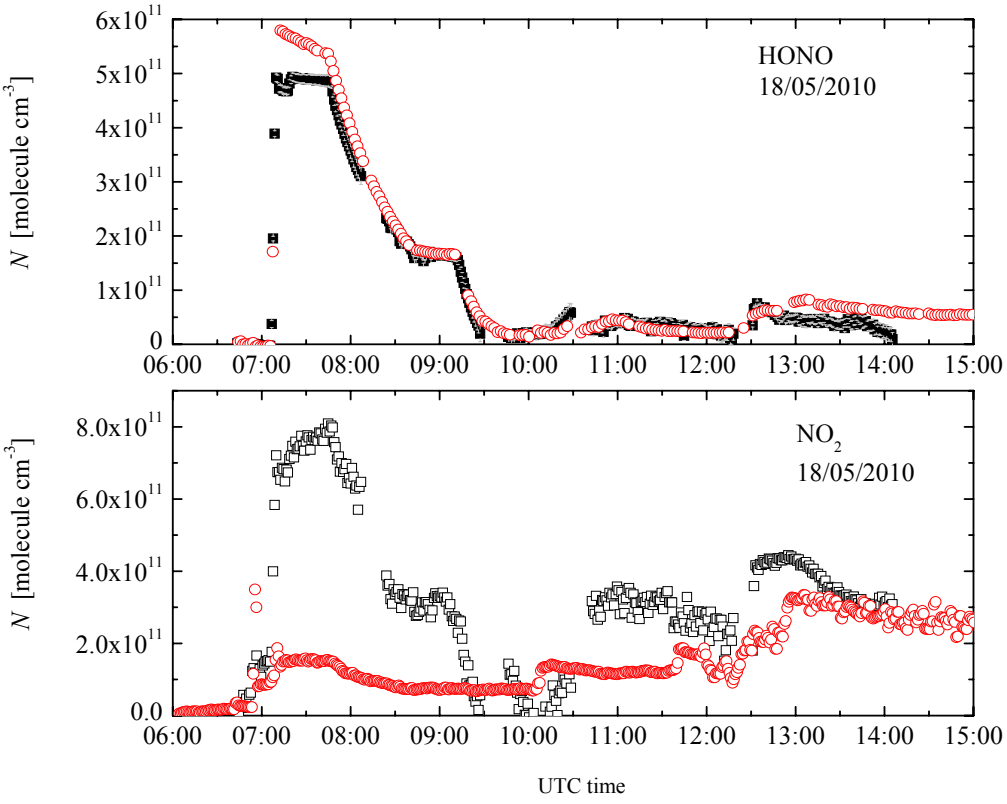


Figure 6.6 Results of IBBCEAS (black) and CEAM-DOAS and CL (red) measurements of HONO and NO_2

Table 6.3 Protocol of expt. 2

Time		Action	Time		Action
Start	**End**		**Star**	**End**	
06:53		NO_2 added	10:13	11:03	Water addition
07:07	07:10	HONO added (15 ppb)	11:38		Methyl nitrite added (10 mLgas)
07:46		Start chamber flushing	12:17		Chamber opened
08:43		Stop chamber flushing	12:47		Chamber closed
09:11		Chamber opened	13:01	13:03	Isopropyl nitrate added (40uL)
10:01		Chamber closed	15:04		Start chamber flushing

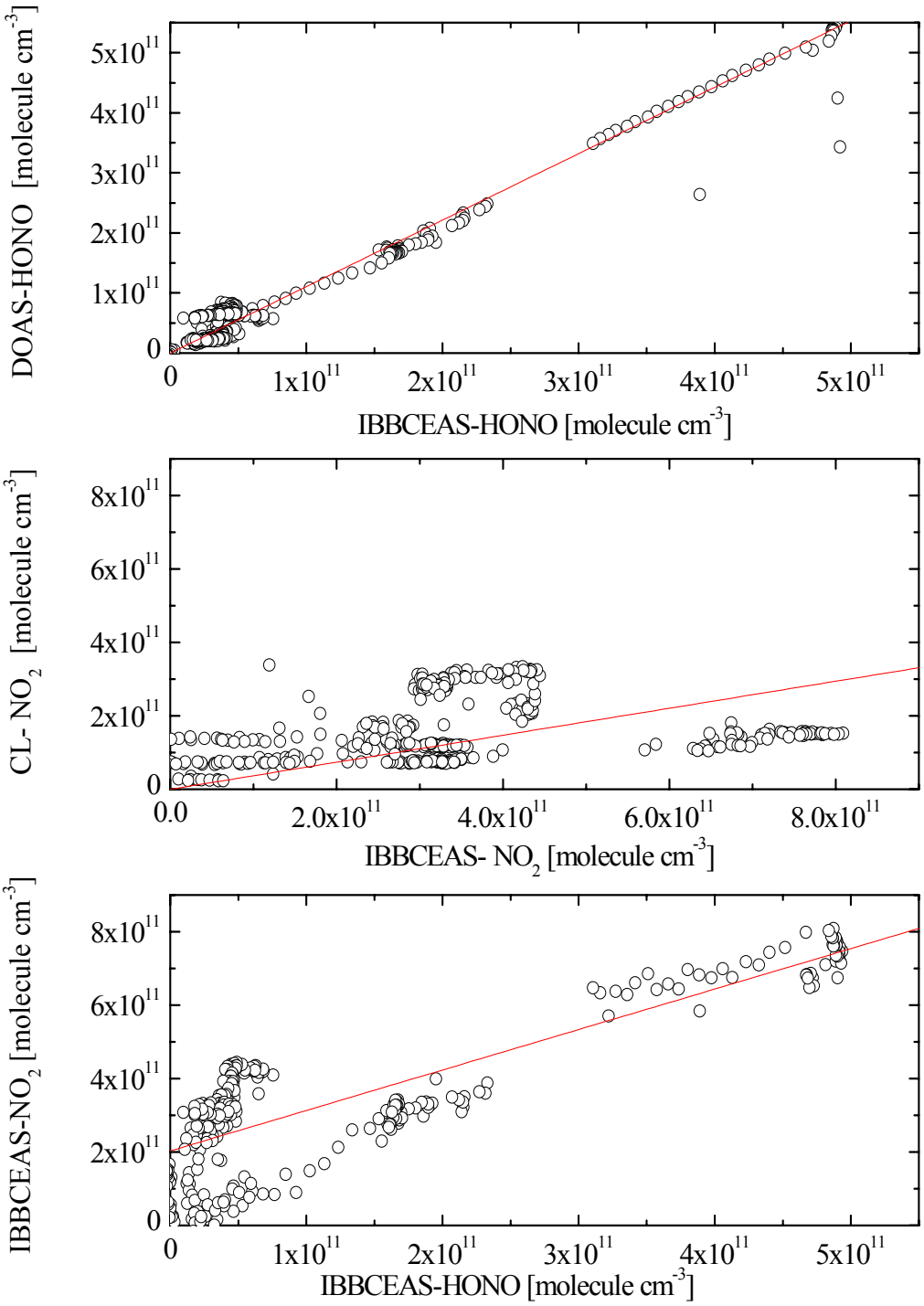


Figure 6.7 Top: HONO correlation between IBBCEAS and CEAM-DOAS and linear fitting (red) with slope = 1.1 and R^2= 0.99. Middle: the NO_2 correlation between IBBCEAS and CL detector and linear fitting (red) with slope = 0.36 and R^2 = 0.66. Bottom: Correlation between IBBCEAS-HONO and IBBCEAS-NO_2 and linear fitting (red) with slope = 1.1 and R^2 = 0.68.

6.4.2 Experiment 3 on 25/05/2010

The motivation for this experiment was to evaluate potential chemical interferences on each instrument's measurements. In some chemical instruments such as LOPAP, high NO and NO_2 levels can result in significant overestimates of HONO concentrations if they are not corrected or measured. In optical absorption instruments such as DOAS, the possibility that HONO is present as an impurity in the NO_2 reference absorption cross-section needs to be treated carefully in the spectral analysis procedure (Kleffmann et al., 2006). In wet denuder systems, formation of HONO from dissolved NO_2 and SO_2 in the aqueous phase leads to artefacts in quantifying HONO (Spindler et al., 2003).

In the morning, 150 ppb NO and 150 ppb O_3 were added to convert NO into NO_2. The high NO_2 levels tested for positive interferences in the chemical instruments as well as negative interferences in the absorption spectrometers. After 2 hours, another 150 ppb of O_3 was added to convert NO_2 to NO_3 and N_2O_5 and evaluate interferences in dark conditions. NO_3 and N_2O_5 were then removed by adding NO. Finally, 30 ppb SO_2 was added to check potential interferences in wet denuder systems.

The measured concentrations of HONO and NO_2 are shown in Fig 6.8 with the spectral fits in Appendix A.7 (09:30) and A.8 (14:00). The IBBCEAS values are much higher than DOAS values. Nevertheless, the retrieved NO_2 concentrations for both the IBBCEAS and the CL instruments showed quite similar trends. The CL detector behaved erratically during NO injections and measured values significantly understated or overstated the expected values. During this experiment the intensity transmitted through the spectrometer fell by about 90% between 08:00 to 11:00 and the results are not reliable.

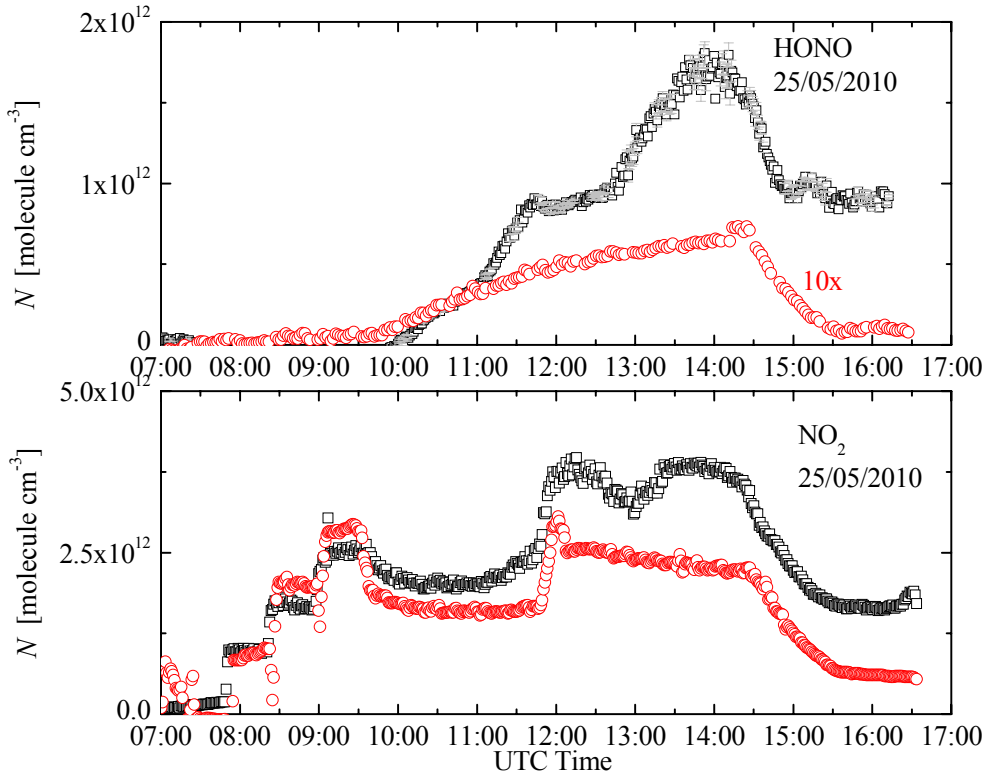


Figure 6.8 Results of IBBCEAS (black) and CEAM-DOAS and CL (red). Note that the DOAS HONO measurements are scaled 10 fold.

Table 6.4 Protocol of expt.3

Time		Action	Time		Action
Start	**End**		**Star**	**End**	
06:34		NO_2 introduction (1 mL)	11:48	12:04	NO second addition (150 ppb)
06:55		NOx range changed	13:08		SO_2 injection (10 ml).
06:59	07:15	NO addition	13:15		Second SO_2 injection (10 ml)
07:21		2nd NO addition (1')	14:27		start flushing
07:49	07:51	O_3 addition	15:33		Stop chamber flushing
08:21	08:23	O_3 addition	15:35		t-butyl hydroperoxide added
08:57	08:59	O_3 addition	16:30		start flushing
09:30	09:36	O_3 addition	15:04		Start chamber flushing

6.4.3 Experiment 4 on 19/05/2010

In order to simulate the full chemical complexity of ambient air without removing the semi-volatile interfering gases, the simulation chamber contents were completely exchanged with ambient air. Interferences for wet chemical instruments also motivated the experiment. For example, nitration of phenols by nitrogen dioxide in solution can form nitrophenols (Coombes et al., 1994). Also, NO_2 in the aqueous phase may react with phenoxide anions in which the overall kinetics are strongly pH dependent. HONO may be subsequently released into the gas phase under acid conditions via protonation of the nitrite ion (Coombes et al., 1994;Ammann et al., 2005).

The chamber was flushed with ambient air early in the morning. The air was directly introduced into the chamber without passing any pipes, tubes or pump to retain the original composition. The roof of the chamber was opened, while flushing with ambient air was maintained. Flushing with ambient air was then stopped and 100 ppb NO_2 was added to the chamber. O-cresol was also added in two steps of 15 ppb mixing ratio each.

HONO in the ambient air was initially at a low level in the morning (Fig. 6.9). Additional HONO was formed after adding NO_2 in the dark around 12:30. The gap in the data before 14:00 arises from the instrument calibration procedure. The IBBCEAS values were very similar to the DOAS results for this ambient air measurement. Although it is close to the HONO detection limit of the IBBCEAS system, the correlation between the instruments is good (0.89) with a slope of 1.1. The NO_2 measurements of both instruments were very similar over much of the day and the overall correlation coefficient was very good with $R^2 = 0.99$. The slope was 1.36, although the IBBCEAS results were higher at the start of the day (Fig. 6.10). Neither of the instruments showed any response upon the addition of o-cresol, but both systems registered a small change in NO_2 concentration when the chamber roof was closed.

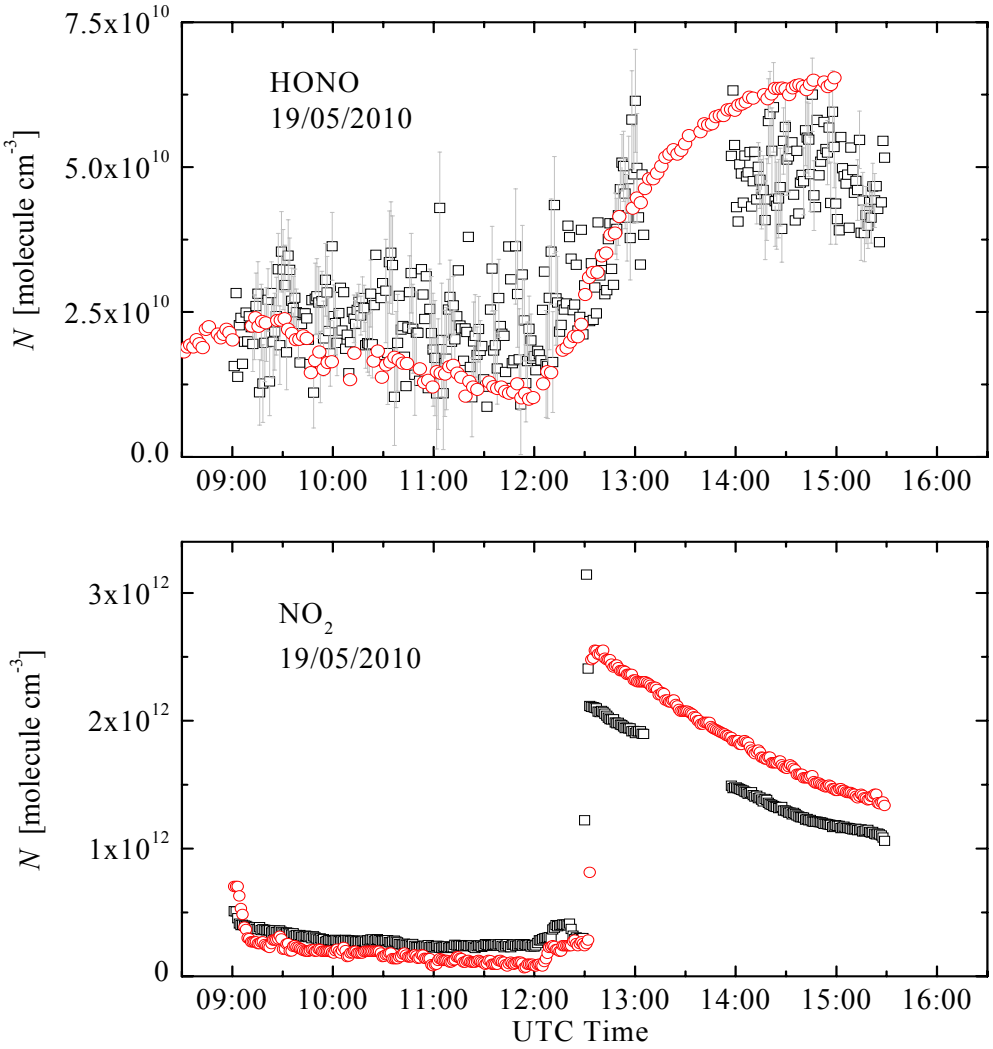


Figure 6.9 Results of IBBCEAS (black) and CEAM-DOAS and CL (red) measurements of HONO and NO_2.

Table 6.5 Protocol of expt. 4

Time		Action
Start	**End**	
10:47		Mixing fan 1 on
11.00		Chamber roof opening
12:00		Chamber closed. Fans stopped. Air inflow set to 40%
12:30		NO_2 addition
13:01	13:07	1st O-cresol addition
14:02	14:09	2nd O-cresol addition
15:25		Start chamber flushing
16:00		Mixing fans on to increase flushing

Spectral fits at 12:00 and 13:00 are included in Appendix A.3 and A.4. At 12:00 when the concentrations of HONO and NO_2 are both low, the NO_2 retrieval appears to be susceptible to residual features in the spectrum. At 13:00, when the NO_2 concentration is high, the spectral fit is much less influenced by such artefacts, and the overall fit clearly matches the obvious NO_2 absorption features.

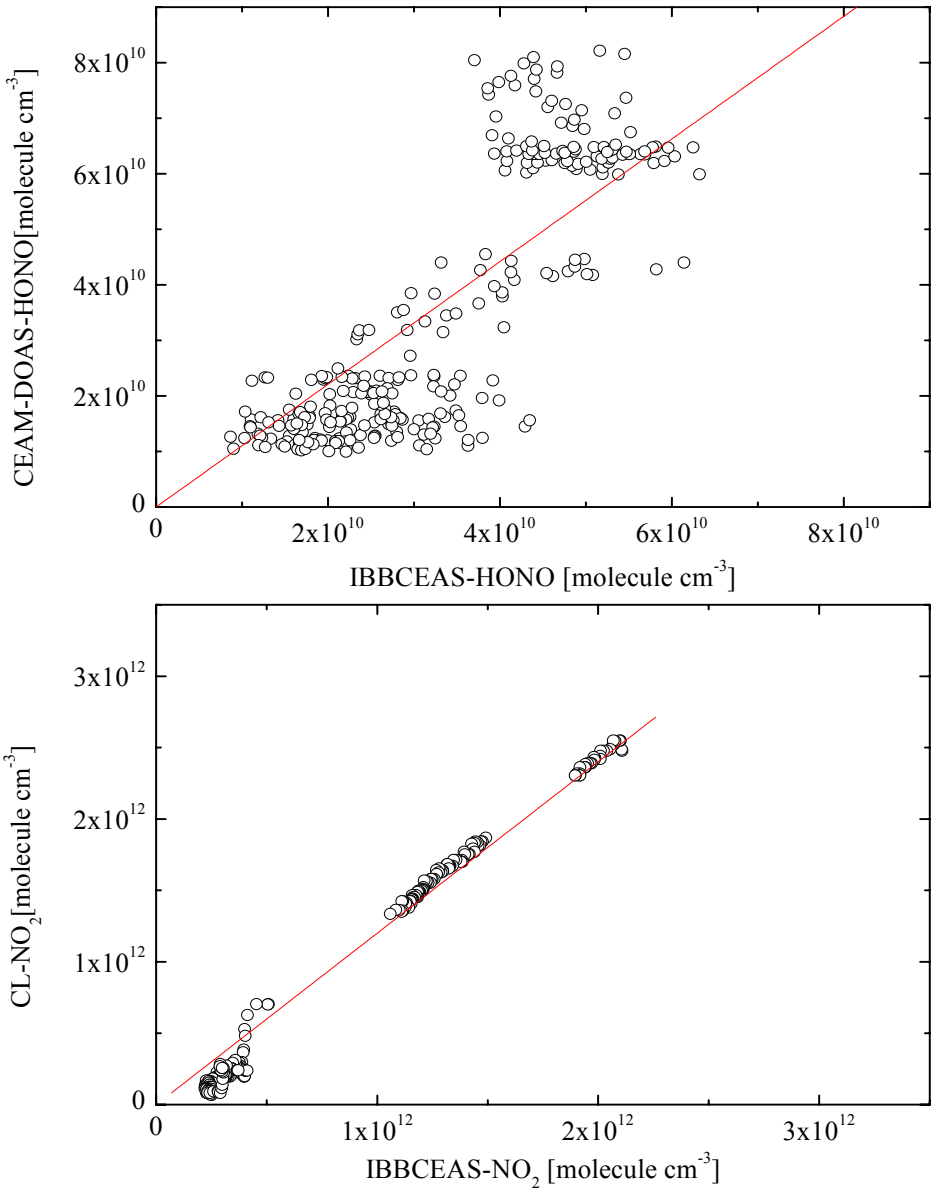


Figure 6.10 Top: the HONO correlation between IBBCEAS and CEAM-DOAS and linearfit (red) with slope=1.1 and R^2=0.89. Bottom: the NO_2 correlation between IBBCEAS and CL detector and linear fitting (red) with slope=1.2 and R^2=0.99

6.4.4 Experiment 5 on 20/05/2010

Isoprene, the most abundant non-methane volatile organic compound (VOC) in the atmosphere, accounts for 34% to 51% of organic carbon emissions. Oxidation of isoprene produces alkyl nitrates in the gas phase and results in secondary organic aerosol (Rollins et al., 2009). The aim of this day's experiment was to investigate the photolytical formation of OH and the resulting oxidation of isoprene. In addition, the influence of particle-bound organic nitrates was studied.

The chamber was flushed overnight and water vapour was added to raise the relative humidity to 40%. Mixing ratios of 30 ppb isoprene and 100 ppb NO were injected into the chamber. Under dark conditions, a maximum of 5-6 ppb HONO was expected to be formed. After opening the roof of the chamber, the OH radical was formed by photolysis of HONO. With the roof open, the maximum HONO concentration expected was 0.9 ppb. After closing the roof of the chamber, α-pinene (30 ppb) and O_3 (100 ppb) were introduced to generate particles and study the influence of particles on the instruments.

HONO was at a low level throughout the experiment and close to the limit of the IBBCEAS sensitivity (Fig. 6.11). IBBCEAS measurements of HONO did not agree well with the DOAS results. The concentration of HONO increased slightly around 10:00. After adding α-pinene and O_3, it decreased to below 1 ppb. However, the sensitivity of the instrument would be degraded due to particle scattering which lowers the effective path length of the system. The NO_2 results from both the IBBCEAS and CL instruments are also shown in Fig 6.11. The retrieved IBBCEAS NO_2 concentration broadly agrees with the results of the CL detector. The CL detector showed interferences from the NO and O_3 introduced into chamber at about 9:00 and 12:00. Different temporal trends of NO_2 are observed from 7:00 to 10:00 and it is unclear why this deviation arises. When the O_3 was added to the chamber at 13:00, the NO_2 concentration was underestimated, possibly due to chemiluminescence from the reaction of NO and O_3. The correlation of the two NO_2 measurements is fair (R^2=0.89) with a slope of 0.95 (Fig. 6.12).

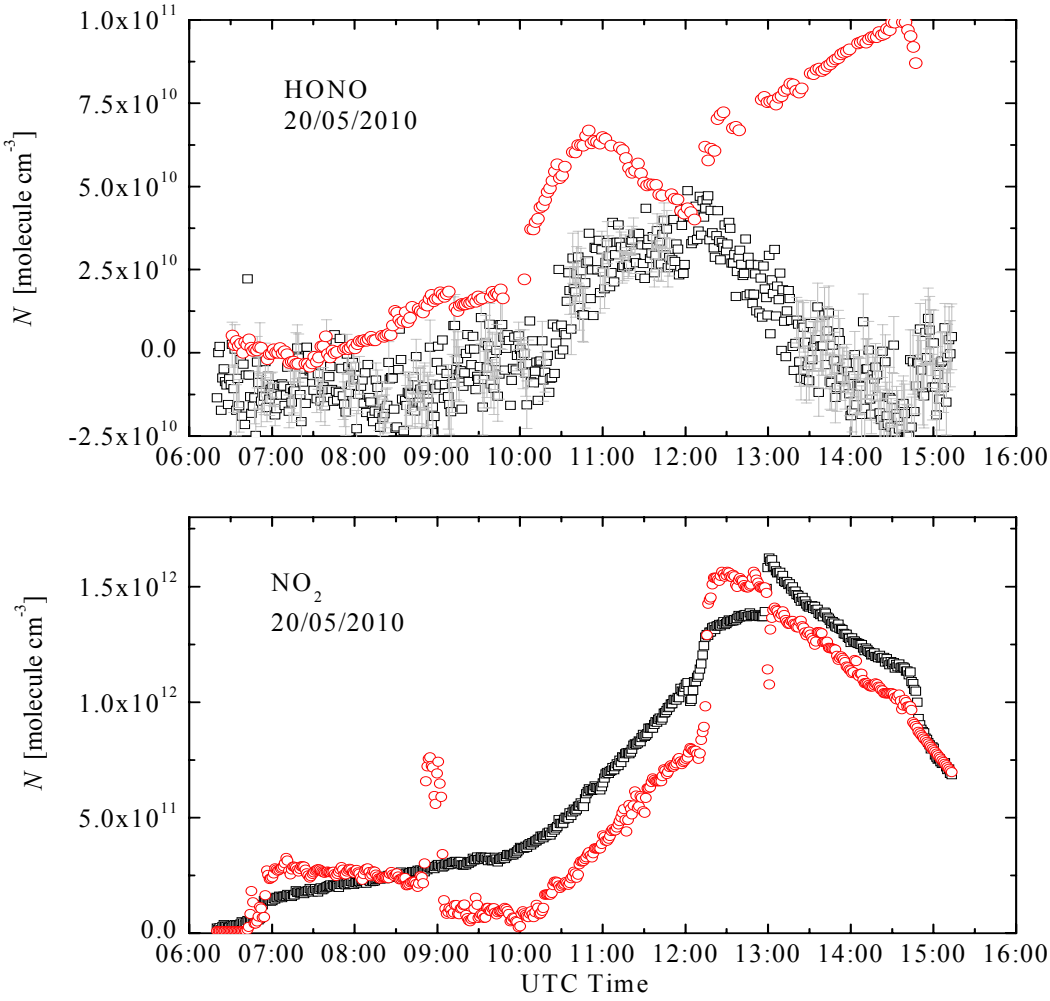


Figure 6.11 Results of IBBCEAS (black) and CEAM-DOAS and CL (red) measurements of HONO and NO_2.

Table 6.6 Protocol of expt. 5

Time		Action
Start	**End**	
06:52		NO_2 introduction (1 mL)
07:23	07:49	Start H_2O introduction
08:38	08:40	Start Isoprene introduction
08:48	09:01	NO addition
09:48		Chamber opened
12:07		Chamber closed
12:14	12:19	Start α-pinene introduction
12:57	13:02	O_3 addition
14:41		Start chamber flushing

Spectral fits at 10:00 and 13:00 are shown in A.5 and A.6. The fitting shows good agreement with the real concentration. At 10:00, when the concentration of HONO is low, there are no readily apparent NO_2 absorption features in the spectrum. In this case the retrieved NO_2 concentration is clearly too high. In contrast, real absorption features of NO_2 are evident at 13:00 and are quite well fitted by the reference spectra. Despite the large difference in absorption at 13:00 and 10:00, however the fit residuals are quite similar.

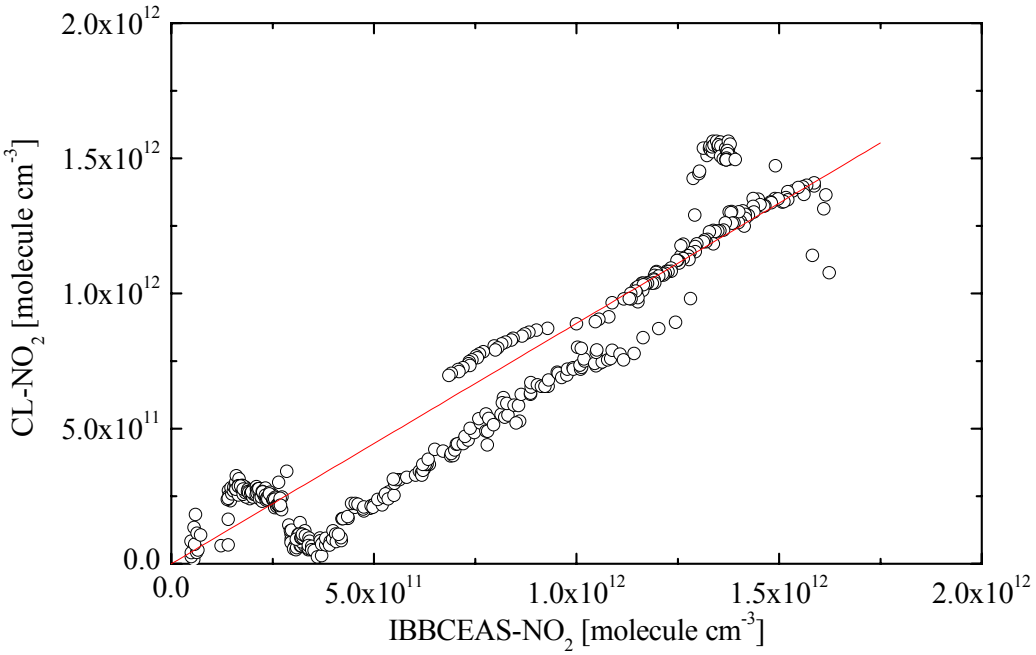


Figure 6.12 The NO_2 correlation between IBBCEAS and CL detector and linear fitting (red) with slope= 0.89 and R^2=0.95.

6.4.5 Experiment 6 on 24/05/2010

This experiment was designed to investigate a recently reported source of HONO via photolysis of nitrophenols (Bejan et al., 2006). The study showed that HONO was produced in a flow photoreactor by near-UV photo-dissociation of 2-nitrophenol (2NP), 3-methyl-2-nitrophenol (3M2NP), 4-methyl-2-nitrophenol (4M2NP) and 5-methyl-2-nitrophenol (5M2NP). The photolysis frequencies (J) were 2.9×10^{-5} s^{-1} for 2NP, 4.4×10^{-5} s^{-1} for 3M2NP, 1.1×10^{-5} s^{-1} for 4M2NP and 2.4×10^{-5} s^{-1} for 5M2NP. Thus the photolysis of nitrophenols may be a significant contribution to HONO formation.

The experiment started from a flushed, dry chamber. 2-nitrophenol at 100 ppb mixing ratio was added to the chamber and half an hour later the roof of the chamber was opened to initiate photolysis.

The observed results from the experiment showed that HONO was present in small concentrations at the start of the experiment (Fig. 6.13). Addition of 2NP is observed as a decrease in the IBBCEAS HONO concentration, while no change is observed for DOAS measurements over this time. This difference arises because the absorption of 2NP was not included in the IBBCEAS spectral analysis. Similar results were also observed in the DOAS results if the 2NP spectrum was omitted from the fit (Ródenas, 2011). In this photochemical reaction system, the NO_2 remains at very low levels and at the limits of detection of both instruments. The strong absorption of 2NP (cf. Chapter 5) results in a reduction of the effective pathlength of the system and the precision of the measurements is notably worse after 12:00.

For this experiment, the concentration of both HONO and NO_2 are close to the instrument detection limit. We therefore did not include correlations with the CEAM measurements and spectra fits.

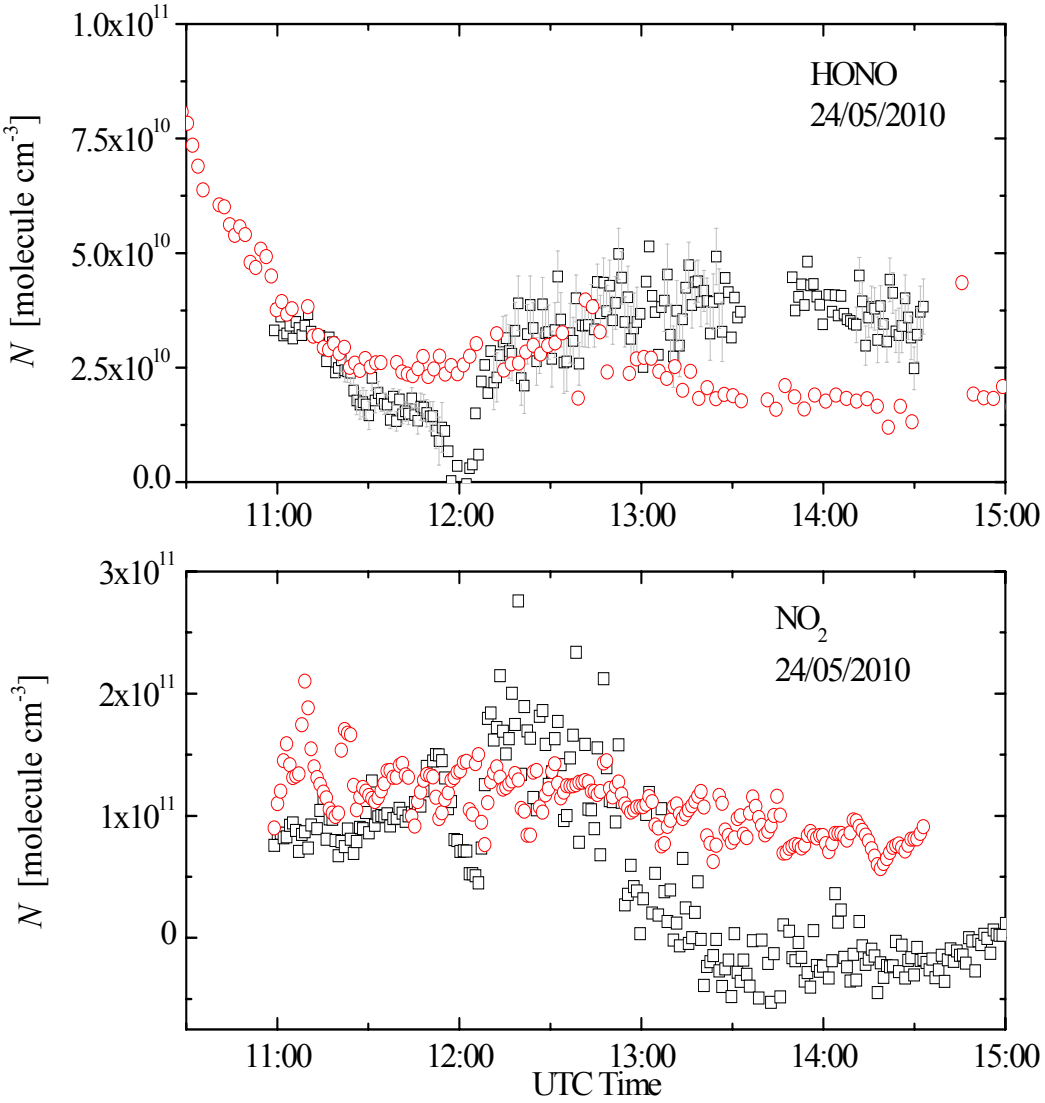


Figure 6.13 Results of IBBCEAS (black) and CEAM-DOAS and CL (red) measurements of HONO and NO_2.

Table 6.7 Protocol of expt. 6

Time		Action
Start	**End**	
11:29	11:29	Flushing stopped
11:40	11:40	Floor cooling on
11:45	12:08	2-nitrophenol introduction (0.1098 g)
12:35		Chamber opened
14:40		chamber closed
14:44	14:44	Start chamber flushing

6.4.6 Experiment 7 on 26/05/2010

This experiment aimed to investigate the formation of PAN from the photolysis of methyl glyoxal. Glyoxal, as one of the most prevalent dicarbonyls in the atmosphere, plays an important role in the formation of secondary organic aerosol (Kroll et al., 2005). Peroxyacetyl nitrate (PAN) is a secondary pollutant present in photochemical smog. The experiment also investigated the role of hydrolysis of PAN in the formation of nitrite.

Up to 130 ppb of O_3 was added to the chamber in three stages, followed by 150 ppb of NO. After formation of NO_2 in the chamber, four additions of 50 ppb of methyl glyoxal were introduced into the chamber. The chamber roof was opened to start the photolysis of methyl-glyoxal and later closed by 30º to evaluate the influence of the actinic flux.

HONO results are shown in Fig 6.14. Levels of HONO were below 1 ppb during the injection of methyl glyoxal. After starting photolysis of the methyl-glyoxal, the HONO concentration rose up to about 2.5 ppb in the chamber. The DOAS instrument observed an increase in HONO after opening the chamber roof. Owing to the low level of HONO being close to both instrument's detection limits, the correlation of the instruments is poor (0.17). In contrast, the NO_2 measurements of the IBBCEAS and CL detector showed good agreement until the chamber roof was opened. NO_2 results from the CL detector again displayed some instability during addition of NO and O_3. After the roof opened, NO_2 results from the IBBCEAS were about 50% higher than those of the CL detector. It is also clear that the IBBCEAS precision degraded between 11:00 and 14:10. The origin of this behavior is not clearly correlated with chemical changes in the chamber and may arise from mechanical interference with the instrument. Another possibility is that SOA formation following photolysis of methyl-glyoxal resulted in a degradation of the effective path length of the IBBCEAS instruments. The different behavior upon opening the chamber roof very likely indicates artefacts in the very long inlet line of the IBBCEAS system. It is also noteworthy that NO_2 from the CL detector recovered after the photolysis of methyl-glyoxal was stopped at 15:00. The correlation of both instruments had an

overall slope of 0.86 (R^2=0.77).

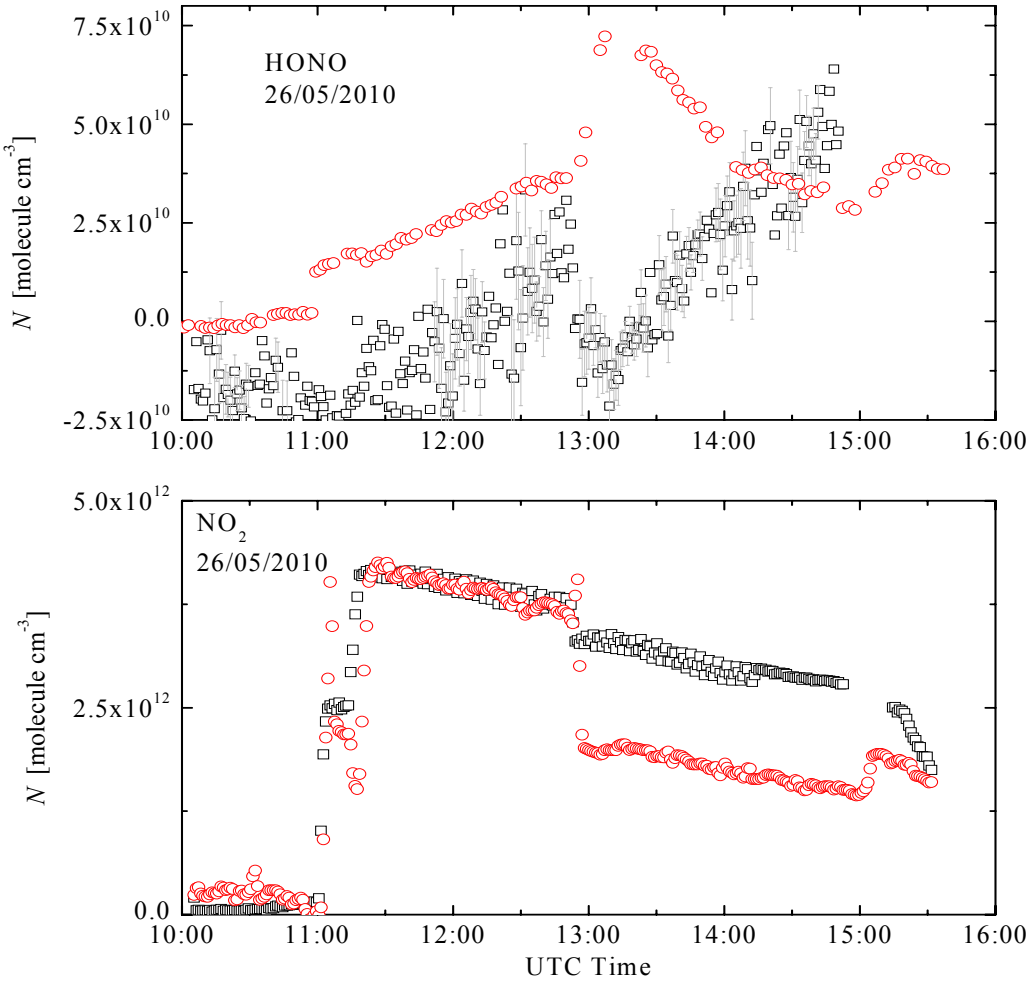


Figure 6.14 Results of IBBCEAS (black) and CEAM-DOAS and CL (red) measurements of HONO and NO_2.

Table 6.8 Protocol of expt. 7

Time		Action	Time		Action
Start	**End**		**Star**	**End**	
10:38	10:45	ozone addition (6'30")	12:07		methyl glyoxal added
10:51	10:55	ozone addition (4'22")	12:19		methyl glyoxal added
10:58	11:02	NO addition (3'29")	12:52		Chamber opened
11:14	11:18	ozone addition (4')	14:09		Chamber cover closed 30°
11:38		methyl glyoxal added	15:00		Chamber closing
11:56		methyl glyoxal added	15:19		Start chamber flushing

Spectral fits at 12:00 and 14:00 are shown in A.9 and A.10. HONO was not clearly observed, but NO_2 was readily identified in both spectra at these high concentrations. The good fit at 14:00 (when CL concentrations were much lower) probably indicates chemical formation of NO_2 in the long inlet line of the IBBCEAS system.

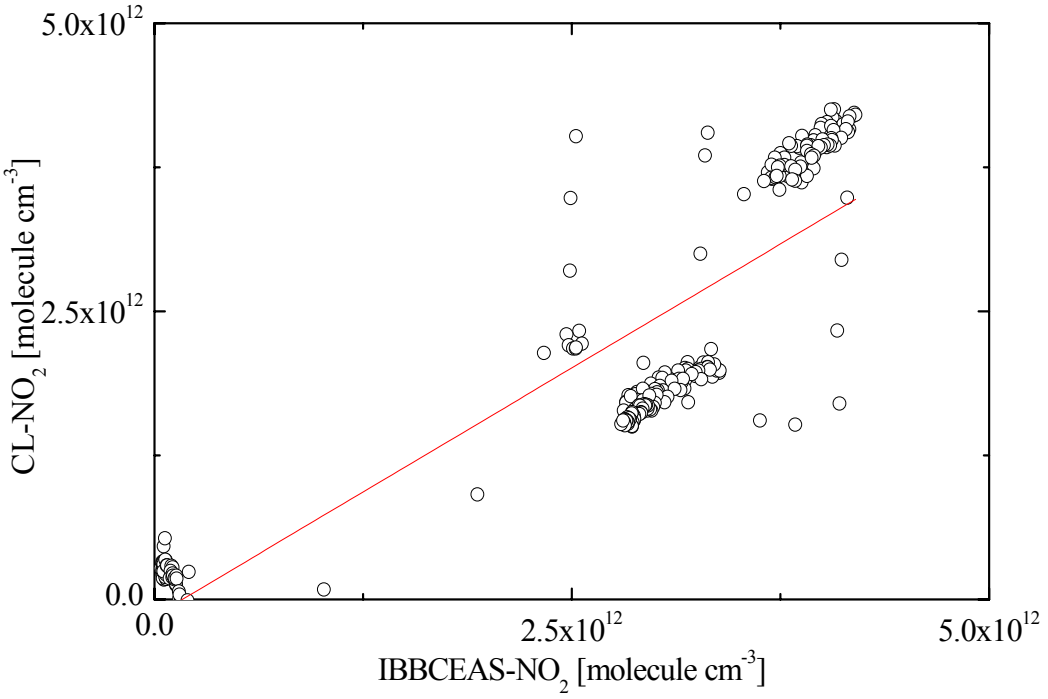


Figure 6.15 The NO_2 correlation between IBBCEAS and CL detector and linear fitting (red) with slope= 0.86 and R^2=0.77

6.4.7 Experiment 8 on 27/05/2010

Direct HONO emissions from automobile exhaust (Kirchstetter et al., 1996;Kurtenbach et al., 2001) and secondary formation on soot particles have recently been investigated (Ammann et al., 1998;Kleffmann et al., 1999;Arens et al., 2001). It is unlikely that direct emissions are a major source of HONO as HONO only comprised 1% of nitrogen oxides. Heterogeneous formation of HONO has been invoked as a possible source, but is still unable to account for the high observed HONO to nitrogen oxides ratio of 0.04 in the atmosphere. Therefore this experiment set out to examine HONO formation from diesel exhaust of semi-volatile and/or water-soluble organics, which have been recently investigated in the laboratory (Gutzwiller et al., 2002).

Hot diesel exhaust gas was added to the clean chamber until about 200 ppb of nitrogen oxides was measured by the CL detector. The roof of the chamber was then opened to start the photochemistry. After an hour, the chamber was re-fueled with exhaust gas and a standard hydrocarbon ('photo smog') mixture of 450 ppb ethene and 150 ppb of mixture of octane and toluene was added.

The HONO results are shown in Fig 6.16. As in Experiment 3, the intensity through the spectrometer dropped significantly over a period of a few hours. The complexity of the diesel exhaust gas appeared to adversely affect the IBBCEAS measurement, resulting in very high observed HONO concentrations of up to 200 ppb. These values are unlikely to represent the actual concentration in the chamber, where a concentration of below 10 ppb of HONO was expected. The concentration observed by DOAS is below 6 ppb. In contrast, the NO_2 results are quite comparable to those from the CL detector. The correlation of both instruments is $R^2 = 0.77$. The CL detector showed quite noisy results, possibly due to interference of the high concentration of organics through the experiment.

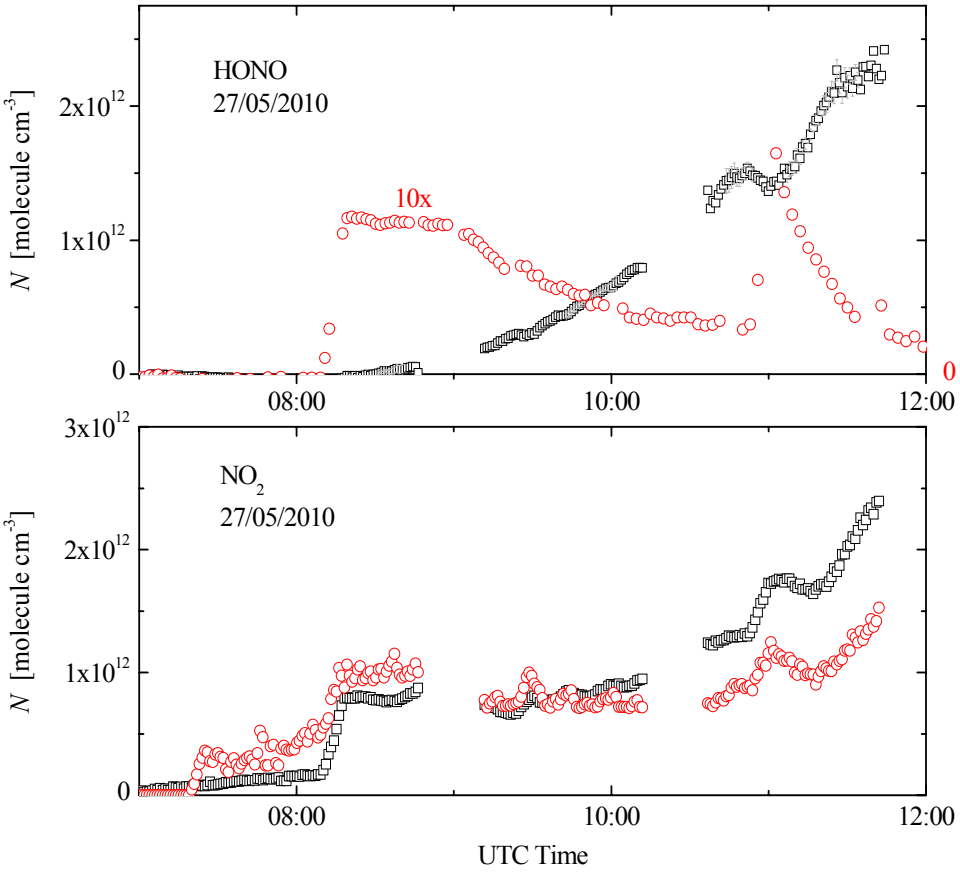


Figure 6.16 Results of IBBCEAS (black) and CEAM-DOAS and CL (red).Note that the DOAS HONO results are scaled by 10 fold.

Table 6.9 Protocol of expt. 8

Time		Action	Time		Action
Start	**End**		**Star**	**End**	
06:48	06:53	p-formaldehyde added	10:53	11:01	diesel exhaust injected
07:29		diesel exhaust injected	11:16		Ethene added (50 ml)
07:36		diesel exhaust injected	11:18		Ethene added (40 ml)
07:42	07:44	diesel exhaust injected	11:21	11:25	octane and toluene added
07:47	08:18	diesel exhaust injected	14:42		Start chamber flushing
08:58		Chamber opened			

6.5 Discussion

6.5.1 Quality of results and estimated uncertainty

Comparison of the IBBCEAS NO_2 values to those of the EUPHORE chamber chemiluminescence (CL) NO_2 values was the principal method of evaluating the IBBCEAS instrument performance before submitting the data for the intercomparison. Despite the large, time-varying deviation associated with the optical stability of the system, NO_2 values from both instruments were usually correlated, especially at higher concentrations. The ratio of measured values varied from about 0.6 to 2.0 for NO_2 concentrations above 40 ppb. The correlation was worse at lower values, where instrumental drift was observed for the IBBCEAS NO_2 values (probably owing to the linear interpolation of I_0 and 1—R), as well as sometimes rather erratic behavior of the CL detector. At low concentrations, the fit procedure is also more susceptible to spectral artefacts from the LED source. The CL detector exhibited some sensitivity to various reactants introduced into the chamber. No evidence of abrupt changes in our instrument response was observed. It would be possible to correct our HONO measurements based on the ratio of NO_2 measurements from the different instruments; however, this approach was rejected as it would introduce into our results any interferences and systematic uncertainties associated with the CL detector. From discussions with CEAM scientists and a first look at the NO_2 data from the intercomparison (Ródenas, 2011), it appears that the CL measurements were generally lower than those of other NO_2 measuring systems.

A robust analysis of the uncertainty is not feasible given the time-dependent variation in the instrument's performance. What follows is an estimate of our uncertainty based on a comparison of the CL and IBBCEAS NO_2 measurements (Fig 6.17). The mean of the ratio of measured NO_2 values from the IBBCEAS system and the CL detector was used to estimate the overall deviation of the measured absorption coefficient. Only CL NO_2 values above 40 ppb were considered (a total of 939 data). The IBBCEAS/CL ratio should scale the retrieved values of both HONO and NO_2 values by the same factor. On average, the NO_2 values reported here were 24% higher than the corresponding CL values, and the standard deviation of the ratio was

0.33. The combined uncertainty of the systematic deviation and the distribution of ratios were used to estimate an uncertainty of 41% in the measured absorption coefficient. Combining this uncertainty with the 15% uncertainty in the HONO cross-sections and 4% uncertainty in the NO_2 cross-sections gives a total uncertainty of around 44% and 41% for HONO and NO_2, respectively. The overall correlation showed that the main underestimations of NO_2 were from Experiment 4 and 7.

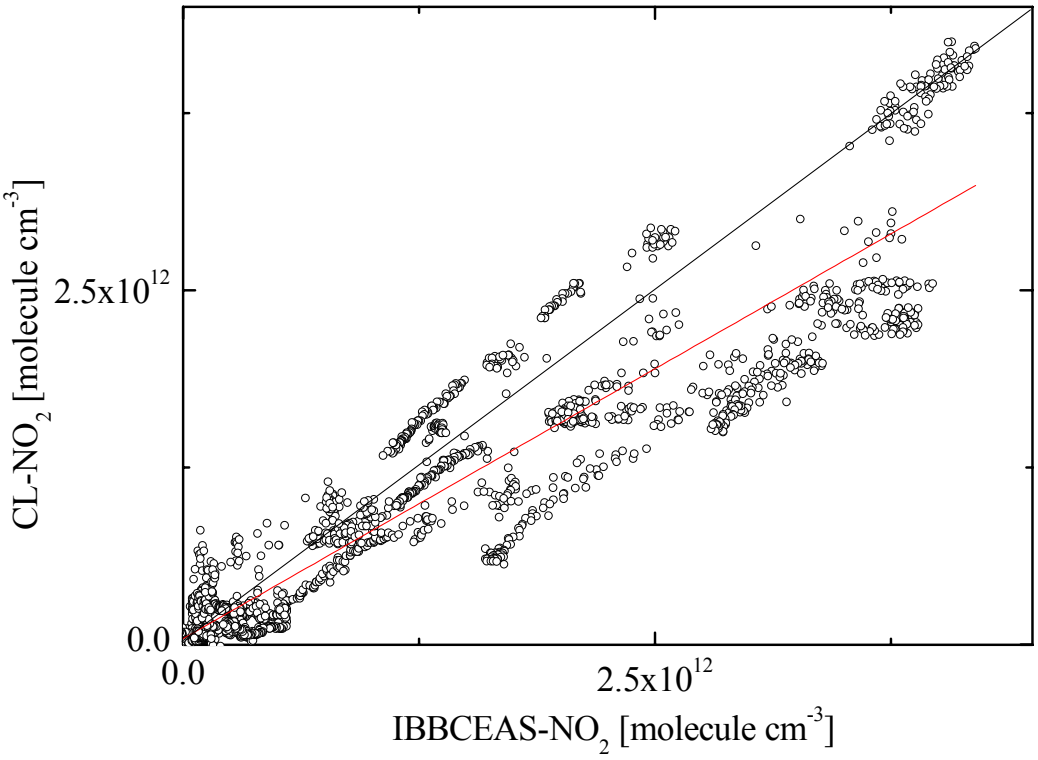


Figure 6.17 Overall comparisons of the IBBCEAS NO_2 measurements with those of the chemiluminescence detector. The linear fitting (red) has a slope=0.76 intercept: 4.36×10^{10} and R^2=0.86. The 1:1 ratio line is shown in black.

6.5.2 Interferences and improvements to the spectrometer

Besides the issue of thermal expansion which degraded the cavity alignment, particles formed during the experiment also influence the IBBCEAS measurements. From Experiments 5, 7 and 8, the formation of particles in the chamber resulted in a loss of sensitivity and over-estimation of NO_2 compared to CL results. However, the influence of species such as SO_2, O_3 and t-butyl nitrite, whose absorption bands overlapped that of HONO, was not observed, mainly because the absorption of these species was weak at the concentrations used in these experiments.

Based on issues encountered during the campaign, the IBBCEAS system performance can be improved in several ways: (a) A more rigid sample tube material with a lower thermal expansion coefficient is needed for the body of the cavity to maintain long term stability of the cavity alignment under high thermal gradients. Reducing the length of the cavity to 1 m would also improve the stability over the longer cavity. (b) The signal-to-noise ratio would be improved by stabilizing the spectral output of the LED by an active temperature stabilization coupled with a low drift constant current driver. (c) As the particles inside the cavity reduce the effective path length and result in a loss of sensitivity, one way to avoid this influence is by filtering the inlet stream. In this case, inlet losses for the species measured would need to be determined beforehand. (d) The inlet line artefacts should be minimized by using a shorter line within 2 m that most other instruments adopted. (e) Regular calibration of the mirrors, such as by SO_2 injection, would help to correct the measurement if system alignment degraded. (f) A wider spectral measurement window, such as with a Xe arc lamp, will help to identify the species more accurately and precisely.

6.6 Conclusions

In this chapter, an extractive-IBBCEAS instrument was developed for the FIONA campaign held in the EUPHORE chamber. The instrument is specifically for measuring HONO and NO_2 in the near-UV band from 355 to 375 nm. From participation in 8 experiments during the campaign, the instrument was tested for extractive measurement of chamber experiment. From a non-blind calibration experiment, the instrument showed good agreement with other techniques. In the blind experiments, the instrument responded to major chemical changes in the chamber. NO_2 retrieved results were compared with those from a CL detector and an overall uncertainty of the instrument was derived from the inter-comparison. Changes in the path length of the IBBCEAS instrument occurred due to thermal instabilities of the system during the experiments. This fact, together with the use of a long sampling line would help to explain most of the differences encountered. Despite the issues met in the campaign, the IBBCEAS instrument developed has a sensitivity of about 10^{-9} cm^{-1}, corresponding to 0.3 ppb of HONO and 0.2 ppb of NO_2. The detection limit of the IBBCEAS system is higher than that of LOPAP and LIF, but is comparable to the multi-pass DOAS instrument on the EUPHORE chamber, which has a similar detection limit for HONO of about 0.4 ppb. The detection limit is better than the FTIR system which about 1.5 ppb. The current instrument would be suited to simulation chamber measurements and to field observations in polluted environments. Having a broader spectral window would improve the instrument's sensitivity and reduce the influence of spectral interferences. Either multiple LEDs (as used by other IBBCEAS instruments) or a Xe arc lamp source would be able to accomplish this. Several other modifications of the instrument were suggested to improve the system performance.

Bibliography

Ammann, M., Kalberer, M., Jost, D. T., Tobler, L., Rossler, E., Piguet, D., Gaggeler, H. W., and Baltensperger, U.: Heterogeneous production of nitrous acid on soot in polluted air masses, Nature, 395, 157-160, 1998.

Ammann, M., Rossler, E., Strekowski, R., and George, C.: Nitrogen dioxide multiphase chemistry: Uptake kinetics on aqueous solutions containing phenolic compounds, Phys. Chem. Chem. Phys., 7, 2513-2518, 2005.

Arens, F., Gutzwiller, L., Baltensperger, U., Gaggeler, H. W., and Ammann, M.: Heterogeneous reaction of NO_2 on diesel soot particles, Environ. Sci. Technol., 35, 2191-2199, 2001.

Bejan, I., Abd El Aal, Y., Barnes, I., Benter, T., Bohn, B., Wiesen, P., and Kleffmann, J.: The photolysis of ortho-nitrophenols: a new gas phase source of HONO, Phys. Chem. Chem. Phys., 8, 2028-2035, 2006.

Chen, J., and Venables, D. S.: A broadband optical cavity spectrometer for measuring weak near-ultraviolet absorption spectra of gases, Atmos. Meas. Tech., 4, 425-436, :10.5194/amt-4-425-2011, 2011.

Febo, A., Perrino, C., and Cortiello, M.: A Denuder Technique for the Measurement of Nitrous-Acid in Urban Atmospheres, Atmos. Environ. A, 27, 1721-1728, 1993.

Febo, A., and Perrino, C.: Measurement of High-Concentration of Nitrous-Acid inside Automobiles, Atmos. Environ., 29, 345-351, 1995.

Ferm, M., and Sjodin, A.: A Sodium-Carbonate Coated Denuder for Determination of Nitrous-Acid in the Atmosphere, Atmos. Environ., 19, 979-983, 1985.

Fiedler, S. E., Hoheisel, G., Ruth, A. A., and Hese, A.: Incoherent broad-band cavity-enhanced absorption spectroscopy of azulene in a supersonic jet, Chem. Phys. Lett., 382, 447-453, 10.1016/j.cplett.2003.10.075, 2003.

Gherman, T., Venables, D. S., Vaughan, S., Orphal, J., and Ruth, A. A.: Incoherent broadband cavity-enhanced absorption spectroscopy in the near-ultraviolet: Application to HONO and NO_2, Environ. Sci. Technol., 42, 890-895, 2008.

Gutzwiller, L., Arens, F., Baltensperger, U., Gaggeler, H. W., and Ammann, M.: Significance of semivolatile diesel exhaust organics for secondary HONO

formation, Environ. Sci. Technol., 36, 677-682, 2002.

Hanst, P. L., Wong, N. W., and Bragin, J.: A Long-Path Infrared Study of Los-Angeles Smog, Atmos. Environ., 16, 969-981, 1982.

Harrison, R. M., Peak, J. D., and Collins, G. M.: Tropospheric cycle of nitrous acid, J. Geophys. Res.-Atmos., 101, 14429-14439, 1996.

Huang, G., Zhou, X. L., Deng, G. H., Qiao, H. C., and Civerolo, K.: Measurements of atmospheric nitrous acid and nitric acid, Atmos. Environ., 36, 2225-2235, 2002.

Kirchstetter, T. W., Harley, R. A., and Littlejohn, D.: Measurement of nitrous acid in motor vehicle exhaust, Environ. Sci. Technol., 30, 2843-2849, 1996.

Kleffmann, J., H. Becker, K., Lackhoff, M., and Wiesen, P.: Heterogeneous conversion of NO_2 on carbonaceous surfaces, Phys. Chem. Chem. Phys., 1, 5443-5450, 1999.

Kleffmann, J., Heland, J., Kurtenbach, R., Lorzer, J., and Wiesen, P.: A new instrument (LOPAP) for the detection of nitrous acid (HONO), Environ. Sci. Pollut. R., 48-54, 2002.

Kleffmann, J., Kurtenbach, R., Lorzer, J., Wiesen, P., Kalthoff, N., Vogel, B., and Vogel, H.: Measured and simulated vertical profiles of nitrous acid - Part I: Field measurements, Atmos. Environ., 37, 2949-2955, 2003.

Kleffmann, J., and Wiesen, P.: Heterogeneous conversion of NO_2 and NO on HNO_3 treated soot surfaces: atmospheric implications, Atmos. Chem. Phys., 5, 77-83, 2005.

Kleffmann, J., Lorzer, J. C., Wiesen, P., Kern, C., Trick, S., Volkamer, R., Rodenas, M., and Wirtz, K.: Intercomparison of the DOAS and LOPAP techniques for the detection of nitrous acid (HONO), Atmos. Environ., 40, 3640-3652, 2006.

Kroll, J. H., Ng, N. L., Murphy, S. M., Varutbangkul, V., Flagan, R. C., and Seinfeld, J. H.: Chamber studies of secondary organic aerosol growth by reactive uptake of simple carbonyl compounds, J. Geophys. Res.-Atmos., 110, 2005.

Kurtenbach, R., Becker, K. H., Gomes, J. A. G., Kleffmann, J., Lorzer, J. C., Spittler, M., Wiesen, P., Ackermann, R., Geyer, A., and Platt, U.: Investigations of emissions and heterogeneous formation of HONO in a road traffic tunnel, Atmos. Environ., 35, 3385-3394, 2001.

Platt, U., Perner, D., Harris, G. W., Winer, A. M., and Pitts, J. N.: Observations of Nitrous-Acid in an Urban Atmosphere by Differential Optical-Absorption, Nature, 285, 312-314, 1980.

Ródenas, G. M.-Personal communication 2011

Ren, X. R., Harder, H., Martinez, M., Lesher, R. L., Oliger, A., Simpas, J. B., Brune, W. H., Schwab, J. J., Demerjian, K. L., He, Y., Zhou, X. L., and Gao, H. G.: OH and HO_2 chemistry in the urban atmosphere of New York City, Atmos. Environ., 37, 3639-3651, 2003.

Rollins, A. W., Kiendler-Scharr, A., Fry, J. L., Brauers, T., Brown, S. S., Dorn, H. P., Dubé, W. P., Fuchs, H., Mensah, A., Mentel, T. F., Rohrer, F., Tillmann, R., Wegener, R., Wooldridge, P. J., and Cohen, R. C.: Isoprene oxidation by nitrate radical: alkyl nitrate and secondary organic aerosol yields, Atmos. Chem. Phys., 9, 6685-6703, 10.5194/acp-9-6685-2009, 2009.

Schiller, C. L., Locquiao, S., Johnson, T. J., and Harris, G. W.: Atmospheric measurements of HONO by tunable diode laser absorption spectroscopy, J. Atmos. Chem., 40, 275-293, 2001.

Spindler, G., Hesper, J., Brüggemann, E., Dubois, R., Müller, T., and Herrmann, H.: Wet annular denuder measurements of nitrous acid: laboratory study of the artefact reaction of NO_2 with S(IV) in aqueous solution and comparison with field measurements, Atmos. Environ., 37, 2643-2662, 2003.

Stutz, J., Kim, E. S., Platt, U., Bruno, P., Perrino, C., and Febo, A.: UV-visible absorption cross sections of nitrous acid, J. Geophys. Res.-Atmos., 105, 14585-14592, 2000.

Voigt, S., Orphal, J., and Burrows, J. P.: The temperature and pressure dependence of the absorption cross-sections of NO_2 in the 250-800 nm region measured by Fourier-transform spectroscopy, J. Photochem. Photobiol. A, 149, 1-7, 2002.

Wang, L. M., and Zhang, J. S.: Detection of nitrous acid by cavity ring down spectroscopy, Environ. Sci. Technol., 34, 4221-4227, 2000.

Zhou, X. L., Civerolo, K., Dai, H. P., Huang, G., Schwab, J., and Demerjian, K.: Summertime nitrous acid chemistry in the atmospheric boundary layer at a rural site in New York State, J. Geophys. Res.-Atmos, 107, DOI: 10.1029/2001jd001539, 2002.

Chapter 7

CONCLUSIONS

7.1 Summary of findings

Incoherent broadband cavity enhanced absorption spectroscopy (IBBCEAS) was developed for sensitive near-UV absorption measurements and tested in several experimental systems. The near-UV is particularly important in tropospheric photochemistry and a number of important atmospherically relevant species can be identified by their electronic absorption in this region. However, there are a limited number of techniques with high sensitivity to near-UV absorptions, and these typically have important drawbacks. In this context, extending the IBBCEAS technique further into the near-UV will help to improve our understanding of the absolute absorption cross-sections as well as the quantification of trace species in the atmosphere or in simulation chamber experiments.

An IBBCEAS spectrometer coupled to a flow cell was developed for laboratory measurements. The system was capable of operating at low pressure as well as at ambient atmospheric pressures. With moderate cavity mirror reflectivity (99.6%), the spectrometer had an absorption sensitivity of around 10^{-8} cm^{-1} between 330 nm and 380 nm. The absorption cross-sections of several atmospheric species which absorb very weakly in this range – SO_2, O_3, acetone, 2-butanone and 2-pentanone – were measured with the spectrometer (Chen and Venables, 2011). The results showed good agreement with the literature cross-sections where these agree among themselves, although where the absorption is very weak the deviation among literature spectra is much larger and our cross-sections are preferable in these circumstances owing to the much higher sensitivity of our technique. The O_4 dimer peak at 360.5 nm was also measured and a cross-section of 4.0×10^{-46} cm^5 $molecule^{-2}$ was determined, in good agreement with earlier work. The reactive halogen species BrO was generated in low

concentration via steady state photolysis of Br_2 and reaction with O_3 in the flow cell. All three species were simultaneously monitored during the experiment, illustrating the value of a wide spectral window.

A near-UV IBBCEAS system was set up on the simulation chamber in the CRAC laboratory. As the simulation chamber provided low wall losses as well as a large volume, it is well suited to measuring spectra of low volatility species as well as the optical properties of secondary organic aerosol (SOA) (Carrasco et al., 2007;Coeur-Tourneur et al., 2009). The system had a 140 nm spectral range that extended from 320 to 460 nm, giving it both the widest spectral window and the shortest wavelength limit of any cavity technique yet reported. The system was calibrated with methyl vinyl ketone to account for the variation of the chamber volume due to the flexible FEP bag. The absorption cross-section of benzaldehyde was determined and showed good agreement compared to the literature spectra (Thiault et al., 2004;Xiang et al., 2009). Spectra of tert-butyl nitrite, isobutyl-nitrite, butyl-nitrite, isopentyl-nitrite, were also determined. Absorption cross-sections of the π (benzene ring) $\rightarrow$ π^* (nitro group) transition of 2-nitrophenol, 3-methyl-2-nitrophenol and 4-methyl-2-nitrophenol were measured and to our knowledge are the first reported gas phase spectra of these compounds (Ishag and Moseley, 1977;Wang et al., 2006). The quantum yields of photolysis of the nitrophenols were refined based on new cross-sections (Bejan et al., 2006). An experiment investigating the photooxidation of isoprene by OH in high NO_x conditions to form SOA was also carried out. Concentrations of HONO and NO_2 were retrieved based on their UV absorptions. The aerosol extinction retrieved by the IBBCEAS system correlated well with particle size and has potential for use in future aerosol studies.

An extractive IBBCEAS instrument was designed and built to participate in the Formal Intercomparison of Nitrous Acid (FIONA) campaign in the EUPHORE chamber (Valencia, Spain). Instead of the Xe arc lamp used in other systems, a high power (250 mW) light emitting diode centered at 365 nm was used as light source in this instrument. With its higher reflectivity mirror (99.95%), the sensitivity of the instrument was *ca.* 10^{-9} cm^{-1} corresponding to around 0.3 ppb of HONO. HONO results from the FIONA experiments were presented and compared with the CEAM-DOAS instrument, while NO_2 results were compared against a chemiluminescence NO_x detector. Regrettably, the IBBCEAS instrument was not stable under the high thermal gradients encountered during the campaign and thermal effects were evident in the LED output. In addition, the long inlet line probably introduced significant sampling artefacts in the measurement of HONO and NO_2. These issues aside, the instrument was still responsive to chemical changes inside the chamber. An overall 40% uncertainty was obtained from comparing with CL NO_2 results during this campaign. Future improvements were suggested for the extractive IBBCEAS instrument.

Two open path configuration IBBCEAS instruments were built for field campaigns in Canada and Ireland. One instrument stood on a heavy duty tripod while the other had a dual cavity (with a single spectrograph) for two spectral windows. Owing to the rather extreme environmental conditions and other setbacks, neither system produced useful results. Nevertheless, these field campaigns indicated the importance (and difficulty) of aligning and maintaining a stable optical cavity (as in the FIONA campaign). In addition the Mace Head campaign demonstrated the feasibility of using a dual cavity IBBCEAS system which was subsequently implemented on the ERI simulation chamber.

The above results demonstrated that the IBBCEAS technique is a sensitive *in-situ* approach for near-UV absorption measurements and can be used to study a number of atmospheric species. The wide spectral window is particularly valuable for monitoring several species simultaneously as well as for measuring useful absorption cross-sections. However, there are some drawbacks and difficulties in the approach. Intensity changes in the light source can introduce spurious absorption features and should be normalized. Lack of high power UV sources is another difficulty. Xe arc lamps provide a wide emission spectrum but need intensive filtering to avoid transmission of high levels of background light into the spectrograph. Although high power LEDs are compact, low cost and efficient – and thus especially suitable for the field instruments – they are only available down to 365 nm. In this study we found that the temperature-dependent spectral output of the LED also introduced artefacts in the extinction spectrum. The IBBCEAS system uncertainty is dominated by the uncertainty of mirror calibration. Currently the absolute calibration uncertainty depends on the deviation of literature cross-sections and the stability of the light source. Last but not least, the mechanical stability for maintaining an optical resonator is a key condition for field instruments.

7.2 Future work

This work has largely focused on gas phase absorption spectra in the near-UV using the IBBCEAS technique. The system coupled to the simulation chamber is clearly a useful tool for measuring the absorption of low volatility compounds and should be extended to the absorption of other organic species. The application of the technique to aerosols has also attracted recent attention but has been restricted to visible wavelengths (Varma et al., 2009). As the UV optical properties of aerosols are not

well known and are important in radiative forcing, the near-UV IBBCEAS instrument could provide valuable insight into these climatically important atmospheric constituents.

Extending the technique to shorter wavelengths to study new species is in principle possible. Shorter wavelengths are more difficult to study owing to the lower output from lamps, poorer efficiency of detectors and greater scattering from gases and particles. However, shorter wavelengths are attractive for studying several important compounds. In particular, the OH radical has a strong absorption near 308 nm and direct quantification in atmosphere simulation chambers would be desirable. As the OH absorption is very narrow with a rotational line width of 2.5 pm, (Dorn et al., 1996) a high resolution echelle spectrograph would be most appropriate for such an instrument. Although the IBBCEAS sensitivity to OH would not match LIF-based systems, it could still be useful under high OH conditions in chamber or laboratory experiments. Another important class of reactants are the aromatic VOCs which absorb strongly between 250 nm and 300 nm. Monitoring oxidation of aromatic compounds would allow reaction pathways and kinetics to be better understood.

Field observations of atmospheric constituents are still an interesting and relatively unexplored application of the technique. Future work needs to develop a more robust mechanical system, while a means to regularly calibrate the system during measurements is highly desirable. If these conditions are fulfilled then important reactive species such as BrO, HONO, IO would be obvious targets and would encourage more extensive deployment of the technique in the field.

Bibliography

Bejan, I., Abd El Aal, Y., Barnes, I., Benter, T., Bohn, B., Wiesen, P., and Kleffmann, J.: The photolysis of ortho-nitrophenols: a new gas phase source of HONO, Phys. Chem. Chem. Phys., 8, 2028-2035, 2006.

Carrasco, N., Doussin, J. F., O'Connor, M., Wenger, J. C., Picquet-Varrault, B., Durand-Jolibois, R., and Carlier, P.: Simulation chamber studies of the atmospheric oxidation of 2-methyl-3-buten-2-ol: Reaction with hydroxyl radicals and ozone under a variety of conditions, J. Atmos. Chem., 56, 33-55, 2007.

Chen, J., and Venables, D. S.: A broadband optical cavity spectrometer for measuring weak near-ultraviolet absorption spectra of gases, Atmos. Meas. Tech., 4, 425-436, 10.5194/amt-4-425-2011, 2011.

Coeur-Tourneur, C., Tomas, A., Guilloteau, A., Henry, F., Ledoux, F., Visez, N., Riffault, V., Wenger, J. C., and Bedjanian, Y.: Aerosol formation yields from the reaction of catechol with ozone, Atmos. Environ., 43, 2360-2365, 10.1016/j.atmosenv.2008.12.054, 2009.

Dorn, H. P., Brandenburger, U., Brauers, T., Hausmann, M., and Ehhalt, D. H.: In-situ detection of tropospheric OH radicals by folded long-path laser absorption. Results from the POPCORN field campaign in August 1994., Geophys. Res. Lett., 23, 2537-2540, 1996.

Ishag, M. I. O., and Moseley, P. G. N.: Effects of UV Light on Dilute Aqueous-Solutions of Meta-Nitrophenol and Para-Nitrophenol, Tetrahedron, 33, 3141-3144, 1977.

Thiault, G., Mellouki, A., Le Bras, G., Chakir, A., Sokolowski-Gomez, N., and Daumont, D.: UV-absorption cross sections of benzaldehyde, ortho-, meta-, and para-tolualdehyde, J. Photochem. Photobiol. A, 162, 273-281, 2004.

Varma, R. M., Venables, D. S., Ruth, A. A., Heitmann, U., Schlosser, E., and Dixneuf, S.: Long optical cavities for open-path monitoring of atmospheric trace gases and aerosol extinction, Appl. Opt., 48, B159-B171, 2009.

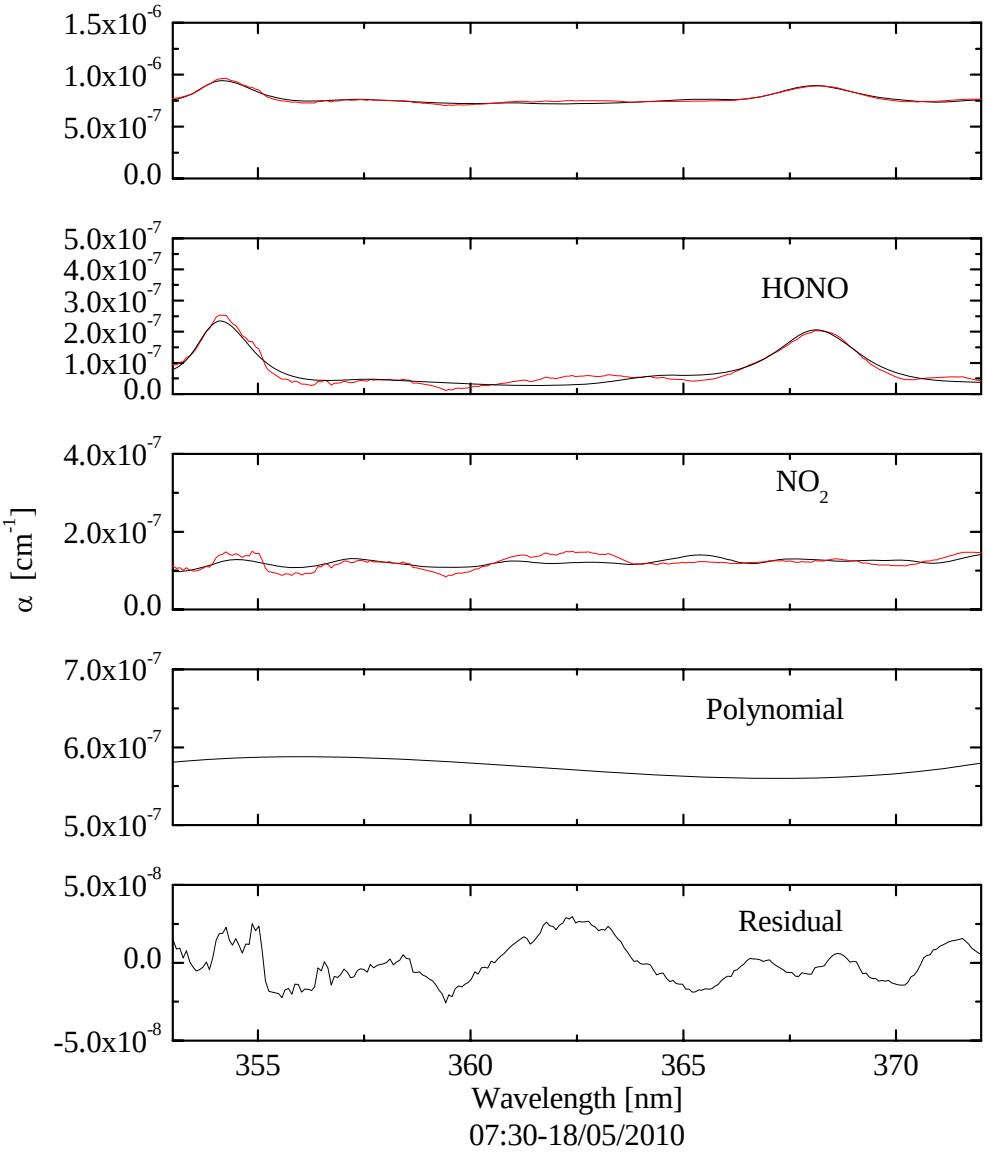
Wang, Y. Q., Wang, H. G., Zhang, S. Q., Pei, K. M., Zheng, X. M., and Phillips, D. L.:

Resonance Raman intensity analysis of the excited state proton transfer dynamics of 2-nitrophenol in the charge-transfer band absorption, J. Chem. Phys., 125, 2006.

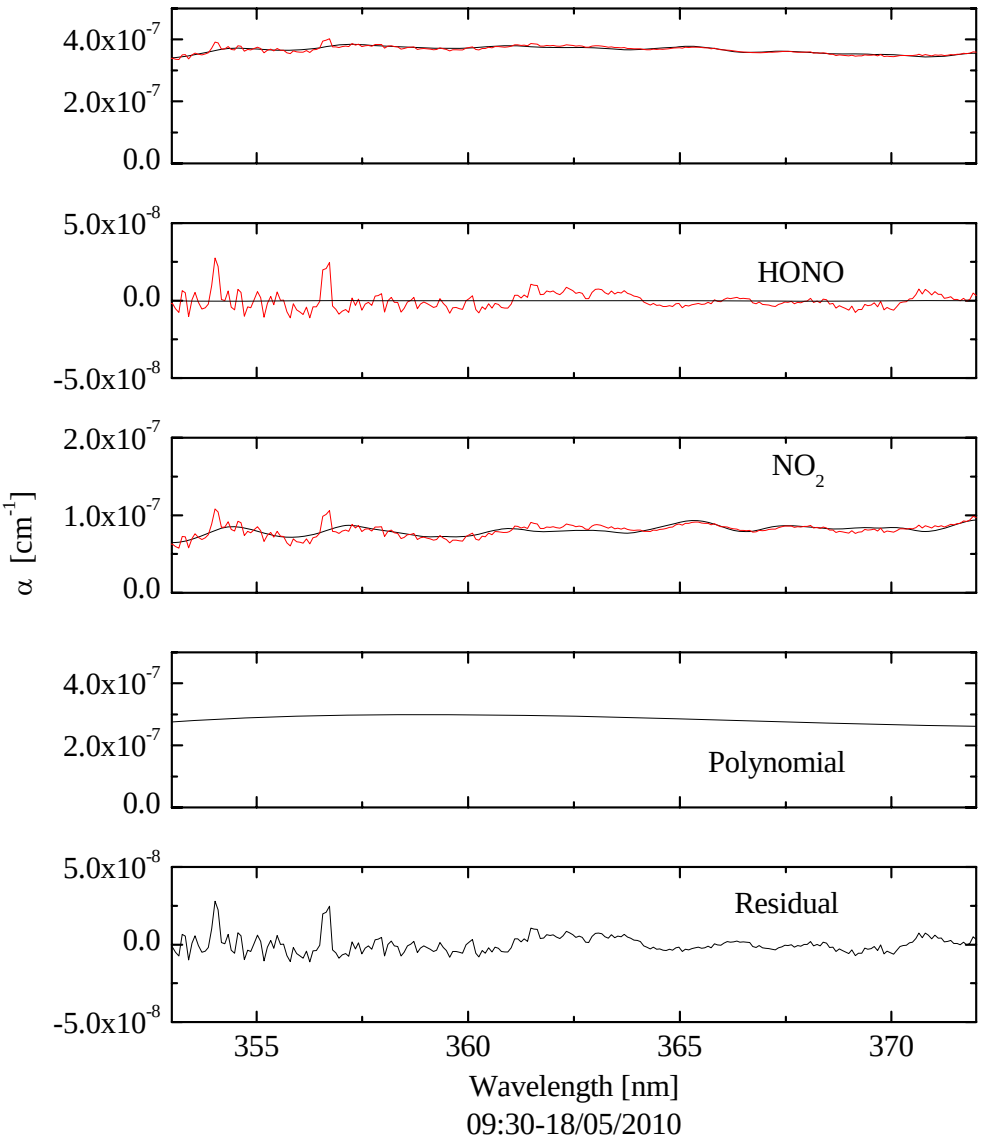
Xiang, B., Zhu, C. Z., and Zhu, L.: Gas-phase absorption cross sections of 2-nitrobenzaldehyde and benzaldehyde in the 285-400 nm region, and photolysis of 2-nitrobenzaldehyde vapor at 308 and 351 nm, Chem. Phys. Lett., 474, 74-78, 2009.

Appendix A

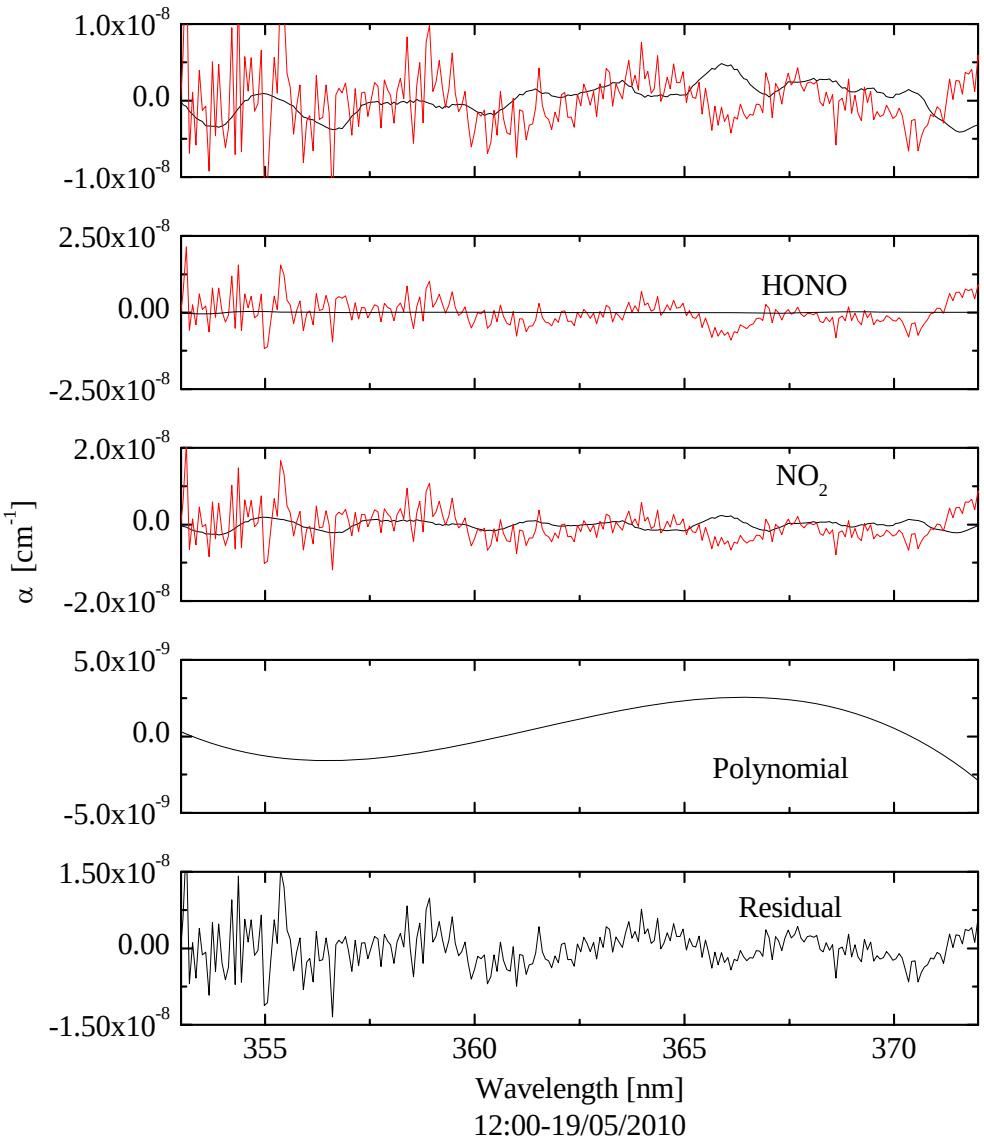
A.1 Spectral fit on 18/05/2010 (07:30)



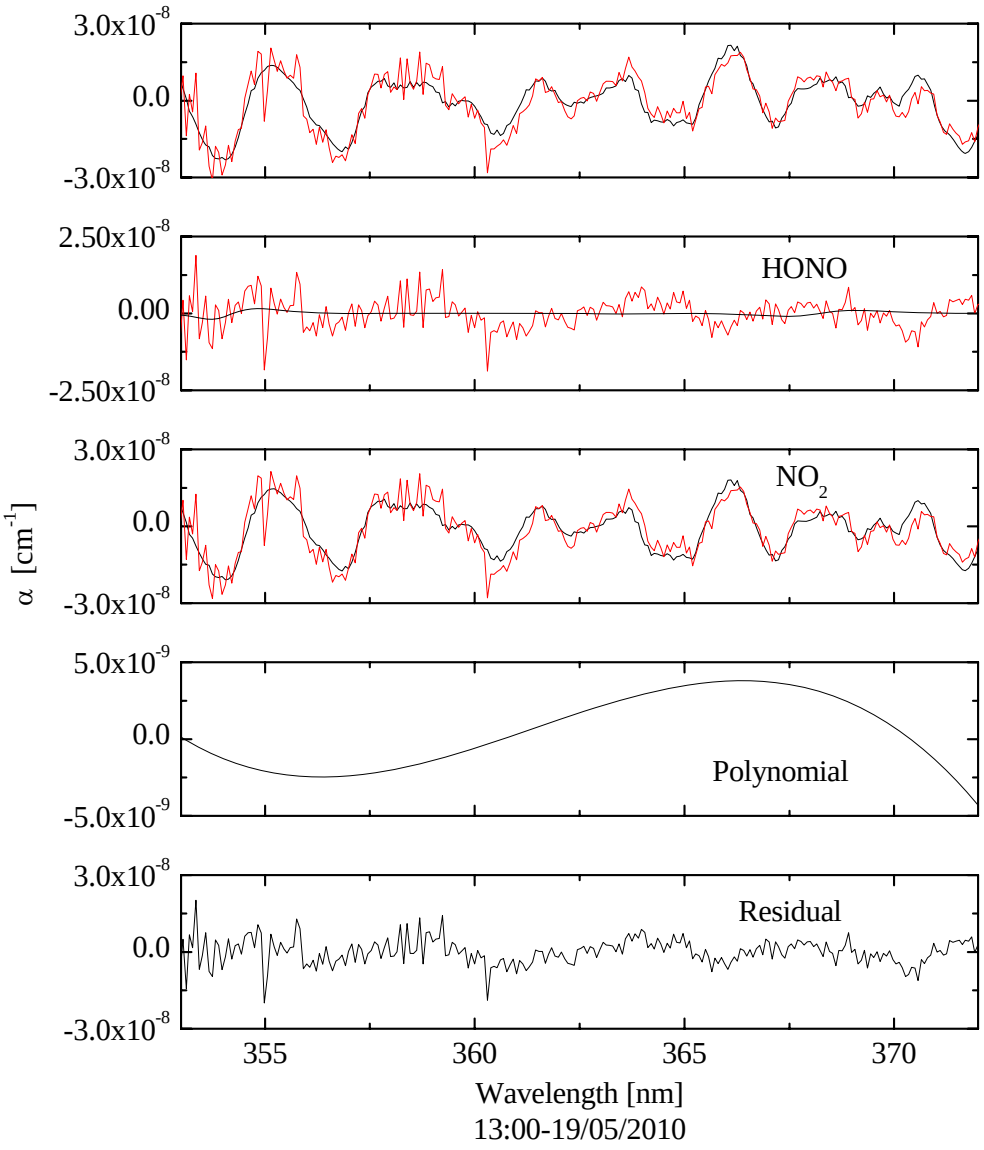
A.2 Spectral fit on 18/05/2010 (09:30)



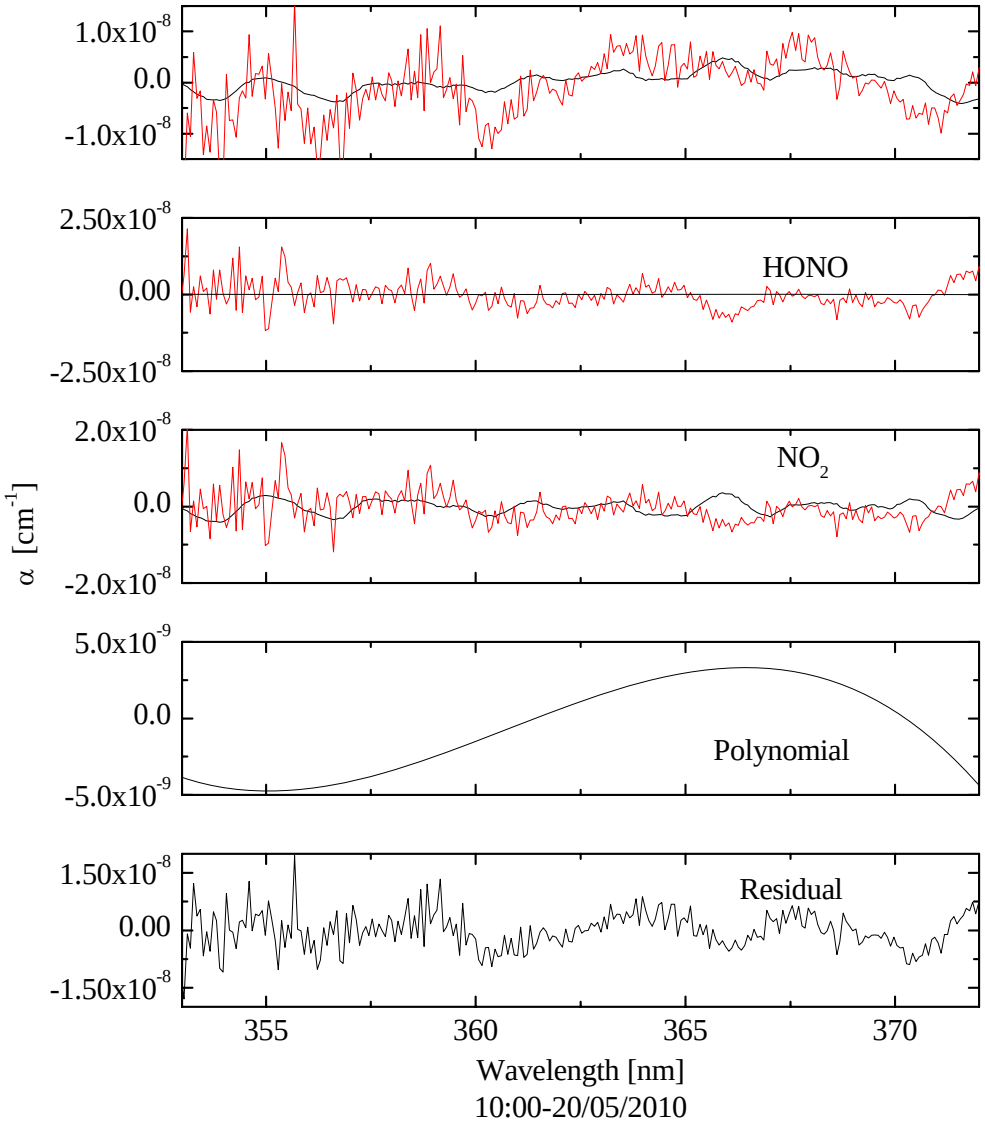
A.3 Spectral fit on 19/05/2010 (12:00)



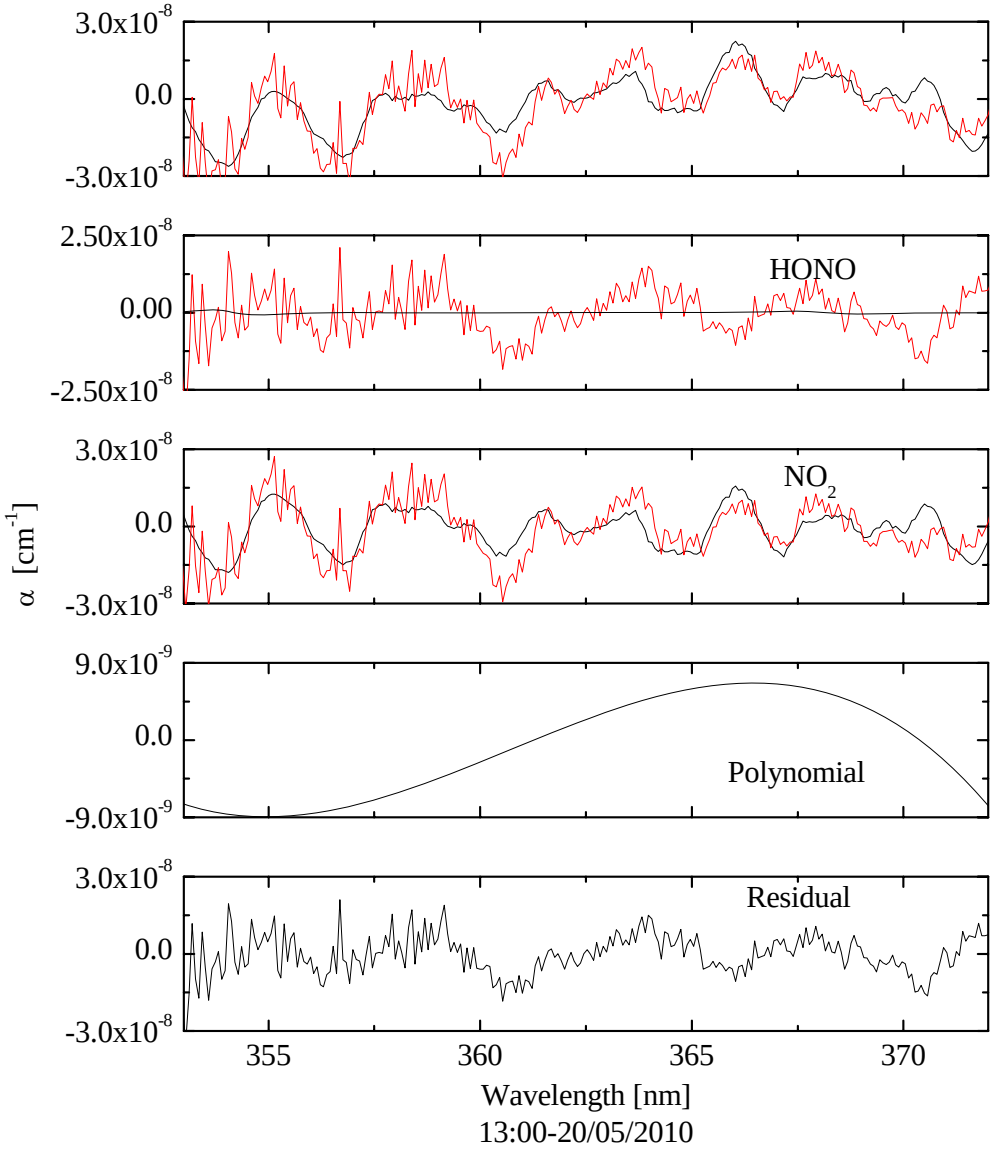
A.4 Spectral fit on 19/05/2010 (13:00)



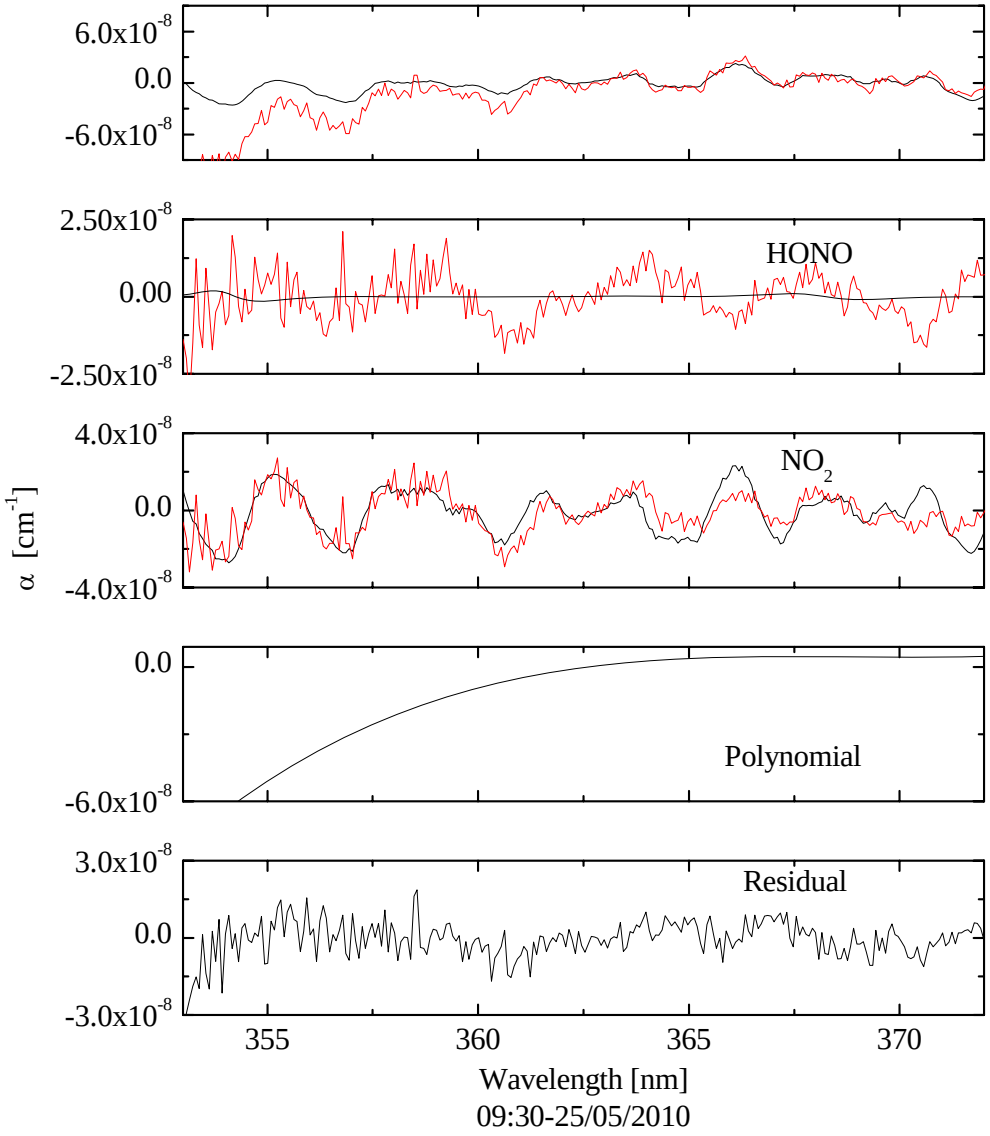
A.5 Spectral fit on 20/05/2010 (10:00)



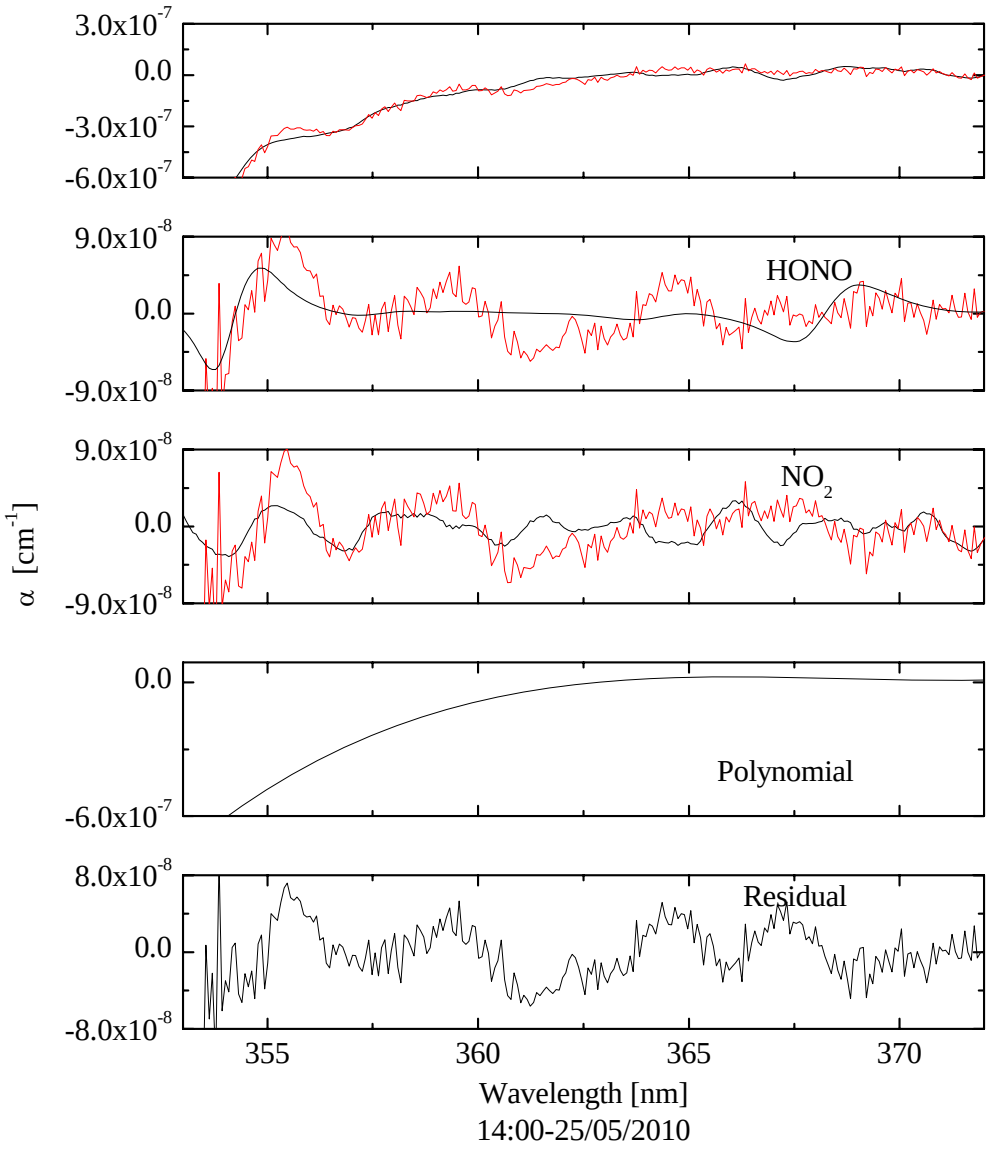
A.6 Spectral fit on 20/05/2010 (13:00)



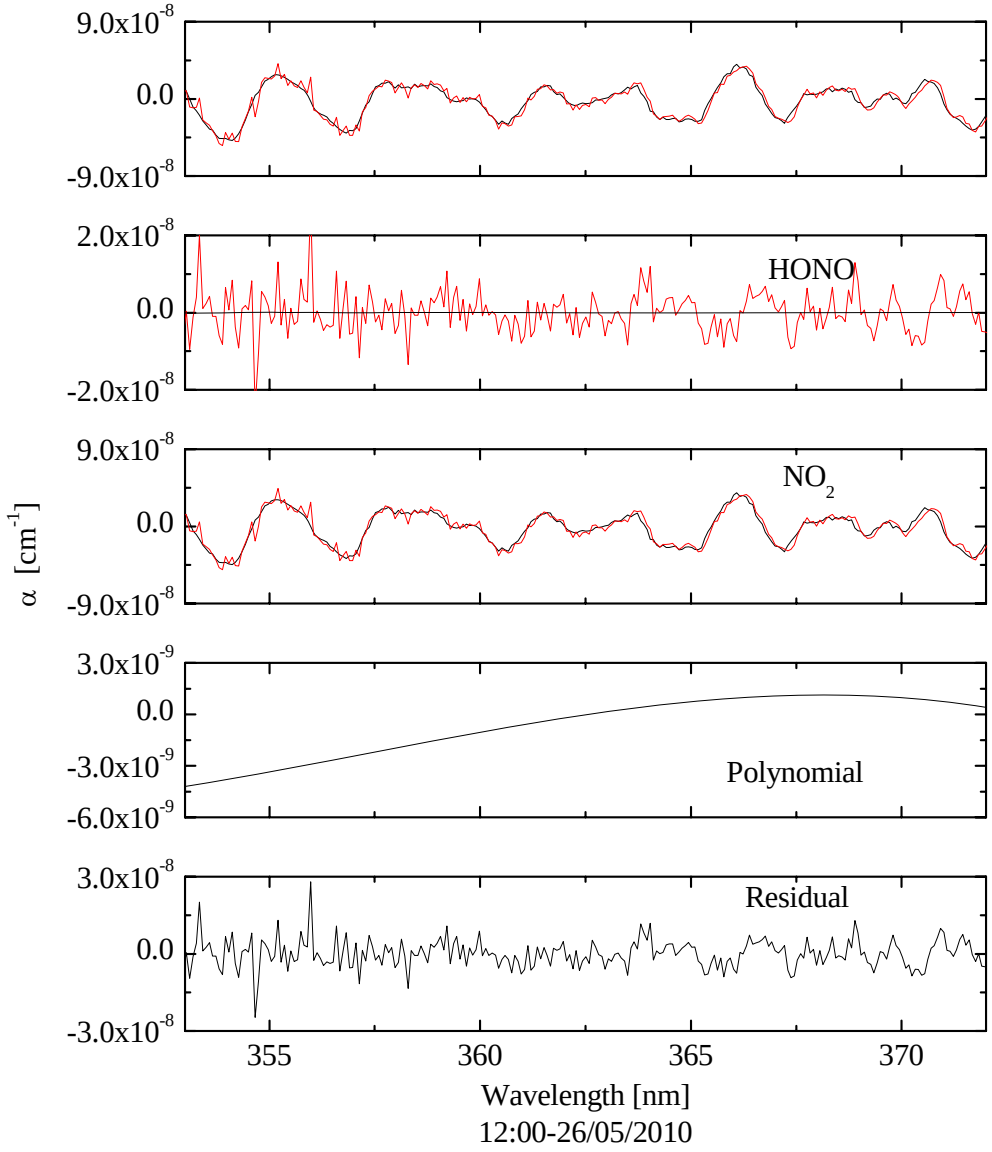
A.7 Spectral fit on 25/05/2010 (09:30)



A.8 Spectral fit on 25/05/2010 (14:00)



A.9 Spectral fit on 26/05/2010 (12:00)



A.10 Spectral fit on 26/05/2010 (14:00)

